PETRO-ELASTIC INTERPRETATION
OF SEISMIC IMPEDANCES

A DISSERTATION
SUBMITTED TO THE DEPARMENT OF GEOPHYSICS
AND THE COMMITTEE ON GRADUATE STUDENTS
OF STANFORD UNIVERSITY
IN PARTIAL FULFILMENT OF THE REQUIREMENTS
FOR THE DEGREE OF
DOCTOR OF PHILOSOPHY

By

Humberto Samuel Arévalo López

June, 2017

Includes supplemental files:

1. Matlab files for running the applet used in the dissertation *(MatlabsThesisPrograms.zip)*
2. Executable file for running the AVAIT program described inside the thesis *(AVAIT.exe)*

I certify that I have read this dissertation and that, in my opinion, it is fully adequate in scope and quality as a dissertation for the degree of Doctor of Philosophy.

Gerald Mavko, Primary Adviser

I certify that I have read this dissertation and that, in my opinion, it is fully adequate in scope and quality as a dissertation for the degree of Doctor of Philosophy.

Mark Zoback

I certify that I have read this dissertation and that, in my opinion, it is fully adequate in scope and quality as a dissertation for the degree of Doctor of Philosophy.

Stewart Levin

Approved for the Stanford University Committee on Graduate Studies.

Patricia J. Gumport, Vice Provost for Graduate Education

To my father, my mother, my wife and my children, with love.

Abstract

Success in petroleum exploration and production is closely linked to correct estimation of the properties of the subsurface. Yet, the state-of-the-art technology lacks a robust deterministic approach to integrate different physical measurements, especially if their scales are different (e.g., well versus seismic data). Such consistent integration can help in interpreting seismic data for as yet unknown petrophysical properties and conditions.

I have created a new methodology to estimate the rock properties (porosity and clay content) at the seismic scale from the seismically-derived impedances: *petro-elastic interpretation*. The basic concept behind this methodology is a rock physics phenomenon known as self-similarity where both the P- and S-wave impedances depend on the same combination of the porosity and clay content. By examining well data, I have found that this effect often does not hold, hence allowing two elastic measurements to determine two petrophysical unknowns. This discovery allows me to go from the seismic-scale impedances to desired rock properties. I tested this methodology on a dataset from NW Australia, where the interpretation results, when compared to blind-test data, fell within acceptable error bars.

The first step in this methodology is to connect two procedures: rock physics diagnostics and simultaneous seismic impedance inversion. Rock physics diagnostics is a method to find the rock physics model that quantitatively describes the measured well data. Simultaneous seismic impedance inversion uses the information from well and seismic data to obtain the elastic properties that satisfy both. The second step is to

take the inversion results (P- and S- wave impedances) and interpret them together to obtain the porosity and clay content at the seismic scale.

One implication of this methodology lies in the importance of S-wave velocity correction and prediction, highlighting its critical role in the accurate estimation of the subsurface properties.

Acknowledgements

First and foremost I want to thank my main advisor Dr. Jack Dvorkin, who by consistently correcting, guiding, showing and encouraging me sculpted a better version of who I am, all of this in a framework of loving patience and clear thinking, which helped me to become better. I will always be grateful for his presence in my life. He is the kind of scientist I would like to become one day.

Second, to Dr. Gary Mavko, for his absolute kindness, willingness to see me succeed, and profound empathetic ability towards me and my family.

Third, to my other advisor Dr. Stewart Levin, who took the time to educate, hear, assist and keep me on the correct path when no solution was evident to my eyes, he is one of the brightest and best people I have ever worked with.

Fourth, to my lovely mother and father who gave me life and always advised, believed and supported me in any enterprise I have taken.

Fifth, to my wife Amor and my kids Mariel, Humberto and Samuel, whose infinite love gave me hope in moments of despair; their mere presence fills me with joy and happiness.

Sixth, to all the people that extended me their friendship during this time at school: Dr. Amos Nur, Christopher Castillo, Lei Jin, Alex Hakso, Taylor (T.J.) Dahlke, Priyanka Dutta, Fatemeh Rassouli, Clara Yoon, Alejandro Cabrales, Patricia León, Zaira Cabrales, Parisa Cabrales, Alexandro Vera, Moisés Hernández, Marisol Morales, Moisés Hernández Jr., Alondra Hernández, Uri Wollner, Abdulla Kerimov, Kali Allison, Gabriel Lotto, Badr Al-Rumaih, Huy Quang Le, Anshuman Pradhan, Jackson

MacFarlane, Noha Farghal, Yujie Zheng, Yunfei (Iris) Yang, Abdulgader Alalli, Dr. Yi Shen, Vishal Das, Dr. Shahar Barak, Dr. Adam Allan, Dr. Ammar El-Husseiny, Dr. Felipe Aaron, Dr. Jorge Barrios, Jocelyn Barrios, Dr. Mark Brinton, Kevin McCormak and Alvaro Juárez.

Finally, to all the other people that also advised and helped me: Dr. Stephan Graham, Dr. Biondo Biondi, Dr. Mark Zoback, Dr. Tapan Mukerji, Dr. Tiziana Vanorio, Dr. Jon Claerbout, Rachel Madison, Margaret Milia, Jared Gregory, Claudia Baroni.

My very deepest and sincere gratitude to all of you. Thank you.

Table of Contents

List of Tables

List of Illustrations

List of Abbreviations

3C	Three multicomponent seismic
α *or* γ	Affine parameter for both impedances
AVO	Amplitude versus offset
AVA	Amplitude versus angle
AVAIT	Amplitude versus angle interactive tool
C	Clay content
D	Filtering function
ϕ	Porosity
φ	Angle in the *kx*-*ky* plane
f	Frequency
f_p	Function for the P-impedances
f_s	Functionfor the S-impedances
γ_p *or* α_p	Affine parameter for P-wave impedance
γ_s *or* α_s	Affine parameter for S-wave impedance
GOR	Gas-to-oil ratio
GR	Gamma ray

$GR_{vertical}$	Vertical ground roll
$GR_{horizontal}$	Horizontal ground roll
GR_z	Measured vertical ground roll
H	Filtering function
I_p	P-wave impedance
I_s	S-wave impedance
Kx	Wave-number in the x-direction
Ky	Wave-number in the y-direction
k_{up}	Upper permeability limit
K_{low}	Lower permeability limit
ν	Poisson's ratio
NPHI	Neutron porosity
r	Radius in the *kx-ky* plane
ρ	Density
RPD	Rock physics diagnostics
R_t	Electrical resistivity
SSII	Simultaneous seismic impedance inversion
S_w	Water saturation
$T_{ground\ roll}$	Time for the ground roll arrival
$T_{reflection}$	Time of arrival for each reflection

$T_{refraction}$	Time of arrival for each refraction
$T_{scatter}$	Time of arrival for each scattered noise
T_{zero}	Time of arrival at the starting point at offset-zero
TWT	Two-way travel time
v	Interval velocity
V_p	P-wave velocity
V_s	S-wave velocity

Chapter 1

Introduction

1.1 General

The oil and gas industry requires the knowledge of the subsurface properties to operate successfully; two very standard techniques to extract such properties are seismic amplitude versus offset (AVO) analysis and simultaneous seismic impedance inversion (SSII). The first technique often allows us to discriminate the hydrocarbon pay from the surrounding non-reservoir rock as well as qualitatively determine the presence of hydrocarbons versus brine in the reservoir. The second technique is much more quantitative. It uses seismic P-to-P reflection data at normal incidence as well as at an angle (offset). Because seismic reflectivity depends on the contrast of elastic properties rather than on their absolute values, this technique also requires well data to anchor the inversion results to the absolute impedances and density.

Rock physics links the elastic properties of porous rock with fluid to such petrophysical variables as the total porosity (ϕ), mineralogy (C the clay content), the pore-fluid bulk modulus and density, as well as the differential stress and the texture of the rock (unconsolidated versus cemented). Quantitatively, an expression of such links is a rock physics model. Once such a model (transform) is established, it is possible, in principle, to solve the inverse problem, i.e., derive the above-mentioned rock properties and conditions from the remotely-measured elastic properties, namely the P- and S-wave impedances (I_p and I_s, respectively) and the bulk density. Several tasks have to be accomplished prior to such interpretation:

(1) Rock physics modeling. The process of establishing such a model is termed rock physics diagnostics (RPD). It is done based on well data that include the P- and S-wave velocity (V_p and V_s, respectively), bulk density (ρ), and other measurements, such as the gamma-ray (GR), neutron porosity (NPHI), and the electrical resistivity (R_t). This task also requires rock properties that are derived from the logs measured in the well, including the total porosity and water saturation (S_w). Very important is also the knowledge of the character and properties of the pore fluid components (oil, gas, and brine), which can be derived from the pore pressure, temperature, brine salinity, oil API gravity, gas-to-oil ratio (GOR), and gas gravity (defined as the ratio of the gas density to that of air at standard conditions).

(2) Correct or re-create missing or spurious well data, especially V_s, based on the model thus established. This step is very important as physically consistent velocity data are key inputs to simultaneous impedance inversion to generate consistent volumes of seismically-derived elastic properties of the subsurface.

(3) Determine the scale dependence of the rock physics transform. This task has been often overlooked in the past and is not simply the upscaling of individual rock properties for which robust mathematical techniques have been developed. Most importantly, it addresses the question of whether rock physics relations established at the well scale

(about one ft) are applicable at the seismic scale (hundreds of ft) since the latter scale dominates the seismic interpretation field.

1.2 Description of chapters

The above mentioned general tasks include elements of both concrete applied and basic science. One such element is the V_s prediction, detailed in Chapter 2, since, we know that generating synthetic seismic gathers based on well data helps understand, calibrate, and quantitatively interpret seismic AVO responses. A crucial part of well data needed for this purpose is the V_s usually measured by the dipole tool. Such measurements are costly since they require time taken away from drilling and completion. Moreover, even where such data are available, they are sometimes unreliable, giving, for example a negative Poisson's ratio or an impossibly high Poisson's ratio in formations bearing hydrocarbons. The V_s measurements started to develop in the early 1990's, however the need of V_s started with the AVO analysis, first introduced in 1982 (Ostrander, 1982 and 1984), this time gap gave rise to the so-called V_s predictors that compute V_s from V_p, mineralogy, and the pore fluid. Such predictors are still very popular in the industry, and there are many of them, with various authors claiming that their predictor is better that those of the others. In fact, any comprehensive rock physics model is a V_s predictor by itself since it relates both V_p and V_s to porosity, lithology, fluid, and other rock properties and condition. The question is shall we use the rock physics model to predict and/or correct measured V_s or shall we combine such a model with a separate V_s predictor? Formally speaking, this question is impossible to answer since in most cases we do not have the "ground truth" velocity data (whatever the "ground truth" may mean). As a result, we reformulate the question by asking if it matters which V_s predictor we use.

Another important role of V_s measurement and prediction is in *SSII* to help estimate absolute elastic properties of the subsurface, meaning the P- and S-wave impedances and, sometimes, the bulk density. In most cases, robust inversion required the knowledge of the subsurface properties in at least one well, including V_p, V_s, and ρ. This information at the well is used to calibrate the seismic data inversion and enable extrapolation of the measured properties away from the well location. The crucial element of impedance inversion is synthetic AVO generation at the well and away from well control. Hence, the above-posed question is also important in impedance inversion.

Chapter 2 has two objectives: (a) analyze the synthetic amplitude versus angle (AVA) responses due to theoretical rock physics models and compare these responses to those produced by existing empirical predictors and (b) the implementation of an amplitude-versus-angle interactive tool (AVAIT) that allows us to understand the effects of various rock properties and conditions and V_s predictors on synthetic seismic amplitude gathers. This tool was used to analyze a number of geologic scenarios that produce various AVA classes. The tool also allows for the generation of "false" AVA responses, as often occurs in non-commercial gas accumulations and/or wet formations. An important feature of AVAIT is that it uses several V_s predictors, which enables us not only to explore reflectivity as a function of rock properties and conditions, but also as a function of the predictor used. This tool can be used to assess the sensitivity of the response to various V_s predictors and interactively select the one deemed most appropriate or simply conclude that no matter which predictor we use, the responses will be at least qualitatively the same.

Having established the V_s to be used, Chapter 3 (published as: Arévalo-López, H.S., and Dvorkin, J., 2016, Porosity, mineralogy, and pore fluid from simultaneous impedance inversion, The Leading Edge, 35, 423-429.) describes our tool to interpret petro-elastic properties based on the finding that in a quartz/clay system, I_p and I_s uniquely depend each on a different linear combination of ϕ and C. This implies that if the pore fluid is known, we can resolve these two seismically derived impedances for ϕ and C. Key to such interpretation is RPD that provides a theoretical rock physics model to quantitatively explain well data by relating I_p and I_s to ϕ, C, and pore fluid. The well data conditioned according to this model serve as input to the SSII. Poisson's ratio or the I_p/I_s ratio serves as the pore fluid identifier. We give an example of such rock-physics-based interpretation of seismically derived impedances for rock properties based on well and seismic data from an offshore oil field.

Another of the aforementioned tasks is described in Chapter 4 (published as: Arévalo-López, H.S., and Dvorkin, J.P., 2017, Rock physics diagnostics of a turbidite oil reservoir offshore Northwest Australia, Geophysics, 82(1), MR1-MR13.) because interpreting seismic data for petrophysical rock properties requires a rock physics model that links the petrophysical rock properties to its elastic properties, such as velocity and impedance. Such a model can only be established from controlled experiments where both groups of rock properties are measured on the same samples. A prolific source of such data is wellbore measurements. We utilize data from four wells drilled through a clastic offshore oil reservoir to perform RPD, i.e., to find a theoretical rock physics model that quantitatively explains the measurements. Using the model, we correct questionable well curves. Moreover, a crucial purpose of RPD is to go beyond the settings represented in the wells and understand the seismic signatures of rock properties varying in a wider range. With this goal in mind, we use the model to generate synthetic seismic gathers from perturbational modeling to address "what-if" scenarios not present in the wells.

The second technique to quantitatively estimate remotely the properties of the subsurface is described in Chapter 5 (published as: Arévalo-López, H.S., and Dvorkin, J.P., 2017, Simultaneous impedance inversion and interpretation for an offshore turbuditic reservoir, Interpretation, 5(3), SL9-SL23.), where by using SSII, we obtained I_p and I_s volumes from angle stacks at a siliciclastic turbidite oil reservoir offshore NW Australia. The model-corrected V_s in the wells were used as input to impedance inversion. The inversion parameters were optimized in small vertical sections around two wells to obtain the best possible match between the seismic impedances and the upscaled impedances measured at the wells. Special attention was paid to the seismically derived I_p/I_s ratio since we relied on this parameter for hydrocarbon identification. Even after performing cross-correlation between the angle gather stacks to correct for two-way travel time (TWT) shifts to align the stacks, these stacks did not show a coherent AVA dependence. To deal with this common problem, we corrected the mid and far stacks by using the near and ultra-far stacks as anchoring points for fitting a $\sin^2$ AVA curve. This choice allowed us to match the seismically derived I_p/I_s ratio with that predicted by the rock physics model in the reservoir. Finally, the rock physics model was used to interpret these I_p and I_s for the fluid, ϕ, and mineralogy. The new paradigm in our inversion/interpretation workflow is that the ultimate quality control of the inversion is in an accurate deterministic match between the seismically-derived petrophysical variables and the corresponding upscaled depth curves at the wells. Our interpretation is very sensitive to the inversion results, especially the I_p/I_s ratio. Despite this fact, we were able to obtain accurate estimates of porosity and clay content in the reservoir and around it.

The tool that allows the petro-elastic interpretation is further studied in Chapter 6 since legacy laboratory data obtained on a large number of clean and shaly sand samples indicate that the dependence of I_p and I_s on ϕ and C can be reduced to their dependence on a linear combination of ϕ and C: $I_p(\phi,C)=f_p(\phi+\gamma_p C)$ and $I_s(\phi,C)=f_s(\phi+\gamma_s C)$. This effect is called *"self-similarity"*. It appears that in the above-mentioned dataset $\gamma_p = \gamma_s$, meaning that both impedances depend on the same linear combination of ϕ and C. Hence, in this case, two elastic measurements, I_p and I_s, cannot be independently and uniquely resolved for ϕ and C. By exploring this phenomenon on other datasets (well data), we find that in some cases, $\gamma_p \neq \gamma_s$, thus allowing us to uniquely interpret the impedances for ϕ and C. We also find that this uniqueness is a property of the rock physics model that describes the specific dataset under examination, meaning that in some models $\gamma_p \approx \gamma_s$, while in other models these coefficients are distinctively different form each other. By analyzing a number of rock physics models relevant to real sediment, we investigate where measured I_p and I_s can be potentially uniquely resolved for the unknown petrophysical variables and where they cannot. Such model-based analysis is an important step in evaluating the feasibility of interpreting SSII results for petrophysical unknowns.

The last part of this thesis involves two independent projects: (a) the percolation through porous media and (b) the attenuation of ground roll via a polarization filter in the fk_xk_y domain for 3D-3C multicomponent synthetic seismic data.

In Chapter 7 the percolation though porous media was analyzed by estimating the effective permeability with a Darcy's flow simulator in a random composite with properties taken from two data-sets: Ottawa sand mixed with different amounts of kaolinite (Yin, 1992), and the Fontainebleau measurements from a sandstone quarry (Bourbie, et al., 1987). The results indicate that the percolation has two distinctive regimes: (1) one stable, for random composites bigger than 13x13x13 elements where the increment in system elements has no effect on the percolation, as anticipated from the theoretical boundaries for a 3D cubic model (Sahimi, M, 1990); and (2) the double percolation system (Sumita et al., 1992), where the percolation is a function of both the percentage of non-permeable elements and the size of the model

In Chapter 8 we tackle the issue that the vertical component of seismic wave reflections is contaminated by ground roll. A common method of removing such ground roll from the vertical component is via velocity filtering and/or multichannel stacking. 3C acquisition technology allows for directly estimating the ground roll components and then removing their effects from the vertical component. Our goal is to implement two methods, first, design this ground roll removal in the Fourier domain by (a) estimating the azimuth of the ground roll propagation from the 3C horizontal components; (b) rotating it by 90°; and (c) subtracting the result from the vertical component. The main obstacle is the uneven acquisition geometry where the cross-line sampling is sparser than the in-line sampling. Directly using the differently spaced data distorts the kx-ky representation of the ground roll. To address this issue, the second method involves modifying the filter used with even sampling to tackle the actual geometry. The method was successfully tested on a multicomponent synthetic dataset based on a 5-layer (4 interfaces) earth model which also included shallow scatterers to simulate near-surface inhomogeneities. Our method also helps remove the effect of these scatterers on the vertical component.

The final Chapter are the general conclusions from all the chapters.

Chapter 2

Shear-wave velocity prediction

2.1 Abstract

Generating synthetic seismic gathers based on well data helps understand, calibrate, and quantitatively interpret seismic AVO responses. A crucial part of well data needed for this purpose is the S-wave velocity (V_s) usually measured by the dipole tool. Such measurements are costly since they require time taken away from drilling and completion. Moreover, even where such data are available, they are sometimes unreliable, giving, for example, a negative Poisson's ratio or an unreasonably high Poisson's ratio in formations bearing hydrocarbons.

AVO analysis was first introduced in 1982 and published in 1984 (Ostrander, 1982 and 1984), while the dipole tool development started in the early 1990's. This time gap gave rise to the so-called V_s predictors that compute V_s from V_p, mineralogy, and the pore fluid. Such predictors are still very popular in the industry and there are many of them.

To this end, we pose a question: *How do the differences between various V_s predictors affect one of the ultimate goals of V_s prediction, that is, producing a synthetic AVO gather catalogue to serve as a field guide for interpreting the observed seismic*

anomaly for rock properties and conditions?

Another important role of V_s measurement and prediction is in simultaneous impedance inversion that helps estimate absolute elastic properties of the subsurface, meaning the P- and S-wave impedances and, sometimes, the bulk density. In most cases, robust inversion required the knowledge of the subsurface properties in at least one well, including V_p, V_s, and bulk density (ρ). This information at the well is used to calibrate the seismic data inversion and enable extrapolation of the measured properties away from the well location. The crucial element of impedance inversion is synthetic AVO generation at the well and away from well control. Hence, the above-posed question is also important in impedance inversion.

This chapter has two objectives: (a) analyze the synthetic amplitude versus angle (AVA) responses due to theoretical rock physics models and compare these responses to those produced by existing empirical predictors and (b) the implementation of an amplitude-versus-angle interactive tool (AVAIT) that allows us to understand the effects of various rock properties and conditions and V_s predictors on synthetic seismic amplitude gathers. This tool was used to analyze a number of geologic scenarios that produce various AVA classes. The tool also allows for the generation of "false" AVA responses, as often occurs in non-commercial gas accumulations and/or wet formations. An important feature of AVAIT is that it uses several V_s predictors, which enables us not only to explore reflectivity as a function of rock properties and conditions, but also as a function of the predictor used. This tool can be used to assess the sensitivity of the response to various V_s predictors and either interactively select the one deemed most appropriate or simply conclude that no matter which predictor we use, the responses will be at least qualitatively the same.

2.2 V_s predictors

How precise does a V_s predictor has to be? What is the criterion? The criterion should be set by the task, namely, why we need to predict V_s. In this study, we entertain one particular criterion: V_s as needed for a pore fluid and lithology indicator, hence the predictor must be accurate enough in its ability to discriminate pore fluids and lithologies. However, reliable shear-wave velocity (V_s) measurements remain scarce, mainly due to the dispersion and anisotropy the shear waves undergo during their propagation in the subsurface (Cheng, 2015). The main use of V_s is to estimate the elastic properties input into the synthetic seismic forward models used to understand the seismic amplitude response versus angle (Ostrander, 1984) via synthetic seismic forward modeling. Such synthetic seismic modeling is often carried out by means of linear approximations to the Zoeppritz equations (Aki and Richards, 2002; Shuey, 1985). These approximations are useful as they explicitly describe the roles of various elastic properties, such as P- and S-wave velocity and density, as well as their contrast at the interface on reflection amplitudes. Yet, in forward modeling we can directly use the exact Zoeppritz equations and, hence, the various published approximations thereof are not employed here.

Let us reiterate that because the amplitude at offset not only depends on V_p and density, but also on V_s, the latter is important in the interpretation of AVA signatures.

In order to overcome the absence of V_s, a host of methods that predict V_s from V_p have been introduced in the past 50+ years (e.g., Picket, 1963; Williams, 1990; Krief, 1990;

Greenberg and Castagna, 1992; Vernik et al., 2002). Other predictors (e.g., Dvorkin, 2007b) use rock physics models to predict both V_p and V_s as a function of porosity, mineralogy, and other rock properties and conditions and, as such, can be also qualified as V_s predictors. The six predictors that we will use in our numerical experiments are described below, all of them assume that the pore-fluid is water.

The Greenberg-Castagna equations (Greenberg and Castagna, 1992) are:

$$V_s = \frac{1}{2}\left\{\left[\sum_{i=1}^{L}\left(f_i \sum_{j=1}^{N_i} a_{ij} V_p^j\right)\right] + \frac{1}{\left[\sum_{i=1}^{L}\left(\frac{f_i}{\sum_{j=1}^{N_i} a_{ij} V_p^j}\right)\right]}\right\} \tag{1}$$

$$\sum_{i=1}^{L} f_i = 1 \tag{2}$$

where L is the number of pure-mineral lithological constituents, N is the order of the polynomial, f is the volume fraction for each constituent, V_p is the measured P-wave velocity in km/s, V_s is the estimated S-wave velocity, also in km/s, and the values a_{ij}, depending on the lithology, are taken from the following table:

Table 2.1. Greenberg and Castagna aij values for different lithologies.

Lithology	a_{i2}	a_{i1}	a_{i0}
Sandstone	0	0.80416	-0.85588
Shale	0	0.76969	-0.86735
Limestone	-0.05508	1.01677	-1.03049
Dolomite	0	0.58321	-0.07775

Vernik's equations (Vernik et al., 2002) are:

$$\mathrm{V_s} = \sqrt{-1.267 + 0.372\mathrm{V_p^2} + 0.00284\mathrm{V_p^4}} \tag{3}$$

for wet sand and

$$V_s = \sqrt{-0.79 + 0.287V_p^2 + 0.00284V_p^4} \tag{4}$$

for wet shale, where V_p is the measured P-wave velocity and V_s is the estimated S-wave velocity, both in km/s.

The Williams' equations (Williams, 1990) are:

$$\mathrm{V_s} = 0.846\mathrm{V_p} - 1.088 \tag{5}$$

for wet sand and

$$\mathrm{V_s} = 0.784\mathrm{V_p} - 0.893 \tag{6}$$

for wet shale, where V_p is the measured P-wave velocity, and V_s is the estimated S-wave velocity, both in km/s.

The Pickett equations (Pickett, 1963) are:

$$V_s = \frac{V_p}{1.9} \tag{7}$$

for limestone and

$$V_s = \frac{V_p}{1.8} \tag{8}$$

for dolomite, where V_p is the measured P-wave velocity and V_s is the estimated S-wave velocity, where both V_p and V_s have to have the same units.

The Krief "critical porosity" equation (Krief, 1990) is:

$$\frac{V_{p-saturated}^2 - V_{fluid}^2}{V_{s-saturated}^2} = \frac{V_{p-mineral}^2 - V_{fluid}^2}{V_{s-mineral}^2} \tag{9}$$

where $V_{p\text{-}saturated}$ is the measured P-wave velocity for the rock with given fluid, $V_{p\text{-}mineral}$ is the P-wave velocity of the pure mineral, $V_{s\text{-}mineral}$ is the S-wave velocity of the pure mineral, V_{fluid} is the velocity of the pore fluid, and $V_{s\text{-}saturated}$ is the estimated S-wave velocity, where the units have to be internally consistent.

The Dvorkin-Raymer equations (2007b) are:

$$V_{s-Dry} = (1-\phi)^2 V_{s-Mineral}\,, \tag{10}$$

$$V_{s-saturated} = V_{s-Dry}\sqrt{\frac{\rho_{b-Dry}}{\rho_{b-Saturated}}} \tag{11}$$

where $V_{s\text{-}Dry}$ is the S-wave velocity of the rock frame, ϕ is the porosity fraction of the rock, $V_{s\text{-}Mineral}$ is the S-wave velocity of the constitutive minerals, $\rho_{b\text{-}Dry}$ is the density of the rock frame, $\rho_{b\text{-}saturated}$ is the density of the saturated rock, and $V_{s\text{-}Saturated}$ is the estimated S-wave velocity. All these formulas resulted from empirical fitting to V_p and V_s measurements from well data, mostly in fast (consolidated) rocks.

There are a number of theoretical rock physics models that predict both V_p and V_s as a function of porosity, mineralogy, and fluid (Mavko et al., 2009). As such, these models can be also categorized as V_s predictors. Because in the case study described below we established that one specific theoretical model, the constant-cement model (CCM) explains the well data, this is one of the theoretical models we discuss here. The other theoretical model under examination is the stiff-sand model (STM), also described by Mavko et al., 2009.

To describe CCM, let us first examine the soft-sand model (SSM). SSM (Dvorkin et al., 2014) is also called the modified lower Hashin-Shtrikman bound. This model heuristically describes the elastic behavior of a pack of identical elastic spheres where porosity reduction is due to the introduction of non-cementing particles into the pore space (Figure 2.1, top).

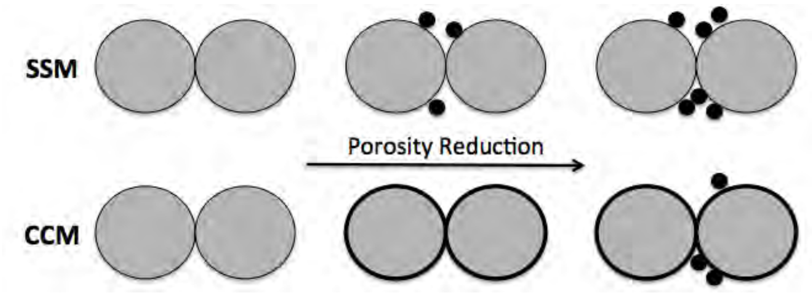

Figure 2.1. Schematic representation of the soft-sand (top) and constant-cement (bottom) models. SSM connects two endpoints in the velocity-porosity plane: the high-porosity endpoint is at the critical porosity ϕ_c while the zero-porosity endpoint corresponds to the elastic properties of the non-porous mineral matrix which can be a mixture of various pure mineralogical components.

The elastic moduli of the high-porosity-endpoint dry grain pack at ϕ_c can be estimated from the Hertz-Mindlin contact theory (Mindlin, 1949) as

$$K_{HM} = [\frac{n^2(1-\phi_c)^2 G^2}{18\pi^2(1-\nu)^2}P]^{\frac{1}{3}}, \quad G_{HM} = \frac{5-4\nu}{5(2-\nu)}[\frac{3n^2(1-\phi_c)^2 G^2}{2\pi^2(1-\nu)^2}P]^{\frac{1}{3}}, \tag{12}$$

where ***P*** is the hydrostatic confining pressure applied to the pack; ***n*** is the coordination number (the average contact number per grain), about 6 to 8; and ***G*** and ***ν*** are the shear modulus and Poisson's ratio of the mineral phase, respectively.

In Equation (12) it is assumed that the grains have infinite friction force (no slip) at their contacts. If we allow only the fraction f of these contacts to have infinite friction while the rest of the contacts are frictionless and can slip, the equation for K_{HM} does not change but G_{HM} becomes now

$$G_{HM} = \frac{2+3f-\nu(1+3f)}{5(2-\nu)}[\frac{3n^2(1-\phi_c)^2 G^2}{2\pi^2(1-\nu)^2}P]^{\frac{1}{3}}. \tag{13}$$

We call parameter f the shear correction factor.

Finally, at any porosity $f < f_c$

$$K = \left(\frac{\emptyset/\emptyset_c}{K_{HM}+\frac{4}{3}G_{HM}} + \frac{1-\emptyset/\emptyset_c}{K+\frac{4}{3}G_{HM}}\right)^{-1} - \frac{4}{3}G_{HM},$$

$$G = \left(\frac{\emptyset/\emptyset_c}{G_{HM}+Z_{HM}} + \frac{1-\emptyset/\emptyset_c}{G+Z_{HM}}\right)^{-1} - Z_{HM},\ Z_{HM} = \frac{G_{HM}}{6}\left(\frac{9K_{HM}+8G_{HM}}{K_{HM}+2G_{HM}}\right) \tag{14}$$

To understand CCM (also in Dvorkin et al., 2014), assume that a high-porosity grain pack has some initial cementation around the grains but any further porosity reduction is due to the deposition of non-cementing material into the pore space (Figure 2.1, bottom). The functional form for CCM is exactly the same as given by Equation 14. The only difference is that instead of using the Hertz-Mindlin endpoint given by K_{HM}, G_{HM}, and z_{HM}, we need to use the endpoint elastic properties at the porosity smaller than the critical porosity, namely the porosity at the initial cementation endpoint (Figure 2.1 bottom, the middle panel).

A way of systematically obtaining these new endpoint elastic constants is to use the Hertz-Mindlin equations and assume an unrealistically high coordination number ***n***. This approach is purely a mathematical convenience, since a pack of identical spherical grains cannot have a coordination number much higher than 8. The resulting CCM curve should not be extended into the porosity range above the porosity of the initial cementation.

In both SSM and CCM, the elastic moduli of the mineral phase are obtained using Hill's (1952) average of the elastic moduli of the constituents, such as quartz and clay.

The counterpart of the SSM is the STM where the bulk and shear moduli at porosity ϕ can be calculated as:

$$K_{Dry} = \frac{1}{\left[\frac{\phi}{K_{HM}+\frac{4G}{3}} + \frac{1-\phi}{K_{HM}+\frac{4G}{3}}\right]} - \frac{4G}{3} \tag{15}$$

$$G_{Dry} = \frac{1}{\left[\frac{\phi}{G_{HM}+\frac{G}{6}\left[\frac{9K+8G}{K+2G}\right]} + \frac{1-\phi}{G+\frac{G}{6}\left[\frac{9K+8G}{K+2G}\right]}\right]} - G_{HM} + \frac{G}{6}\left[\frac{9K+8G}{K+2G}\right] \tag{16}$$

Where K_{HM} and G_{HM} are the bulk and shear moduli of the dry pack, respectively, calculated from Hertz-Mindlin theory, K and G are the bulk and shear moduli of the grains, respectively. In this case, unlike in CCM, the coordination number has to be physically realistic, namely between 5 and 8.

2.3 Modeling in the AVA space

Because different pore fluids have distinctive effects on the AVA response, namely on the seismic amplitude plotted against the offset/incidence angle before stacking, also known as the AVO/AVA effect (Ostrander, 1984), V_s predictors have been extensively used in hydrocarbon exploration. The seismic analysis of this pre-stack property can aid in the location of undiscovered reservoirs and in the delimitation of the extent of hydrocarbon bearing zones.

Seismic amplitudes have been studied for more than 100 years. The theoretical basis for these studies is the partitioning of the seismic energy at an interface described mathematically by Knott in 1893 and reformulated in simpler terms by Zoeppritz (1919). The most popular approximation to the Zoeppritz equations is that of Aki and Richards (2002), that was further simplified by Shuey in 1985:

$$\mathrm{R}(\theta) \approx \mathrm{A} + \mathrm{B}\sin^2(\theta) + \mathrm{C}[\sin^2(\theta) - \tan^2(\theta)] \tag{17}$$

where:

$$A = \frac{1}{2}\left(\frac{\Delta V_p}{V_p} + \frac{\Delta\rho}{\rho}\right);\ B = \frac{1}{2}\frac{\Delta V_p}{V_p} - 2\left(\frac{V_s}{V_p}\right)^2\left(\frac{\Delta\rho}{\rho} + \frac{2\Delta V_s}{V_s}\right);\ C = \frac{1}{2}\frac{\Delta V_p}{V_p}, \tag{18}$$

Where the Δ terms refer to the difference for the same property between the lower and upper layers at the interface, while V_p, V_s and ρ refer to the average of each property between these two layers, and θ is the angle of incidence. For angles below $\theta = 30°$ the C term may be neglected, thus reducing Equation 16 to the form known as "the two term approximation". The A term is also known as the "intercept" and the B term as the "gradient". The cross-plot of these two variables is called the AVA or intercept-gradient space, and is used to assess the pore fluid at a prospective well location.

2.4 Methodology for predicting Vs

In order to compare the AVA response due to different shear-wave velocity predictors, we require a predefined P-wave velocity as input to the V_p-based V_s predictors. The predictions of V_s are then compared in a common space that is related to the specific objective, e.g., fluid discrimination, to ascertain their differences. The work-flow (Figure 2.2) used to estimate the shear wave velocity with the different predictors is as follows:

1) The elastic properties of each pore fluid, e.g., water, oil, and gas, are estimated by the Batzle and Wang (1992) equations using the salinity, gas-oil-ratio, pressure, temperature, as well as the oil API density and gas gravity presented as an example in Table 2.2.
2) We then used the soft-sand model to generate P-wave velocity values based on the porosity and clay content, for each pore fluid, for the seal and for the reservoir.

These parameters are interactively chosen as a function of porosity and clay content range in a Matlab® applet (ModelAVOUncertainty.exe) created to compare the properties of the different predictors (Figures 2.3-2.19). The differential pressure, a required input in some of the rock physics models is computed as 40 MPa minus the pore pressure listed in Table 2.2.

3) The calculated V_p values for the reservoir saturated with each pore fluid and the seal were then used as inputs for the Greenberg-Castagna, Vernik, and Williams (the latter three for siliciclastic) or Picket, Krief and Greenberg-Castagna predictors to estimate V_s for carbonates.

Table 2.2. Example parameters used for the numerical experiments below.

Property	*Value*
Salinity	150,000 ppm
Oil gravity	30° API
Gas gravity	0.65
Gas to oil Ratio	160 l/l
Pore pressure	20 MPa
Temperature	75° C

Once the Vs values have been estimated, the respective seismic responses were compared in the AVA space as a function of the respective pore fluid (Figures 2.3 - 2.19). In order to quantify the differences between the predictors we:

- computed the amplitude of the seismic response at each angle of incidence for each pore fluid at the interface between the reservoir and the seal.
- performed a linear regression to $\sin^2 \theta$ for angles below 25^o to obtain the intercept and gradient between the seal rock and the water or hydrocarbon bearing reservoir, and
- plotted the results in the AVA space.

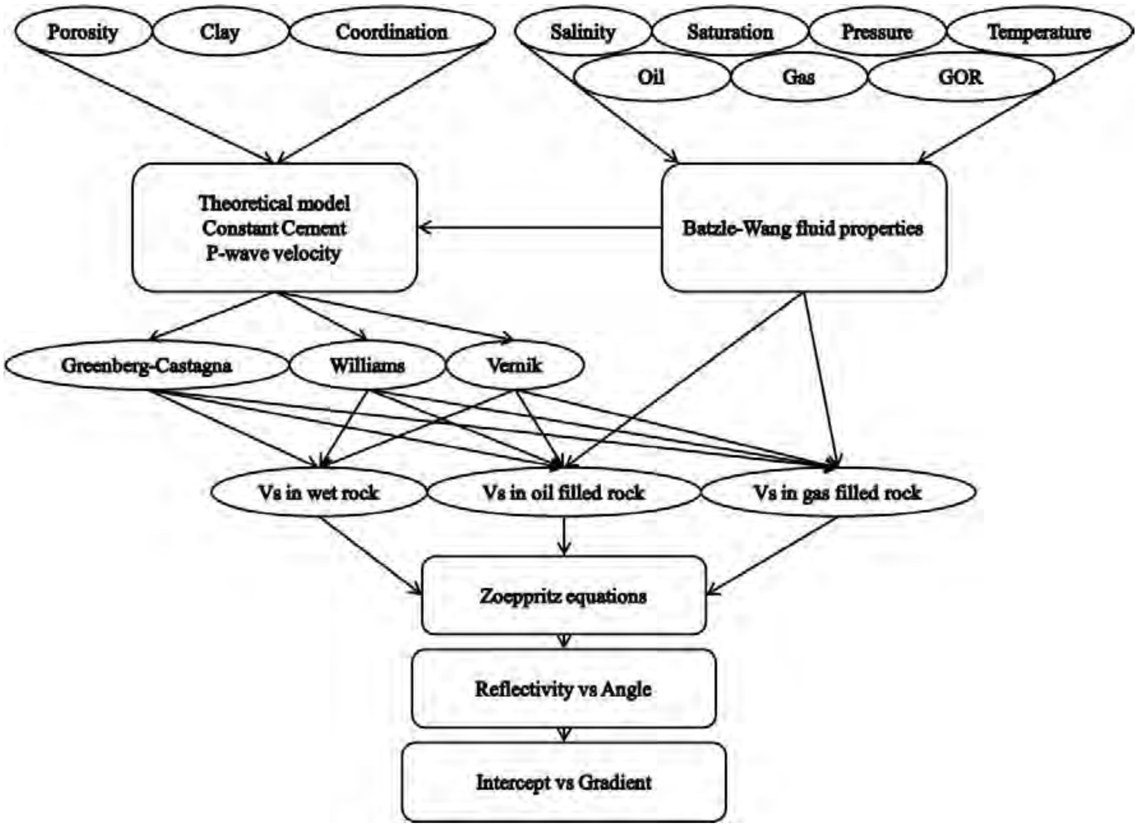

Figure 2.2: Workflow used to generate the different Vs predictions and their comparison in the AVA space.

Using this methodology we generated different geological scenarios to compare the effect of the V_s predictors and differences ensuing from using them. The following scenarios are plausible situations in siliciclastic hydrocarbon-bearing reservoirs used in the examples below:

- High porosity, low clay content reservoir combined with a low porosity, high clay content seal (Figure 2.3).
- High porosity, low clay content reservoir combined with a high porosity, high clay content seal (Figure 2.4).
- Low porosity, low clay content reservoir combined with a low porosity, high clay content seal (Figure 2.5).
- Low porosity, low clay content reservoir combined with a high porosity, high

clay content seal (Figure 2.6).

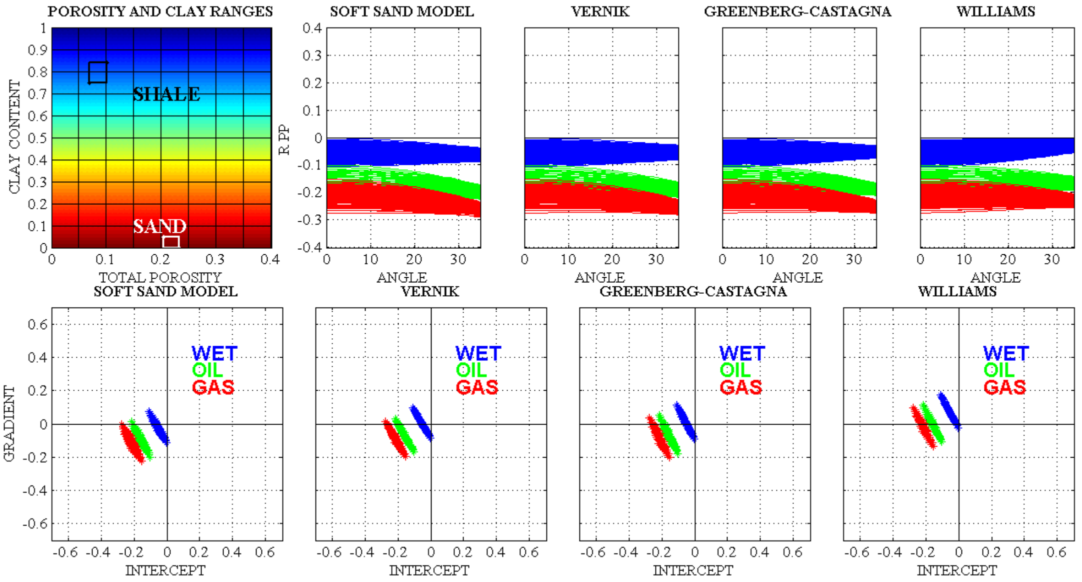

Figure 2.3: Soft sand model (SSM). High porosity, low clay content reservoir with a low porosity, high clay content seal (upper left corner) with the amplitude versus angle response for each Vs predictor (upper right side) and gradient versus intercept computed from the respective AVA curves. The color indicates the pore fluid: blue for water; green for oil and red for gas.

Using a different model for the P-wave velocities will modify the estimation of V_p as a function of porosity and clay content and, as a result, the predicted V_s values. For this purpose, Figure 2.7 was generated using the stiff-sand model for the same reservoir and seal characteristics as those used to generate Figure 2.3. The response is similar to the one obtained with the soft-sand model, however the positions of the possible responses in the gradient-intercept space changed. In the case where we used the stiff-sand model, the intercept increased and the gradient decreased towards negative values. One conclusion following the above examples where both the sand’s and shale’s elastic properties were computed according to SSM is that the seismic response is fairly stable among the three V_s predictors used (SSM, Vernik (2002), Greenberg-Castagna (1992)). The Williams (1990) predictor provides slightly higher gradient than the previous three predictors. Still, using any of the above four predictors does not produce qualitative variations in the

AVA response and, as a result, in seismic-based interpretation for fluid and lithology.

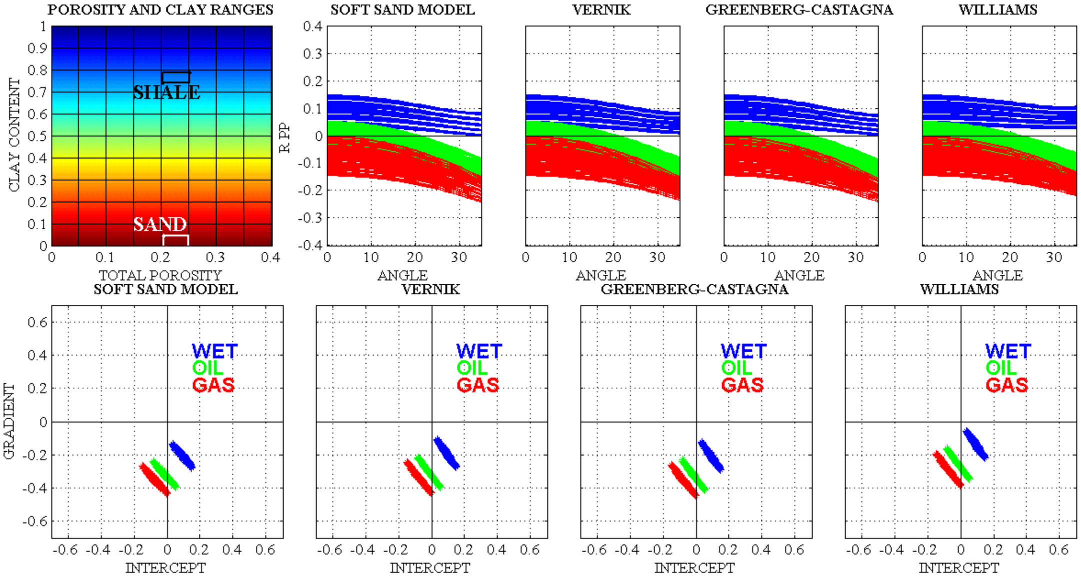

Figure 2.4: Soft sand model (SSM). High porosity, low clay content reservoir with a high porosity, high clay content seal. All other inputs are the same as in Figure 2.3.

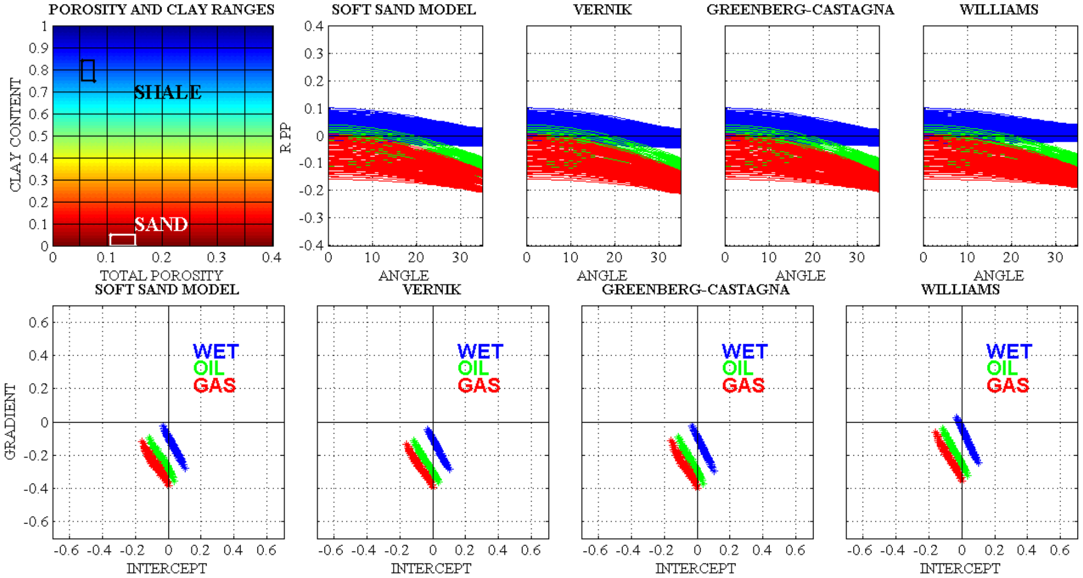

Figure 2.5: Soft sand model (SSM). Low porosity, low clay content reservoir with a low porosity, high clay content seal. All other inputs are the same as in Figure 2.3.

Using STM (Figure 2.7) versus SSM (Figure 2.3) with the same inputs produces different AVA responses, yet, within each separate model, different V_s predictors produce quite similar results. In this case, we only provide one example with the porosity and clay content ranges the same as in Figure 2.3. Other examples not shown here also provide qualitatively similar AVA response among the four predictors used.

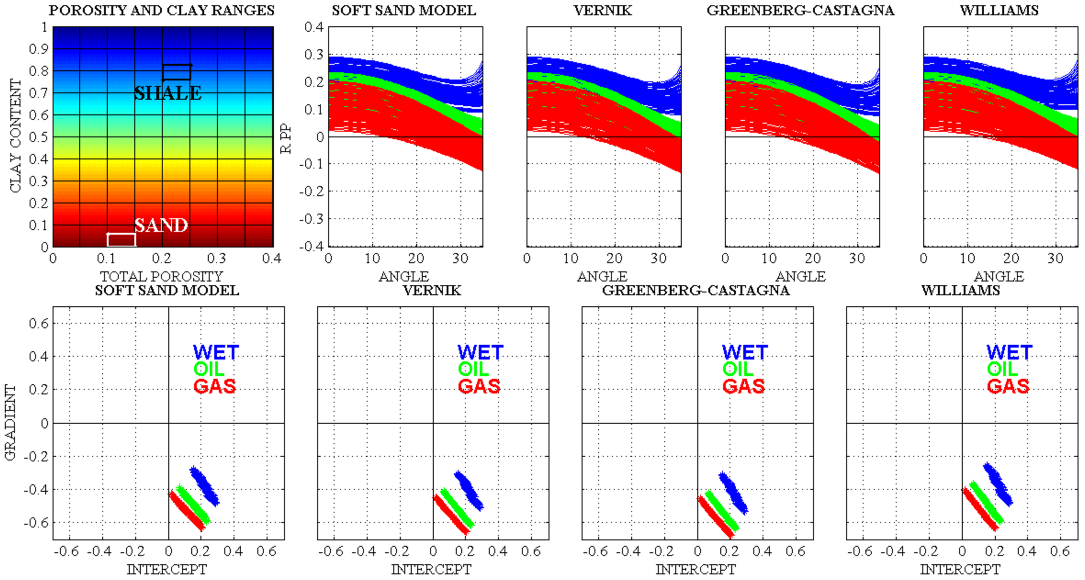

Figure 2.6: Soft sand model (SSM). Low porosity, low clay content reservoir with a higher porosity, high clay content seal. All other characteristics are as in Figure 2.3.

The question then becomes, which of the predictors to use? For consistency, we recommend the model-based predictors, since both V_p and V_s are consistently computed from porosity, mineralogy, and fluid, based on the same model. This choice will also simplify the interpretation of elastic seismically-derived variables. (See the field example in the following chapters.) Of course, the simple applets presented here should be used in each specific field study to ensure that indeed the difference between different predictors is small as far as the seismic response is concerned.

The sensitivity of various inputs, such as porosity, clay content, pressure and temperature, as well as the pore-fluid properties is explored later in this chapter.

In the applets shown in Figures 2.3 to 2.7, the selection of the porosity and clay content is inside an interactively selected rectangle in the porosity-clay space. In essence, we assume that porosity and clay content are not related to each other and vary within the selected ranges according to uniform probability distribution.

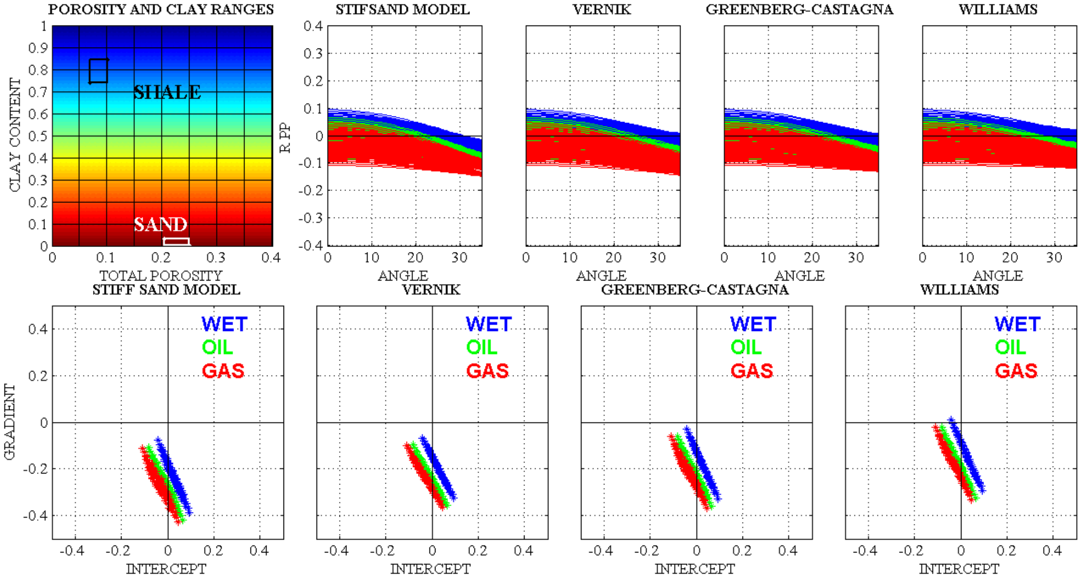

Figure 2.7: Stiff-sand model (STM) applied to generate a high porosity, low clay content reservoir with a low porosity, high clay content seal (upper left corner). The other parameters are the same as used in Figure 2.3.

At the same time, many examples (e.g., Dvorkin et al., 2014) show that porosity and clay content can be related to each other. In sand as it evolves from very clean to shaly state, the higher the clay content the smaller the porosity. The turning point in this trend is where the entire pore space in the zero-clay sand is filled with the shale that has its own, non-zero, porosity. Past this point, the porosity of the sand/shale system increases with the increasing shale content until we arrive at a 100% shale rock (illustrated in Figure 2.8).

This effect is quantified by the Thomas and Stieber (1975) model. This phenomenon is often observed in well data where the porosity is plotted versus a shale indicator, e.g., a gamma ray curve (Dvorkin et al., 2014). The Thomas-Stieber model was used by Marion (1990) who conducted lab experiments and quantified the impacts of this model on the elastic and fluid flow properties.

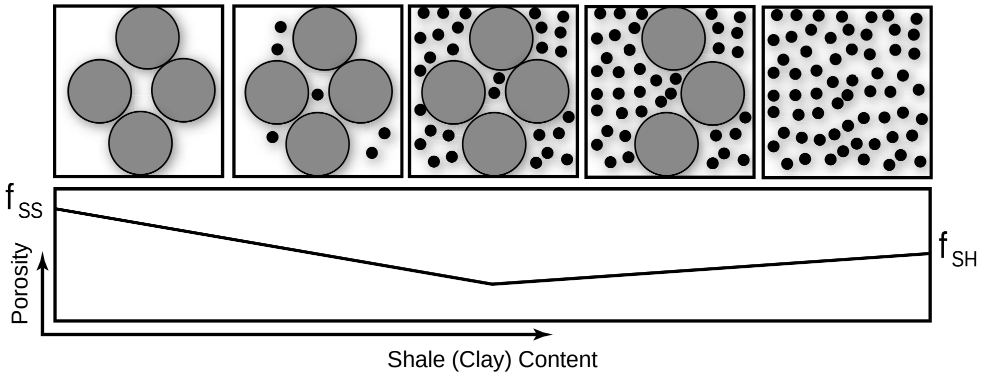

Figure 2.8: Transition from zero-shale (pure) sand (large grains shown on the left) to 100% (pure) shale (small grains on the right). The porosity of the sand end-member is ϕ_{SS} while that of the shale end-member is ϕ_{SH}. The porosity at the turning point is ϕ_{SS}-ϕ_{SH}. It is smaller than both end-member porosity values.

The Thomas-Stieber model allows us to select the ranges of porosity and clay content in a geologically-consistent way for both sand and shale. The setup process is essentially the same as in the above-discussed applet. The difference is that now the porosity-clay domains are fit into a *V*-shape like in Figure 2.8 and are bounded by the upper and lower V-shape lines (the oblique black diamonds in Figure 2.9).

Using this geologically-consistent approach, we compared the responses with the same characteristics but within the geologically-consistent porosity and clay ranges. The results for the case of high porosity and low clay content in the reservoir and the seal with low porosity and high clay volume are shown in Figure 2.9. Once again, the AVA responses due to different V_s predictors are similar to each other.

Another example for high-porosity sand and high-porosity shale is shown in Figure 2.10. The response difference between different V_s predictors is, once again, is small, except for the Williams (1990) predictor that shows positive gradient for some of the porosity-clay combinations. Generally, no matter which predictor we use, we can separate the responses to the fluid, water, oil, and gas.

Other plausible scenarios not shown here may include

- Tight reservoir: low porosity, medium clay content reservoir with a low porosity and high clay content seal.

- Shale reservoir: low porosity, high clay content reservoir with a low porosity and high clay content seal.

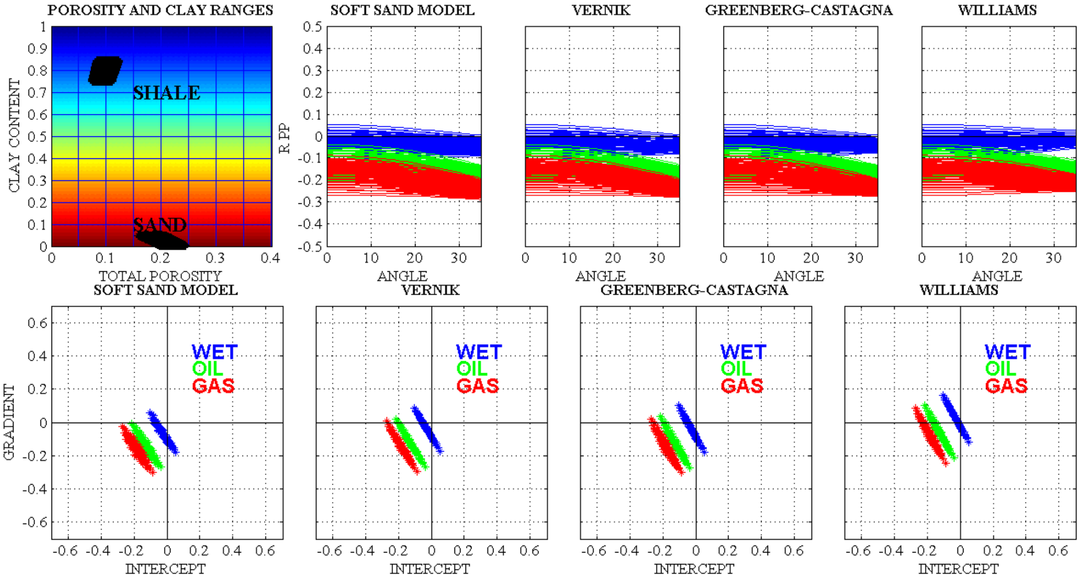

Figure 2.9: Soft-sand model (SSM). Geologically-consistent lithology space for a high porosity, low clay content reservoir with a low porosity, high clay content seal (upper left corner). All the other characteristics are the same as in Figure 2.3.

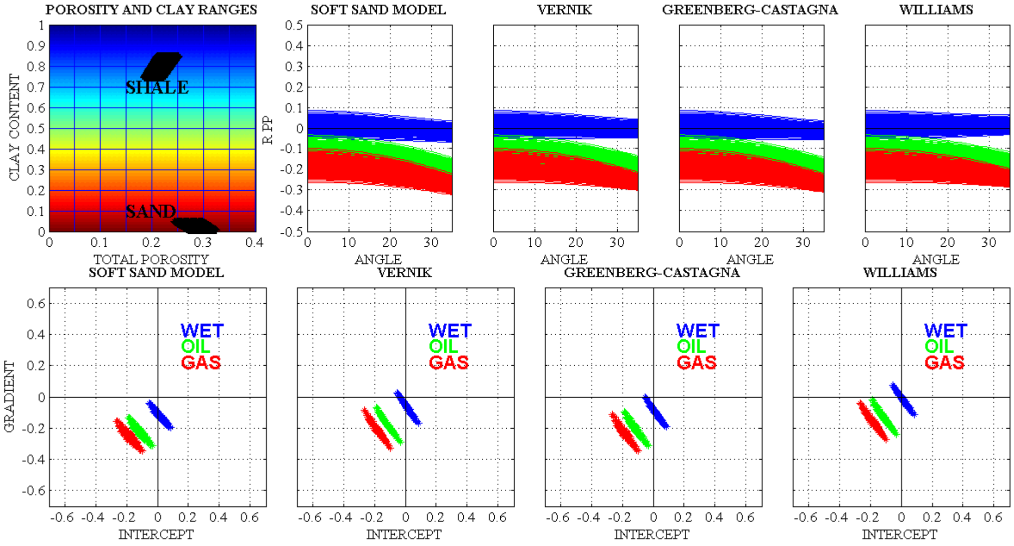

Figure 2.10: Soft-sand model (SSM). Geologically-consistent lithology space for a high porosity, low clay content reservoir with a high porosity, high clay content seal (upper left corner). All the other characteristics are the same as in Figure 2.3.

The forward modeling may be also based on another V_p-porosity model, such as the

Raymer-Dvorkin (2007b) model. This model produces both V_p and V_s and, hence, is a V_s predictor itself. Alternatively, as in the previous examples, we can use the V_p from the Raymer-Dvorkin (2007b) model and combine it with a different V_s predictor. Two examples using this approach are given in Figures 2.11 and 2.12, where we explore, respectively, the response at the interface between high-porosity low-clay-content sand and low-porosity high-clay-content shale (Figure 2.11) and medium-porosity low-clay-content sand and medium-porosity high-clay-content shale (Figure 2.12). Because the Raymer-Dvorkin model produces rock much stiffer than the soft-sand model for the same porosity and clay content, it is now much more difficult to separate gas from oil from water. Still, the responses due to different V_s predictors are similar among the predictors selected in these examples.

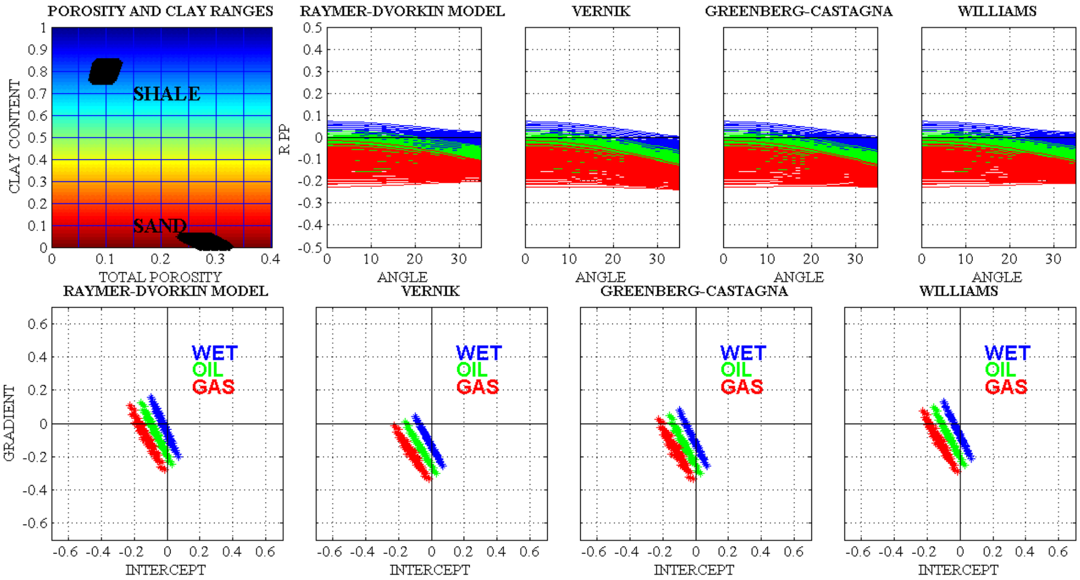

Figure 2.11: Raymer-Dvorkin model. Geologically-consistent lithology space for a high porosity, low clay content reservoir with a low porosity, high clay content seal. All the other characteristics are the same as in Figure 2.3.

Let us now explore synthetic seismic response at a limestone/dolomite interface, where the dolomite is the reservoir and limestone is the seal. Because these rocks are fast and stiff, in this case we will use the stiff-sand model (STM) appropriate for carbonates (e.g., Dvorkin et al., 2014). Also, for V_s prediction we selected the Pickett, Greenberg-Castagna, and Krief models with appropriate mineralogy inputs.

Murray (1960) showed that in certain cases the porosity-limestone fraction behavior produces a *V*-shape, similar to the Thomas-Stieber plot for clastics. Hence, in the following examples, we use the same geology-consistent approach as shown in Figures 2.9 to 2.12. Also, let us remember that a dolomite reservoir usually has porosity higher than the adjacent limestone.

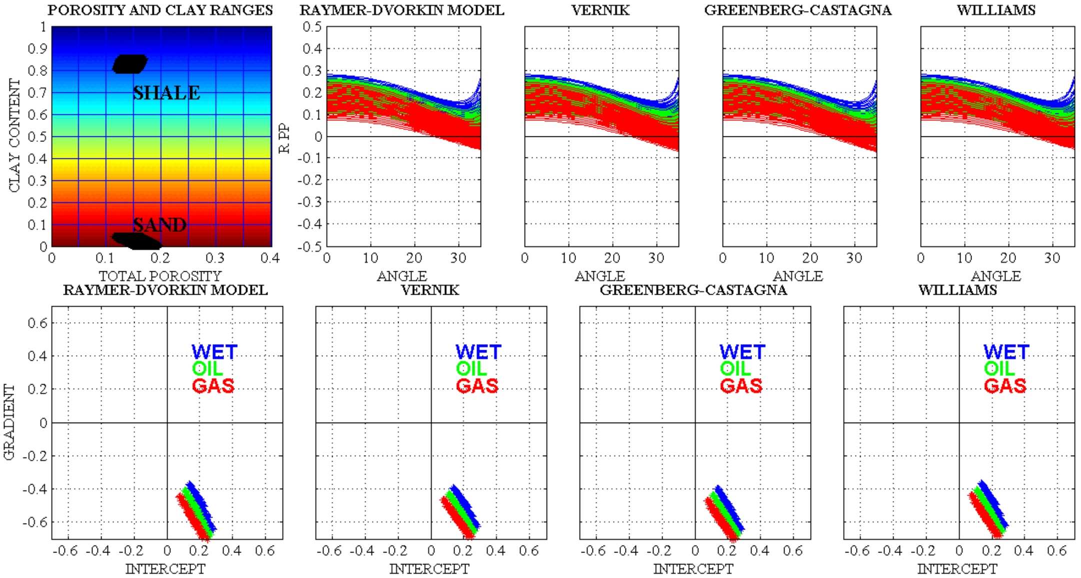

Figure 2.12: Raymer-Dvorkin model. Geologically-consistent lithology space for a medium porosity, low clay content reservoir with a medium porosity, high clay content seal. All the other characteristics are the same as in Figure 2.3.

Figure 2.13 displays the results of forward modeling for the scenario where the porosity of the dolomite reservoir varies approximately between 17 and 23% and the calcite fraction in the reservoir varies between zero and 9%. The porosity of the limestone seal is approximately between 5 and 10% and the calcite content is between 85 and 95%. The AVA response is mostly Class IV and approximately the same no matter which V_s predictor is used.

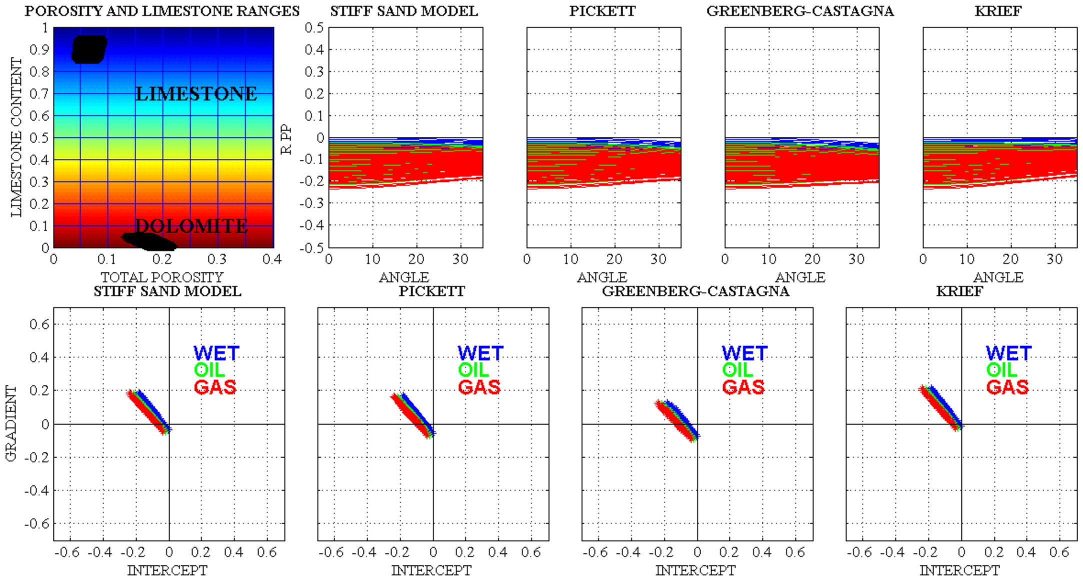

Figure 2.13: Stiff sand model (STM). Limestone and dolomite. All the other characteristics are the same as in Figure 2.3.

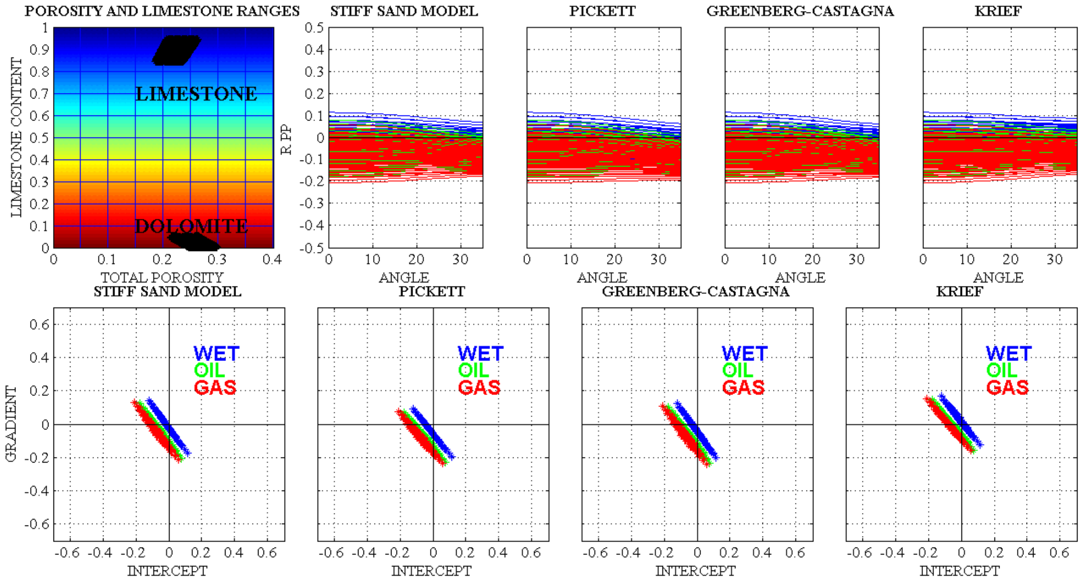

Figure 2.14: Stiff sand model (STM). Limestone and dolomite. All the other characteristics are the same as in Figure 2.3.

In Figure 2.14 we use a high-porosity (22 to 30%) dolomite reservoir with zero to 5% calcite content capped by a relatively high-porosity (18 to 27%) limestone seal with 85 to 95% calcite content. Interestingly, in this case the gradient becomes partly negative implying that some of the responses within the selected ranges of porosity and calcite content can be Class I or Class II.

The examples above are based on concrete scenarios. In order to explore the effect of inputs outside of these scenarios on the AVA response for each predictor separately, a sensitivity analysis was performed in which we varied inputs into the rock physics model and computed the sensitivity of the synthetic response in the intercept-gradient space. Below we limit our sensitivity analysis to only siliciclastic rocks.

2.5 Sensitivity Analysis

The workflow used in this sensitivity analysis is a follows: (a) Select the base inputs as listed in Table 2.3; (b) vary only one parameter at a time with the ±20% range around its base value while all other inputs are kept constant as listed in the base-input table; (c) compute the resulting intercept and gradient as the selected input varies; (d) measure the Euclidean distance of this point from the origin in the intercept-gradient plane (I could have used other measures but they were not implemented); and (e) plot the absolute values of this Euclidean distance for each input within the range of its variation.

Table 2.3 lists the base inputs for the example discussed here. The above-described Euclidean distance is plotted as a tornado plot in Figure 2.15. The elastic properties of the reservoir and seal were computed using the constant-cement model with the fixed coordination number 20. The overburden pressure was also fixed at 40 MPa. The differential pressure required by the model was the difference between the fixed overburden and varying pore pressure. We examined two cases for (a) oil and (b) gas reservoir with water saturation varying around its base value of 20%.

Table 2.3. Standard parameters used for the sensitivity analysis.

Property	Value
Salinity	150,000 ppm
Oil gravity (OilAPI)	30° API
Gas gravity	0.65
Gas to oil Ratio (GOR)	160 l/l
Pore pressure	20 MPa
Temperature	75° C
Water saturation	80%
Porosity of the reservoir (PhiSS)	20%
Clay content of the reservoir (ClaySS)	10%
Porosity of the seal (PhiSH)	5%
Clay content of the seal (ClaySH)	80%

Figure 2.15 indicates that the sensitivity of the response to the changes in the inputs is fairly small. It does not exceed 12% for the oil reservoir and 10% for the gas reservoir. Of course, it is important to bear in mind that these results are for a specific set of base inputs (Table 3). This sensitivity may change for a different set of base inputs and/or different rock physics model.

It appears that the sensitivity to the variation of the porosity in the reservoir is the greatest in all cases shown in Figure 2.15 and all predictors. For oil reservoir, the next parameter affecting the variation in the response is the gas-to-oil ratio (GOR), followed by the clay content in the reservoir. For gas reservoir, the parameter affecting the response the most is the clay content in the reservoir, followed by the pore pressure.

The other parameters have negligible effect compared to those listed above. The sensitivity of the parameters is not far from expected in the sense that some of the parameters were known to be more important than others. However the fact that all of the V_s predictors behave in the same manner implies that, regardless of which V_s predictor is used, they are equally capable of discriminating between hydrocarbons and water-bearing siliciclastic reservoirs.

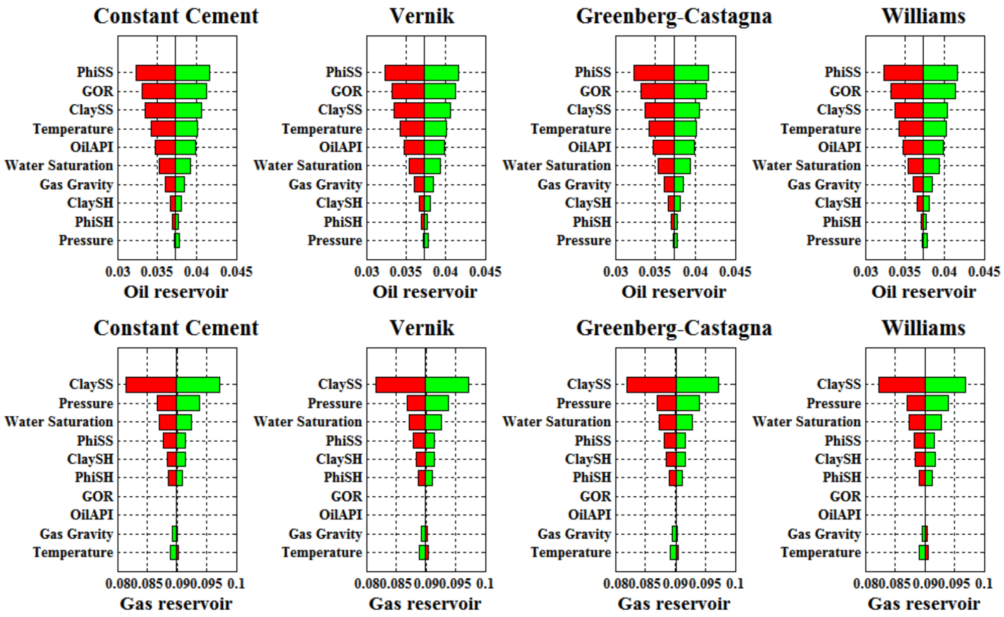

Figure 2.15: Tornado plots for the sensitivity of the AVA response (expressed as the Euclidean distantce) to the inputs for four different *Vs* predictors. As before, *Vp* was computed using CCM and *Vs* was computed from this *Vp* using the Vernik, Greenberg-Castagna, and Williams predictors. The first (left-side) plot in each row is for Vs from CCM. The centerline in each plot is the Euclidean distance of the point produced using the base inputs listed in Table 2.3 from the origin in the intercept-gradient plane. The horizontal bars against each input show the variation of this distance as the respective input varies within the ±20% of its base value. The abbreviations for the inputs are also listed in Table 2.3.

2.6 AVAIT

As shown before, the seismic amplitude's insensitivity to the pore fluid, especially so in fast rocks (Figures 2.11 to 2.14), as well as uncertainty in V_s measurements/predictions poses a problem in hydrocarbon prediction.

To address this problem via forward modeling, we have constructed an AVA Interactive Tool (AVAIT, in the file AVAIT.exe), which allows the user to directly assess the effect of several rock properties on the seismic amplitude. Currently, the variables included in AVAIT are reservoir thickness, wavelet frequency, pore fluid, and the porosity and clay contents of the seals and reservoirs.

This work presents the implementation of AVAIT for five V_s predictors. The main purpose is to identify, in a specific geological setting, the differences in the offset amplitude caused by the use of different V_s predictors.

We have found that, although the predictors give different V_s values, in most cases the AVA responses of a reservoir with oil or gas are qualitatively the same no matter which predictor we use. This indicates that most of these predictors can be effectively used for hydrocarbon identification.

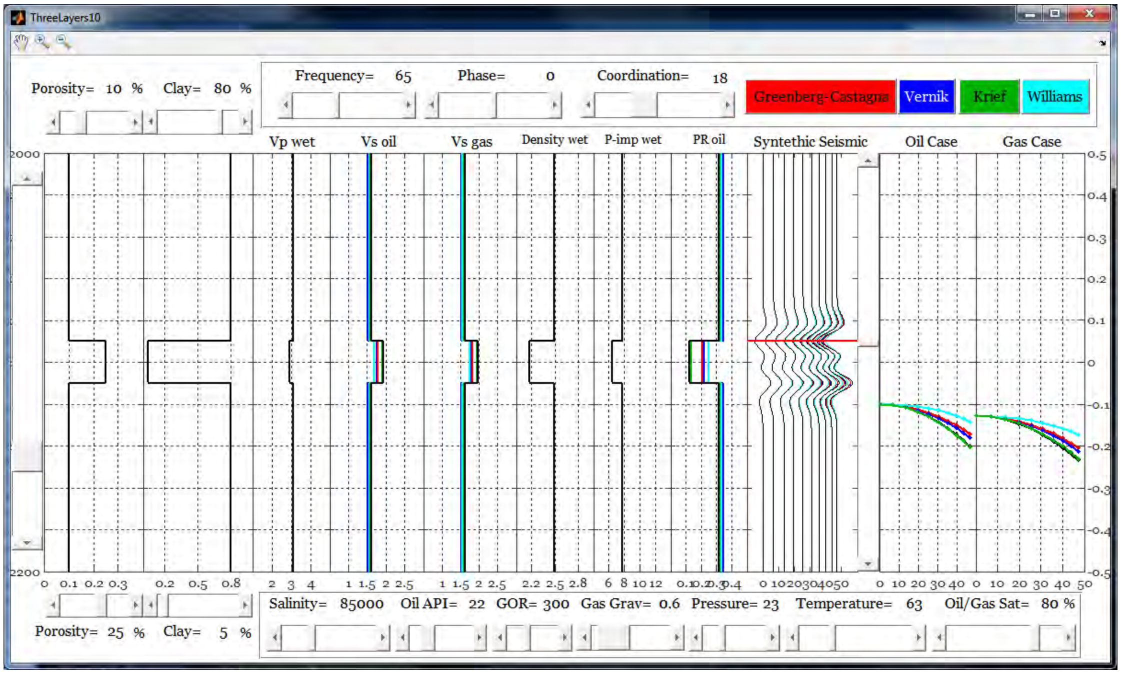

Porosity= 10 %
Clay= 80 %
Frequency= 65
Phase= 0
Coordination= 18
Salinity= 85000
Oil API= 22
GOR= 300
Gas Grav= 0.6
Pressure= 23
Temperature= 63
Oil/Gas Sat= 80 %
Porosity= 25 %
Clay= 5 %

Figure 2.16. Base case scenario of the AVAIT as described in the text. Using the slider bars at the top, we can adjust the porosity (default 10%) and clay content (default 80%) in the host shale. The next two slider bars at the top adjust the frequency of the wavelet (default 35 Hz) and its phase (default zero). The next slider bar on the top adjusts the coordination number in CCM. The following four colorbars are simply color-codes for various Vs predictors, namely Greenberg-Castagna, Vernik, Krief, and Williams, described earlier in this chapter. The slider bars at the bottom adjust the porosity (default 25%) and clay content (default 5%) in the reservoir. The slider bars that follow these two adjust the formation water salinity (default 85000 ppm); oil API gravity (default 22); GOR (default 300); gas gravity (default 0.65); pore pressure (default 23 MPa); temperature (default 63 ºC); and oil or gas saturation which are the same in this applet (default 80%). These base case selected values are shown at the respective slider bars. The overburden (confining) pressure is fixed (hardwired) at 40 MPa in all computations. It can be changed inside the code. The Vs predictors used are color-coded as shown in the top-right corner of the panel. The same colors are used to mark the respective AVA curves as well as synthetic seismograms and the velocity curves. Black curves represent the constant-cement model.

Figure 2.16 shows the tool interface, which consists of 11 tracks and 16 sliders. The tracks are as follows: porosity, clay content, P-wave velocity, S-wave velocity for the oil-only case, S-wave velocity for the gas-only case, density, P-wave impedance for the oil case, Poisson's ratio for the oil case, synthetic seismic gather versus angle for the oil case, amplitude versus angle (AVA) for the oil case and, separately, AVA for the gas case.

The sliders allow us to vary the following properties: porosity and clay content of the host rock, porosity and clay content of the reservoir rock; frequency and phase of the wavelet used for the synthetic ray-tracing; coordination number for the constant-cement model; water salinity; oil API; gas to oil ratio (GOR); gas gravity; differential pressure; temperature; water saturation in the reservoir; thickness of the reservoir; and the depth value for amplitude extraction for the AVA curves.

The inputs and outputs are plotted as vertical curves versus depth in the first 9 tracks in the panel in Figure 2.16. The first track is the total porosity. The second one is the clay content. The third one is the wet-rock V_p computed according to CCM. The fourth and fifth tracks show the predicted V_s for the oil and gas case, respectively, where the color correspond to the four predictors used while the CCM V_s prediction is shown in black. The 6th and 7th tracks show the wet-rock density and I_p, respectively. The 8th track shows Poisson's ratio, only for the oil case, colored according to the predictors used and using black color for the CCM predictor. The seismic gather with the angle of incidence from zero to 50° in the 9th track is colored according to the predictors used. Finally, in the last two tracks we show the AVA curves extracted from the gathers at the position of the horizontal red line shown in the gather display. This position can be interactively changed using the vertical slider bar on the right of the gather track. The 10th track is for the oil case while the 11th track is for the gas case. The extracted AVA curves are plotted as solid lines. They are compared to the dots that are computed using Zoeppritz (1919) equations at the interface between two half-spaces represented by the upper shale and the reservoir (not necessarily at the horizontal red line in the gather track), which in the of Figure 16 are above the continuous lines . The vertical axis on the right is the amplitude.

2.6.1 Rock physics model inside AVAIT

The rock physics model (CCM) used in the AVAIT allows the user to compare two rock physics models alternatives by modifying the coordination number, i.e., the soft sand model (coordination number = 6) and the constant cement model (6 < coordination number <= 40). These models are described by Mavko et al. (2009). The main input parameters are the porosity and clay content for the host and reservoir rocks as well as the coordination number, which is the same for the host non-reservoir rock and for the reservoir (Figure 2.16). The upper porosity and clay content sliders correspond to the host rock, which is the same above and below the reservoir. The bottom sliders for porosity and clay content represent the middle layer, which is the reservoir.

2.6.2 Pore fluid and differential pressure modeling in AVAIT

Batzle and Wang (1992) describe the dependence of the pore fluid's bulk modulus and density on pore pressure, temperature, and fluid characteristics; we implemented these relations (Mavko, et al., 2009) in our tool. The fluid controls are the following: salinity in ppm, gas to oil ratio in liters/liter, gas gravity, temperature in °C, and saturation in % (Figure 2.16). The pore pressure set up by the respective slider is used uniformly in the entire interval. The overburden is constant 40 MPa throughout the interval. The differential pressure (the overburden minus the pore pressure) can be varied by varying the pore pressure. Since both the pore and overburden pressure are constant, the differential pressure is also constant in the entire interval.

2.6.3 Ray tracing

Ray tracing is a method for calculating the path of seismic waves based on the velocities of contrasting interfaces. Once the travel time is computed, the angle-dependent reflectivity from an interface, estimated via the Zoeppritz equations, is convolved with the input wavelet to obtain the synthetic gather. We use a Ricker wavelet (Ricker, 1943) whose frequency and phase can be modified by the user.

2.6.4 V_s predictors

All V_s predictors are applied to V_p as computed from CCM. The clay content in the shale and reservoir are also used as inputs to the predictors as required. Initially, both V_p and V_s are computed for 100% wet rock as most of the predictors have been created for wet rock. In order to obtain V_s at a desired water saturation, we assume that the rock's shear modulus G does not depend on the pore fluid. Then we change the bulk density ρ_b as a function of saturation and compute V_s as the square root of G/ρ_b. V_s is used as input to the ray tracer for each V_s predictor. V_s predictions are color coded according to the boxes in the top right corner appearing in the following tracks: V_s for the oil case, V_s for the gas case, Poisson's ratio for the oil case, synthetic seismic gather versus angle, AVA curves for the oil case, and AVA curves for the gas case.

2.6.5 Selected geologic and pore fluid scenarios

We use AVAIT to generate a default geologic scenario and then vary the pore fluid, porosity of the reservoir, and clay content in the host rock, one parameter at a time, to quantify their effects on AVA. This base case scenario is shown in Figure 2.16. In all examples shown below, the amplitude extracted from the seismograms was picked at the top of the reservoir, not at the peak of the traces.

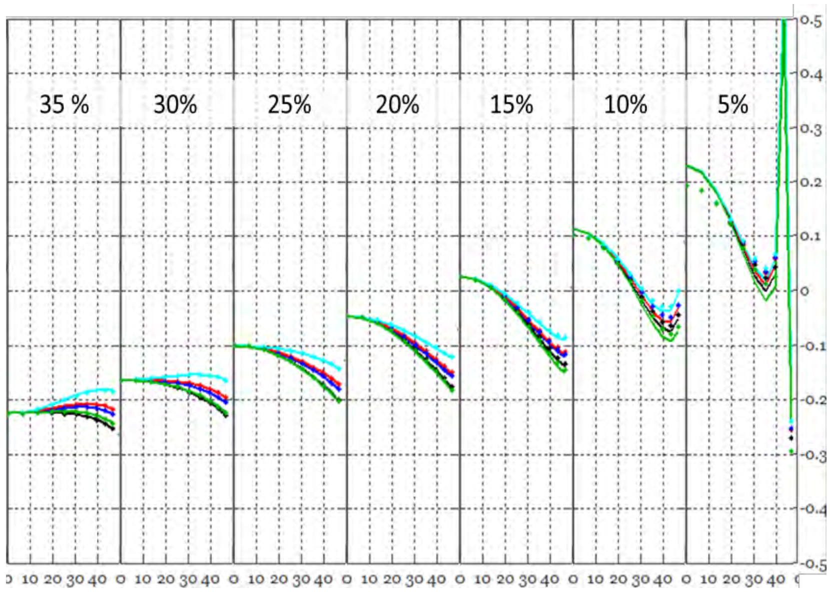

Figure 2.17. 20-m thick reservoir with oil. AVA plots for different porosities in the reservoir. From left to right: 35, 30, 25, 20, 15, 10 and 5% porosity, respectively, with the other inputs from the base case scenario (Figure 2.16).

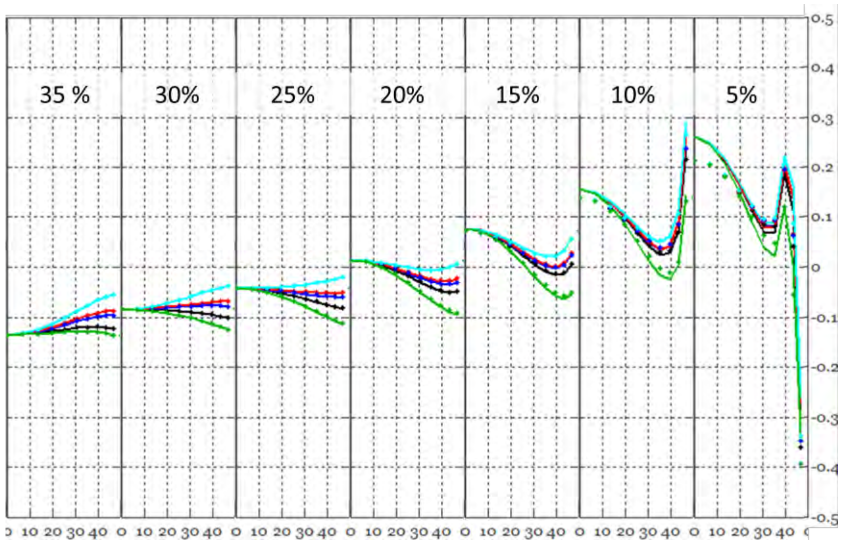

Figure 2.18. Same as Figure 2.17, but for 100% wet reservoir.

In the first modeling set we assumed that the reservoir contained oil with the parameters set forward in the base case scenario and varied the reservoir's porosity between 5 and 35% (Figure 2.17). Figure 2.18 shows the results of the same porosity variation but for the 100% wet reservoir.

The next forward modeling scenario was implemented by using the base case and varying the clay content in the host rock (Figure 2.19). Figure 2.20 illustrates the same exercise carried out for a wet reservoir.

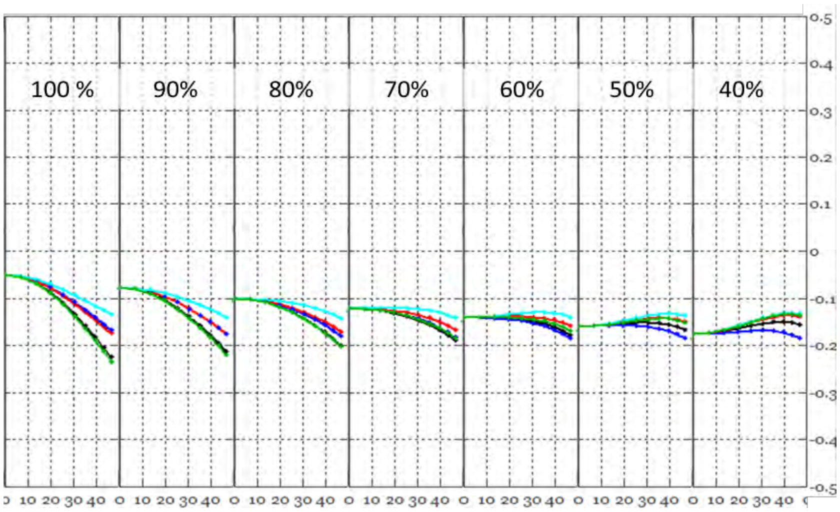

Figure 2.19. Reservoir with oil; reservoir thickness is 20 m. AVA plots for different clay content in the host rock, which varies from 100% (pure clay) to 40%. From left to right: 100, 90, 80, 70, 60, 50 and 40% clay content above the reservoir, using the base case scenario from Figure 2.16.

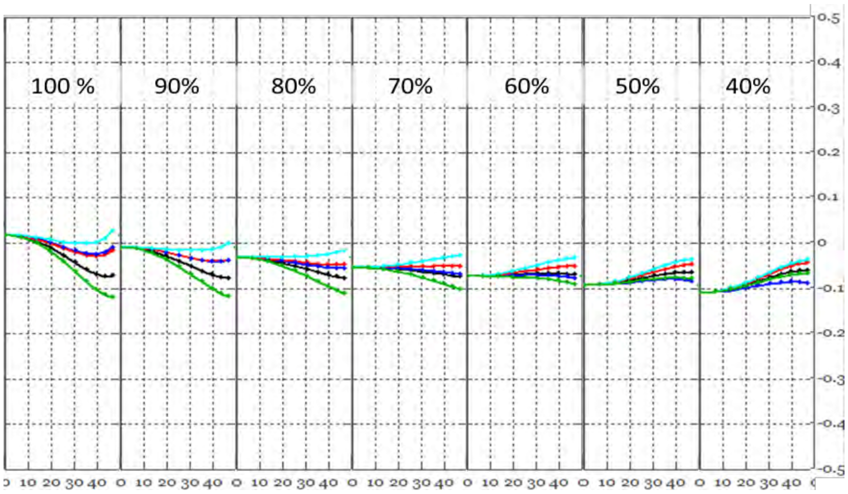

Figure 2.20. Same as Figure 2.19 but for a 100% wet reservoir.

Next, the frequency effect on AVA was investigated to quantify the constructive and destructive interference for a 20 m thick reservoir. The oil reservoir case is shown in

Figure 2.21, where the solid AVA curves come from the ray tracer generated seismograms. The dotted curves are from a single interface modeled using full Zoeppritz (1919) equations. At high frequencies, the dotted and solid curves are practically the same, while at lower frequencies, the ray-tracer amplitudes first become larger (40 and 30 Hz) due to the constructive interference and then become smaller at lower frequencies due to the destructive interference between reflections from the top and bottom of the reservoir. As a result, these extracted curves deviate from the single-interface AVA curves.

We carried out the same exercise for a wet reservoir (Figure 2.22).

Next we investigated the occurrence of the so-called false AVA, such as occurs in the case of non-commercial hydrocarbon saturation. Figure 2.23 shows a well-defined class III response with high levels of oil and gas saturation (and only 10% water saturation). Figure 2.24 shows the response of the same reservoir, but with only 16% oil and gas saturation (84% water saturation). Despite changes in saturation, the AVA remains practically unchanged; this case is known as the fizz-gas effect.

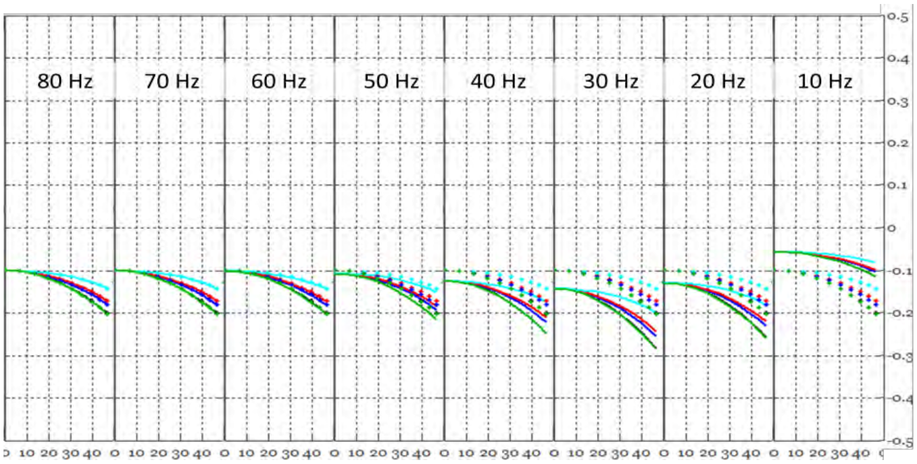

Figure 2.21. 20 m thick reservoir with oil. AVA plots for different frequencies of the wavelet. From left to right: 80, 70, 60, 50, 40, 30, 20, and 10 Hertz for the central frequency of the wavelet, using the base case scenario from Figure 2.16.

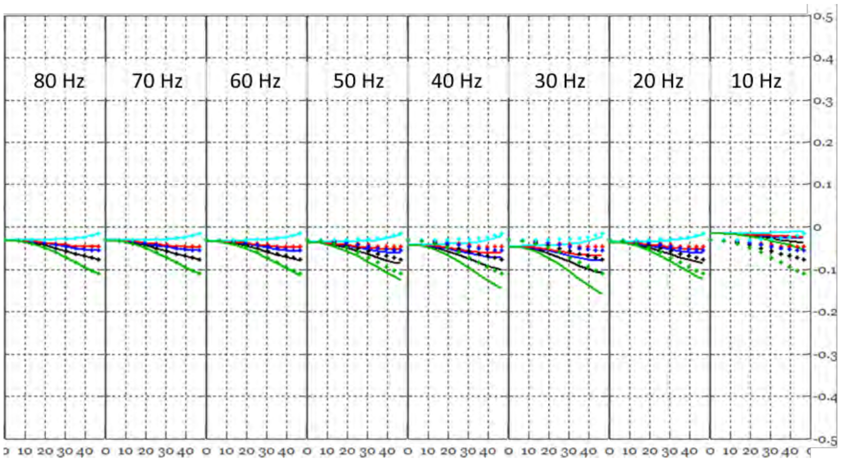

Figure 2.22. Same as Figure 2.21 but using wet reservoir.

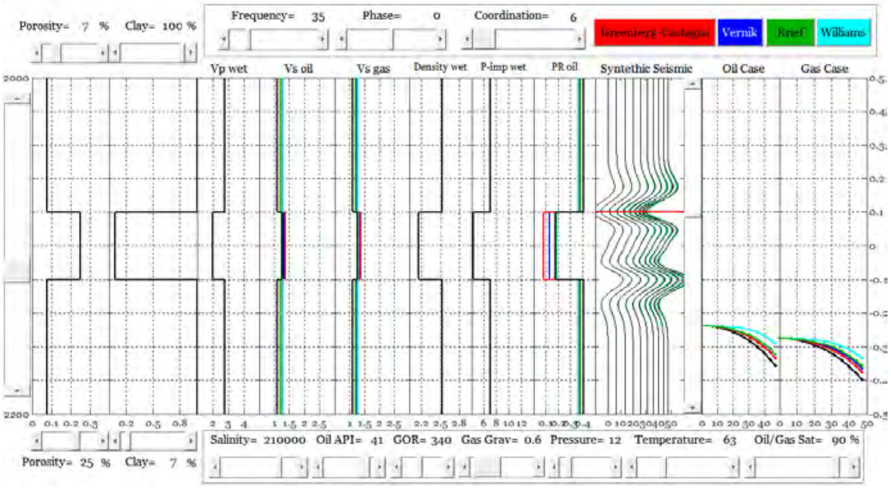
Porosity= 7 %
Clay= 100 %
Frequency= 35
Phase= 0
Coordination= 6
Salinity= 210000
Oil API= 41
GOR= 340
Gas Grav= 0.6
Pressure= 12
Temperature= 63
Oil/Gas Sat= 90 %
Porosity= 25 %
Clay= 7 %

Figure 2.23. AVAIT display for a typical class III anomaly in a reservoir with high oil or gas saturation.

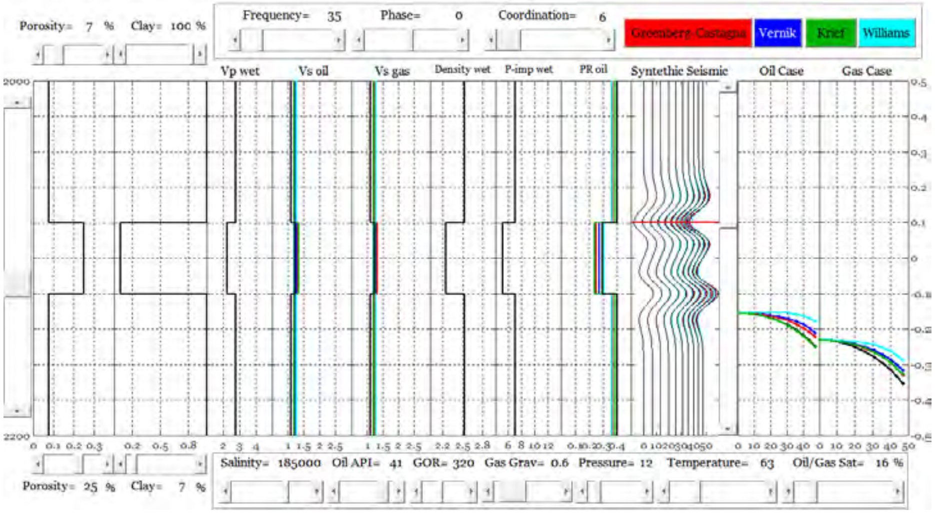
Porosity= 7 %
Clay= 100 %
Frequency= 35
Phase= 0
Coordination= 6
Salinity= 185000
Oil API= 41
GOR= 320
Gas Grav= 0.6
Pressure= 12
Temperature= 63
Oil/Gas Sat= 16 %
Porosity= 25 %
Clay= 7 %

Figure 2.24. Same as Figure 2.23 but for small, non-commercial, hydrocarbon saturation (only 16%), showing an effect known as a fizz gas anomaly. This response is practically the same as shown in Figure 2.23.

Figure 2.25 shows Class II response from an oil reservoir with only 10% water saturation. Figure 2.26 shows the same class response but from a 100% wet reservoir whose porosity and clay content as well as those in the shale were changed as compared to those used in Figure 2.25 to obtain a similar Class II response.

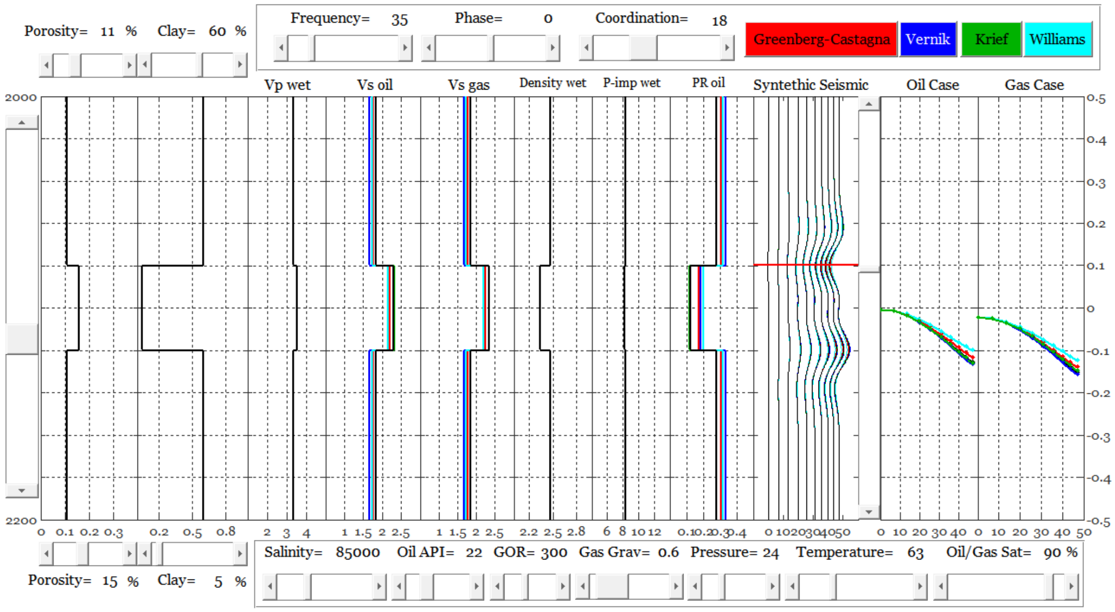
Porosity= 11 % Clay= 60 %

Frequency= 35 Phase= 0 Coordination= 18

Salinity= 85000 Oil API= 22 GOR= 300 Gas Grav= 0.6 Pressure= 24 Temperature= 63 Oil/Gas Sat= 90 %

Porosity= 15 % Clay= 5 %

Figure 2.25. Class II AVA anomaly from a reservoir with hydrocarbons at low water saturation.

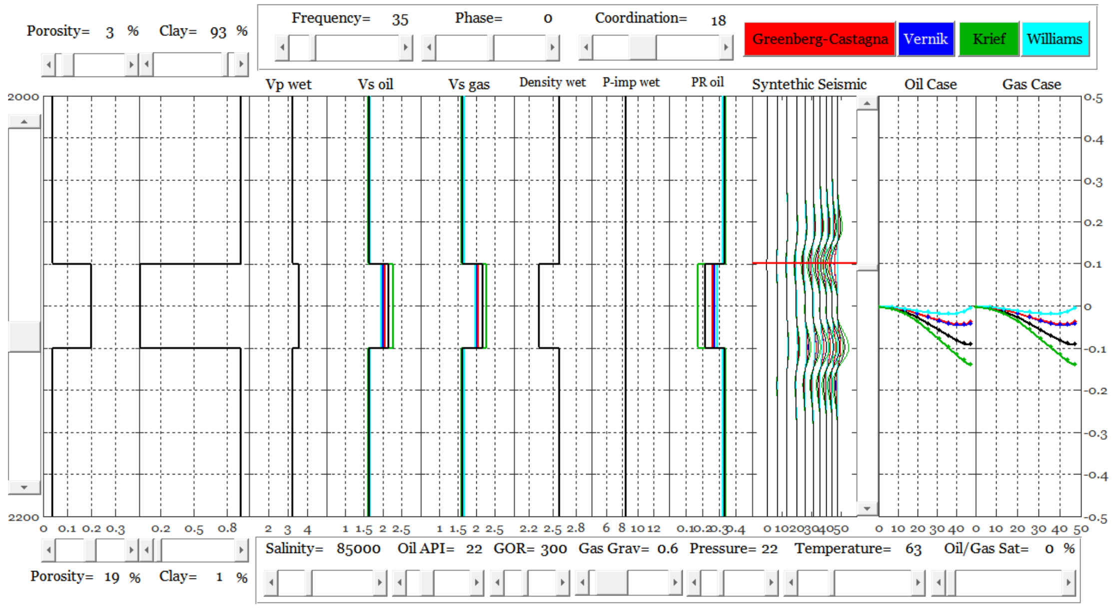
Porosity= 3 % Clay= 93 %

Frequency= 35 Phase= 0 Coordination= 18

Salinity= 85000 Oil API= 22 GOR= 300 Gas Grav= 0.6 Pressure= 22 Temperature= 63 Oil/Gas Sat= 0 %

Porosity= 19 % Clay= 1 %

Figure 2.26. False Class II AVA anomaly from wet reservoir whose porosity, clay content, and shale properties are different from those shown in Figure 2.25.

These two examples, one for true and the other for false AVA, show that lithological variations may produce a response from a wet reservoir, similar to that from a reservoir with oil or gas.

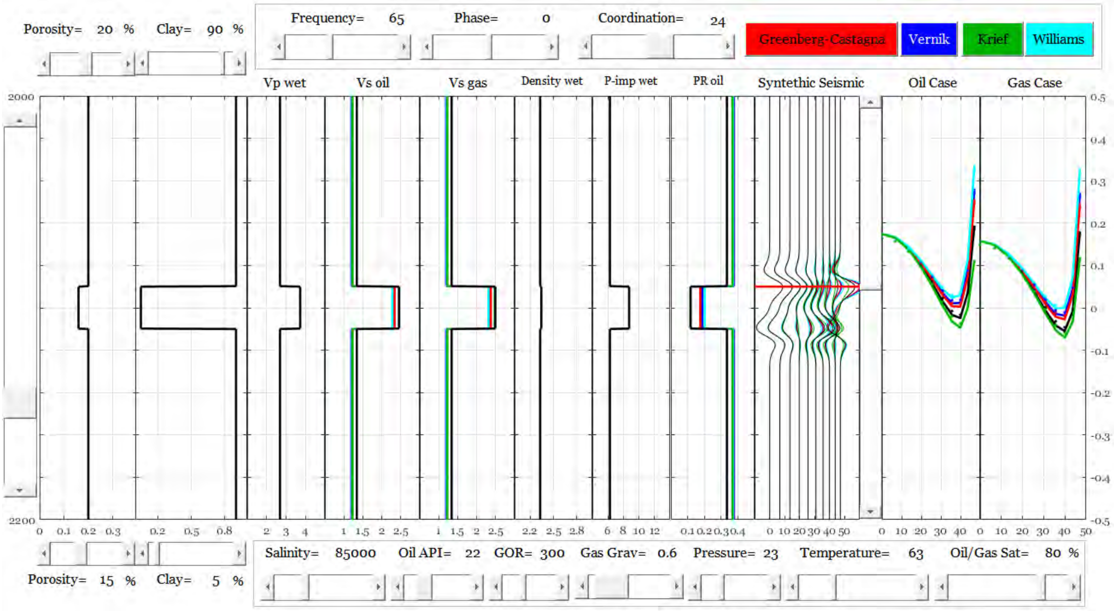
Porosity= 20 %
Clay= 90 %
Frequency= 65
Phase= 0
Coordination= 24
Salinity= 85000
Oil API= 22
GOR= 300
Gas Grav= 0.6
Pressure= 23
Temperature= 63
Oil/Gas Sat= 80 %
Porosity= 15 %
Clay= 5 %

Figure 2.27. Class I AVA anomaly from oil and gas reservoirs.

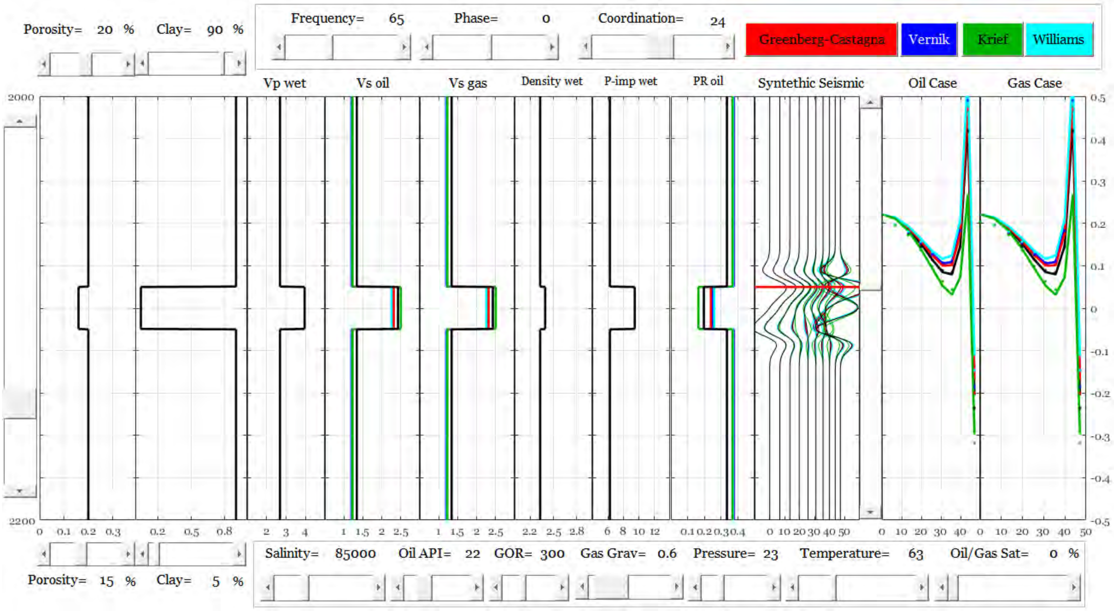
Porosity= 20 %
Clay= 90 %
Frequency= 65
Phase= 0
Coordination= 24
Salinity= 85000
Oil API= 22
GOR= 300
Gas Grav= 0.6
Pressure= 23
Temperature= 63
Oil/Gas Sat= 0 %
Porosity= 15 %
Clay= 5 %

Figure 2.28. Same as Figure 2.27 but for 100% wet reservoir.

A similar situation but for Class I response is shown in Figures 2.27 and 2.28. The wet-rock false AVA response shown in Figure 2.28 is essentially the same as in Figure

2.27 because the selected coordination number is high (24) and porosity is small (15%) thus making the rock fairly stiff. In such rocks, the fluid response is muted. In other words, in stiff fast rocks, it is difficult to determine the pore fluid from seismic data because the elastic properties are not very sensitive to the pore fluid.

2.7 Discussion

By looking at the geologic scenarios presented here, I made some general observations:

- Reducing the porosity of an oil reservoir can affect the AVA response, changing it from class III to II and to I (Figure 2.17). When the reservoir is 100% water saturated, the response varies between class II and I (Figure 2.18).
- Decreasing the clay content of the host rock results in flattening of the Class III AVA response at an oil reservoir (Figure 2.19).
- In the case of a water-filled reservoir, a decrease in the clay content of the host rock will result in transition from class II to class IV (Figure 2.20)
- Reducing frequency will first act to generate a stronger Class III response due to constructive interference (meaning that the amplitude is increased) and then act to weaken the response due to destructive interference (the attenuation of the amplitude) (Figure 2.21).

The false AVA responses shown above indicate that an AVA anomaly does not necessarily indicate commercial accumulations hydrocarbons. It is critical to be aware of such non-uniqueness before drilling a prospect.

2.8 Conclusion

The applets presented in this chapter as well as the AVAIT tool were developed to allow the seismic interpreter to understand the seismic amplitude implications of specific geological and pore-fluid scenarios and to assess the effects of using different V_S predictors. The results indicate that although different predictors, strictly speaking, produce different responses, these responses are quite similar at a reservoir with hydrocarbons. Moreover, as inputs, such as porosity, clay content, and frequency vary, the AVA responses due to different predictors consistently vary along the same pattern, no matter which predictor is used (Figure 2.17 to 2.22). Notice also that different V_S predictors provide qualitatively similar responses where hydrocarbons are present and somewhat differ at the wet reservoir.

Exploring various scenarios, we have found that, in many cases, the choice of V_S predictor will not affect the capability to forecast the presence of hydrocarbons from seismic data.

Chapter 3

Porosity, Mineralogy, and Pore Fluid from Simultaneous Impedance Inversion

3.1 Abstract

We find that in a quartz/clay system, the P- and S-wave impedances (I_p and I_s, respectively) each depend on a different linear combination of the total porosity and clay content. This implies that if the pore fluid is known, we can resolve these two seismically derived impedances for porosity and clay content. Key to such interpretation is rock physics diagnostics that provides a theoretical rock physics model to quantitatively explain well data by relating I_p and I_s to porosity, clay content, and pore fluid. The well data conditioned according to this model serve as input to simultaneous impedance inversion. Poisson's ratio or the I_p/I_s ratio serves as the pore fluid identifier. We give an example of such rock physics-based interpretation of seismically derived impedances for rock properties based on well and seismic data from an offshore oil field.

3.2 Introduction

Seismic reflections directly depend on the elastic property contrast in the subsurface. It is possible, in principle, to use seismic reflections to obtain two absolute (rather than relative, by using the low frequency information from the wells) elastic attributes, such as P- and S-wave impedances, the process known as simultaneous impedance inversion. Of course, it is important not to stop at the inversion stage but proceed towards interpreting the elastic attributes in terms of rock properties such as porosity, mineralogy, and pore fluid. This is perhaps the ultimate task of seismic interpretation.

Arguably, the key issue of such interpretation is the fact that I_p and I_s depend on more than two variables, including the total porosity, clay content, the pore fluid's density and compressibility, overburden and pore pressure, and, finally, any diagenesis-related texture of the rock that governs the "velocity-porosity" transform (also known as the rock physics model). Such a model is usually established based on well data that include the elastic-wave velocities and impedances, mineralogy (clay content), porosity, and hydrocarbon saturation. This process is known as rock physics diagnostics (Dvorkin et al., 2014).

The properties of the fluid components in the well (water and hydrocarbon) are measured in the lab or directly in the well. The estimates of the overburden and pore pressure are also available through standard calculations and/or measurements. The question is how to use this knowledge away from well control, where only I_p and I_s are available, to quantify the porosity, clay content, and the presence of hydrocarbons.

To approach this problem, assumptions have to be made: (a) the differential pressure throughout the seismic volume is approximately the same as at the well; (b) the properties of the pore fluid components are also the same; and (c) the rock physics model established at the well holds throughout the volume under examination. What remains is two inputs, I_p and I_s, that have to be resolved for three variables, porosity, clay content, and hydrocarbon saturation.

Mathematically, this problem is underdetermined, meaning that we need an additional assumption. Such an assumption can be made if we settle for *categorical* (or Boolean) rather than quantitative determination of saturation by simply assuming whether the hydrocarbon is present or not. Fortunately, where the compressibility of the hydrocarbon phase is significantly different from that of the formation water, we can use a fairly robust attribute, Poisson's ratio (ν):

$$\nu = \frac{1}{2}\frac{(I_p / I_s)^2 - 2}{(I_p / I_s)^2 - 1}. \tag{3.1}$$

The criterion adopted is simple: if ν is smaller than a certain threshold determined at the well, hydrocarbons are present, while if it is larger, the pore fluid is only water. After making this discrimination, we made the strong assumption that where hydrocarbons are present, the water saturation S_w is constant and approximately the same as in the reservoir sampled by the well and then compute the effective density ρ_f of the water/hydrocarbon system as

$$\rho_f = (1 - S_w)\rho_h + S_w \rho_w, \tag{3.2}$$

where ρ_w and ρ_h are the densities of water and hydrocarbon, respectively. The effective bulk modulus K_f (inverse of compressibility) of this system is

$$K_f = [(1 - S_w)K_h^{-1} + S_w K_w^{-1}]^{-1}, \tag{3.3}$$

where K_w and K_h are the bulk moduli of water and hydrocarbon, respectively.

Now, assuming that the properties of the pore fluid are known, the problem is reduced to finding two unknowns, the total porosity (ϕ_t) and clay content (C) from two inputs, I_p and I_s obtained from simultaneous impedance inversion. This is a well-defined mathematical problem unless the two equations with two unknowns are not independent of each other.

Dvorkin (2007) found that they are *not* independent, namely, that both I_p and I_s are functions of approximately the same linear combination of ϕ_t and C: $\phi_t + \alpha C$ (Figure 3.1). The heuristic explanation behind this finding is that in some shaly sands, clay is not load-bearing, meaning it merely occupies the pore space with only minor contribution to the elastic properties (Figure 3.2). Hence, even if we have both impedances available, we cannot resolve these data separately for ϕ_t and C but rather only for the $\phi_t + \alpha C$ combination.

Here, by analyzing a dataset from an offshore clastic oil reservoir, we find that such result is far from universal:

$$I_p = f_p(\phi_t + \alpha_p C); \quad I_s = f_s(\phi_t + \alpha_s C), \qquad (3.4)$$

where $\alpha_p \neq \alpha_s$ and f_p and f_s are the impedance-porosity models for clean sand. Specifically, we find that $\alpha_p \approx 0.17$ while $\alpha_s \approx 0.23$. We find that this difference is large enough to resolve Equations 3.4 separately for ϕ_t and C.

Efforts to estimate porosity from seismic velocity date more than 30 years back (Angeleri and Carpi, 1982). These authors used Wyllie's time average for sand with clay, and then to predict the clay content in the seismic section by interpolating the well data. Dolberg et al. (2000) produced a porosity volume from the acoustic impedance by using a best-linear-fit impedance-porosity transform from well data, ignoring the effect of clay.

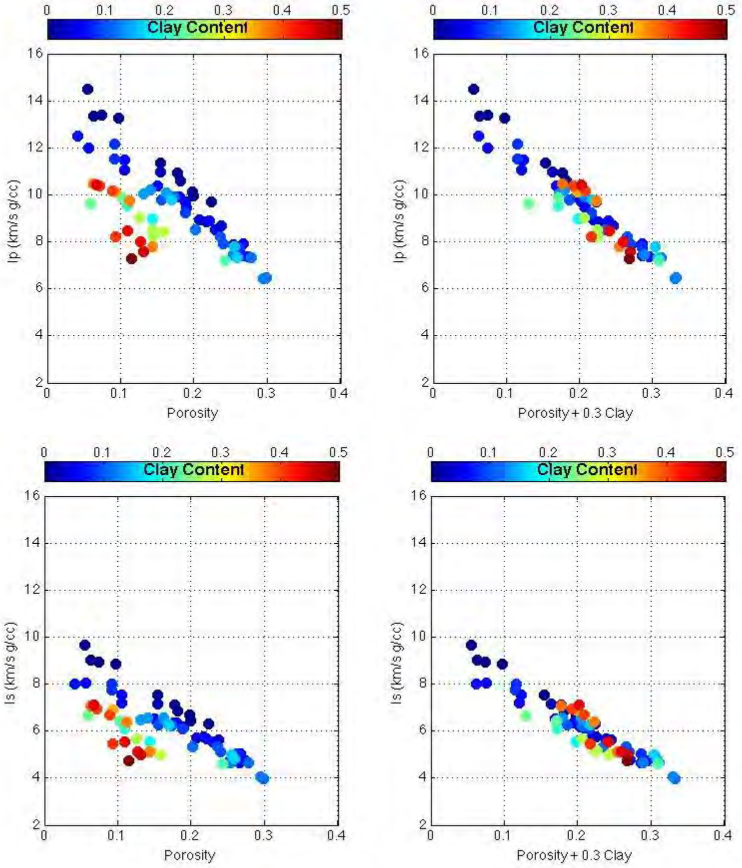

Figure 3.1. P- (top) and S-wave (bottom) impedance versus the total porosity (left column) and versus the linear combination $\phi_t + \alpha C$ (right column) with $\alpha = 0.3$. The data are from Han's (1986) and Jizba's (1991) laboratory measurements conducted at 40 MPa confining pressure on room-dry sandstone samples with the clay content varying between zero and 50% (shown in colorbars).

Avseth et al. (2005) used statistical analysis of rock physics data to determine lithofacies, such as wet sand, oil sand, and shale, from seismic impedances. Spikes (2008) used a probabilistic reservoir-characterization technique to simultaneously predict up to four reservoir properties and associated uncertainty corresponding to a reflection from a potential reservoir unit. This method involves exhaustive forward modeling of the prior earth model and a full-grid search in the inverse problem to answer the question of what properties of rock stand behind recorded seismic reflections. Valenti (2009) used artificial neural networks applied to well data to obtain an impedance-porosity transform which was then applied to the seismic impedance.

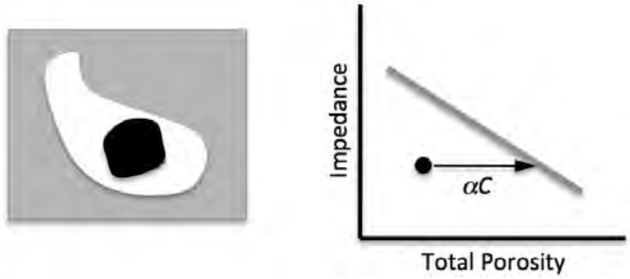

Figure 3.2. Left: Schematic porous rock made of quartz (gray) with clay (black) inside the pore space. Right: Impedance versus the total porosity (scheme) with the gray curve showing the pure quartz model and black dot representing the position of sand with clay. By adding the product αC to the total porosity of the shaly sand we shift this data point to the right where it falls on the clean sand model curve, similar to the data shown in Figure 3.1.

In contrast, we use a deterministic rock physics model established at a well and tested it at three other wells; demonstrating that the same model is valid at the seismic scale; and then apply this model to seismically-derived I_p and I_s to first determine the presence of oil and then predict the porosity and clay content in the seismic volume. This prediction passed the blind test at three wells.

3.3 Rock Physics Model (Rock Physics Diagnostics)

Figure 3.3 shows well data from one of the four wells (Well A) drilled through an offshore oil reservoir. Water depth is about 800 m, TVD at the reservoir is about 2250 m. The net pay thickness reaches 20 m. The depositional environment is turbiditic from neritic to open marine. Rock type is fine- to medium-grain-size sandstone interbedded by silty claystone.

In order to find a rock physics model that quantitatively explains these data, we cross-plot the wet-rock I_p (computed from the measured elastic properties by fluid substitution) versus the total porosity ϕ_t. The latter was computed from the measured bulk density ρ_b using the mass-balance equation

$$\phi_t = (\rho_s - \rho_b)/(\rho_s - \rho_f), \tag{3.5}$$

where the mineral density ρ_s was assumed 2.65 g/cc and the pore-fluid density ρ_f was the arithmetic average of the water and oil densities weighed by the water saturation Sw. The cross-plot is shown in Figure 3.4 where the data points are color-coded by the difference between the neutron (ϕ_N) and density-derived porosity (ϕ_ρ), the latter computed according to Equation 3.5 but with $\rho_f = 1$ g/cc.

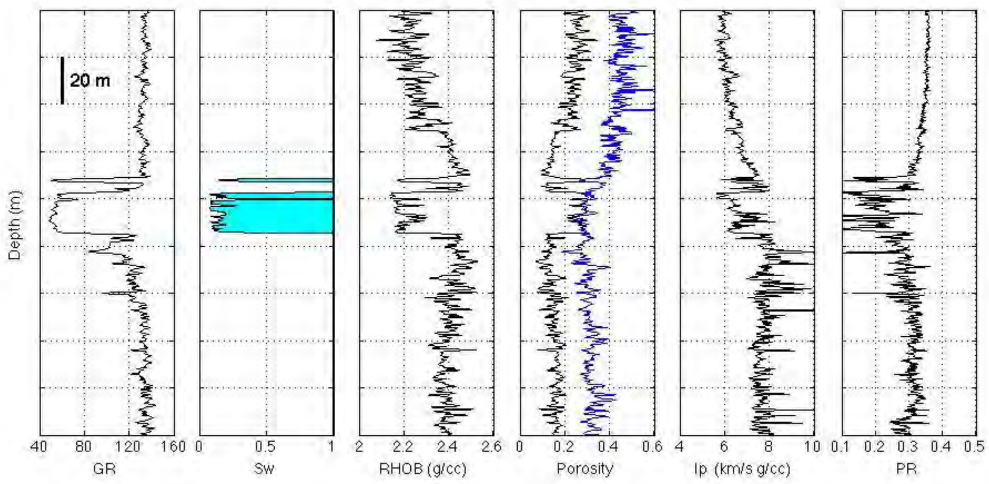

Figure 3.3. Well log curves in Well A. From left to right: GR; water saturation; bulk density; density-derived porosity (black) and neutron porosity (blue); the P-wave impedance; and Poisson's ratio.

The curves superimposed on the data in Figure 3.4 come from the constant-cement model (Mavko et al., 2009) where the porosity varied between zero and 0.40 and the clay content varied between zero (upper curve) and 100% clay content (bottom curve). We observe that the ϕ_N-ϕ_ρ difference serves as a robust clay content indicator with the dark blue symbols falling on the low-clay-content curves and red symbols falling on the high-clay-content curves.

The next step in rock physics diagnostics is to ensure that this model reproduces the velocity and density curves along the entire 200m interval around the reservoir. To apply the model to the interval we need to know the clay content *C*. To obtain it, we assume that the total porosity, density and V_p curves are correct and then back-calculate *C* using the constant-cement model (Dvorkin et al., 2014).

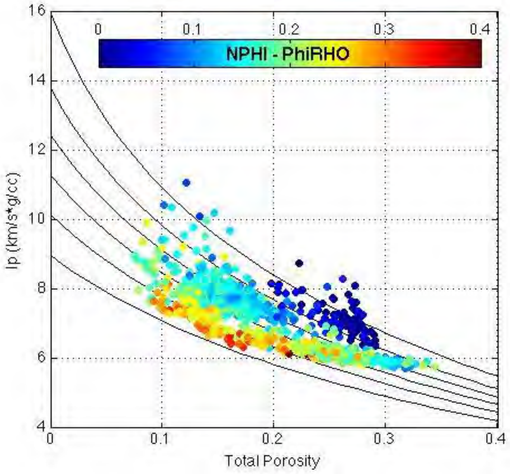

Figure 3.4. Well A. Wet-rock P-wave impedance versus the total porosity color-coded by the neutron and density-derived porosity difference ($\phi_N - \phi_\rho$), as explained in the text. The curves are from the constant-cement model with the upper curve for zero clay content and the bottom curve for 100% clay content with 20% clay increment for the curves in between.

The clay content thus obtained is plotted versus depth in Figure 3.5 (first track) in red. It appears to be very close to the clay content obtained by normalizing the ϕ_N-ϕ_ρ difference (same track, black), which roughly confirms our clay content estimation method. The density and elastic properties computed using *C*, ϕ_t, and other parameters used in the constant cement model for the model curves shown in Figure 3.4 are plotted in Figure 3.5 where they are compared to the measured properties.

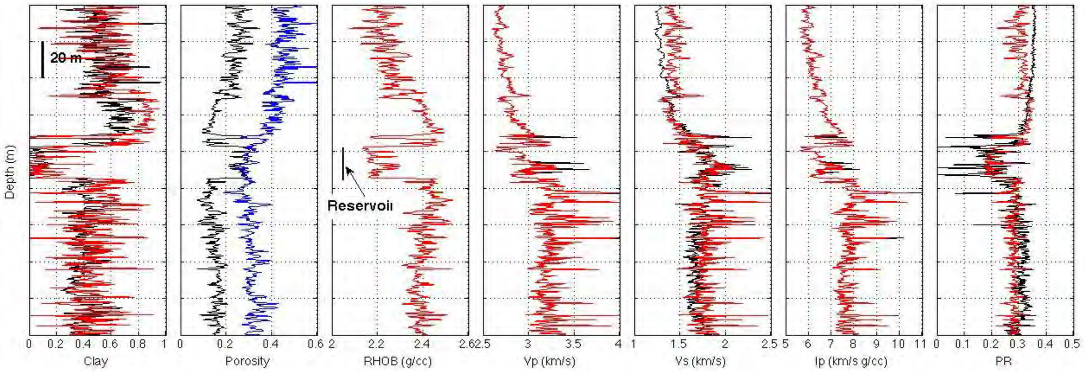

Figure 3.5. Well log curves for Well A. From left to right: clay content from the normalized difference between neutron porosity and density-derived porosity (black) and from porosity and velocity (red) as explained in the text; density-derived porosity (black) and neutron porosity (blue); *Vp*; *Vs*; *Ip* and Poisson's ratio (black). The red curves in the last 5 tracks show the curves computed from the constant cement model using the clay content (red curve in 1st track), total porosity, and fluid properties at in-situ conditions.

The model-based curves obviously match the bulk density, V_p, and I_p (the latter two except for a few spurious spikes), since the assumption was that they were correct in order to invert for the clay content. The match between the model based V_s and ν and the measured values is also reasonably good, especially around the reservoir.

3.4 From Elastic to Petrophysical Properties

As our ultimate objective is to obtain the total porosity, clay content, and pore fluid from seismically-derived impedances (I_p and I_s), we first test this interpretation on well data. The method is as follows: (a) To determine where oil is present, we use Poisson's ratio as the threshold, namely if $\nu < 0.23$, we assume that water saturation is constant, Sw = 0.1, otherwise Sw = 1.0. This allows us to estimate the fluid's density and bulk modulus according to Equations 3.2 and 3.3, respectively. (b) For each set of fluid properties, we use the constant-cement model to create look-up tables for I_p and I_s as a function of ϕ_t and C. (c) Finally, we use these tables at each depth station to obtain ϕ_t and

C from the measured I_p and I_s. The results are shown in Figure 3.6 where the ϕ_t and C computed from I_p and I_s in the well are in good agreement with the data.

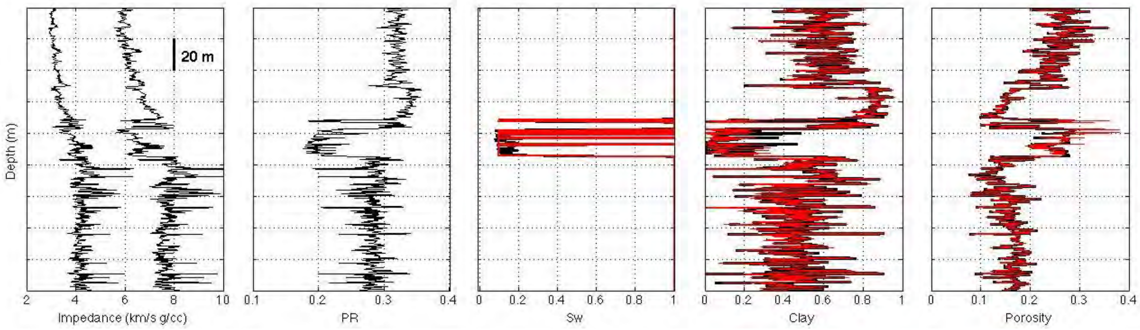

Figure 3.6. Well A. From left to right: Ip and Is; Poisson's ratio; Sw; clay content; and the total porosity. In the last three tracks, black is for the data while red is for the properties computed from ν, Ip, and Is.

Let us make clear that the lookup tables used to obtain the porosity and clay content from I_p and I_s strongly depend on the pore fluid whose properties are selected based on the Poisson's ratio cutoff as explained in the text. As a result, this interpretation has discontinuity where the pore fluid changes. Because in our case study the compressibilities of water and oil are similar, this discontinuity is relatively weak. In the case of a strong compressibility contrast as in presence of gas, the discontinuity is expected to be much stronger. The ν threshold will change as well. We need to state again that accurate knowledge of the pore fluid properties is essential to obtaining correct porosity and clay content using our method.

To assess whether this method works with the seismically-derived impedances, we used the running-window Backus average in Well A and repeated this method now using the upscaled elastic inputs (Figure 3.7). In this case S_w was also assumed using the ν threshold. Afterwards, this rectangular shape S_w curve was arithmetically averaged, which resulted in the trapezoidal shape shown in red in the 3rd track in Figure 3.7. Then the interpretation algorithm was applied to these upscaled properties. Once again, the ϕ_t

and *C* computed from the Backus-upscaled I_p and I_s are in good agreement with the arithmetically upscaled porosity and clay content data, except in the reservoir-shale transition zones above and below the reservoir. By-and-large, our method give small errors, meaning that it is suitable when using the upscaled Well A data. It also had small errors on the remaining three wells for both the well- and seismic-scale curves (shown in Chapter 4).

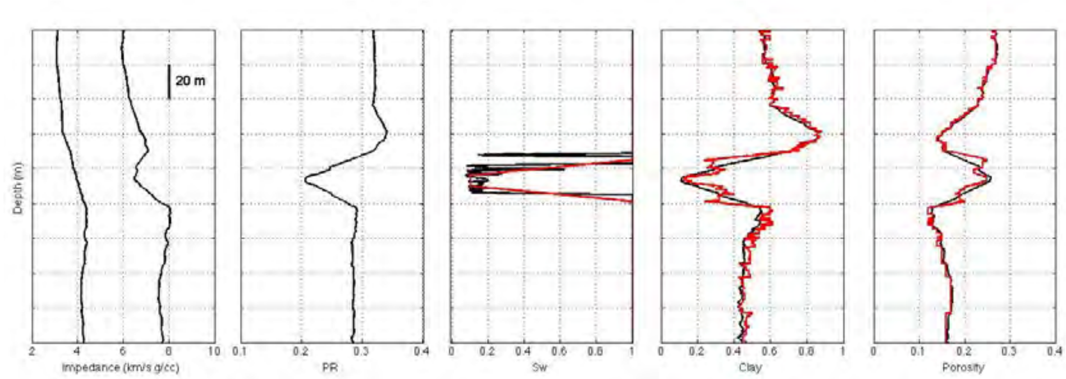

Figure 3.7. Same as Figure 3.6 with the Backus averaged well log curves upscaled to imitate the seismic scale.

It is important to mention that here we used rectangular smoothing. However, in real seismic data low frequencies are usually missing. This means that our upscaling approach, although making the point, is somewhat different from the actual seismic impedance inversion where the background model fills the gap.

3.5 Petrophysical Properties from Seismic Inversion

Simultaneous sparse-spike impedance inversion was conducted using Jason Geoscience Workbench (courtesy CGG) with the low-frequency model obtained from the rock-physics-model conditioned elastic curves at Well A. Although during inversion the P- and S-wave energies often get mixed to some degree, we rely here on the inversion package which presumably alleviates this problem by scaling the wavelets for each angle gather.

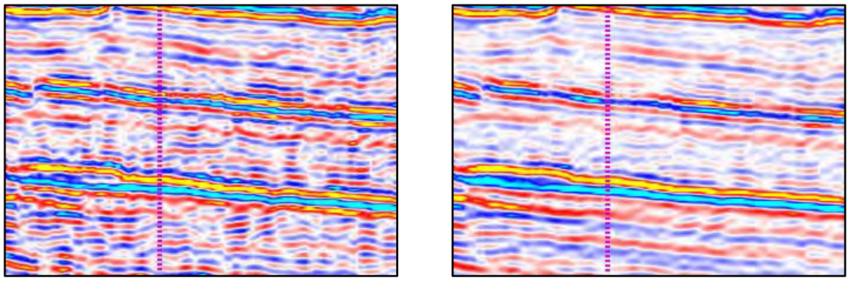

Figure 3.8. Vertical sections for the near (left) and far (right) angle stacks around Well A (vertical dotted line). The reservoir is the lowest bright negative-positive pair. The color scale is the same in both displays with red-yellow for negative and cyan-blue for positive.

Figure 3.8 shows the near (left) and far (right) angle stacks around Well A. The reservoir appears as a bright negative (red-yellow) event immediately followed by a positive amplitude (cyan).

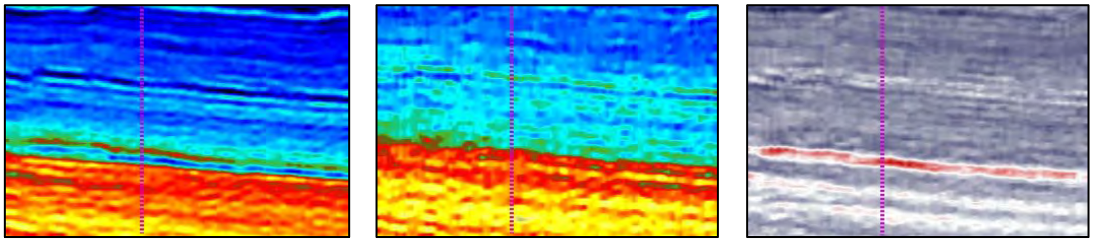

Figure 3.9. Vertical sections for Ip (left), Is (middle), and Poisson's ratio ν (right) from simultaneous inversion, shown around Well A (vertical dotted line). Color scale for Ip is between 5.5 (cyan) and 9.0 (yellow) km/s g/cc. Color scale for Is is between 2.5 (cyan) and 5.0 (yellow) km/s g/cc. Color scale for ν is between 0.1 (red) and 0.4 (dark-blue).

The results for I_p, I_s, and ν (computed from I_p and I_s according to Equation 3.1) are shown in Figure 3.9. In the I_p section, the reservoir appears as a blue (low-impedance) stripe surrounded by red (higher impedance), consistent with the upscaled Well A impedance curve (Figure 3.7). The I_s section shows gradual increase of the impedance from top to bottom, also consistent with the upscaled S-wave impedance at Well A (Figure 3.7). Poisson's ratio at the reservoir appears as a red stripe surrounded by higher values, also consistent with the ν curve in Figure 3.7.

The results of model-based interpretation of these seismically-derived I_p, I_s, and v for hydrocarbons, clay content, and porosity, using exactly the same method as described in the previous section are shown in Figure 3.10. The S_w section is binary, obtained by thresholding Poisson's ratio as described in the previous section. The clay content at the reservoir is very small, consistent with the well data (Figure 3.6). The total porosity is about 0.30, also consistent with the well data.

There are two relatively low clay content and high porosity stripes below the reservoir, which stem from the impedance inversion artifacts (Figure 3.11). In the saturation section we also observe low S_w artifacts below the reservoir which are due to the selected Poisson's ratio threshold as well as the impedance inversion artifacts driven by seismic data. Generally, our method provides accurate clay content and porosity estimates at and around the reservoir.

In Figure 3.11, we compare the seismically derived variables (blue) to those model-conditioned at Well A (black). The match is good, except for the two low Poisson's ratio features below the reservoir (see discussion at the end of this section). These features show as low Poisson's ratio stripes below the reservoir (Figure 3.9) and result in low clay content and high porosity artifacts in Figure 3.10.

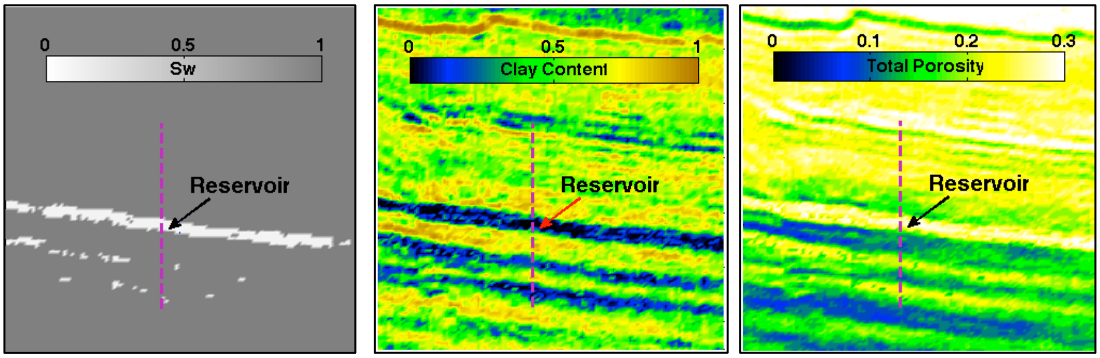

Figure 3.10. Results (vertical sections) of simultaneous impedance inversion interpretation for water saturation (left), clay content (middle), and porosity (right).

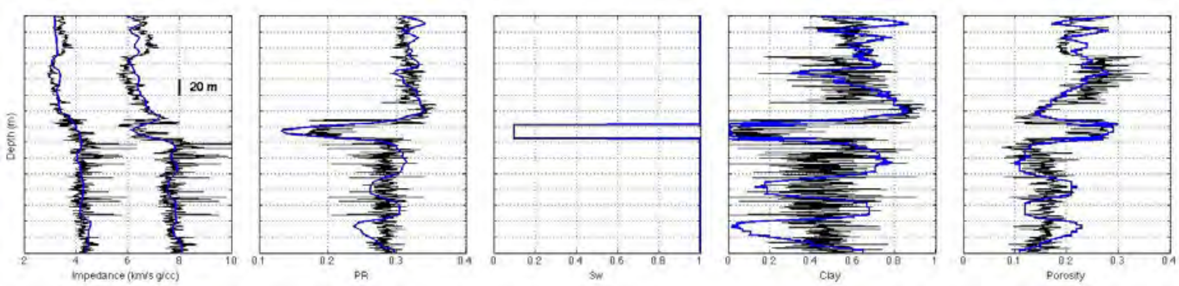

Figure 3.11. Well A. Comparison between well data (black) and seismically derived impedances, Poisson's ratio, clay content, and porosity (blue). In the Sw track only the Boolean seismically derived curve is shown.

The same comparison is shown in Figure 3.12 for Well B which was a blind-test well not used in impedance inversion. Once again, the match between the seismically derived properties and those at the well is satisfactory. Our method also passed blind tests at the two remaining wells, including the well where the hydrocarbons were absent.

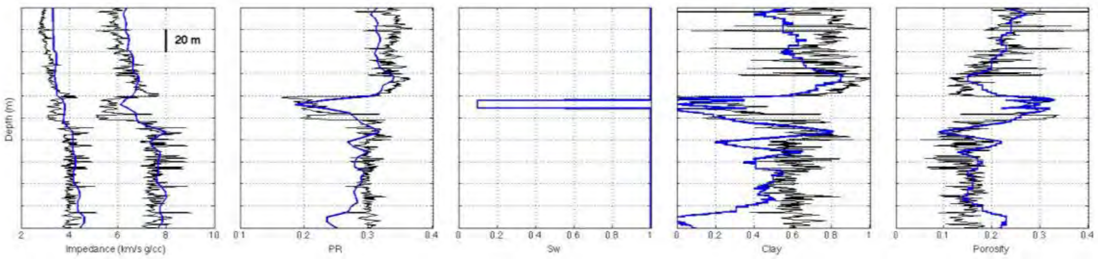

Figure 3.12. Same as Figure 3.11 but for Well B.

There are three low Poisson's ratio features below the reservoir. They are responsible for the low clay content and high porosity artifacts below the reservoir.

An obvious question is: If there are artifacts below the reservoir, how can we trust the details within the reservoir? One reason for these artifacts is less than perfect match between the well-measured and inverted impedance starting about 20 m below the reservoir. The match is satisfactory above this point, which ensures the quality of petrophysical interpretation of seismic inversion in the intervals of main interest. The artifacts below the reservoir may be due to a number of reasons. The first that Poisson's ratio is extremely sensitive to small variations in I_p and I_s. What we can hardly notice in an I_p versus I_s cross-plots becomes quite evident once we examine v. The second one is that ϕ_t and C are also very sensitive to the input impedance data and fluid (ν cutoff). This means that we need to use an inversion method as robust as possible and constantly strive to improve the quality of the simultaneous impedance inversion. We deem the sparse-spike inversion method used here satisfactory, although it may create artifacts in low-contrast depositional environments (as below the reservoir) as it enforces the placement of high-contrast reflectors.

3.6 Conclusion

Key to successful interpretation of seismic data for petrophysical properties is the rock physics diagnostics and the respective conditioning of well log curves to be used in simultaneous impedance inversion. The main tool of such interpretation is a rock physics model also obtained from rock physics diagnostics. This means that the solution offered here is site specific as the rock physics model depends on well data specific to the field under examination. Of course successful rock physics diagnostics can only be performed on high quality well data.

Also, high quality and conditioned angle gathers or angle stacks are necessary to ensure the success of impedance inversion and petrophysical interpretation. As usual, the background model needs to be correctly calibrated for the impedance inversion.

Once these prerequisites are met, we can accurately estimate the presence of hydrocarbons, porosity, and clay content from seismic data as shown in the examples presented here.

Notice that here we assume a binary quartz/clay mineralogy consistent with the lithological analysis of rock samples provided to us, so that we could obtain the two unknowns (porosity and clay content) from two inputs (I_p and I_s) once the presence of hydrocarbons is established from, e.g., Poisson's ratio. The situation may become more complicated (if not unresolvable) in more complex mineralogy where such facies as feldspar and calcite are present.

Still, the present case study proves that accurate petrophysical rock physics and seismic based interpretation is possible.

Chapter 4

Rock Physics Diagnostics of a Turbidite Oil Reservoir Offshore NW Australia

4.1 Abstract

Interpreting seismic data for petrophysical rock properties requires a rock physics model that links the petrophysical rock properties to its elastic properties, such as velocity and impedance. Such a model can only be established from controlled experiments where both groups of rock properties are measured on the same samples. A prolific source of such data is wellbore measurements. We utilize data from four wells drilled through a clastic offshore oil reservoir to perform rock physics diagnostics, i.e., to find a theoretical rock physics model that quantitatively explains the measurements. Using the model, we correct questionable well curves. Moreover, a crucial purpose of rock physics diagnostics is to go beyond the settings represented in the wells and understand the seismic signatures of rock properties varying in a wider range via forward seismic modeling. With this goal in mind, we use the model to generate synthetic seismic gathers from perturbational modeling to address "what-if" scenarios not present in the wells.

4.2 Introduction

We examine well data from the Stybarrow oil reservoir located 65 km offshore to the north-west of Australia. The reservoir is composed of turbiditic sandstones interbedded with claystones of Early Cretacious (Valanginian and Berriasian) age (Geoscience Australia, 2015). By analyzing samples from the Barrow group, Daniel and Kaldi (2012) found that the feldspar originally present in the sand has been converted into clay (kaolinite). Core analysis reveals that the sandstone is generally fine-grained, well sorted, and poorly cemented by very small amounts of siderite, or, in many places unconsolidated (Ementon et al., 2004). Stagg et al. (2004) report that there is a number of minerals present in the rock under examination, including small amounts of carbonate, siderite, glauconite, and pyrite.

Our goal is to conduct rock physics diagnostics (RPD), i.e., find a theoretical rock physics model that will quantitatively explain the well data from this reservoir in order to: (a) correct the velocity curves where they are possibly erroneous; (b) eventually use these corrected curves in simultaneous impedance inversion; and (c) conduct perturbational modeling using hypothetical geologically plausible scenarios, such as fluid substitution as well as porosity and mineralogy variations.

RPD has been gradually finding its way into quantitative seismic interpretation (Avseth et al., 2005). Published examples of RPD include Uden et al. (2003); Kittridge (2006); Gutierrez and Dvorkin (2010); Avseth et al. (2010); Draege (2011); Hossain and Newton (2013); and Yu et al. (2014). Dvorkin et al. (2014) discuss RPD in detail and present a number of case studies from several formations with different rock physics models. Here we use RPD in a specific case study in a clastic oil reservoir offshore NW Australia.

The rock physics diagnostics workflow requires a number of assumptions, the most important being an assumption about the mineralogy of rock under examination. In practice it is difficult (if not impossible) to account for the mineralogical diversity present in rock, simply because the fractions of various minerals are essentially not known in the well and, moreover, even if some of them are determined (from, e.g., spectral GR), the assignment of the elastic properties to these minerals is somewhat uncertain as they may span a range for each mineral (Mavko et al., 2009). Hence, we concentrate on the predominant facies, namely quartz and clay in this case, thereby assuming that the properties assigned to these elements reflect the combined effect of other facies present. In fact, we treat quartz and clay as "elastic" facies (rather than lithological elements) with fixed elastic moduli and density (Table 4.1).

The contact cement between the sand grains is reported to be siderite. Dvorkin et al. (1991) show that the properties of the grain-contact cement only weakly affect the elastic properties of a granular composite, rather it is the extent of cementation that has the dominant influence on the effective elastic properties. This fact further justifies our assumption about binary quartz/clay mineralogy. Specifically, we assume that the properties of the cement are the same as those of the dominant mineral matrix.

Our rock physics diagnostics is performed using data from two of the four wells available and confirmed by the data from the other two wells. First, we discuss the properties of the minerals and fluids used in rock physics modeling. Next, we provide "first-look" plots of the depth curves as well as the respective impedance-porosity cross-plots. Rock physics diagnostics follows, where we select a theoretical rock physics model to honor the data and correct the V_s curves accordingly. Next, we generate synthetic seismic gathers using the corrected curves and compare them to the actual seismic gathers. Finally, we explore synthetic seismic response in "what-if" scenarios where the overburden and reservoir properties are chosen outside of the ranges present in the well data.

This work is the first to present a systematic rock physics diagnostics approach to the west Australia field under examination. The rock physics model thus established can serve as a foundation for interpreting seismic data for petrophysical parameters. I feel that the approach taken here goes far beyond a case study by laying a basic physics foundation for quantitative seismic interpretation.

4.3 Properties of Minerals and Fluids

The elastic moduli and density of quartz selected are from Mavko et al. (2009). The elastic properties assigned to the clay are those of "gulf clay" (Tosaya, 1982, as listed in Mavko et al., 2009). Although the listed density of the selected clay type is 2.60 g/cc, we assume for simplicity (in order to keep a constant density term) that it is 2.65 g/cc, same as in quartz. The impact of this assumption is in the total porosity calculations and is not significant in the reservoir. Of course, this assumption should not be used in non-conventional reservoirs (e.g., oil sands, tight oil and oil shale) where the clay-phase properties may be quite different from those in conventional shale and, hence, have larger ramifications for the effective density and elastic property computations.

The oil present in the reservoir is biodegraded (Napalowski et al., 2010) with a low gas-to-oil (GOR) ratio 51 and a low API density 21. The gas gravity is 0.65. The pore pressure and temperature are 23 MPa and 63° C, respectively. The water salinity is 85000 ppm. Using these inputs, we computed the bulk moduli and densities of oil and water (Table 4.1) according to Batzle and Wang (1992).

Table 4.1. Properties of the minerals and fluids used in rock physics diagnostics.

Material	Bulk Modulus (GPa)	Shear Modulus (GPa)	Density (g/cc)
Quartz	36.6	45.0	2.65
Clay	21.0	7.0	2.65
Water	2.91	0	1.05
Oil	1.36	0	0.85

4.4 Well Data and Cross-Plots

Figures 4.1 to 4.4 present well log curves for the four Stybarrow wells. Wells 1 and 2 penetrate thick (~ 20 m) oil reservoirs. The reservoir is thinner (~ 10 m) in Well 4 and practically absent in Well 3. The porosity track shows three curves: the standard density-derived porosity ϕ_ρ, where the density of the mineral is 2.65 g/cc and that of water is 1.00 g/cc (e.g., Schlumberger, 1987); neutron porosity ϕ_N; and total porosity ϕ_t computed from the bulk density ρ_b using the in-situ density of the pore fluid ρ_f (Equation 4.1).

$$\phi_\rho = (2.65 - \rho_b)/(2.65 - 1)\,; \quad \phi_t = (2.65 - \rho_b)/\left(2.65 - \rho_f\right);$$

$$\rho_f = S_w \rho_w + (1 - S_w)\rho_o \qquad (4.1)$$

where ρ_w and ρ_o are the densities of water and oil, respectively, as listed in Table 4.1. Because of the slight density contrast between water and oil, ϕ_t is close to ϕ_ρ.

In this analysis we used the fast shear-wave velocity data. The quality of these data is questionable in some parts of Wells 2 and 4 as manifested by a blocky shape of the V_S curves and negative Poisson's ratio values (Figures 4.2 and 4.4, respectively). These V_S problems could be due to, among other reasons, the tool malfunctioning and/or the dipole full-waveform interpretation of the arrivals.

Next, conduct the rock physics diagnostics on Well 1 and then check the validity of the model using the remaining three wells. The impedance versus porosity cross-plots for Well 1 are shown in Figure 4.5. The symbols are color-coded by GR, the ϕ_N-ϕ_ρ difference, and depth.

An interesting feature in these cross-plots is that the P-wave impedance in oil sand is very close to that in the shale in the same porosity range, while the S-wave impedance is clearly differentiated. This is clearly the effect of the pore fluid as the bulk modulus of oil is about half of that of the water. It also appears that the ϕ_N-ϕ_ρ difference is a better indicator of shale (clay) content than GR as the former provides a more clear discrimination for the data along the impedance axis. Finally, we can observe compaction with depth that acts to simultaneously reduce the porosity and increase the impedance.

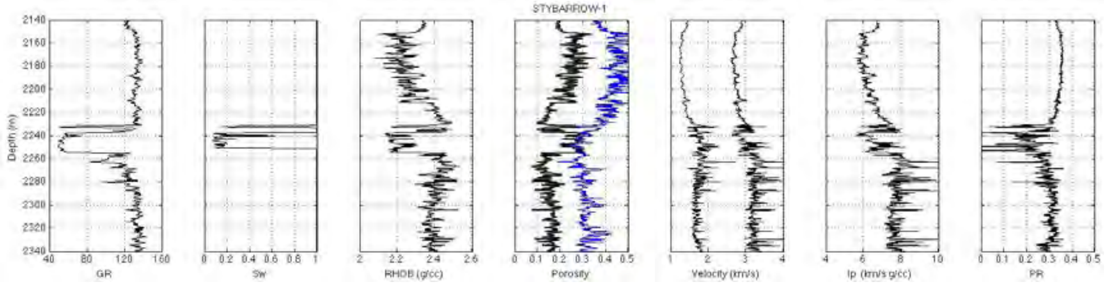

Figure 4.1. Log curves for Well 1. From left to right: GR; Sw; bulk density; porosity; velocity (P and S); P-wave impedance; and Poisson's ratio. In the porosity track, gray is for the density-derived porosity while black is for total porosity (these two curves are very close to each other) computed as explained in the text, and blue is for neutron porosity.

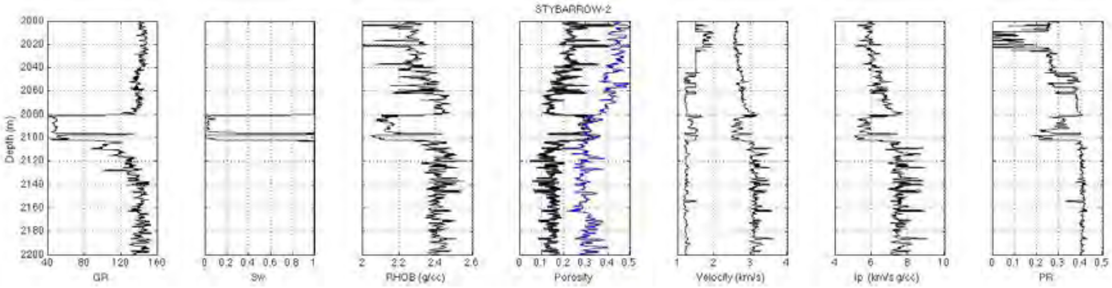

Figure 4.2. Log curves for Well 2. Display is the same as in Figure 4.1.

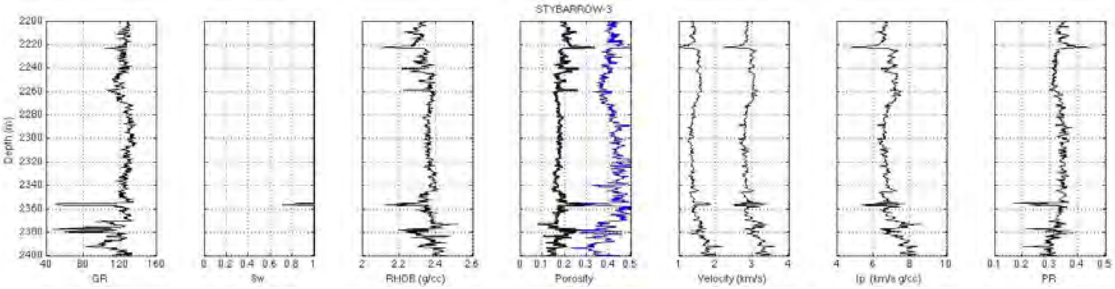

Figure 4.3. Log curves for Well 3. Display is the same as in Figure 4.1.

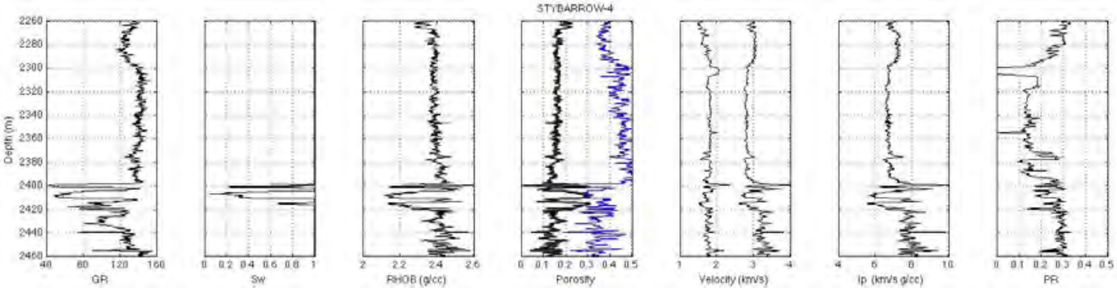

Figure 4.4. Log curves for Well 4. Display is the same as in Figure 4.1.

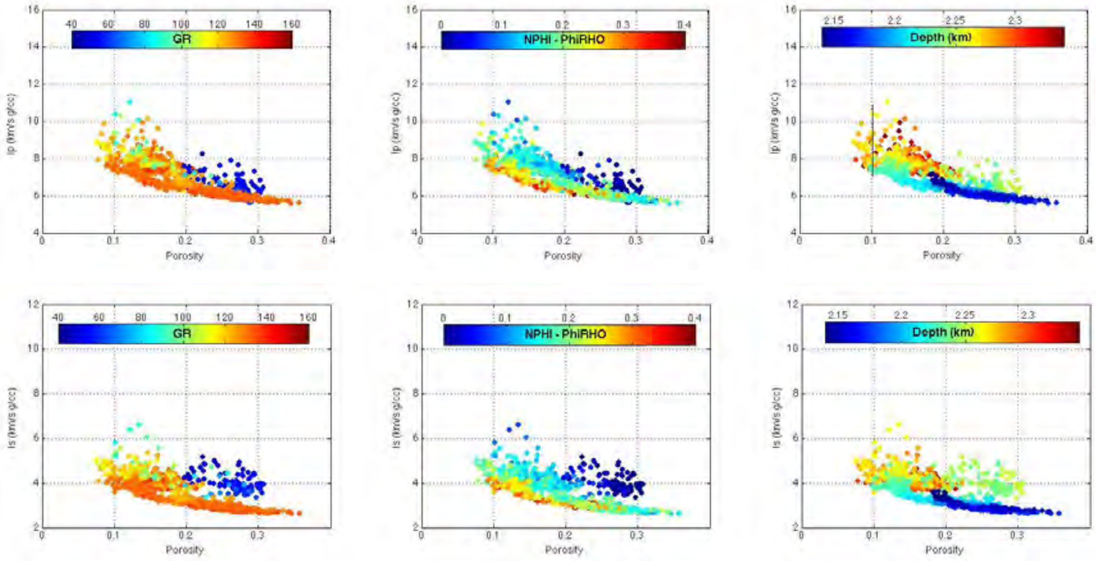

Figure 4.5. Well 1. Ip (top) and Is (bottom) versus the total porosity color-coded by GR (left), porosity difference (middle); and depth (right).

4.5 Rock Physics Diagnostics (RPD)

RPD is the operation of finding an empirical or theoretical rock physics model that accurately mimics the site-specific elastic behavior of sediment. It is usually performed on well log data and includes two steps: (a) bringing the entire interval under examination to a common fluid denominator by theoretically substituting the in-situ pore fluid with, e.g., the formation brine and (b) finding model curves that fits these "wet-rock" data.

The bulk modulus of the pore fluid K_f was computed as the Reuss (1929) average of those of the two phases:

$$K_f^{-1} = S_w K_w^{-1} + (1 - S_w) K_o^{-1}, \qquad (4.2)$$

where K_w and K_o are the bulk moduli of water and oil, respectively (Table 4.1).

Figure 4.6 shows the wet-rock I_p versus ϕ_t cross-plots for Well 1 (top) and Well 2 (bottom). Since the quality of some of the V_s data is questionable, we arrived at the wet-rock elastic properties by using the V_p-only fluid substitution (Mavko et al., 2009).

The model curves superimposed on the data in Figure 4.6 come from the constant-cement model (Mavko et al., 2009) which is essentially the soft-sand model but used with the artificially high coordination number (Dvorkin et al., 2014). This model requires a number of inputs, including the properties of the pore fluid, the total porosity, mineralogy (to compute the elastic properties of the mineral matrix), differential pressure, critical porosity, coordination number (the average number of contacts per grain), and the so-called "shear correction factor" that artificially changes the Hertz-Mindlin (Mindlin, 1949) tangential stiffness between two grains in contact.

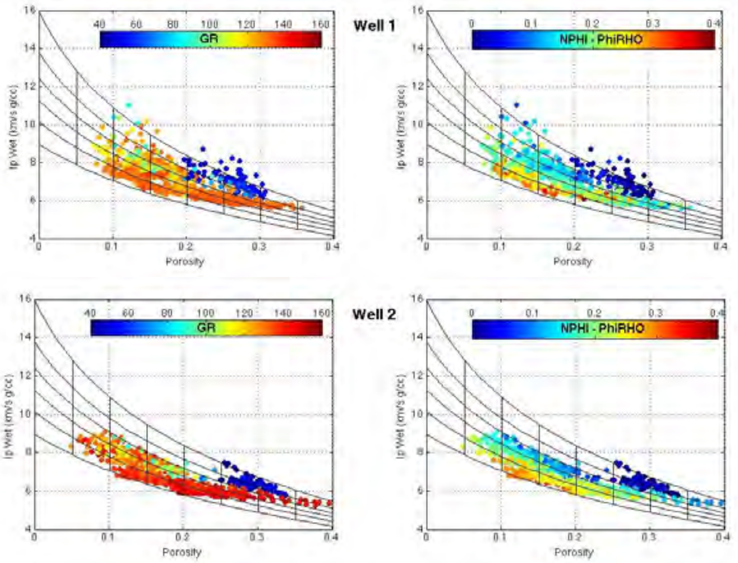

Figure 4.6. Well 1 (top) and Well 2 (bottom). Wet-rock Ip versus the total porosity color-coded by GR (left) and the porosity difference (right). The model curves come from the constant cement model as explained in the text. The upper curve is for zero clay content while the bottom curve is for 100% clay content, with the clay content increment 20% for the curves in between. The vertical lines are each for fixed porosity and the clay content varying between zero and 100%.

The pore fluid used in the model has to be exactly the same as the common fluid denominator, which is the formation water (Table 4.1). The mineralogy is binary, quartz/clay, and the elastic moduli of the mixed mineral phase is computed according to Hill's (1952) average and using the constants listed in Table 4.1. The differential pressure used in the model was assumed to be 17 MPa, which is the average difference between the overburden and pore pressure at the reservoir. The critical porosity was 0.40, coordination number 20, and the shear correction factor 1, meaning that we did not alter the Hertz-Mindlin tangential stiffness.

As shown in Chapter 3, the porosity difference ϕ_N-ϕ_ρ appears to be a more accurate clay content indicator than GR, in terms of the comparison between the inverted clay content and the one derived from this measurement, i.e., with the dark-blue datapoints falling onto the low-clay-content model curves, cyan and yellow on the intermediate clay content curves, and red on the high clay content curves.

Next, we need to ensure that the model thus established matches the well data at all points along the interval. In other words, we have to apply the model to the clay content, total porosity, and fluid properties (bulk modulus and density) curves along the depth. The only variable not immediately available is the clay content.

Usually the clay content C is provided from petrophysics using GR, SP, and/or the ϕ_N-ϕ_ρ difference. Here we take a different, model-based, approach: we assume that the total porosity ϕ_t as well as V_p and S_w (and the ensuing pore-fluid properties) data are correct and the rock physics model established is applicable in all wells. Next, using these inputs (ϕ_t, V_p, and S_w), we compute C by running our model in reverse, i.e., finding the clay content that will allow us to match V_p at given porosity and pore fluid properties. Once this clay content is established, it can be used to predict V_s.

This approach seems to be self-serving since by using C computed from the model we will certainly match the input V_p. The reason for this operation is to predict V_s. It is only justified if the model-derived C is consistent with that estimated from independent measurements (e.g., GR and/or the ϕ_N-ϕ_ρ difference).

The model-based C curves are compared to those obtained by normalizing the porosity difference and GR are shown in Figure 4.7. It appears that the match of the model-derived C with that obtained from the porosity difference is better than with the GR-derived C. Of most concern is the mismatch observed in the reservoir in Well 2 where the porosity differences as well as GR imply very low clay content while the model-based C is much higher in the middle of the reservoir. This mismatch results from the fact that the reservoir datapoints (dark blue in the bottom-right graph in Figure 4.6) fall upon the high-clay-content model curves. This fact defies the expectation that with the same fluid in the pores and the same clay content, the lower-porosity samples should have higher impedance. In principle, we could have assumed low clay content in the reservoir and then correct the velocity data. However, here we follow the selected methodology and correct the clay content instead.

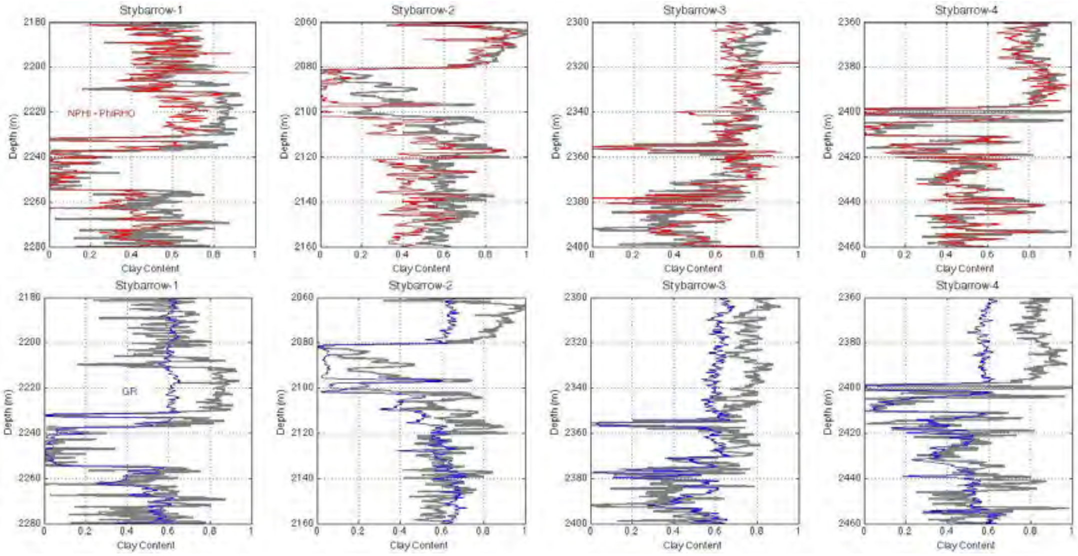

Figure 4.7. Model-based clay content prediction for all four wells (dark gray curves) compared to the clay content derived from normalizing the porosity difference (red curves in top row) and GR (blue curves in bottom row).

Of course, the discrepancy between measured and modeled clay content may be due to the characteristics of the sediment not captured in our assumptions and model. It may also result from the less-than-perfect data quality in the interval under examination. The modeler needs to make a choice whether to give preference to the model or to the data that do not match the model. Because the model-derived C appears to reasonably well match that derived from the porosity difference in the other three wells, we in this case give preference to the model. The resulting model-predicted curves at in-situ conditions are compared to the measured data in Figure 4.8.

In this case, we obtain an almost perfect match between the modeled and recorded density, V_p, and I_p curves in all wells. The match for V_s is also very accurate in Well 1 and 3. Where the S-wave data quality is questionable (the entire interval in Well 2 and the upper portion in Well 4) the match is expectedly poor. One indicator of the poor V_S quality in the upper portion of Well 4 is that the Poisson's ratio is unreasonably small (close to 0.1) in water-saturated shale. Therefore, the decision is to rely now on the modeled data.

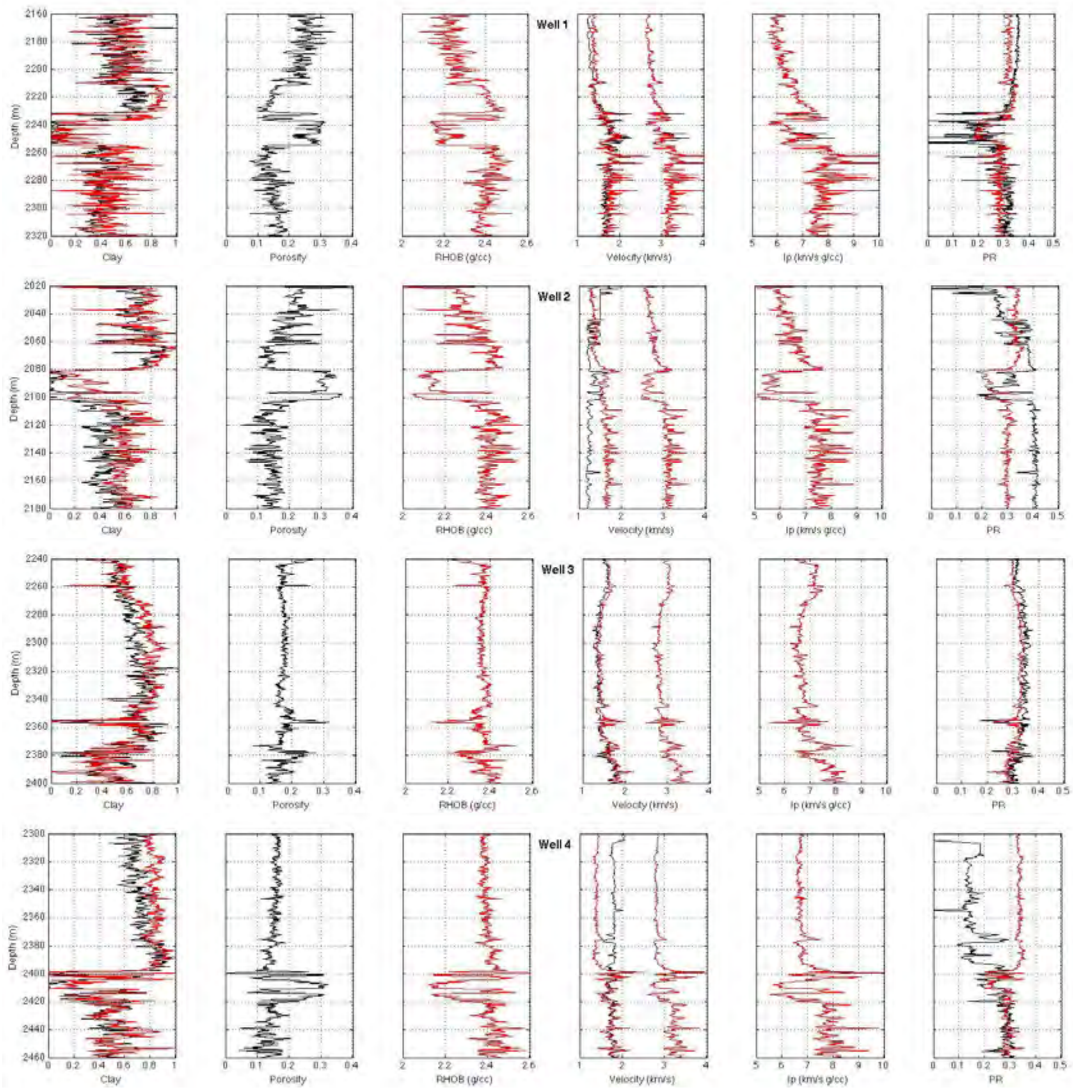

Figure 4.8. Model-based curves (red) and measured curves (gray) for Wells 1, 2, 3, and 4. The modeled density, Vp, and Ip curves often fall on top of the respective data, so that the latter is not visible.

In order to proceed with exploiting the rock physics model established in this section, we need to make another assumption: the model is applicable not only at the wells but also in the entire volume surrounding the reservoir.

4.6 Model-Based Synthetic Gathers

The rock physics model based elastic curves allow us to produce synthetic gathers at the wells and compare them to real seismic data. We concentrate on producing synthetic gathers at Well 1 (massive reservoir) and Well 3 (practically no reservoir) using Ricker's 30 Hz wavelet in a raytracer (Figure 4.9). While Well 1 shows fairly flat AVO Class III response at the reservoir, Well 3 shows a very weak reflection. This is consistent with recorded seismic data (Figure 4.10 for Well 1 and Figure 4.11 for Well 3).

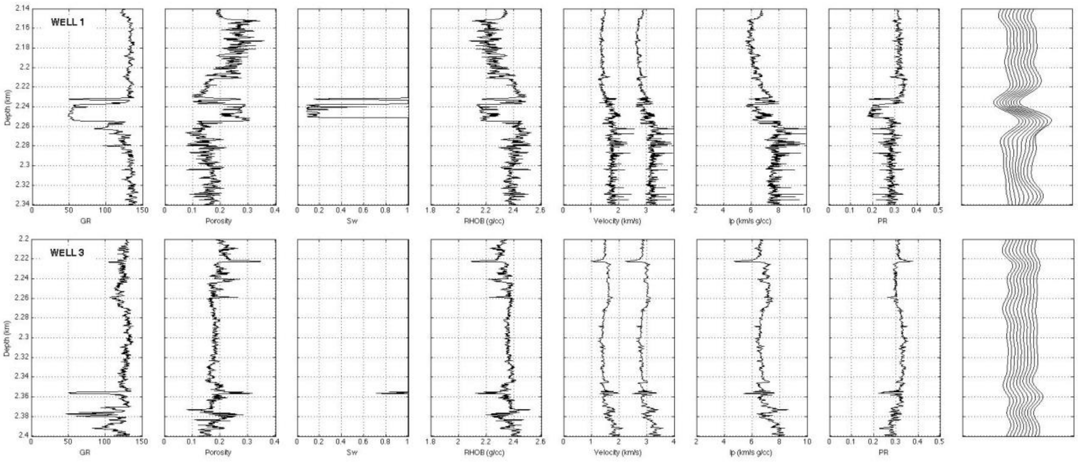

Figure 4.9. Synthetic seismic gathers at Wells 1 (top) and 3 (bottom) using a raytracer and a 30 Hz Ricker's wavelet. Synthetic gathers are shown in the last track. Model-based in-situ conditions curves were used. The maximum incidence angle is about 45o. In Well 3 we observe destructive interference of the reflections at the reservoir which renders the reservoir essentially undetectable at this well.

Pevzner et al. (2011) discuss noticeable stress-induced azimuthal anisotropy in the area under examination. The presence of this anisotropy was taken into account during seismic processing. As a result, the partial angle stacks shown in Figures 4.10 and 4.11 have been already corrected for azimuthal velocity anisotropy.

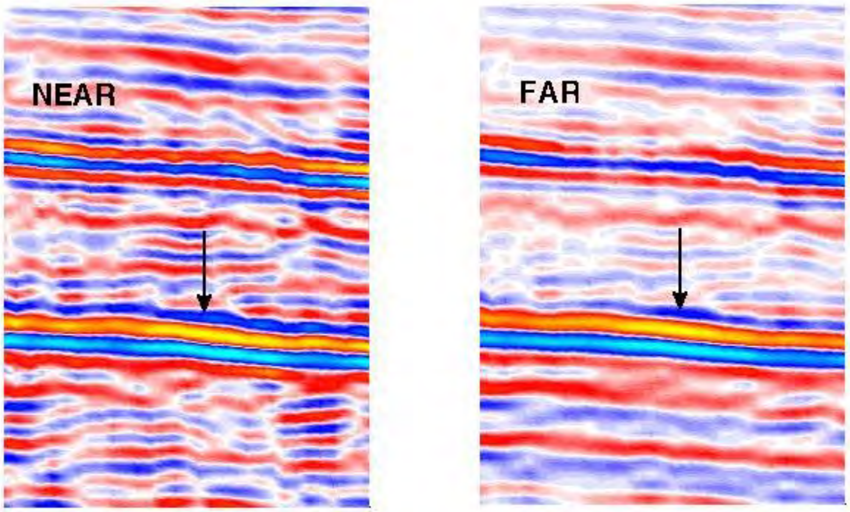

Figure 4.10. Near (left) and far (right) angle stacks at Well 1 showing essentially flat Class III amplitude (yellow) at the reservoir pointed at by the arrows.

4.7 Seismic What-If Scenarios

The rock physics model established here allows us to vary the ranges of porosity and clay content in sand and shale as well as to change the properties of the pore fluid and obtain the respective seismic responses. One implementation of perturbational forward modeling is shown in Figure 4.12 where we can select the desired porosity and clay content ranges in the reservoir and overburden as well as alter the API and GOR of oil and then use full Zoeppritz (1919) equations to generate a gather and the respective AVA curves at the top of the reservoir which is the interface between two half-spaces, shale on top and sand at the bottom. Examples shown in Figure 4.12 produce AVA curves for wet, oil, and gas sand cases. In the case where the fluid properties were the actual in-situ properties and the ranges selected for sand and shale were also close to the actual case in

Well 1, this rock physics template produces a flat AVO Class III response, similar to that at the reservoir in Well 1 (Figure 4.9, top).

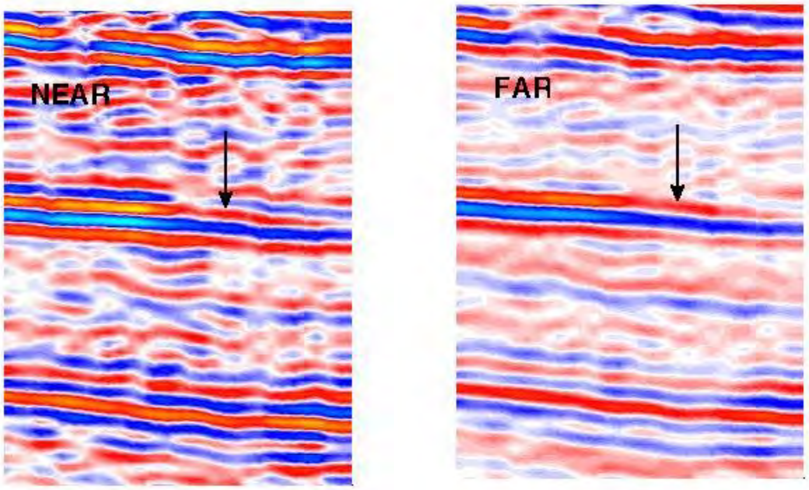

Figure 4.11. Near (left) and far (right) angle stacks at Well 3 showing the loss of the amplitude (left to right in both panels) at the well pointed at by the arrows.

The next case is for much lighter oil where the response from the oil reservoir expectedly moves closer to the gas response. The 3rd case is the same as the 1st case but the porosity of the sand is smaller and the clay content larger. The response changes and becomes Class I. Finally, where the porosity of both sand and shale are assumed very high (which can be the case at shallower depths), the response is Class II.

Another type of rock physics template is where we plot the elastic properties of shale and sand in the I_p - Poisson's ratio (ν) plane. The input for AVA modeling is set by selecting points in the overburden and reservoir. The curves are produced using Hilterman's (1989) approximation, because his formulation is in terms of the I_p and ν, where the intercept and gradient are extracted. This modeling allows for estimating the response for varying overburden and reservoir as well as the fluid's properties. Examples are given in Figure 4.13.

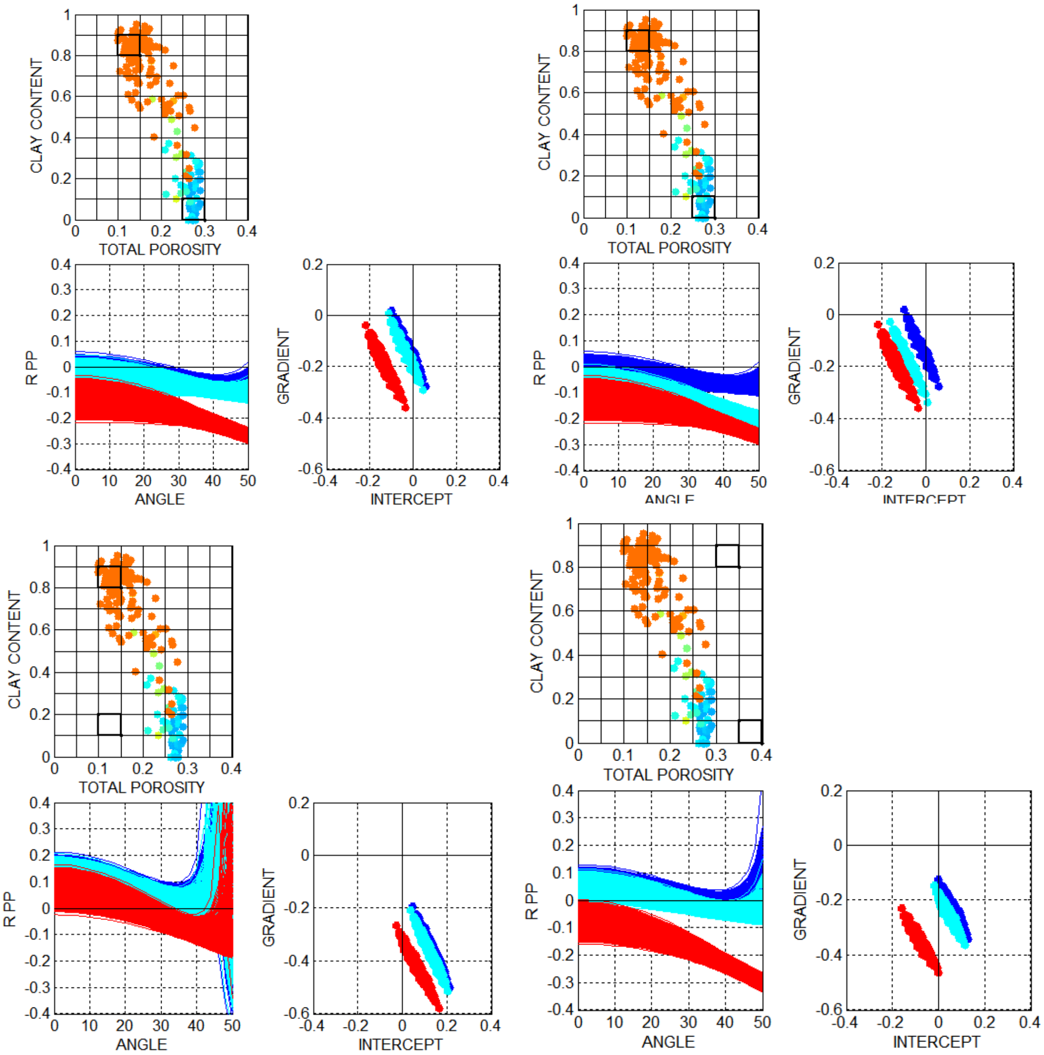

Figure 4.12. Forward modeling rock physics template. AVA curves are generated at the interface using full Zoeppritz equations. Gradient and intercept are computed using AVA curves between zero and 25° incident angle. In the clay content – porosity panel, the selected ranges in the reservoir and overburden are shown by black boxes. In the same panel we display data points from Well 1, color-coded by water saturation (light blue is for oil reservoir). Top left: sand's porosity and clay content vary from 0.25 to 0.30 and zero to 0.10, respectively, while for the overburden these ranges are from 0.10 to 0.15 and 0.80 to 0.90. The pore fluids have the original in-situ properties. The AVA curves are generated for interfaces between the overburden and wet sand (blue), oil sand (cyan), and gas sand (red). Top right: same as top left but with oil gravity 30 API and GOR 500 l/l. Bottom left: the original pore fluids but the sand has increased clay content (0.10 to 0.20) and reduced porosity (0.10 to 0.15). Bottom right: high porosity sand and shale with the original fluid properties.

In the first example in Figure 4.13 we generate a response between cap-rock shale of porosity about 0.10 and clay content about 0.70 and reservoir oil sand of porosity 0.20 and small clay content (case "1"). This scenario is compared to the case where the sand's porosity is 0.30 (case "2"). In both scenarios we observe AVO Class III. The next example is the same but for the reservoir filled with light oil which expectedly produces a stronger Class III. The final example is for reflections between oil and water sand. Where the porosities in both sands are similar, we obtain a curve with positive intercept and small but positive gradient. Where the porosity of the oil sand is much higher than that of the wet sand, we obtain flat positive response. This simple forward modeling tool is fairly versatile as we can model the response for many “what-if” scenarios, including at an oil-water contact within the reservoir.

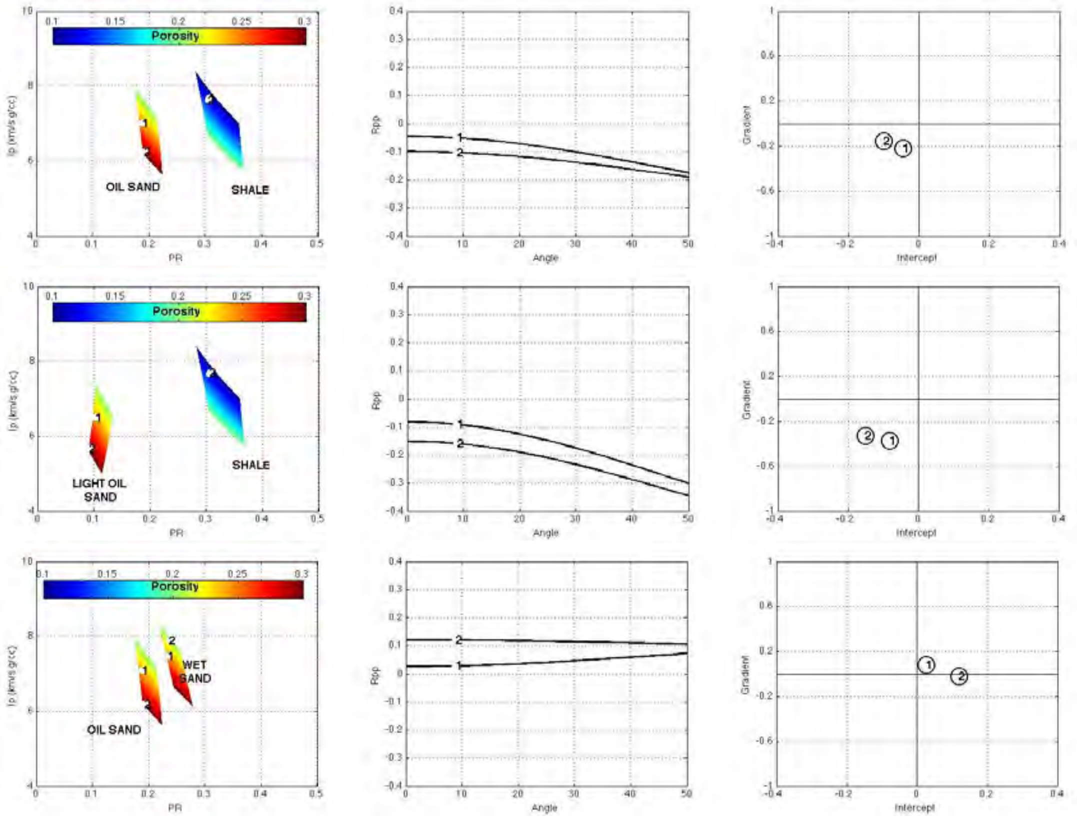

Figure 4.13. Half-space AVA modeling using Hilterman’s (1989) approximation. The colored shapes in the Ip versus ν plane correspond to the model-based elastic properties of shale and sand where the shale’s porosity and clay content vary between 0.10 and 0.20 and 0.60 and 1.00, respectively. These ranges for the sand are 0.20 to 0.30 and zero to 0.20. The color code is porosity. The horizontal extent of these shapes is due to varying clay content. The AVA curves as well as intercept and gradient are computed between the two selected points in the Ip - ν plane and numbered accordingly. Top: the original in-situ fluids; from low-porosity shale to medium-porosity sand. Middle: the light oil case (API 30 and GOR 500). Bottom: reflections at the hypothetical oil-water contact within a reservoir (original fluids).

4.8 Discussion

Why do we need theoretical rock physics modeling? An alternative is to, e.g., plot velocity versus porosity in a reservoir and overburden, make regressions and then use these equations for interpreting the remotely sensed elastic properties. The latter approach, although often used, may be strongly influenced by the quality of well data and produce quite different equations for different wells in the same reservoir. Even if the data quality is perfect, such regressions can produce illogical results, for example velocity increasing with increasing porosity. Only careful rock physics analysis may reveal that small variations in the clay content or rock texture are responsible for such behavior (Avseth et al., 2005; Dvorkin et al., 2014).

In contrast, theoretical rock physics models, although idealized, are usually verified by many datasets from different geographical locations and basins, which makes them quite general and robust. In addition, such models are based on physical principles. Of course, any physics-based modeling of nature requires assumptions. The main assumption used in the case study presented here is the binary quartz/clay mineralogy. This simplifying assumption has to be questioned in each case study, yet it appears to be consistent with the data under examination here. The advantage of using a theoretical rock physics model is its flexibility in exploring various "what-if" scenarios not necessarily present in the well data as these data may not necessarily sample all geologically plausible variants in the basin.

We use this approach, often called the rock physics diagnostics, in four wells from the same oil reservoir and find that the same model explains the data from all these wells. One use of this model is to correct questionable well data, the S-wave velocity in our case. Another advantage is to cover scenarios where the pore fluid as well as lithology varies and produce synthetic seismic signatures of such rock properties and conditions.

An ultimate check of the validity of a model is in real seismic data. Once the model give small errors in the interpretation, it can be directly applied to seismic impedance inversion to estimate the porosity, clay content, and in-situ fluid (as shown in Chapter 3).

4.9 Conclusion

Based on well data from four wells, we established a rock physics model for an offshore oil reservoir and surrounding shale. This model enabled us to (a) correct the apparently ambiguous V_S data and (b) explore the seismic response of various geologically plausible scenarios not present in the wells. Such forward modeling can serve as a guide for understanding the rock properties and conditions behind recorded seismic data. A model can also be used to quantitatively derive these properties and conditions from remotely sensed elastic properties of the subsurface obtained from simultaneous impedance inversion. This work goes well beyond a mere case study by providing an initial building block for such interpretation.

Chapter 5

Simultaneous Impedance Inversion and Interpretation for an Offshore Turbiditic Reservoir

5.1 Abstract

By using simultaneous impedance inversion, we obtained P- and S-wave impedance (I_p and I_s) volumes from angle stacks at a siliciclastic turbidite oil reservoir offshore NW Australia. The ultimate goal was to interpret these elastic variables for fluid, porosity, and mineralogy. This is why an essential part of our workflow was finding the appropriate rock physics model based on well data. The model-corrected S-wave velocity (V_s) in the wells was used as input to impedance inversion. The inversion parameters were optimized in small vertical sections around two wells to obtain the best possible match between the seismic impedances and the upscaled impedances measured at the wells. Special attention was paid to the seismically derived I_p/I_s ratio since we relied on this parameter for hydrocarbon identification. Even after performing cross-

correlation between the angle stacks to correct for two-way travel time (TWT) shifts to align the stacks, these stacks did not show a coherent AVA dependence. To deal with this common problem, we conditioned the mid and far angle stacks in a manner similar to residual statics by using the near and ultra-far stacks as anchoring points for fitting a $\sin^2\theta$ AVA curve. This choice allowed us to match the seismically derived I_p/I_s ratio with that predicted by the rock physics model in the reservoir. Finally, the rock physics model was used to interpret these I_p and I_s for the fluid, porosity, and mineralogy. The new paradigm in our inversion/interpretation workflow is that the ultimate quality control of the inversion is in an accurate deterministic match between the seismically-derived petrophysical variables and the corresponding upscaled depth curves at the wells. Our interpretation is very sensitive to the inversion results, especially the I_p/I_s ratio. Despite this fact, we were able to obtain accurate estimates of porosity and clay content in the reservoir and around it.

5.2 Introduction

The main interpretation issue addressed here is expressing the seismic amplitudes (seismically-derived elastic attributes) in terms of the geological properties of the subsurface.

The seismic reflections depend on the *contrast* of the elastic properties in the subsurface. The desired rock properties and conditions (e.g., porosity, clay content, and pore fluid) are usually tied to the *absolute* values of the elastic properties. Impedance inversion is a way of translating seismic data to these absolute elastic variables.

Simultaneous impedance inversion provides, in principle, three seismic-scale variables, the P- and S-wave impedances (I_p and I_s, respectively) and the bulk density (ρ_b).

In this case study, the density results are low-quality and noisy. Likely reasons for the low-quality of the seismically-derived density are at least two: (a) the maximum angle stack was of only 39 degrees, while depending on the contrast at the interface, the contribution of the tangent term in the Aki-Richards (2002) equation may become meaningful only at larger angles and (b) the angle stacks available to us did not show a clear AVO picture as discussed later in this chapter.

This practical conclusion is in line with the results presented by, e.g., Soldo (2006); Alves Vanzeler et al. (2014); and Qin and Lambare (2016), indicating that obtaining reliable seismically-derived density is challenging and can be somewhat improved by using multicomponent data including P-to-S converted waves (see also Hampson et al., 2005; and Leiceaga et al., 2010) and fairly involved special algorithms for FWI (e.g., Jeong and Min, 2012).

Still, even if reliable I_p and I_s volumes are available, they are the elastic rather than petrophysical properties of the subsurface. Our objective is to reliably quantify the latter, namely the porosity, clay content, and pore fluid. This is why rock physics modeling that provides a link between the elastic and petrophysical properties and conditions has to be an integral part of the inversion/interpretation workflow. Matching these seismically-derived petrophysical properties rather than only the impedances with well data is the preferred quality control of the inversion results.

Our other objective here is to show how to use standard single-component prestack time migrated seismic data as well as simultaneous pre-stack inversion combined with rock physics modeling to produce reliable volumes of porosity and clay content as well as delineate hydrocarbons in a siliciclastic environment. Of course, this aspiration is not new. All earlier attempts involved rock physics models to a certain extent. As early as 1982, Angeleri and Carpi used Wyllie's time average equation that relates the travel time to porosity and the velocity in the mineral and fluid phases to estimate the clay content in the seismic section by interpolating well data. Later, Dolberg et al. (2000) generated a seismically derived porosity volume using I_p combined with a statistical impedance-porosity fit with an assumed fixed clay content.

A somewhat different, statistics-based approach was described by Avseth et al. (2005), where seismic elastic lithofacies were defined based on well data and theoretical rock physics and then used to classify these facies in the seismic domain. A similar approach was also used by Spikes (2008) to quantify several reservoir properties and the associated uncertainty by conducting exhaustive forward modeling at the top of the reservoir unit.

Of course, the rapidly exploding machine learning approach can always provide an answer. Yet we feel that deterministic cognitive analysis supported by robust physics is absolutely necessary to constrain and verify any such answer. This is why our study is focused on deterministic analysis that includes obtaining a site-specific theoretical rock physics model, using this model to correct well data of questionable quality, and then directly applying this model to seismically derived I_p and I_s.

This chapter addresses the steps we undertook to obtain the elastic properties needed for our petrophysical interpretation. The initial task was to conduct rock physics diagnostics on well data to obtain a porosity-mineralogy-velocity model. This model was used then to correct V_s curves which were questionable in two of the four wells. Even where V_s data appeared to be of acceptable quality, using the model helped us remove spurious spikes. Of course, the site-specific rock physics model is not only used to correct the well data but, most importantly, it served as the basis for interpreting the seismically derived I_p and I_s for porosity and clay content away from the wells. Of special importance is the I_p/I_s or Poisson's ratio n since the rock physics transform depends on the pore fluid which was identified in the seismic volume by thresholding n.

Part of the workflow was to deal with the commonly observed fact that even after aligning the angle stacks in time, they still did not show a coherent AVA dependence. We addressed this problem by correcting the mid and far stacks using the near and ultra-far stacks as anchoring points for fitting a $\sin^2\theta$ AVA curve.

I performed three variants of simultaneous impedance inversion: (a) using Well 1 for the low-frequency model; (b) using Well 3 for the low-frequency model; and (c) using both Well 1 and 3 for the low-frequency model. The last gave us the best match between the impedances in all four wells and I_p and I_s from inversion. This variant also resulted in satisfactory match of the seismically derived porosity and clay content with the upscaled well data.

The main novelty of this work is in combining rock physics with deterministic simultaneous impedance inversion by (a) using a low-frequency model based on corrected well data and (b) using rock physics to interpret the inversion results for seismic-scale petrophysical parameters.

5.3 Dataset

The seismic and well data is the same used throughout the whole thesis; it comes from Stybarrow oil field from offshore NW Australia. This field is part of Exmouth sub-basin which is inside the Carnarvon basin (Ross and Vail, 1994). This basin is divided into three sub-basins named the Dampier, Barrow, and Exmouth. These sub-basins are separated by high-angle normal faults as well as strike-slip faults. The deposits in the Exmouth basin are predominantly Mesozoic. Their thickness ranges between 10 and 15 km. The oil reservoir under examination is of Berriasian age (Early Cretacious) located within Barrow Group D, also called Malouet formation, which is a submarine fan sequence.

Dominant facies include basin-floor fan sandstones, pro-delta to fore-set claystones, and top-set sandstones (Geoscience Australia, 2016). The sandstone is mainly quartz and has fairly high porosity and permeability. It is fine-grained, well sorted, and has some contact cementation (Ementon et al., 2004).

The source rock is the Upper Jurassic Dingo claystone. It is considered to be the source of the commercial oil accumulations within the basin. The seal of Stybarrow reservoir is the Muderong shale. The structural trap style is a tilted fault block (Geoscience Australia, 2016).

Daniel and Kaldi (2012) report that the original feldspar in the reservoir was converted into kaolinite clay. Stagg et al. (2004) report the presence of small amounts of carbonate, siderite, pyrite, and glauconite. Still, since quartz and clay are the dominant minerals in and around the reservoir, we assume a binary quartz/clay mineralogy for the purpose of rock physics modeling (as was discussed in Chapter 4).

5.3.1 Well Data and Rock Physics Model

By analyzing the data from four wells, as shown in Chapter 4, I have found that the compressional modulus-porosity-clay relation is governed by the constant-cement model (Mavko et al., 2009). In the last chapter it was also established that the difference between the neutron porosity ϕ_N and density-derived porosity ϕ_P appeared to serve as a robust proxy for the clay content as shown in Figure 5.1. In this figure we use the wet-rock elastic modulus obtained from the well data by the V_P-only fluid substitution (Mavko et al., 1995), meaning that we brought the entire intervals under examination to the common fluid denominator, the formation water in this case. The datapoints are color-coded by the aforementioned ϕ_N-ϕ_P difference. The respective colorbar is only shown in the first cross-plot and is the same for all four cross-plots in this figure. This technique is part of rock physics diagnostics and is used to remove the influence of one of the variables, the fluid, and concentrate on the two remaining variables, the porosity and clay content.

The parameters of the rock physics model used are described in Chapter 4. This is the model that we used to correct the V_s curves to obtain model-consistent Poisson's ratio (ν) curves (Figure 5.2). The ν versus depth plots in this figure indicate that the rock physics model fairly accurately reproduces V_s measured in Well 1 and 3. Figure 5.2 shows a very poor fit between the model-based and measured ν. Such mismatch may not be recognized in commonly used quality-control plots, such as V_p versus V_s or V_s versus depth. However it becomes very clear in Poisson's ratio data. This is the main reason why Figure 2 presents ν curves.

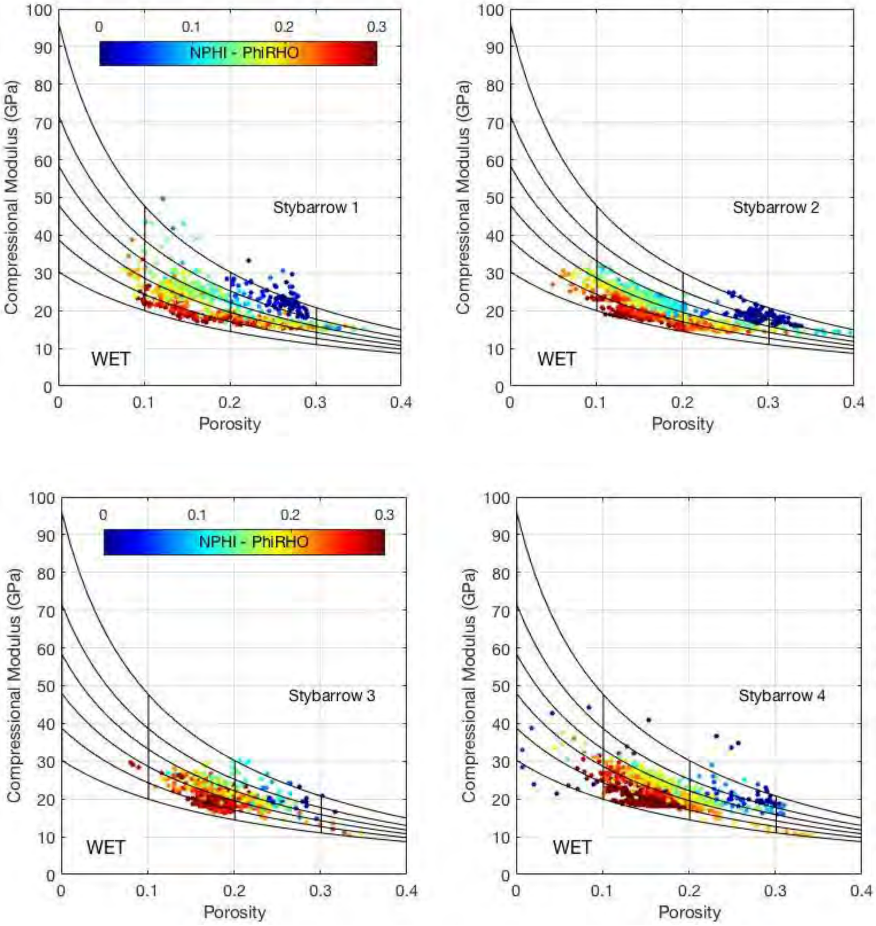

Figure 5.1. Four wells from Stybarrow reservoir. The wet-rock data compressional modulus versus porosity, color-coded by the ϕ_N - ϕ_ρ difference as previously explained. Dark-blue color is indicative of the relatively clean reservoir. It changes into cyan, yellow, and red as the clay content in the rock increases. The subhorizontal model curves are from the constant-cement model with coordination number 20 and for 100% wet rock. In each plate, the upper curve is for zero clay content while the bottom curve is for 100% clay content. The curves in between are for clay content increasing from zero to 100% with constant increment 20%. The vertical model lines are for constant porosity and the clay content varying from zero to 100%. The colorbar is the same for all four panels.

One advantage of using the rock physics model for V_s prediction is that it removes the spikes present in the reservoir interval in Wells 1 and 4 (and the resulting spikes in Poisson's ratio as shown in Figure 5.2). It also corrects the clearly spurious ν data in the entire Well 2 interval and above the reservoir in Well 4 (Figure 5.2). In the end, this model served as the basis for petrophysical interpretation of the seismically derived impedances.

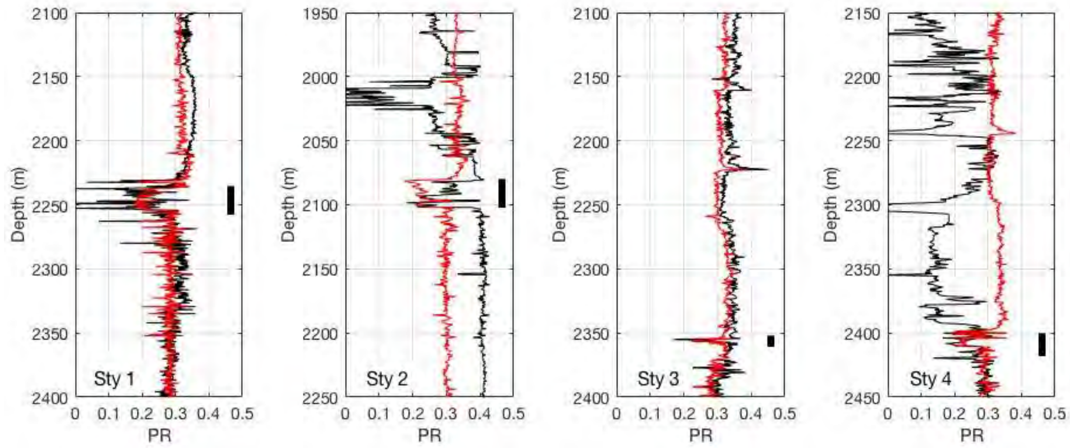

Figure 5.2. Four wells from Stybarrow reservoir. Poisson's ratio versus depth. Black curves are measured data while red curves are based on the constant-cement model. In each track, the reservoir interval is marked by a vertical black bar. Notice that the depth range is different for each well with the shallowest reservoir located in Well 2 and the deepest in Well 4. Well 3 has practically no reservoir.

5.3.2 Seismic Data

3D marine zero-phase seismic data covering the field under examination underwent standard processing. Specific steps to improve the quality of the data included shot-domain *fk* filtering, two passes of velocity analysis, 4th order NMO correction, Radon multiple attenuation, fold leveling for optimum offset distribution, 2D Kirchhoff DMO, and final pre-stack 3D time migration. The NMO-corrected angle gathers were produced using amplitude preservation and four angle stacks were generated from the gathers.

Figure 5.3 shows the seismic amplitude in-line sections for the near (zero to 15°) and ultra-far (29° to 39°) angle stacks at three selected wells. The second angle stack is from 13° to 23° while the third one is from 21° to 31°. In the first well, Stybarrow 1, the reservoir is located at approximately 2290 ms TWT and appears as a triple feature with the low amplitude (yellow-red) surrounded by a weak peak (cyan-blue) above and much stronger and thicker peak below. In Stybarrow 2, the reservoir is located at about 2190 ms and shows as a negative/positive amplitude pair. In Stybarrow 3, the barely developed reservoir at 2330 ms is manifested by a pair of positive peaks with a weak negative reflection in between. The seismic signature degrades from a high-amplitude positive-negative-positive triplet to the left and updip. The fourth well, Stybarrow 4, was drilled from the same position as Well 3 but was deviated updip to reach a well-developed oil sand. Figure 5.4 shows the same angle stacks but in the cross-line section. As shown in Figures 5.3 and 5.4 (well data curves), the reservoir in each well has the P-wave impedance lower than in the surrounding background.

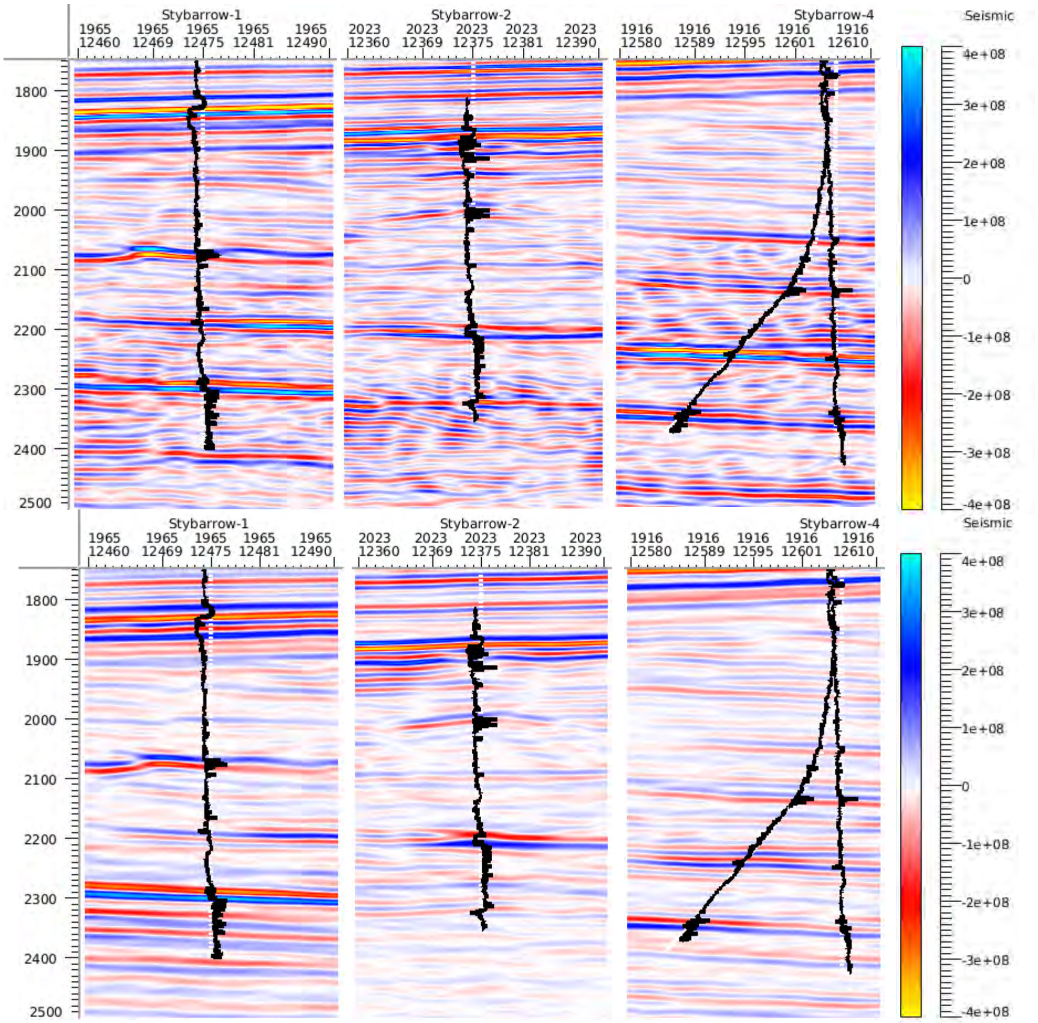

Figure 5.3. In-line sections of near (top) and ultra far (bottom) angle stacks for Wells 1 to 3 and 4 (left to right). Dotted white lines are the traces of the wells while the black curves around these traces are for Ip measured in the wells. Red is for troughs while blue is for peaks. Wells 3 and 4 are shown in the last tracks. Well 3 is vertical while Well 4 is deviated.

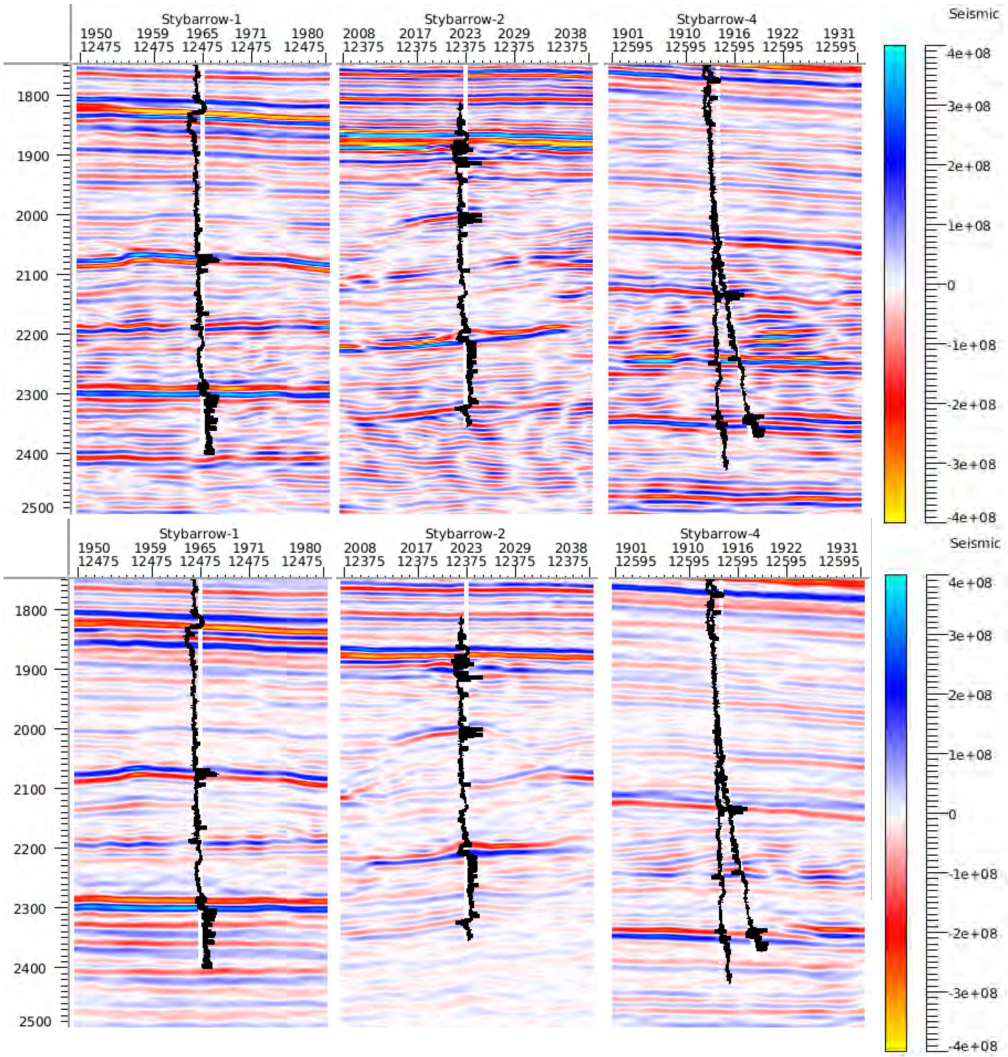

Figure 5.4. Same as Figure 5.3 but for the cross-lines.

5.4 Inversion Procedure

Simultaneous impedance inversion was performed using a constrained sparse-spike inversion algorithm based on the L1 norm optimization (e.g., Latimer et al., 2000; Pendrel, 2006). This algorithm creates a set of elastic models using multiple seismic partial angle stacks. At each CMP, the synthetic seismic is generated as the convolution of reflection coefficients with a wavelet. These reflection coefficients are produced from the elastic models using the Aki-Richards (2002) AVO approximation. The inversion is constrained by well data. In our case, we used the well data corrected by the rock physics model referred to earlier in the text.

The steps included loading the data; cross-correlation between the angle stacks to align the stacks in time; seismic-to-well tie; wavelet extraction for each angle gather; horizon interpretation based on the near-stack amplitude; constructing well- and horizon-based low-frequency I_p, I_s, and density earth model; inversion parameter optimization; and quality-control of the inversion results.

We conducted three variants of inversion: (a) using Well 1; (b) using Well 3; and (c) using both Well 1 and 3. Here we describe the steps of the first variant. Analogous procedures were implemented in the other two variants.

Even after the cross-correlation step, the recorded angle stacks did not produce a clear AVO picture (Figure 5.5, left). To mitigate this problem, we corrected the mid and far gathers by using the near and ultra-far angle gathers as anchoring points and assuming that the angle stack amplitudes linearly depend on $\sin^2$ of the angle of incidence q (Figure 5.5, right):

$$R(q) = A + B\sin^2 q, \qquad (5.1)$$

where, for the Aki-Richards (2002) approximation and retaining only the first two terms,

$$A = \frac{I_{p2} - I_{p1}}{I_{p2} + I_{p1}}; \quad B = \frac{V_{p2} - V_{p1}}{V_{p2} + V_{p1}} + 4\left(\frac{V_{s2} + V_{s1}}{V_{p2} + V_{p1}}\right)^2 \left(\frac{r_{b2} - r_{b1}}{r_{b2} + r_{b1}} + 2\frac{V_{s2} - V_{s1}}{V_{s2} + V_{s1}}\right) \qquad (5.2)$$

and subscripts “1” and “2” refer to the upper and lower half-space at the reflecting interface.

This decision was based on the criterion that the seismically derived Poisson’s ratio computed from I_p and I_s as

$$n = \frac{1}{2}\frac{(I_p / I_s)^2 - 2}{(I_p / I_s)^2 - 1} \tag{5.3}$$

was close to the Backus-upscaled model-based n at the well. Using only the near and ultra-far angle stacks allowed us to satisfy this criterion (see below). The angle stacks thus corrected were used in the subsequent steps of inversion for the whole traces.

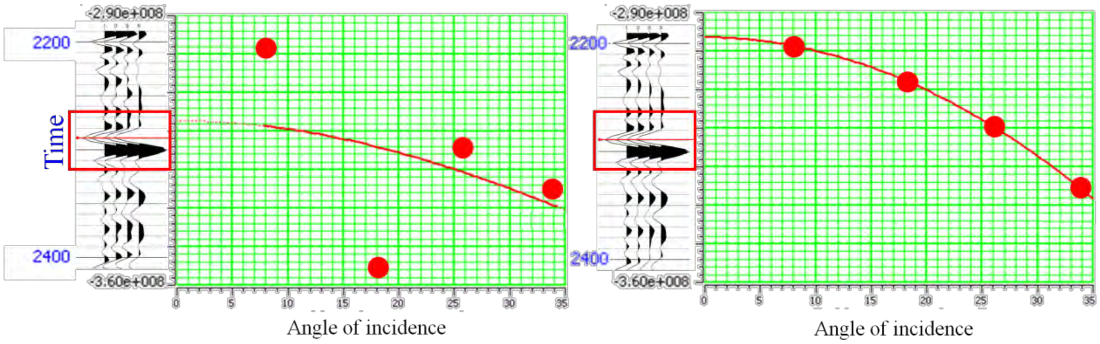

Figure 5.5. Left: Original angle stacks at the reservoir in Well 1 and the amplitude versus angle. The red curve is the best fit to the original angle gather amplitudes. Right: Corrected angle stacks using a linear $\sin^2\theta$ dependence of the amplitude.

The seismic-to-well tie was conducted using these corrected angle stacks. The initial tie was accomplished using a 35 Hz Ricker wavelet. Once we were satisfied with the tie, we extracted wavelets for each angle stack at and around the reservoir (Figure 5.6).

The results of the final tie are shown in Figure 5.7 for the near and ultra-far angle stacks using these wavelets. The cross-correlation quality appears to be high at the reservoir (2290 ms) for both angle stacks.

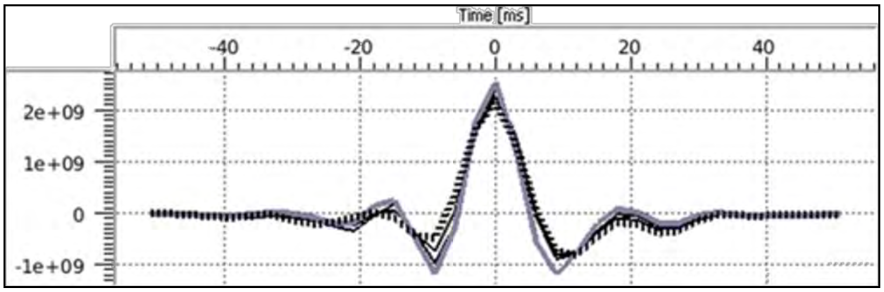

Figure 5.6. Wavelets extracted at and around the reservoir at Well 1. The near angle wavelet is shown in gray, the ultra-far angle wavelet is shown as a dotted curve. The two wavelets in between are for the mid and far angle stacks.

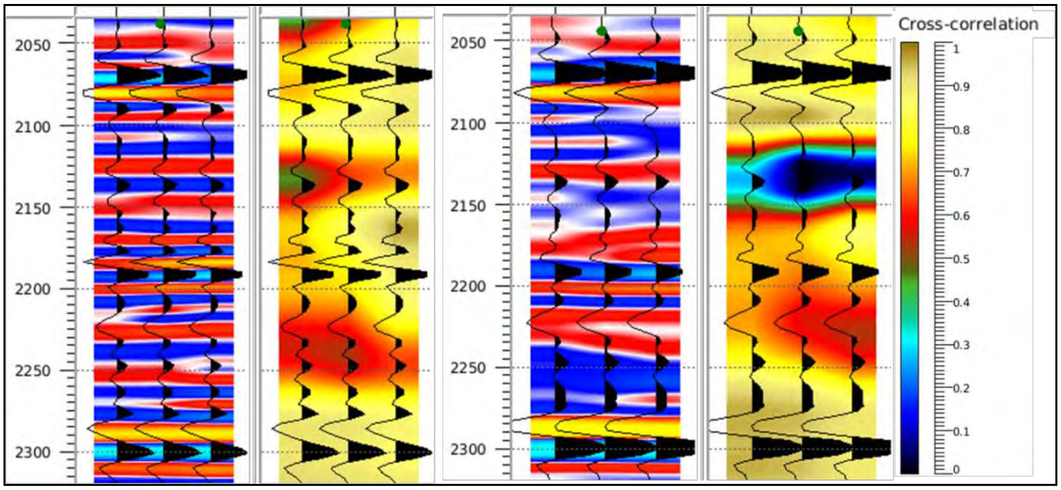

Figure 5.7. Stybarrow 1. Left: Near-angle original seismic data (in color) with the synthetic traces (black) superimposed. The second track shows the cross-correlation quality with the gold color indicating the best cross-correlation with the same synthetic traces superimposed. The reservoir is located at 2290 ms TWT. Right: The same but for the ultra-far angle stack.

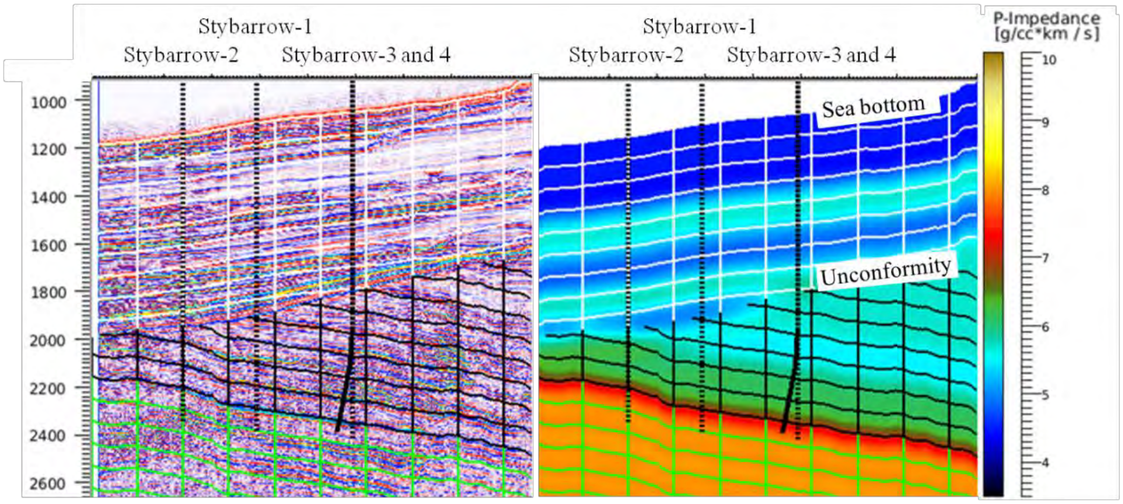

Figure 5.8. Left: Horizon-based mesh with the original near-angle seismic amplitude in the background. The reservoir is located along the bottom subhorizontal black mesh line. Right: the same mesh with the low-frequency P-wave impedance in the background (the colorbar). The sea bottom is at the top followed by the unconformity approximately in the middle of the picture. The reservoir is at the boundary where the color transits from green to red.

The horizons were tracked using the original near-angle stack seismic data. Specifically, we identified the sea bottom, unconformity, reservoir, as well as the bottom horizon. Based on these horizons, a coarse mesh was created and the low-frequency model based on the Well 1 data was generated (Figure 5.8).

5.5 Inversion Results

The inversion parameters were optimized to obtain the best possible I_p, I_s, and density fit between the seismically derived values and the Well 1 data. Afterwards, these parameters were used to obtain the simultaneous impedance inversion for the entire seismic cube. The most important optimization parameter was the “contrast misfit” that controls the elastic parameter variance between the inversion results and low-frequency well data. As mentioned in the above section, the key in selecting this parameter was to match the seismically-derived Poisson’s ratio (Equation 5.2) with the upscaled Poisson’s ratio at Well 1 in the vicinity of the reservoir.

Figure 5.9 shows this seismically derived Poisson’s ratio, as well as I_p and I_s, in a vertical section that includes all four wells. Optimizing the inversion parameters allowed us to arrive at fairly low ν in the reservoir at Wells 1, 2, and 4, consistent with the model-based curves shown in Figure 5.2 and expected in a mid-to-high porosity clean clastic sediment filled with oil.

Figure 5.10 shows the same results but for inversion variant “b” where Well 3 was used for calibration. Figure 5.11 shows the results for variant “c” where Wells 1 and 3 were used together. By visually comparing the results of these three inversion variants, we decided to use variant “c” where both Well 1 and 3 were used, since it produced the impedances and Poisson’s ratio more consistent with the Backus-upscaled curves in all four wells. Notice that the match between the seismically derived and Backus-upscaled Poisson’s ratio is poor below the reservoir in Wells 1 and 2. This mismatch so well pronounced in the Poisson’s ratio graphs is the expression of the mismatch in I_s, barely visible in Well 1. We believe that the source of this mismatch is the relatively weak reflection events below the reservoir appearing in the ultra-far angle stacks (Figure 5.3, bottom) at about 2360 ms TWT but not visible in the near-angle stacks. The respective variations in the elastic properties are not present in the well data. We cannot explain the source of these seismic anomalies.

The bulk density obtained during this inversion lacked spatial continuity and was very noisy. This is why it is not shown here and was not used in our interpretation.

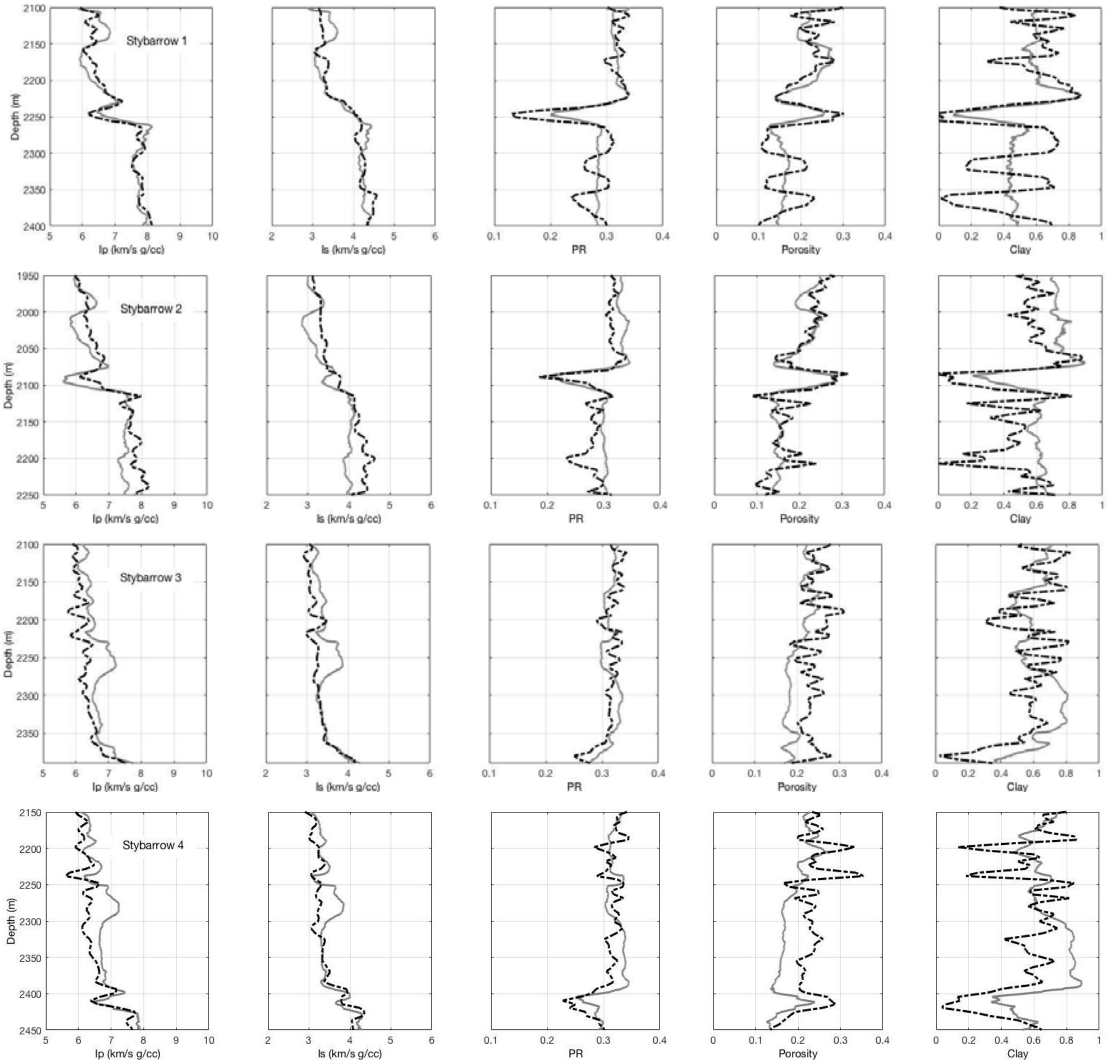

Figure 5.9. Inversion and interpretation results (dashed curves) compared with Backus-upscaled elastic well data (first three tracks) and arithmetically upscaled porosity and clay content (last two tracks) at Well 1, 2, 3, and 4 (top to bottom). Inversion variant "a" where only Well 1 was used.

Figure 5.12 shows seismic scale Poisson's ratio section through all four wells computed from seismically derived I_p and I_s according to Equation 5.2. The continuous low-ν band (dark blue) coincides with the location of the reservoir. Notice also that this seismically-derived ν becomes relatively high at Well 3 where the reservoir is practically absent. However, only a small distance updip from this location, where Well 4 was completed, ν becomes low again, indicating the presence of a developed oil reservoir.

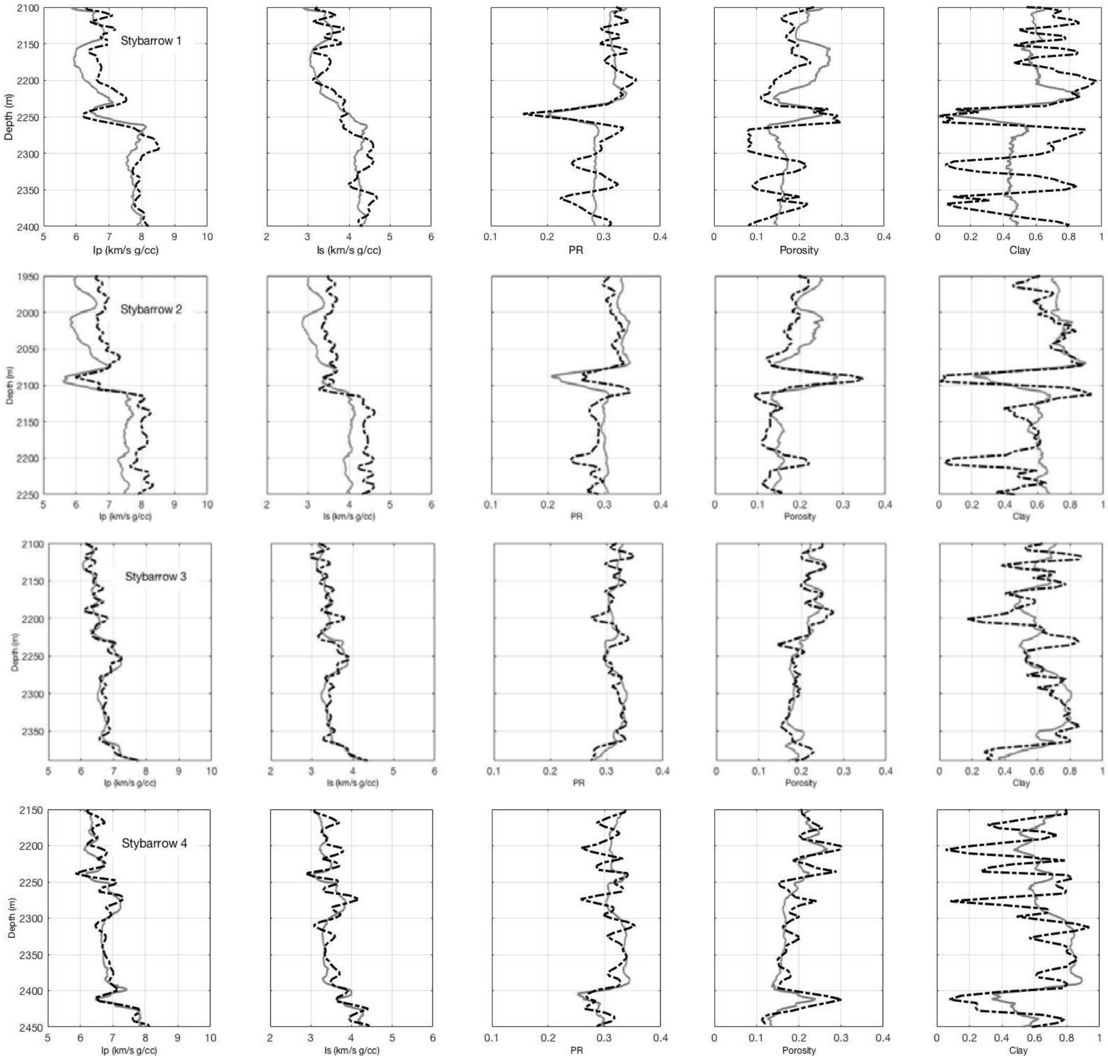

Figure 5.10. Same as Figure 5.9 but for inversion variant "b" where only Well 3 was used.

An intriguing low-ν dark-blue feature is discernable at the right edge of the image at about 2149 ms. This feature terminates against a normal fault tracing from the bottom of the image upwards and to the right at about 45° degrees inclination. We have no factual evidence to whether this is a structural trap filled with hydrocarbon or an imaging artifact.

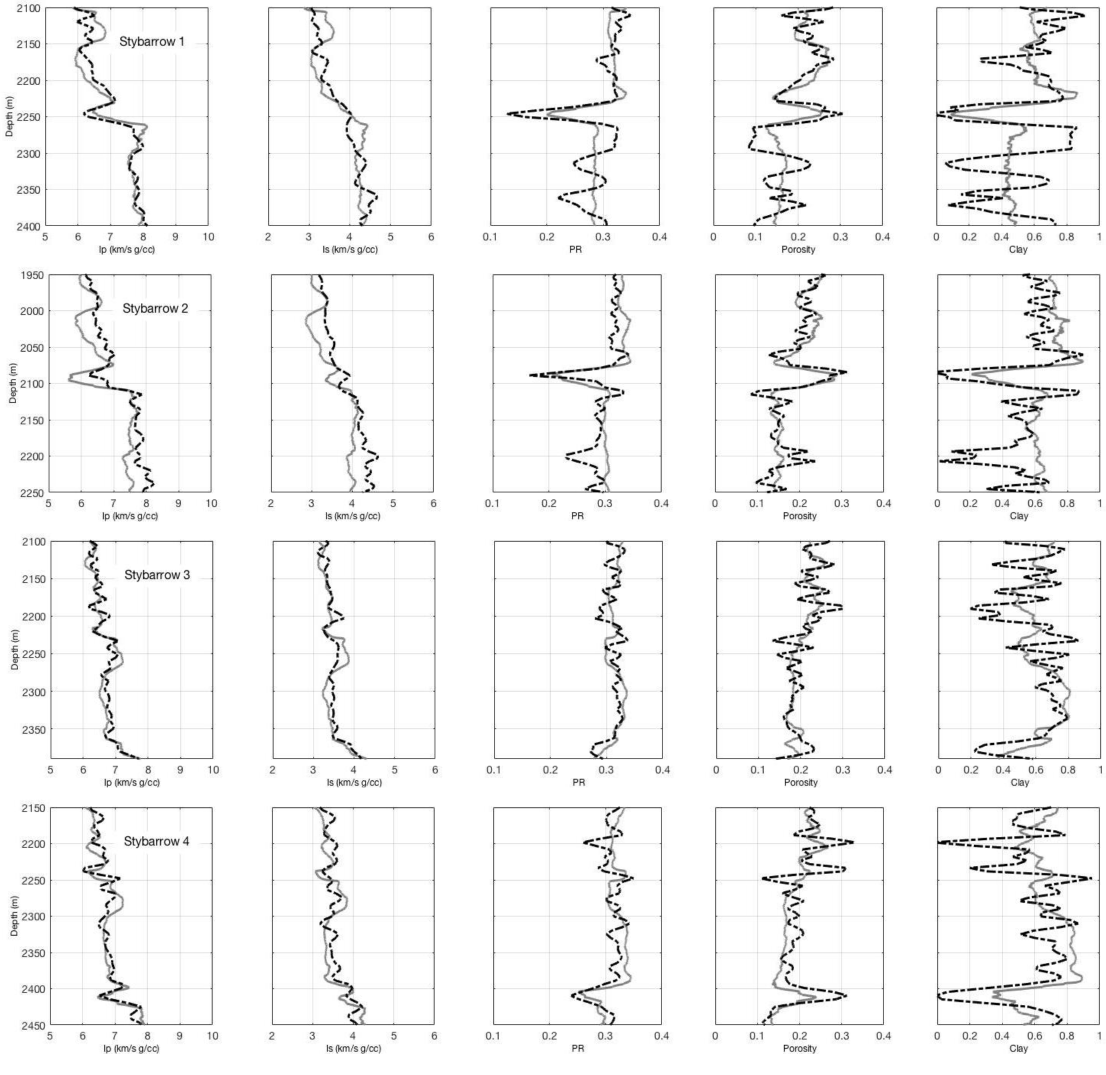

Figure 5.11. Same as Figure 5.9 but for inversion variant "c" where both Well 1 and Well 3 were used.

The same vertical section but for I_p from simultaneous impedance inversion is shown in Figure 5.13. The reservoir is the green band just above the yellow high-impedance domain in the lower part of the image. It has a thin yellow high-I_p band above it. This high-to-low-to-high impedance sequence generates the amplitude trough at the top of the reservoir (Figure 5.3 and 5.4). The well-to-seismic match at the reservoir in Well 2 is not as good as in the other wells. The relative difference is only about 8%.

The I_s section is shown in Figure 5.14. Because this impedance is hardly sensitive to the pore fluid, we do not observe here the reservoir band as clearly pronounced as in the ν and I_p sections.

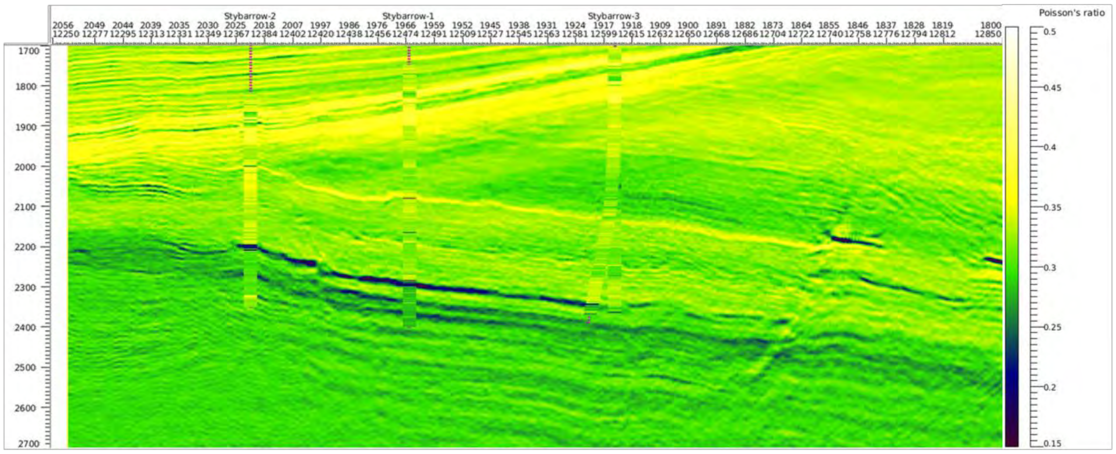

Figure 5.12. Seismic scale Poisson's ratio computed from Ip and Is obtained by simultaneous inversion in variant "c" where both Well 1 and 3 were used. Vertical bands mark the wells, Stybarrow 2 on the left, Stybarrow 1 to the right of Stybarrow 2, and Stybarrow 3 and 4 to the right of these two. These bands are colored by the upscaled Poisson's ratio in the wells. The reservoir is the dark-blue band crossing these four wells. Stybarrow 4 is at the same location as Stybarrow 3 but completed updip where Poisson's ratio is relatively low.

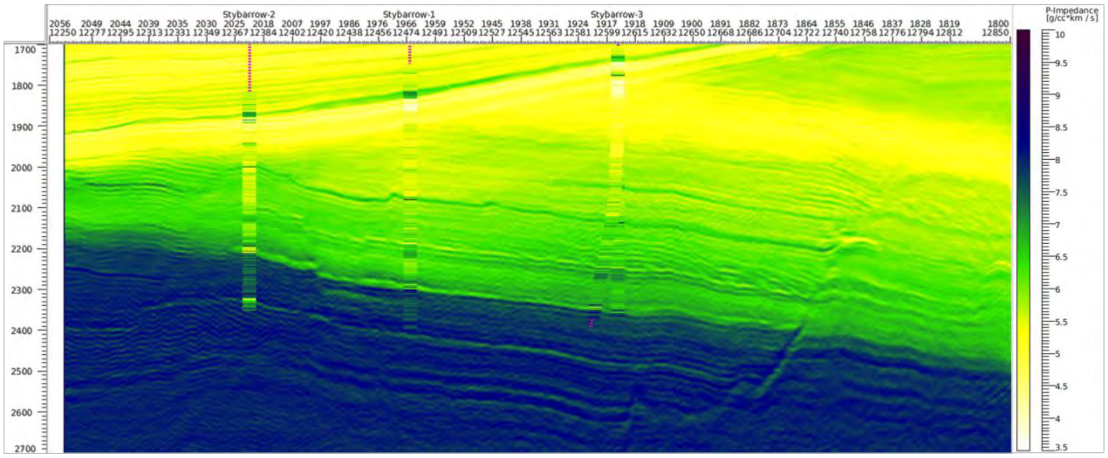

Figure 5.13. Same section as in Figure 12 but for the seismically derived P-wave impedance.

Figure 5.15 shows a map of seismically derived Poisson's ratio in the ±15 ms TWT window around the reservoir horizon. The well locations are shown as red symbols. Clearly, both producing wells, Stybarrow 1 and 2, fall within the low-η region. Stybarrow 3 is outside of the low-ν geobody, consistent with the fact that this well has practically no reservoir.

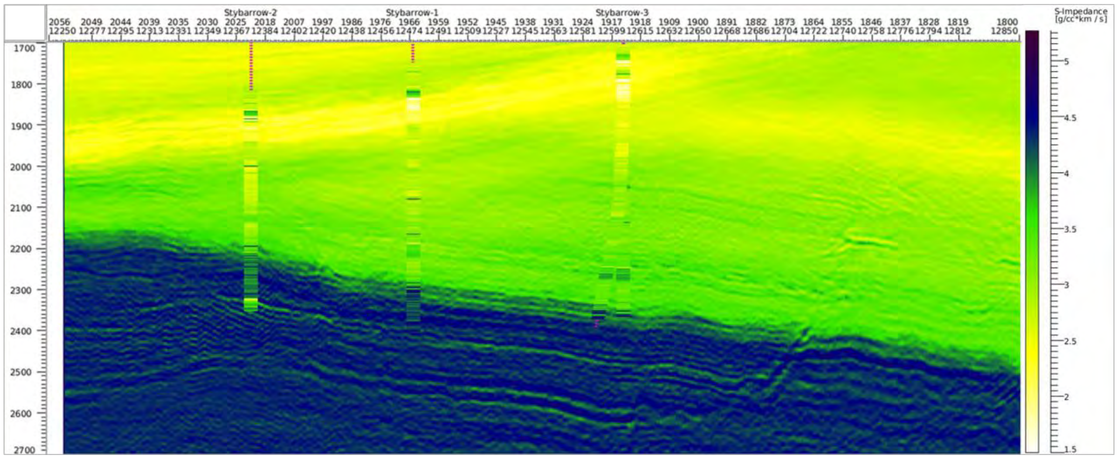

Figure 5.14. Same section as in Figure 5.12 but for the seismically derived S-wave impedance.

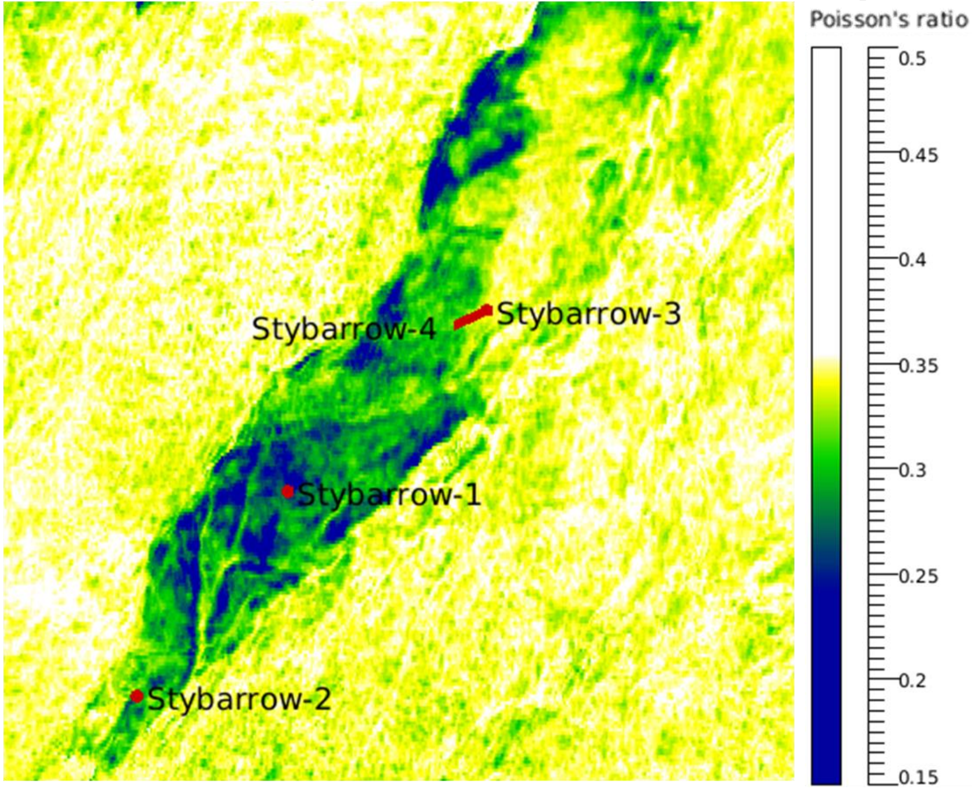

Figure 5.15. Seismically-derived Poisson's ratio map at the reservoir.

5.6 Interpretation for Porosity, Mineralogy, and Fluid

Our method of interpreting the P- and S-wave impedance for porosity and clay content is rock physics based and described in Chapter 3. It relies on the rock physics model established using the well data (Figure 5.1). The three principal variables that affect the impedances (I_p and I_s) according to this model are the total porosity ϕ, clay content C, and the bulk modulus and density of the pore fluid, K_f and ρ_f, respectively. Hence, because we only have two seismically-derived variables, I_p and I_s, our interpretation method requires the knowledge of the pore fluid.

To assess whether the rock was wet or contained oil, we used a seismically-derived Poisson's ratio cutoff 0.23 assuming that where ν is below 0.23, the rock has 20% water saturation (S_w) and the rest is oil. Where ν is above 0.23 we assume $S_w = 100\%$. This cutoff was selected based on ν measured and modeled in the wells (Figure 5.2). Once the presence of hydrocarbons was established in the seismic volume, K_f was computed as the S_w-weighted harmonic average of those of the water and oil, while ρ_f was the arithmetic average of the individual densities of the pore-fluid phases.

Now that the properties of the pore fluid are identified in the seismic volume, we are left with the two impedances from simultaneous seismic inversion that need to be resolved for two unknowns, ϕ and C.

In our earlier work, we found that for this specific rock physics model, the two impedances, I_p and I_s, approximately depend of two *different* linear combinations of ϕ and C (as discussed in Chapter 4):

$$I_p = f_p(\phi + \alpha_p C); \quad I_s = f_s(\phi + \alpha_s C), \tag{5.4}$$

where a_p ¹ a_s and f_p and f_s are the rock physics transforms according to the constant-cement model established for the wells under examination.

Using the concept expressed in Equations 5.4, we can numerically solve the system of model-based equations. In our case, we used look-up tables for I_p and I_s as a function of ϕ and C constructed separately for the reservoir and non-reservoir volumes using the respective K_f and ρ_f. A least-squares objective function norm minimization technique was used to derive the two desired petrophysical properties.

The resulting porosity and clay content curves at all four wells are compared with the linearly upscaled porosity and clay content curves at the wells (Figures 5.9 to 5.11). These seismically derived variables in the seismic section going through the four wells are also shown in Figure 5.16. The reservoir is clearly discernable in the clay content section as the upper dark-blue band sloping downwards from left to right. It matches the high-porosity dark-blue band in the porosity section.

Notice that in the clay content section, there are two fairly discontinuous low-C bands beneath the reservoir. They are matched by the high-porosity bands (Figure 5.11, Well 1 and 2 as well as Figure 5.17, top). Well data (as discussed in Chapter 4) do not show low clay content or high porosity beneath the reservoir.

These events can be traced back to the low-ν bands beneath the reservoir (Figure 5.12) which are arguably produced by the reflections that follow the reservoir event clearly seen in the ultra-far offset in-line and cross-line sections (Figures 5.3 and 5.4, bottom).

This mismatch between our seismic interpretation results and well data is also shown in Figures 5.9 to 5.11 where we compare the seismically derived ϕ and C to these variables in the wells. The two high-ϕ and low-C events interpreted from seismic data are present in Well 1 beneath the reservoir, while only one such event is present in Well 2.

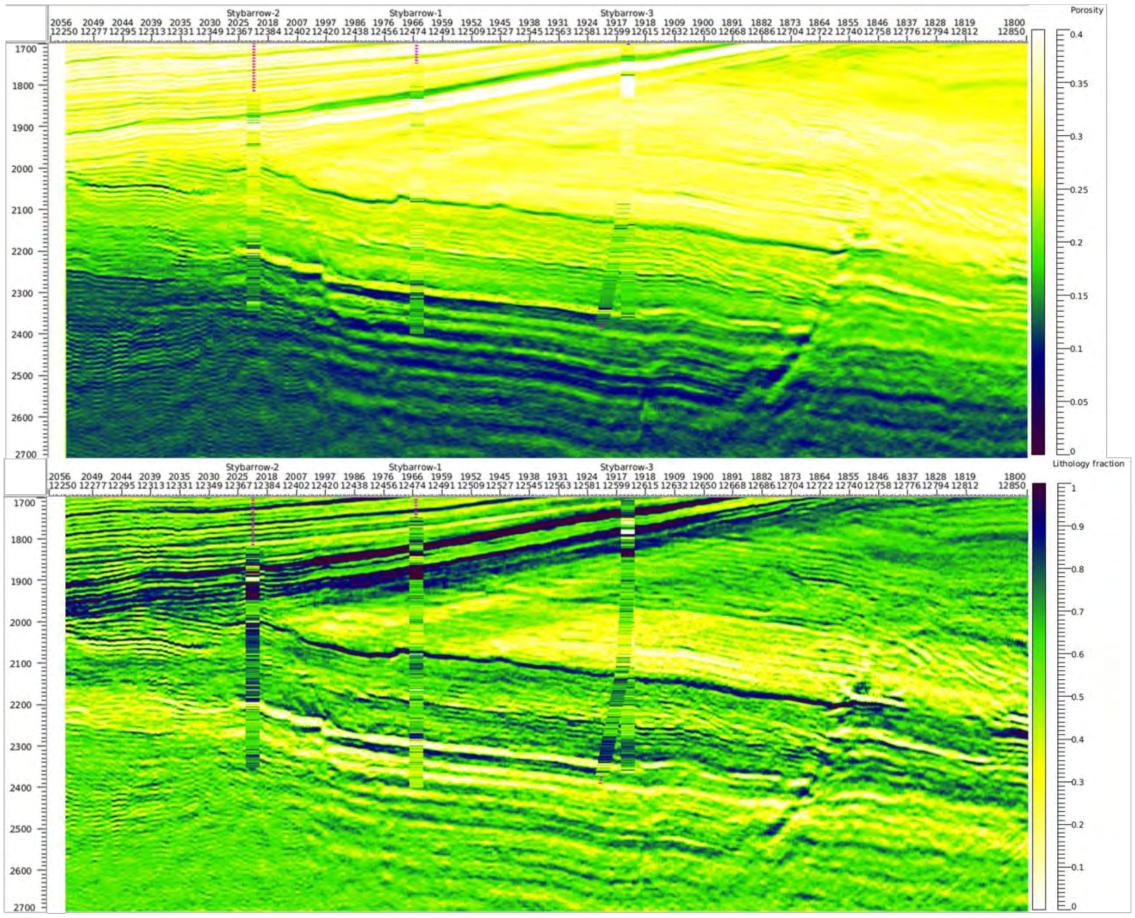

Figure 5.16. Vertical section of porosity (top) and clay content (bottom) transecting the four wells whose positions are shown by dotted red vertical lines. Wells 3 and 4 are located at the same position.

5.7 Discussion

The workflow presented here is, to the best of our knowledge, the first method that combines deterministic inversion with careful rock physics modeling (rock-physics diagnostics) to derive petrophysical variables as well as pore fluid from seismic data. We show how to derive and then apply site-specific “velocity-porosity” relations to seismic scale variables. The results are sensitive to the seismically-derived impedances. This sensitivity stems from basic physics. The challenges are that we not only need to produce reasonably plausible impedance volumes but also plausible volumes of porosity and clay content. Hence this adds yet another quality-control step that needs to be undertaken to validate the inversion results. The advantage of the method is that now we can characterize the subsurface not only in terms of its elastic variables but, most importantly, its petrophysical variables. We feel that this is a step forward in interpretation, albeit one that requires additional effort and integration of rock physics, seismic processing, and inversion.

5.8 Conclusion

The goal of the simultaneous impedance inversion method discussed here was to create a data volume that could be used to apply a rock-physics-based method of interpreting the P- and S-wave impedances for porosity and clay content. This method is quite sensitive to the inputs. We believe that the robustness and veracity of such interpretation is the ultimate test for the quality of seismic impedance inversion. Because Poisson's ratio computed from the seismically derived I_p and I_s is key to fluid detection, special care has to be taken to obtain realistic ν values. This is yet another important quality control for inversion. Finally, the artifacts that appear in the inversion results need to be acknowledged and understood. In our case, such artifacts of low ν can be seen below the reservoir (Figure 5.12). We assume that this is the result of (a) artifacts in the original seismic data and (b) of the sparse-spike inversion algorithm used here where the artificial high-contrast reflectivity features are forced into a relatively homogeneous low-contrast background.

Chapter 6

From Seismically Derived Impedances to Rock Properties: Self Similarity in Rock Physics

6.1 Abstract

Legacy laboratory data obtained on a large number of clean and shaly sand samples indicate that the dependence of P- and S-wave impedances (I_p and I_s, respectively) on the total porosity ϕ and clay content C can be reduced to their dependence on a linear combination of ϕ and C: $I_p(\phi, C) = f_p(\phi + \gamma_p C)$ and $I_s(\phi, C) = f_s(\phi + \gamma_s C)$. This effect is called self-similarity. It appears that in the above-mentioned dataset $\gamma_p = \gamma_s$, meaning that both impedances depend on the *same* linear combination of ϕ and C. Hence, in this case, two elastic measurements, I_p and I_s, cannot be independently and uniquely resolved for porosity and clay content. By exploring this phenomenon on other datasets (well data), we find that in some cases, $\gamma_p \neq \gamma_s$, thus allowing us to uniquely interpret the impedances for ϕ and C. We also find that this uniqueness is a property of the rock physics model that describes the specific dataset under examination, meaning that in

some models g_p » g_s, while in other models these coefficients are distinctively different form each other. By analyzing a number of rock physics models relevant to real sediment, we investigate where measured I_p and I_s can be potentially uniquely resolved for the unknown petrophysical variables and where they cannot. Such model-based analysis is an important step in evaluating the feasibility of interpreting simultaneous impedance inversion results for petrophysical unknowns.

6.2 Introduction

By using Han's (1986) ultrasonic velocity measurements on sandstone samples with varying amounts of clay, Gal et al. (1999) have shown that the P- and S-wave velocities, both functions of two independent variables, the total porosity (ϕ) and clay content (C), are approximately unique functions of a single variable, a linear combination of ϕ and C. The physical explanation of this effect was that part of the clay present in the mineral frame is not load bearing. Hence, replacing this part of the clay with additional pore space should not affect the elastic properties.

In Figure 6.1 we show the wet-rock P-wave impedance I_p measured at 40 MPa (Han, 1986). The clay content in the 80 samples varies between zero and 51%. The dependence of the impedance on two inputs, the total porosity and clay content, observed in Figure 6.1a is reduced to its dependence on a single variable, $f + 0.25C$ in Figure 6.1b. If the Gal et al. (1999) physical interpretation of the observed effect is correct, it will not only be valid for I_p but also for I_s. Indeed, this appears to be true (Figure 6.2).

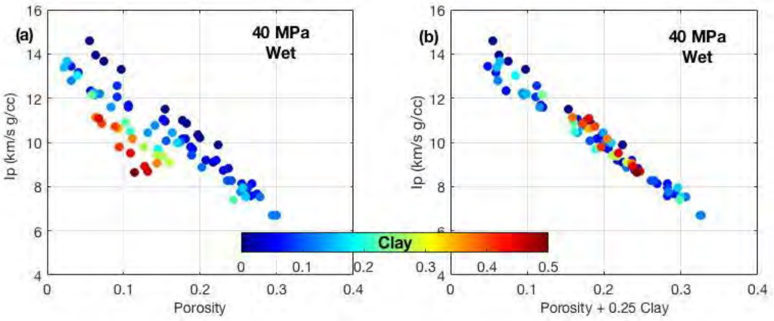

Figure 6.1. Han's (1986) data. Ultrasonic I_p data from wet-rock samples at 40 MPa confining pressure. The clay content range is between zero and 51%. (a) I_p versus the total porosity color-coded by the clay content. (b) I_p versus a linear combination porosity plus 0.25 times the clay content, also color-coded by the clay content. The colorbar is the same for both plots.

In Figure 6.3 we plot the same data but with rock physics model curves superimposed. The model used is the Raymer-Dvorkin model (Dvorkin, 2007b). The model curves accurately match the data with the upper (zero clay) curves matching the zero-clay Han's (1986) data and the high-clay-content data points falling in between the 40% and 60% clay content model curves. In the same figure we plot the impedances versus $f + 0.25C$. Not only the data collapse to a single trend but also the model curves show now a single fairly tight trend.

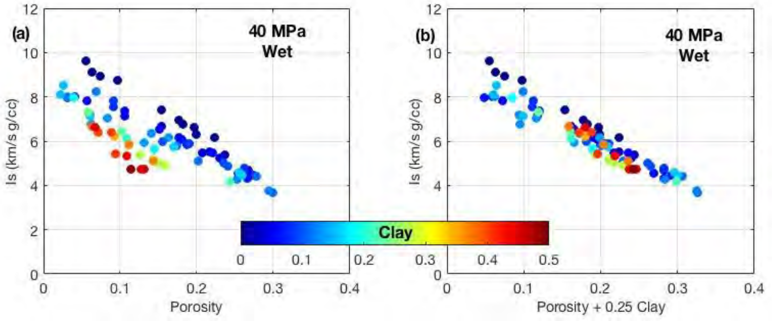

Figure 6.2. Same as Figure 6.1 but for I_s.

This effect also becomes apparent in the I_s versus I_p cross-plot using the same data (Figure 6.4). The color of the datapoints according to the clay content (Figure 6.4a) or porosity (Figure 6.4b) is irregularly distributed along the observed trend. At the same time, in the plot where the data are colored by $f + 0.25C$ (Figure 6.4c), we observe a very regular gradation of the color from high (red) to low (blue) values of this linear combination.

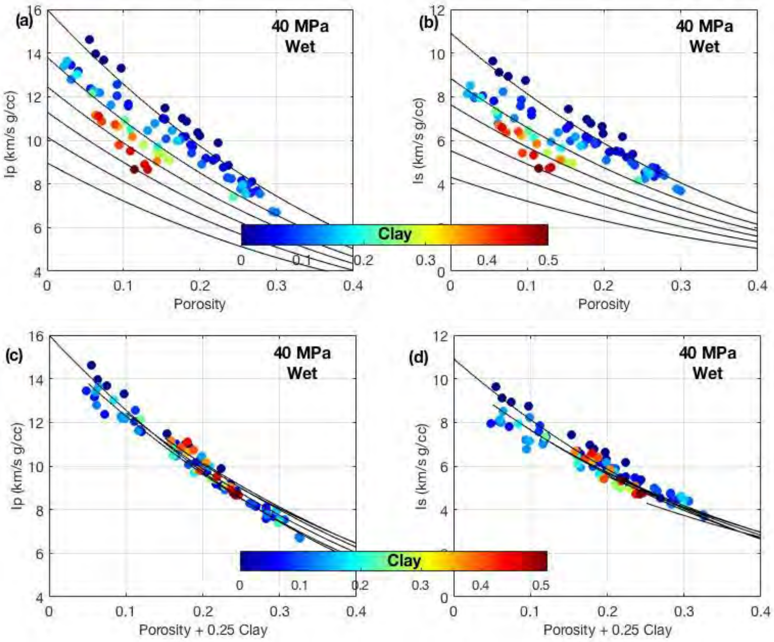

Figure 6.3. Han's (1986) data. Impedances in wet-rock samples at 40 MPa confining pressure from ultrasonic velocity and density data. The clay content range is between zero and 50%. I_p (a) and I_s (b) versus porosity color-coded by the clay content. The same impedances (c and d) but versus $\phi + 0.25\ C$, also color-coded by the clay content. The colorbar is the same for all plots. Black curves are from the Raymer-Dvorkin (Dvorkin, 2007b) model computed in the 0% to 40% porosity range and 0% to 100% clay content range. These curves are plotted versus porosity (a and b) where the top curve is for 0% while the bottom curve is for 100% clay content with the curves in between with 20% clay content increment. The same curves are plotted versus $\phi + 0.25\ C$ in c and d.

The effect shown in Figures 6.1 to 6.4 is called self-similarity. This is a situation in physics where a function of several variables is fully determined by a combination of these variables (e.g., Barenblatt, 2003). A well known example is the Reynolds number that determines the transition from laminar to turbulent flow in hydrodynamics:

$$\mathrm{Re} = \frac{rVL}{m}, \qquad (1)$$

where r is the density of the fluid; V is the velocity of the flow; L is a characteristic linear dimension (e.g., the radius of the pipe); and m is the dynamic viscosity of the fluid.

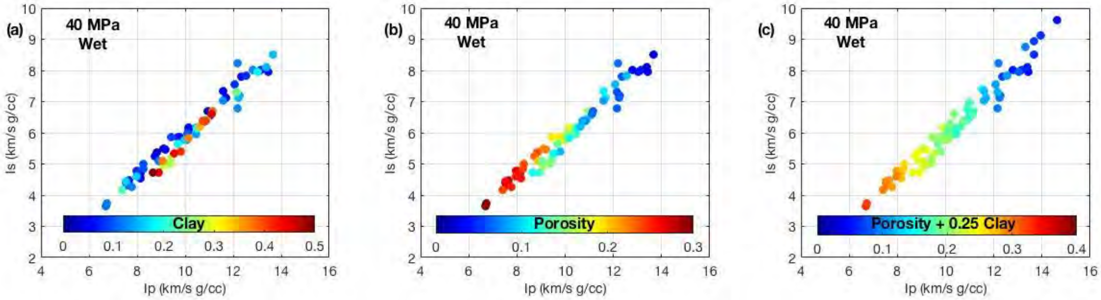

Figure 6.4. Han's (1986) data. Wet-rock samples at 40 MPa confining pressure. I_s versus I_p color-coded by the clay content (a); total porosity (b); and the linear combination $\phi + 0.25\ C$ (c).

This remarkable property of certain physical processes is extensively used in mechanics to scale experiments and predict the outcomes of field tests. Yet, it can have negative implications for interpreting seismic data for petrophysical properties. Indeed, if both seismically derived impedances, I_p and I_s, depend on the same combination of porosity and clay content, they cannot be resolved for these two variables but only for the said combination thereof (Dvorkin, 2007). Specifically, the system of two equations

$$\begin{aligned} I_p(f,C) &= f_p(f+g_pC); \\ I_s(f,C) &= f_s(f+g_sC), \end{aligned} \qquad (2)$$

where f_p and f_s are the respective functions and g_p and g_s are the linear coefficients, cannot be independently resolved for f and C if $g_p = g_s = g$, but can only be resolved for a single variable $f + gC$.

The purpose of this chapter is to investigate the cases where the two seismic observables, I_p and I_s, that are obtained from simultaneous impedance inversion can be resolved for two seismic-scale petrophysical properties and where they cannot be resolved. The main assumption is that the dependence of the elastic properties on petrophysical inputs is governed by a rock physics model (as shown in Figure 6.3). This assumption allows us to conduct our analysis in the rock physics model space. Most importantly, we outline a workflow that allows us, once a rock physics model is established based on lab or well data, to determine the feasibility of such seismic-based interpretation.

6.3 More Lab and Well Data on Sandstones with Clay

Figure 6.5 shows the wet-rock Han's (1986) data measured at 10 MPa confining pressure. Apparently the self-similarity rule where the P- and S-wave impedances both approximately depend on the same linear combination $f+0.25C$ also holds for these samples at a much lower differential pressure. Notice that in this example, the I_s versus $f+0.25C$ is not as tight as for the 40 MPa data.

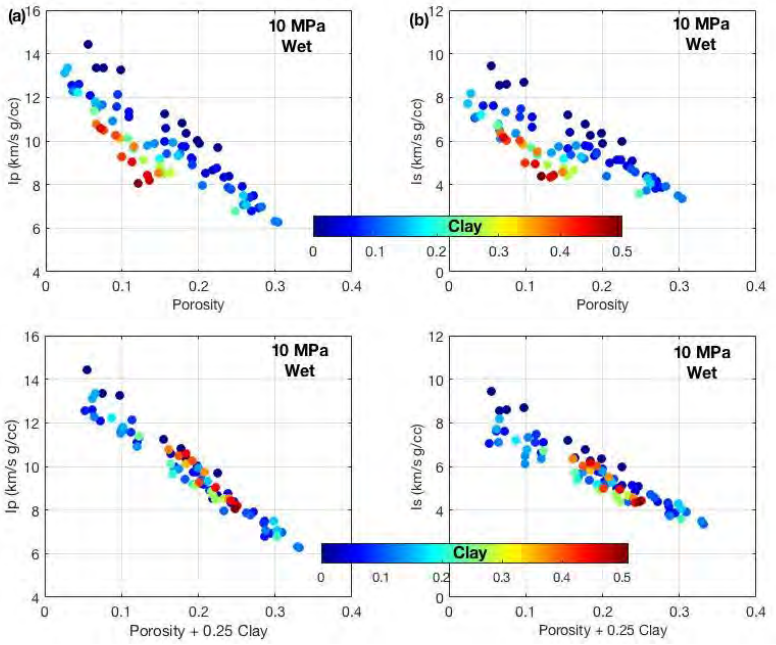

Figure 6.5. Same as Figure 6.3 but for 10 MPa confining pressure.

The same samples show an analogous self-similarity behavior if the dry-rock measurements are used (Figure 6.6). Although these data do not exhibit the impedance-porosity-clay behavior as regular as the wet-rock data (Figure 6.3), we can still observe relatively compact trends between the dry-rock impedances and the $f + 0.25C$ linear combination.

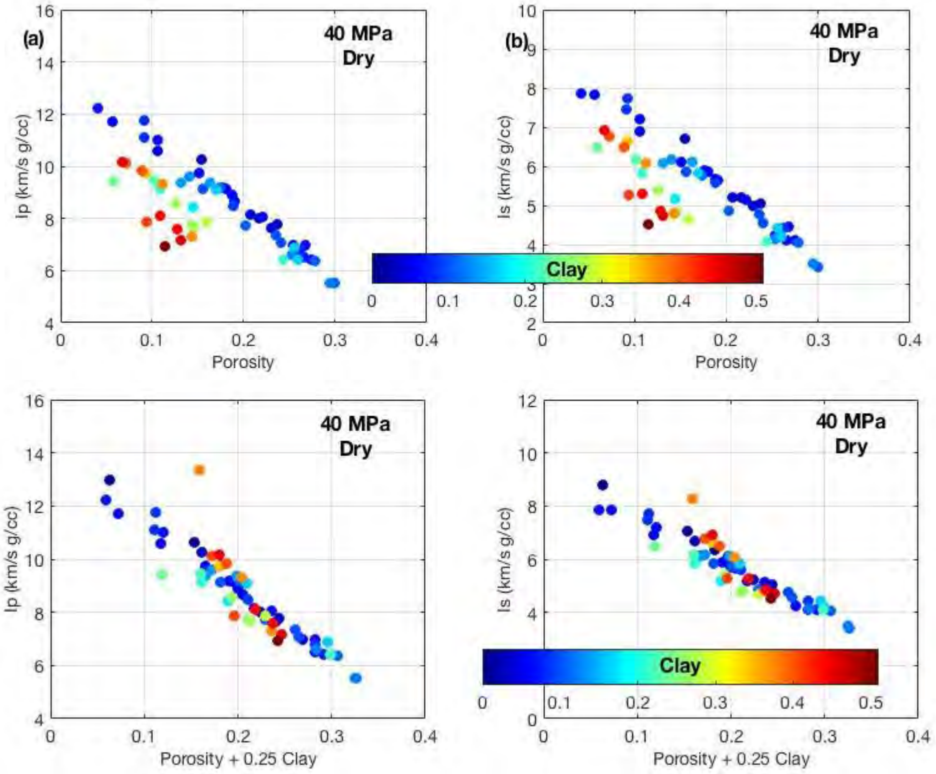

Figure 6.6. Same as Figures 6.1 and 6.2 but for dry-rock data.

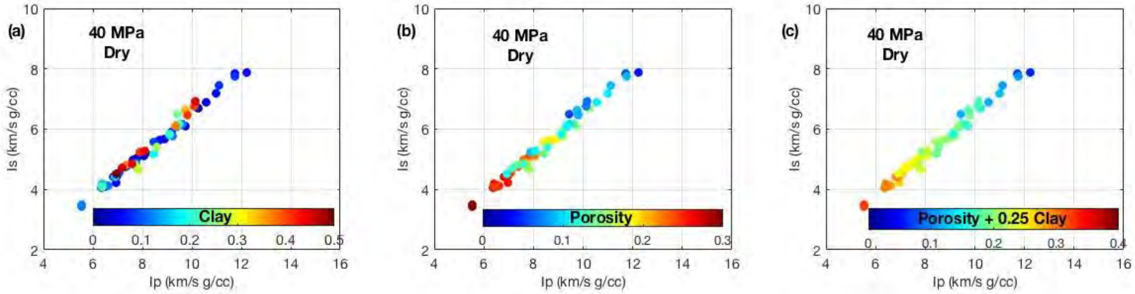

Figure 6.7. Han's (1986) data. Dry-rock samples at 40 MPa confining pressure. I_s versus I_p color-coded by the clay content (a); total porosity (b); and the linear combination $\phi + 0.25\ C$ (c).

Figure 6.7 shows I_s versus I_p cross-plots for the same dry-rock data as shown in Figure 6.6. Once again, similar to Figure 6.4, we observe a systematic color progression where the datapoints are color-coded by $f + 0.25C$.

It is essential to state before we proceed further that:

(a) The self-similarity in Han's (1986) data has been discovered heuristically, by simply plotting the data versus a linear combination of the porosity and clay content.

(b) This linear combination is not necessarily the ultimate single variable that governs the elastic properties; there are likely to be other combined variables, more complex, that simultaneously affect I_p and I_s.

(c) The self-similarity apparent in the plots presented here is valid where the samples are saturated with the same fluid or are simply dry. It will certainly break down if we compare, e.g., gas sand with the surrounding wet shale.

(d) The physical explanation that the source of the observed self-similarity is the non-load-bearing clay may not be entirely correct since where the clay content is high, at least part of the clay present in the rock has to be load-bearing. Yet, we observe the self-similar behavior in Han's (1986) data with the clay content up to 50% and in the model that matches these data with clay content up to 100%.

(e) Finally, although the self-similarity phenomenon discussed here is fascinating by itself, the practical importance of this behavior is in whether we can resolve two seismically derived elastic variables, namely the impedances from simultaneous impedance inversion, for two independent petrophysical variables.

Self-similarity is sometimes apparent in well data. Figure 6.8 shows depth curves from a Gulf Coast light-oil well drilled in a clastic environment. Fluid substitution was used to compute the wet-rock velocity and impedances. The wet-rock density and impedances are plotted in blue in plots (c) and (d). The density-derived porosity ϕ_ρ was computed from the measured bulk density ρ_b using the mass-balance equation and assuming that the mineral matrix has density 2.65 g/cc and the pore fluid has density 1.00 g/cc:

$$\phi_\rho = (2.65 - \rho_b)/(2.65 - 1.00), \tag{3}$$

while the total porosity ϕ was also computed from the mass-balance equation but now using the actual density of the pore fluid ρ_f as

$$\phi = (2.65 - \rho_b)/(2.65 - \rho_f), \tag{4}$$

where ρ_f was obtained from water saturation (S_w) and the densities of the oil (ρ_o) and water (ρ_w) as

$$\rho_f = (1 - S_w)\rho_o + S_w \rho_w. \tag{5}$$

By cross-plotting the wet-rock I_p and I_s versus ϕ (Figure 6.9) and color-coding the datapoints by the difference ($\Delta\phi$) between the neutron (ϕ_N) and density-derived (ϕ_ρ) porosity

$$\Delta\phi = \phi_N - \phi_\rho, \tag{6}$$

we can observe that this porosity difference serves as a robust differentiator for the impedance at the same porosity with the lower impedance corresponding to higher $\Delta\phi$ and higher impedance corresponding to lower $\Delta\phi$. As a result, we conclude that $\Delta\phi$ can serve as a proxy for the clay content C with the high-C data having lower impedance at the same porosity, as in Han's (1986) data discussed in the previous section.

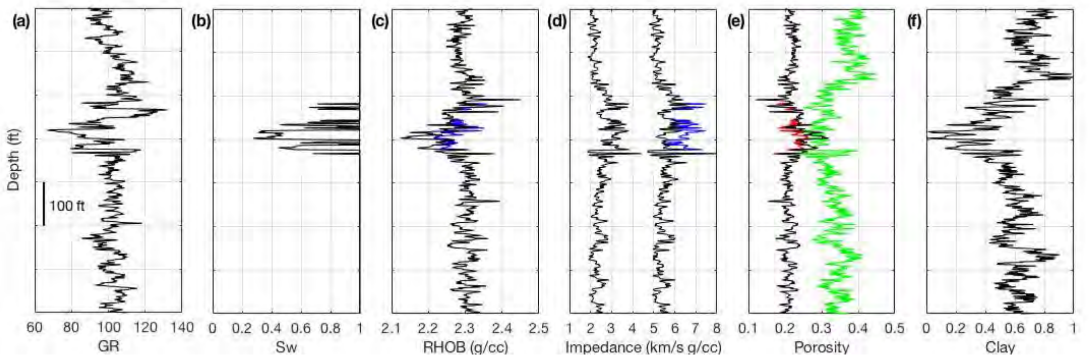

Figure 6.8. Gulf Coast well. GR (a); water saturation (b); bulk density (c); P- and S-wave impedances (d); density-derived porosity in black, neutron porosity in green, and the total porosity in red (e); and the computed clay content (f) versus depth.

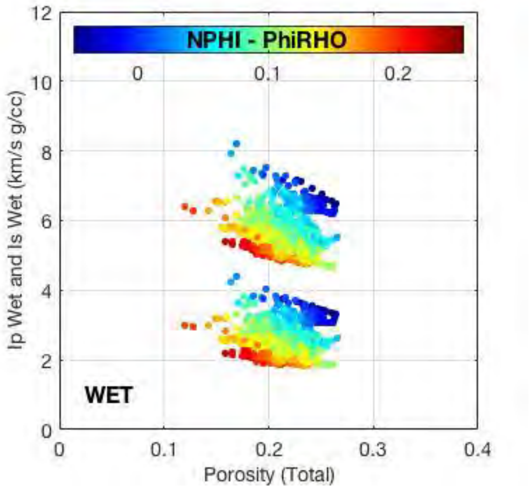

Figure 6.9. Wet-rock I_p (upper cluster) and I_s (lower cluster) from Figure 6.8 versus the total porosity and color-coded by difference between the neutron and density-derived porosity.

This observation led us to compute the clay content C by normalizing the porosity difference $\Delta\phi$ between zero and one as:

$$C = \frac{\Delta\phi - \min(\Delta\phi)}{\max(\Delta\phi) - \min(\Delta\phi)}. \tag{7}$$

The clay content thus derived is plotted versus depth in Figure 6.8f. It is also used to color-code the wet-rock impedance versus the total porosity cross-plots in Figure 6.10. The data shown in this figure span the clay content range between zero and 80%. The impedances are plotted versus a linear combination $\phi + \gamma C$, where the coefficient γ

varies between zero and 0.28 with a constant increment 0.04. The impedance-porosity plots arguably collapse to fairly tight trends as I_p and I_s are plotted versus $f + gC$ with g ~ 0.16 for I_p and g ~ 0.20 for I_s.

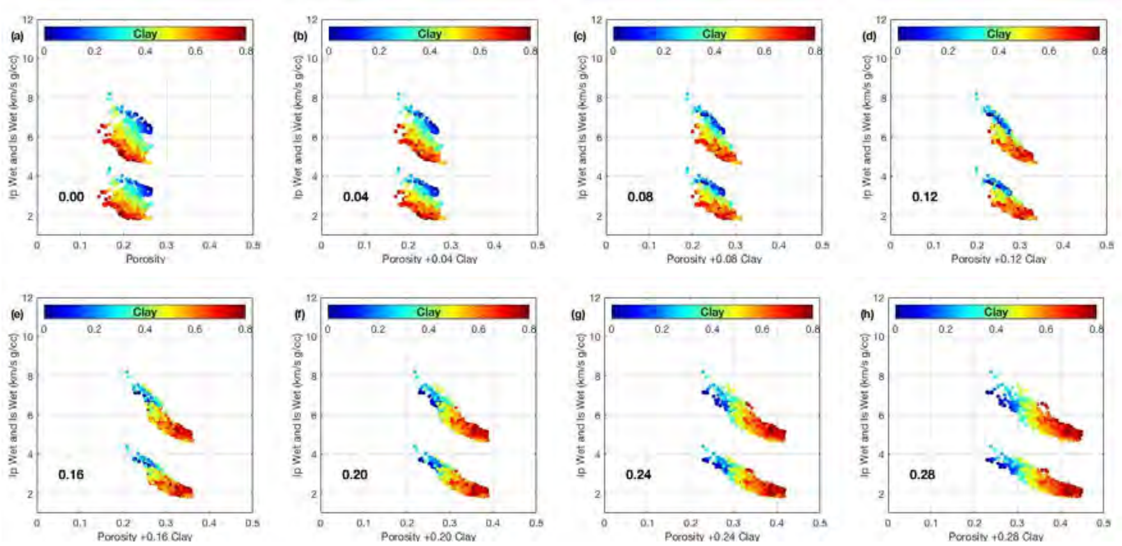

Figure 6.10. Wet-rock I_p (upper cluster) and I_s (lower cluster) from Figure 6.8 versus a linear combination of the total porosity clay content, $\phi + \gamma C$, with γ listed in each plot. The color is the clay content derived according to Equation 7.

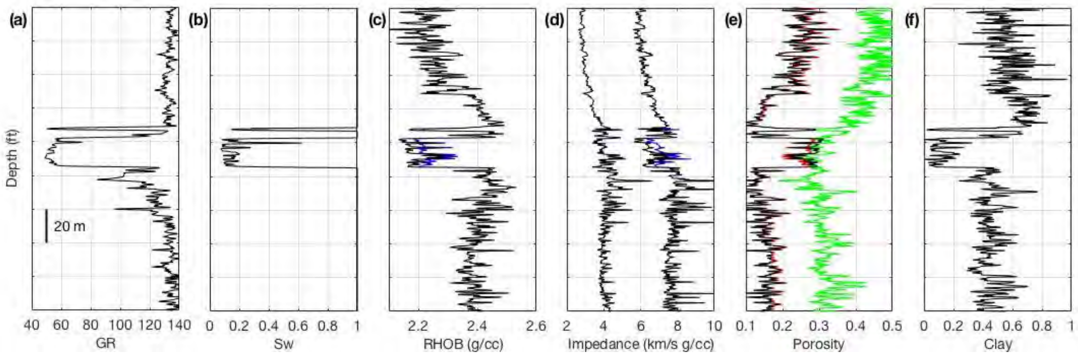

Figure 6.11. Same as Figure 6.8 but for an offshore oil well drilled through a turbidite clastic environment with a low-API and low-GOR oil reservoir.

Another example is for an offshore well drilled in a turbidite clastic environment and penetrating a low-API oil reservoir with very low GOR as in Chapter 4. Figure 6.11 shows the depth curves for this well with the display the same as used in Figure 6.8. As in the previous example, the $Df = f_N - f_r$ difference appeared to be a robust proxy for the clay content. The latter was computed according to Equation 7 and is shown in Figure 6.11f.

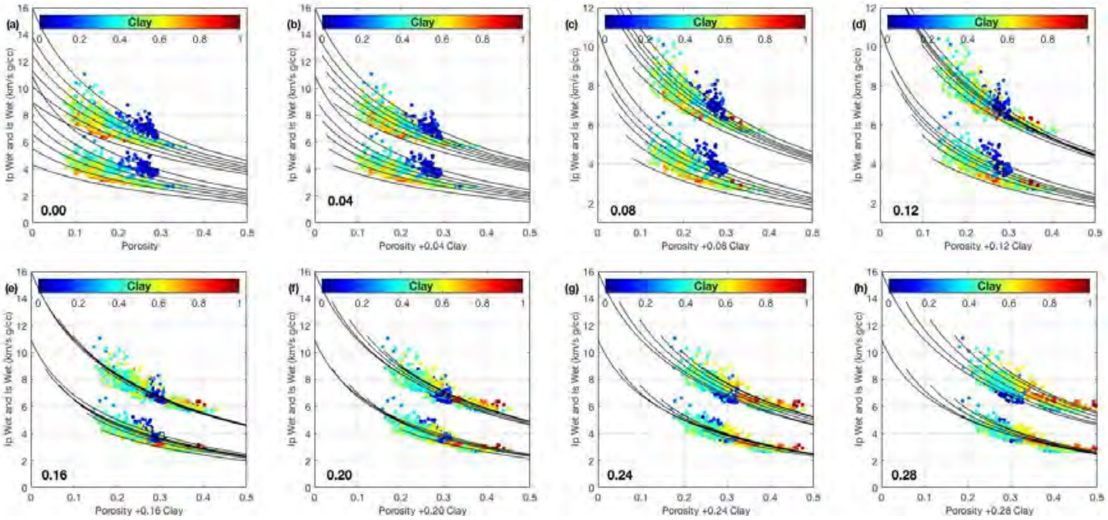

Figure 6.12. Same as Figure 6.10 but for an offshore oil well drilled through a turbidite clastic environment with a low-API and low-GOR oil reservoir.

Figure 6.12 shows cross-plots of the wet rock impedances versus a linear combination $f + gC$, with g varying in the same range and with the same increment as in the case presented in Figure 6.10. Superimposed upon the data are the model curves according to the constant-cement model, also for the wet rock and with the differential pressure 17 MPa, coordination number 20, critical porosity 0.40, and the shear correction factor 1 (the model is described in detail in Chapter 2).

As the coefficient g increases, the data gradually converge to relatively tight trends. What is important here is that the model curves, also plotted versus $f + gC$, also converge to tight trends with $g \sim 0.16$ for I_p and $g \sim 0.24$ for I_s.

6.4 Self-Similarity in Rock Physics Models

Figure 6.12 indicates that where a rock physics model can be found to describe the data, the model-computed impedances versus $f + gC$ converge to tight trends. In this case, the coefficients g_p and g_s (Equation 2) that allow for this convergence are not equal to each other. Hence, potentially, I_p and I_s can be simultaneously resolved for f and C if these impedances are obtained from, e.g., simultaneous impedance inversion at the same point in the subsurface. This conclusion does not hold for all rock physics models. Figure 6.3 indicates that Han's (1986) wet-rock data can be represented by the Raymer-Dvorkin (Dvorkin, 2007b) model. The respective model curves collapse into a tight trend for $g_p = g_s \sim 0.25$. The same is true for Han's (1986) dry-rock data, also with $g_p = g_s \sim 0.25$. This means that where the data are described by the Raymer-Dvorkin model, relevant to stiff, fast rock, there may be a problem in simultaneously resolving I_p and I_s for f and C.

Therefore, our recommendation regarding the feasibility of interpreting the seismically derived impedances for petrophysical rock properties is to (a) perform rock physics diagnostics to find the model that describes well or laboratory data and then (b) check whether the coefficients g_p and g_s are approximately equal to each other or are substantially different from each other. In the case g_p » $g_s = g$ such interpretation for f and C can be problematic since only the combination $f + gC$ can be obtained from either I_p or I_s.

In this section we explore several rock physics models for various lithologies where the rock is saturated with the same fluid but the properties of this fluid can be variable between the cases.

For this exercise, we select three different pore fluids: (a) gas with water; (b) oil with water; and (c) 100% water. In the first two cases, we assume that the water saturation is constant S_w = 20%. The properties of the fluid components, gas, oil, and water, were computed from the Batzle-Wang (1992) equations for the pore pressure 20 MPa and temperature 65 ^{o}C. The gas gravity selected for these examples was 0.65. The oil gravity was 30 API with the gas-to-oil ratio (GOR) 200 Sm^3/Sm^3. The water salinity was 80,000 ppm. The results for the bulk moduli and densities of these components are listed in Table 6.1.

To compute the effective bulk modulus of a hydrocarbon/water system we used the harmonic average of the moduli of the components:

$$\frac{1}{K_f} = \frac{S_w}{K_w} + \frac{1 - S_w}{K_h}, \tag{8}$$

while the effective density was computed as the arithmetic average of the densities of the components:

$$\rho_f = S_w \rho_w + (1 - S_w)\rho_h, \tag{9}$$

where K_f and ρ_f are the bulk modulus and density of the hydrocarbon/water system, respectively; K_w and ρ_w are those of the formation water; and K_h and ρ_h are those of the hydrocarbon (gas or oil).

In all examples presented in this section, we use three binary mineralogies: (a) quartz/clay; (b) feldspar/clay; and (c) dolomite/calcite. The elastic moduli and densities of these minerals are listed in Table 2. These values were selected from the tables in Mavko et al. (2009). All rock physics models used in this section are described in Mavko et al. (2009).

Table 6.1. Properties of the fluids used in the examples.

Fluid	Bulk Modulus (GPa)	Density (g/cc)
Gas	0.042	0.155
Oil	0.562	0.694
Water	2.869	1.045
Gas/Water at $S_w = 20\%$	0.052	0.333
Oil/Water at $S_w = 20\%$	0.670	0.764

Table 6.2. Properties of the minerals used in the examples.

Mineral	Bulk Modulus (GPa)	Shear Modulus (GPa)	Density (g/cc)
Quartz	36.60	45.00	2.65
Clay	21.00	7.00	2.65
Feldspar	75.60	25.60	2.63
Calcite	76.80	32.00	2.71
Dolomite	94.90	45.00	2.87

6.5 Soft-Sand, Constant-Cement, and Stiff-Sand Models for Quartz/Clay.

Figure 6.13 shows I_p and I_s versus f as well as I_p versus $f + g_p C$ and I_s versus $f + g_s C$ for the *soft-sand model*. The parameters used in this model are: the differential pressure 20 MPa; coordination number 6; critical porosity 0.40; and the shear correction factor 1. The coefficients g_p and g_s were found by visually determining the tightest I_p versus $f + g_p C$ and I_s versus $f + g_s C$ trends. It appears that for all three pore fluid types, these coefficients are close to each other, $g_p \sim 0.11$ and $g_s \sim 0.14$.

It is clear from Figure 6.13 that a tight trend can only be obtained for I_p versus $f + g_p C$ for the 100% wet case. In all other cases, the self-similarity is not as well pronounced, likely because we examined the case with wide porosity and clay content variations: ϕ between zero and 40% and C between zero and 100%.

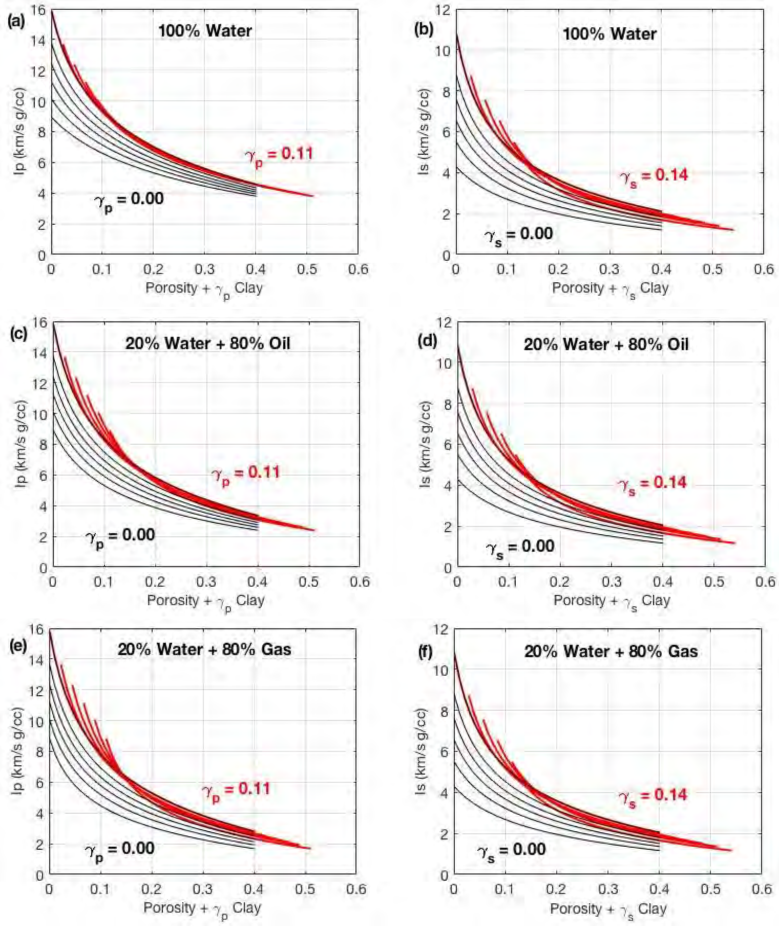

Figure 6.13. The soft-sand model, quartz/clay mineralogy. I_p (left column) and I_s (right column) versus $\phi + \gamma_p C$ and $\phi + \gamma_s C$, respectively (bold red curves) for the clay content varying between zero and 100% with a 20% increment. The values of the γ_p and γ_s coefficients are listed in red. Black curves are the same impedances but plotted versus porosity for the six gradually increasing C values (top to bottom). For these (black) curves $\gamma_p = \gamma_s = 0$ as listed in the plots. The pore fluid used in this modeling is described in each of the plots.

Indeed, if we vary porosity between 20 and 40% as appropriate for the soft-sand model, the impedance-porosity trends in the entire clay range (zero to 100%) collapse to tight trends much better (Figure 6.14). In this case the linear coefficients g_p and g_s are different from those obtained for the zero to 40% porosity variation. For both the wet and oil case, $g_p = 0.12$ and $g_s = 0.20$. For the gas case, these coefficients are different: $g_p = 0.15$ and $g_s = 0.19$. This means that where sand and shale can be described by the soft-sand model, the seismically-derived impedances can be uniquely resolved for porosity and clay content if the pore fluid is identified. Such identification can be made using the I_p/I_s ratio or Poisson's ratio (e.g., Dvorkin et al., 2014; and as in Chapter 3).

Of course, in order to quantify the pore fluid type and its properties during frontier exploration, assumptions have to be made about whether the reservoir is oil or gas, as well as about the properties of the hydrocarbons, the temperature and the pore pressure. This task becomes more certain during development when information about the fluid type and properties becomes available from well testing and well data. Moreover, well data are essential in quantitative interpretation of seismic data for petrophysical variables, as having these data allows us to conduct rock physics diagnostics and, by so doing, establish a site-specific rock physics model.

The fact that the linear coefficients vary depending on the porosity range selected (compare Figure 6.13 to Figure 6.14) means that using a linear combination of porosity and clay content as a single variable affecting the impedances is far from universal. Finding that the linear coefficients are different for I_p and I_s simply means that these measurements can be resolved for two petrophysical variables. The actual quantitative routine should not directly use these linear combinations but instead lookup tables derived from the rock physics model, as discussed in Chapters 3 and 4.

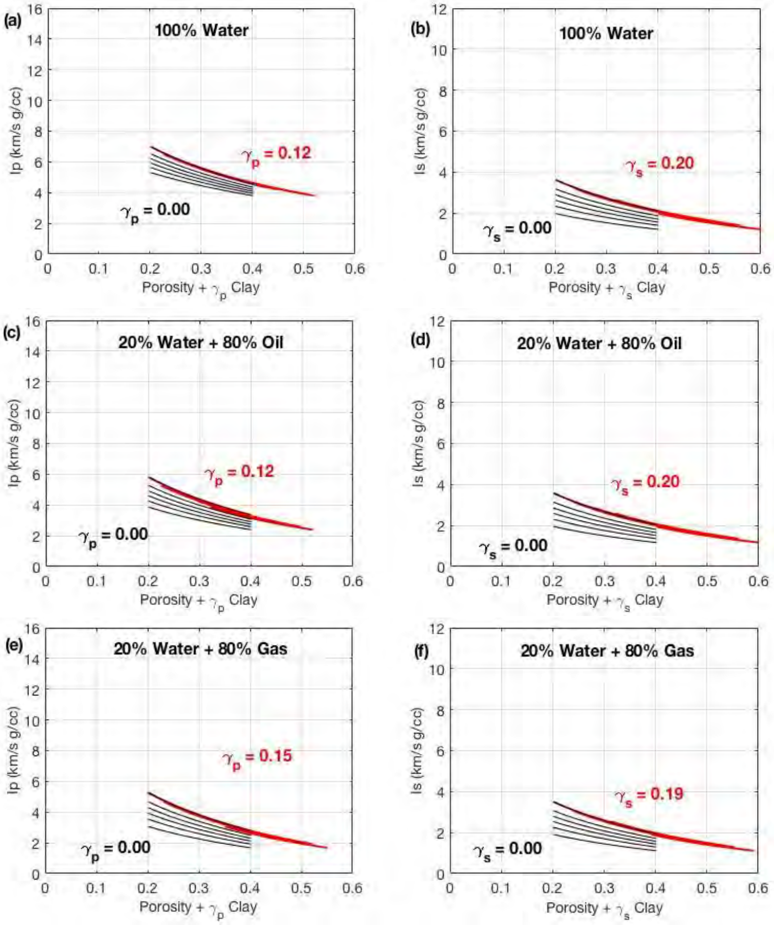

Figure 6.14. Same as Figure 13 but for porosity range between 20 and 40%.

To explore the self-similarity of the *constant-cement model* we now constrain the porosity range between 10 and 30%. The constant-cement model has the same functional form as the soft-sand model but with artificially high coordination number (Dvorkin et al., 2014). In this example we select the coordination number 20. Here the self-similarity coefficients for I_p for the wet, oil, and gas-saturated rock are approximately the same, 0.17 to 0.18 and are also the same (~ 0.24) for I_s (Figure 6.15). In this case, g_p is approximately fluid-independent, unlike for the soft-sand model. This is because the constant-cement model describes a stiffer rock.

Finally, for the stiff-sand model we select a porosity range between 5 and 25%. The coordination number used in this model is 6. Figure 6.16 indicates that because the rock is stiff, the self-similarity coefficients weakly depend on the pore fluid, same as for the constant-cement model. These coefficients are different for I_p and I_s: g_p ~ 0.22 to 0.23 and g_s ~ 0.30, meaning, once again, that the impedance can be uniquely resolved for the total porosity and the clay content.

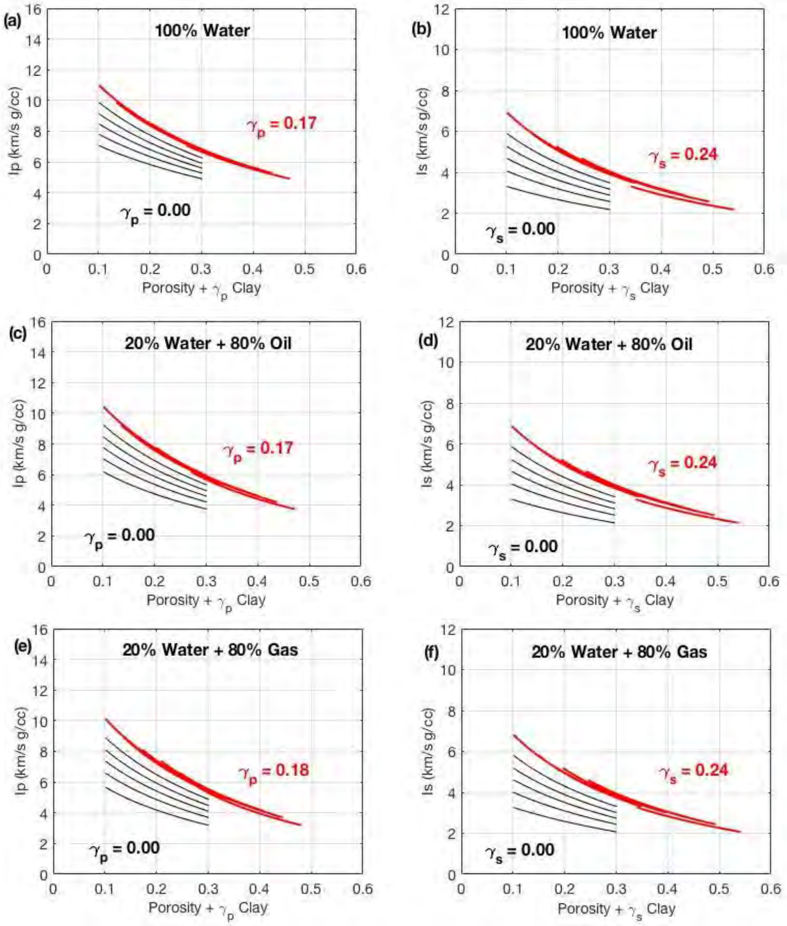

Figure 6.15. Same as Figure 6.14 but for the constant-cement model and in the porosity range between 10 and 30%.

6.6 Soft-Sand Model for Feldspar/Clay.

In this example, we repeat the soft-sand exercise conducted for the quartz/clay mineralogy, but replace quartz with feldspar. This lithology substitution reflects the difference between a pure-quartz and arkosic sand (e.g., Dvorkin et al., 2014). Other model parameters are exactly the same as in the soft-sand quartz/clay exercise. Feldspar's properties are listed in Table 6.2.

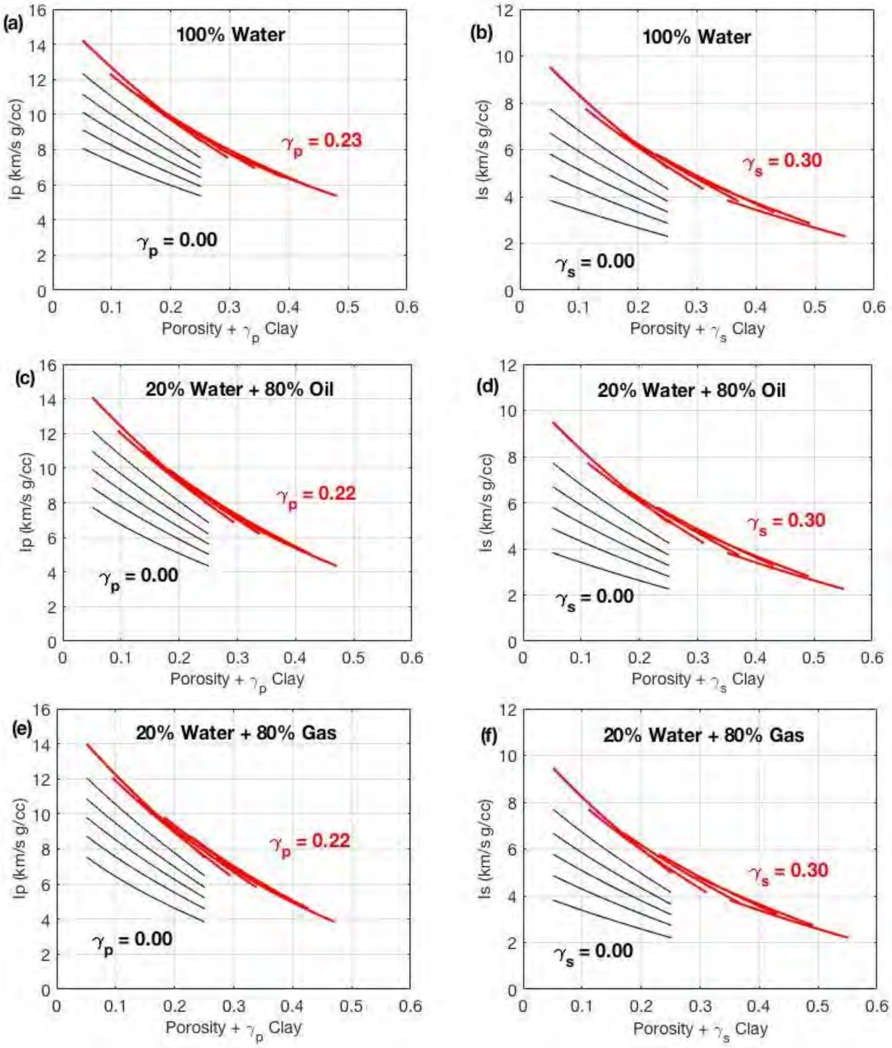

Figure 6.16. Same as Figure 6.15 but for the stiff-sand model and in the porosity range between 5 and 25%.

The results are shown in Figure 6.17. Unlike in the quartz/clay system, g_p and g_s in this case are closer together, arguably, because the Poisson's ratios of clay and feldspar are essentially identical (0.35), unlike those of clay and quartz (0.35 and 0.06, respectively). Hence, uniquely deriving ϕ and C from I_p and I_s may be problematic in feldspar-rich sand.

6.7 Stiff-Sand Model for Dolomite/Calcite.

The final example in this section is for a binary dolomite/calcite mineralogy. Because carbonate rocks are usually stiff, an appropriate model for this mineralogy is the stiff-sand model. As in the quartz/clay system, we select a porosity range between 5 and 25% and the coordination number 6. Because this stiff system is hardly sensitive to the changes in the pore fluid, we limit this exercise to only two cases: wet and gas rock.

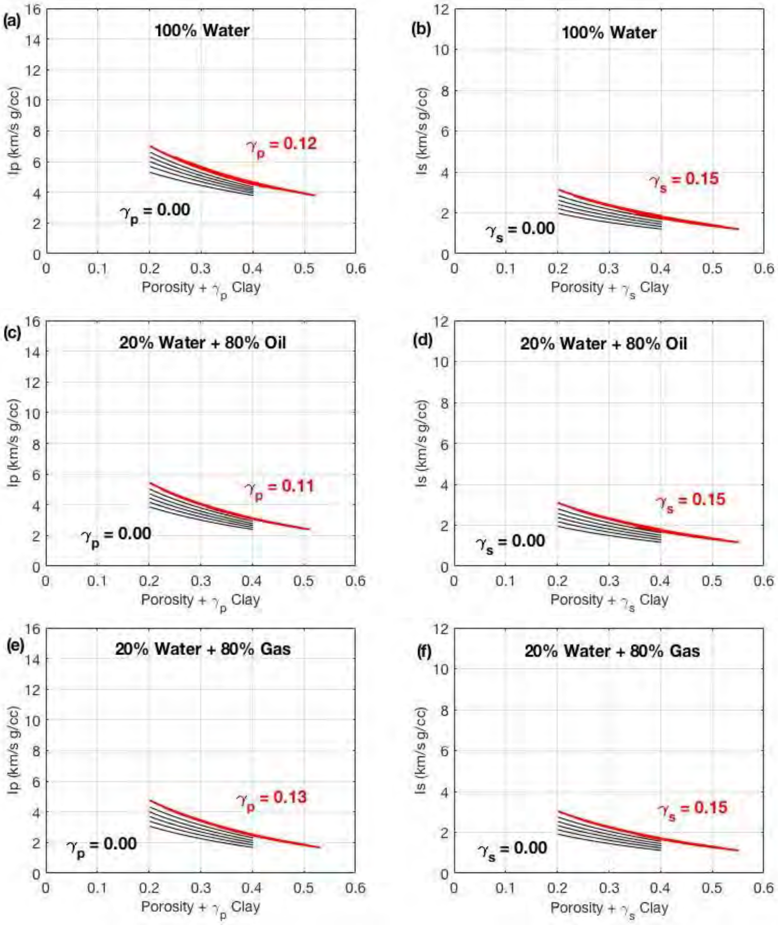

Figure 6.17. Same as Figure 6.14 but for the feldspar/clay mineralogy.

The modeling results shown in Figure 6.18 indicate that the self-similarity coefficients g_p and g_s are very close to each other (0.05 and 0.07, respectively) and do not vary as the pore fluid changes.

On the one hand, this means that it might be mathematically challenging to uniquely derive the porosity and dolomite content from I_p and I_s. This is the case where geological reasoning should guide the mathematical logic. Indeed, in many fields dolomitization acts to increase porosity. Hence, mineralogy variation and porosity development can go hand-in-hand (e.g., Landes, 1946).

Coincidentally, this is often the case in a clastic system where the addition of clay to the clean-sand framework acts to reduce the total porosity (Thomas and Stieber, 1975).

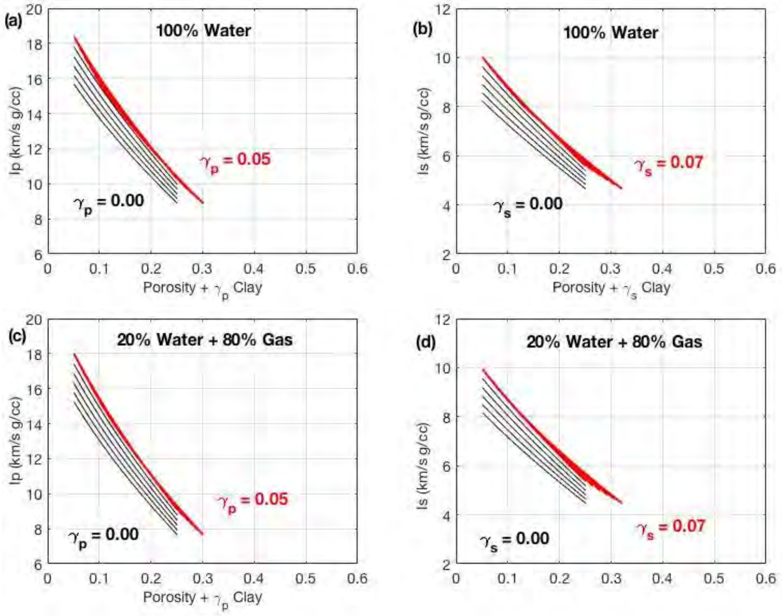

Figure 6.18. Same as Figure 6.16 but for the calcite/dolomite mineralogy.

6.8 Discussion

The subject of self-similarity in rock physics emerged as a result of analyzing Han's (1986) laboratory data and discovering that both I_p and I_s depend on the same linear combination of the porosity and the clay content. One implication of this fact was that even where we have both impedances measured, we cannot uniquely resolve these two measurements for two petrophysical variables, ϕ and C (Dvorkin, 2007). We realize, by looking at the I_p versus I_s plot (Figure 6.7), that in these data, I_s uniquely depends on I_p, meaning that within these data realm, an I_s measurement is redundant. This means, in turn, that even where we have both impedances *and* they are uniquely dependent on each other, they cannot be resolved for two different petrophysical unknowns. This is how self-similarity expresses itself in the realm of V_s predictors.

After discovering self-similarity in Han's (1986) data, we kept looking for the same effect in other datasets, mainly in well data, and discovered that it is far from universal. Such example is shown in Figure 6.12 where g_p (~ 0.16) and g_s (~ 0.24) were substantially different form each other, which, in principle, would allow for uniquely resolving both measured impedances for ϕ and C.

This effect emphasizes the importance of rock physics diagnostics as a means of establishing a site-specific rock physics model prior to attempting an interpretation of simultaneous impedance inversion for petrophysical unknowns. An example of such workflow is given in Chapters 3 and 4. An important element of this workflow is to explore self-similarity in relevant ranges of porosity and mineralogy, as well as for different pore fluid systems.

Another, graphical, interpretation of the self-similarity phenomenon is in the C versus ϕ cross-plot upon which model-based constant-impedance curves are superimposed. In Figure 6.19 we show such plots separately for the Raymer-Dvorkin and constant-cement models for 100% wet rock. The Raymer-Dvorkin constant I_p and I_s contours are almost parallel to each other, meaning that where both impedances are known, it may be difficult to find the intersection of these impedance contours and, hence, uniquely determine ϕ and

C. The situation is different for the constant-cement model where the constant I_p and I_s contours are not parallel to each other and, as a result, provide for a unique ϕ and C pair.

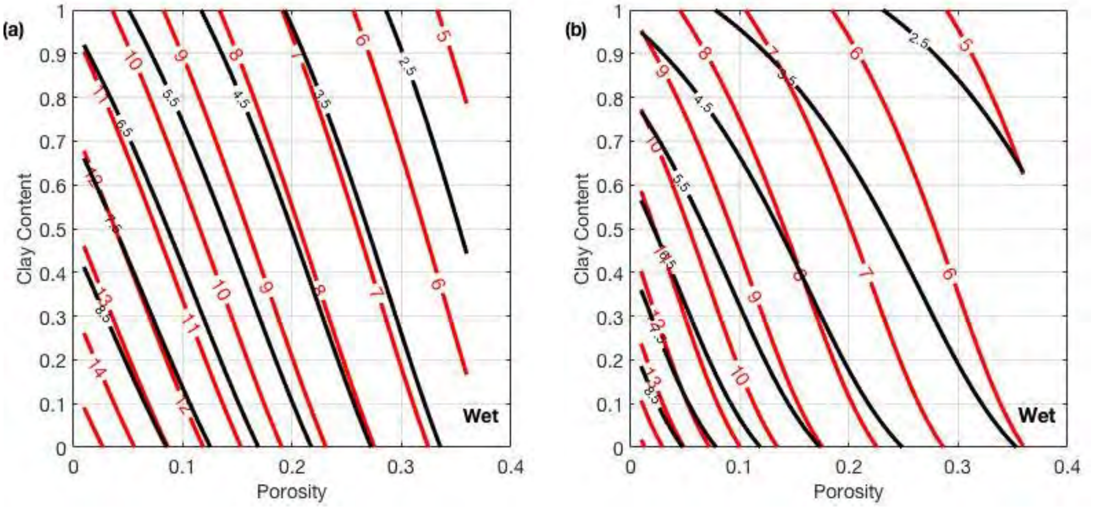

Figure 6.19. Clay content versus porosity spaces with the constant I_p (red) and I_s (black) contours superimposed. The numbers on the contours indicate the impedance values in km/s times g/cc. (a) The Raymer-Dvorkin model and (b) the constant-cement model. Both models are for 100% wet rock.

6.9 Conclusion

The self-similarity, originally discovered in laboratory data, can be an obstacle for interpreting I_p and I_s from simultaneous impedance inversion for porosity and mineralogy. Finding a data-based rock physics model and exploring the effect of self-similarity in the model domain helps establish whether such interpretation is mathematically feasible. The examples discussed here can be interpreted as extending the original self-similarity concept where both I_p and I_s depend on the same linear combination of the porosity and clay content to a situation where such a linear combination for I_p differs from that for I_s. Where this is indeed the case, an interpretation of the elastic variables for petrophysical unknowns becomes feasible and reliable.

Even where the original self-similarity persists, meaning that both impedances approximately depend on the same combination of porosity and, e.g., the clay content, geological reasoning has to be invoked to find if there is a dependence between porosity and mineralogy, such as in dispersed quartz/clay systems or during carbonate dolomitization. Such geological reasoning may aid in reducing uncertainty in interpretation.

Chapter 7

Percolation in binary permeability systems

7.1 Abstract

The percolation though porous media was analyzed by estimating the effective permeability with a Darcy's flow simulator in a random composite with properties taken from two data-sets: Ottawa sand mixed with different amounts of kaolinite (Yin, 1992), and the Fontainebleau measurements from a sandstone quarry (Bourbie, et al., 1987). The results indicate that the percolation has two distinctive regimes: (1) one stable, for random composites bigger than 13x13x13 elements where the increment in system elements has no effect on the percolation, as anticipated from the theoretical boundaries for a 3D cubic model (Sahimi, M, 1990); and (2) the double percolation system (Sumita et al., 1992), where the percolation is a function of both the percentage of non-permeable elements and the size of the model.

7.2 Introduction

Permeability is one of the most important properties in reservoir characterization since it is directly related to the recoverable amount of hydrocarbons a reservoir will ultimately provide. The purpose of this chapter is to characterize how the fluctuation in reservoir permeability, through fluid flow simulation, can be used to estimate the effective permeability and therefore the percolation of the total system.

The numerical approach to this problem is computationally expensive, almost two weeks of computation for each experiment in a 4 Xeon® core machine; however the results obtained highlight the importance of this methodology. The laboratory measurements of 500 samples would take significantly more time than a numerical experiment, and we would not have the same control in the permeability proportions in real samples.

7.3 Yin's Data Set

Yin (1992) conducted permeability and porosity measurements on mixtures of Ottawa sand and kaolinite particles for clay content varying between zero and 100%. The data were collected at essentially zero confining pressure, therefore the total porosity of the kaolinite powder appeared to be large, about 0.62, while the porosity of pure sand was about 0.39. These data are shown in Figure 7.1.

Based on these data, we can compute the upper and lower permeability bounds for a mixture of 12 samples where each sample has the same volume fraction (i.e., 1/12). The upper permeability bound $\mathbf{k_{up}}$ for such a composite is the arithmetic average of the elemental permeabilities, while the lower bound $\mathbf{k_{low}}$ is their harmonic average:

$$k_{Up} = \langle k \rangle, \quad k_{Low} = \langle k^{-1} \rangle^{-1} \quad . \qquad (1)$$

In Figure 7.1, these bounds are plotted versus the mean porosity and mean clay content.

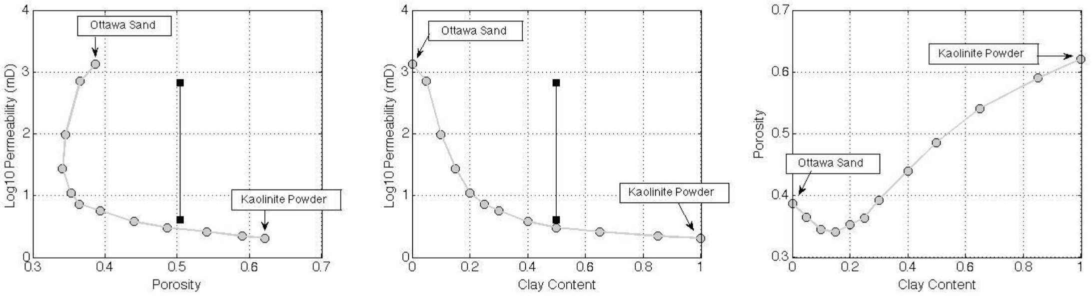

Figure 7.1. Permeability versus porosity, permeability versus the clay content, and porosity versus the clay content data from Yin's (1992) experiments. Black squares in the first two plots are the upper and lower permeability bounds.

7.4 Posing two questions

Suppose that the 12 samples whose properties are displayed in Figure 7.1 are combined in a composite. *What is the effective permeability of this composite? How is it related to the average porosity and clay content of the composite?*

7.5 Approach

A composite will be made as an equal-sized 3D block whose elements will have the porosity, clay content, and permeability drawn from the laboratory data-set under examination. A finite difference Darcy's flow simulator will be used to compute the effective permeability of this block along its vertical direction. Effective porosity and clay content will be computed as the arithmetic averages of the respective elemental properties.

7.6 Making a Composite

In our first exercise, we will randomly draw elements from the dataset including all 12 samples and randomly arrange them in 3D space (Figure 7.2). The size of the composite will be gradually increased from a small 2 x 2 x 2 block to the final 13 x 13 x 13 block. The effective properties will be computed as explained and plotted on top of the elemental trends shown in Figure 7.1.

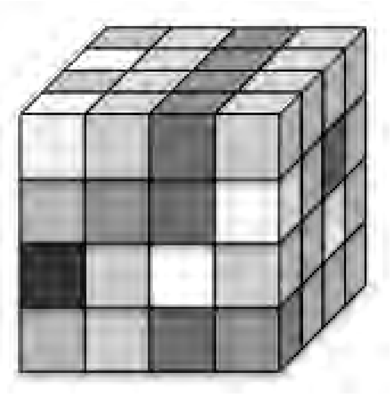

Figure 7.2. Cubical block made of 4 x 4 x 4 elements randomly drawn from Yin's (1992) dataset.

7.7 Results

Figure 7.3 shows the cross-plots of the effective permeability versus the average porosity, average clay content, and average porosity versus clay content. The red symbols in each plot represent the results computed for thousands of random realizations of the composite cube. These effective-property data are highly scattered for the composites with only a few elements.

However, as the number of the elements increased, the results from all realizations appear to converge to the same values, thus forming a tight cluster in the permeability versus porosity, permeability versus the clay content, or porosity versus clay content space.

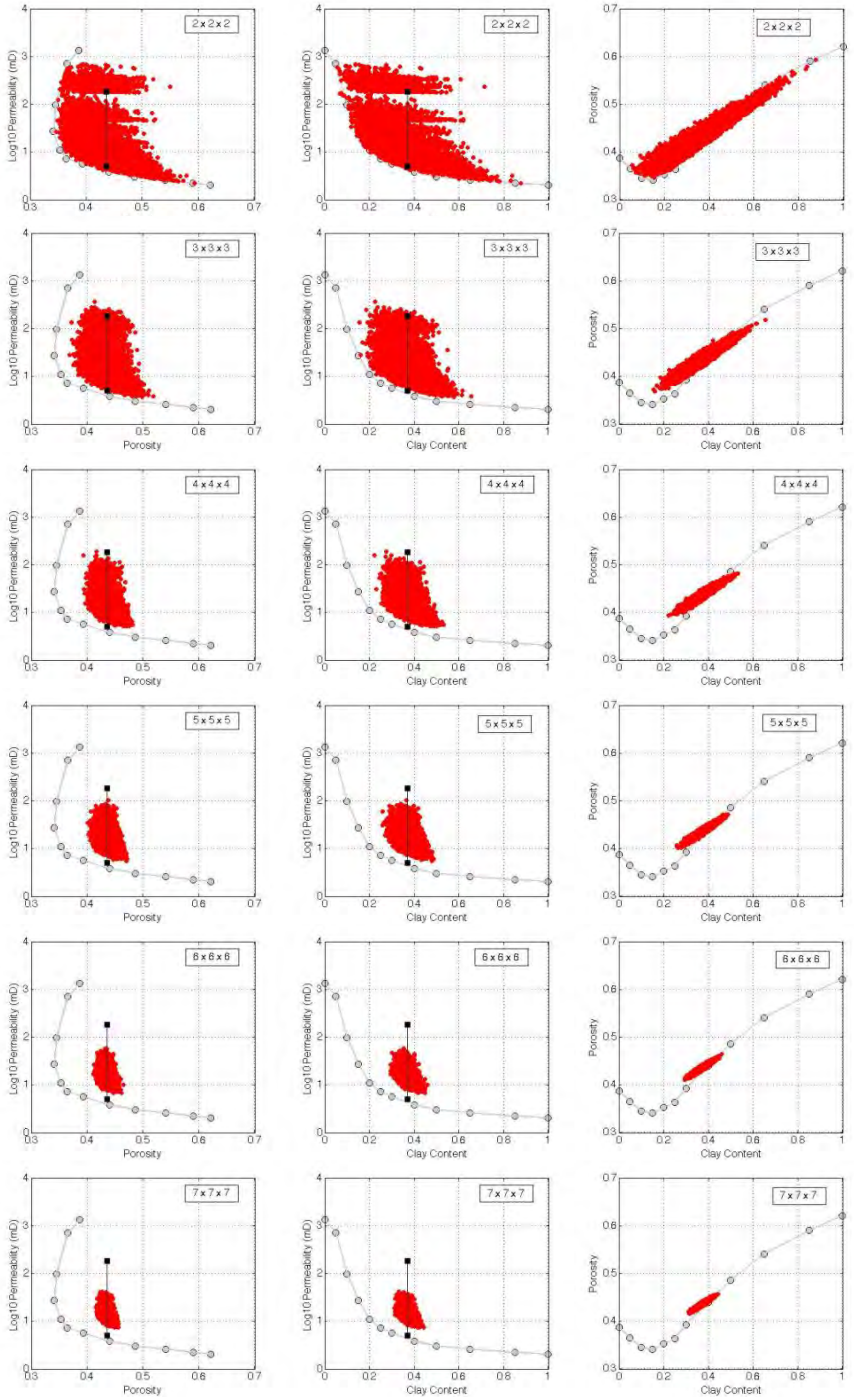

Figure 7.3. Cross-plots of the effective properties computed as explained in the text for the composite cube size from 2 x 2 x 2 to 7 x 7 x 7 at the bottom. Gray symbols are for the elemental data, same as in Figure 7.1. Red symbols are from thousands of random realizations for the composite cube. Squares are the permeability bounds as in Figure 7.1.

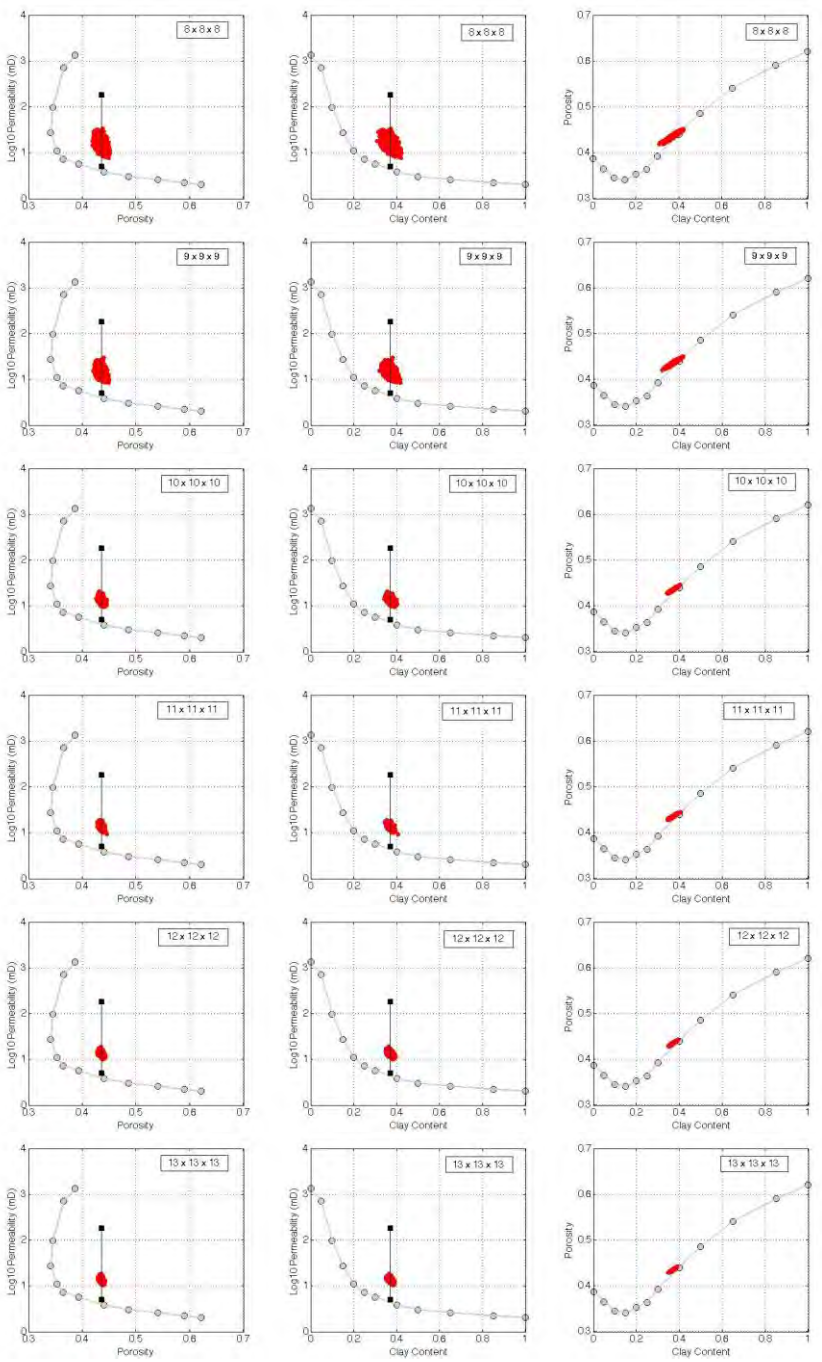

Figure 7.3 continued. Composite cube sizes from 8 x 8 x 8 to 13 x 13 x 13.

This is expected as the number of the elemental data points is fixed (twelve), while the number of the elements in a composite can be as large as $13^3 = 2197$. As a result, we encounter more and more repetitions in a large composite which, in turn, draw the effective properties computed for random realizations closer together.

7.8 Binary Composites

We will now experiment with various statistical ways of constructing the composite cube. We will only use one elemental data point for the pure Ottawa sand sample and one data point for pure kaolinite sample. We will be randomly drawing the elemental properties from these two data points with equal probability (Binary A). The upper and lower permeability values for these two elements are 667 and 4 mD, respectively. The permeability simulation results are plotted in Figure 7.4.

Now, in the Binary B example, we draw the permeability, porosity, and clay content values from 6 elements. One element is pure Ottawa sand while the remaining five are pure kaolinite powder. The mean porosity for these 6 elements is 0.582 while the mean clay content is 0.833. The upper and lower permeability bounds are 224 and 2.5 mD, respectively. These bounds are plotted in Figure 7.5 together with the permeability simulation results.

The effective permeability results break into two distinct clusters, one around the upper permeability value and the other around the lower value. As the size of the composite cube increases, the lower cluster becomes tighter but remains in place, while the upper cluster becomes smaller and moves towards the lower one near the lower permeability bound. Eventually, the upper cluster all but disappears. Although the high-permeability elements may form a continuous network in smaller-size composites, the low-permeability elements dominate in higher-size composites and prevent the hydraulic percolation of the composite by the high-permeability paths.

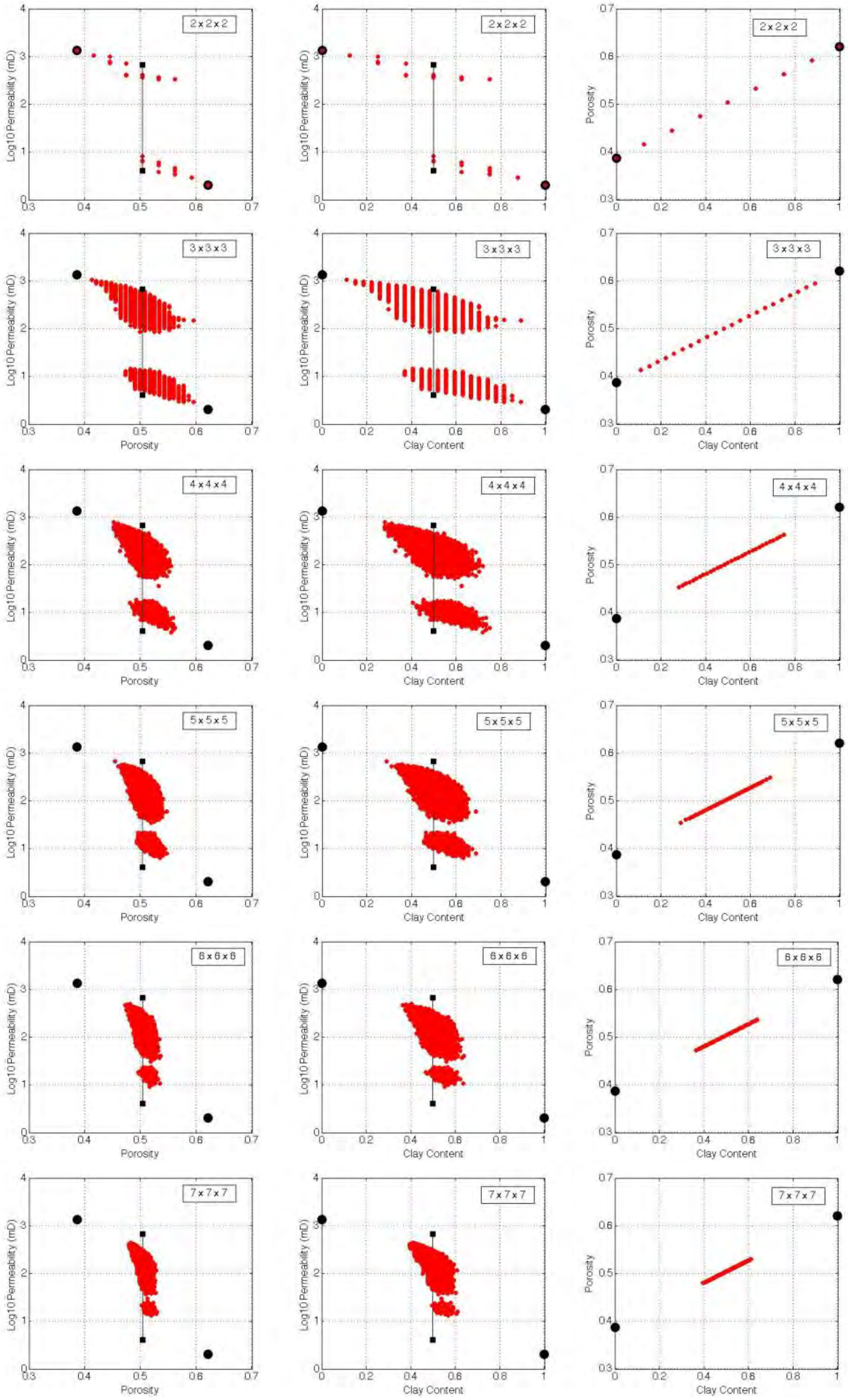

Figure 7.4. Same as Figure 7.3 but for a binary composite constructed from two equiprobable elements (Binary A), pure Ottawa sand and pure kaolinite powder, from size 2 x 2 x 2 to 7 x 7 x7.

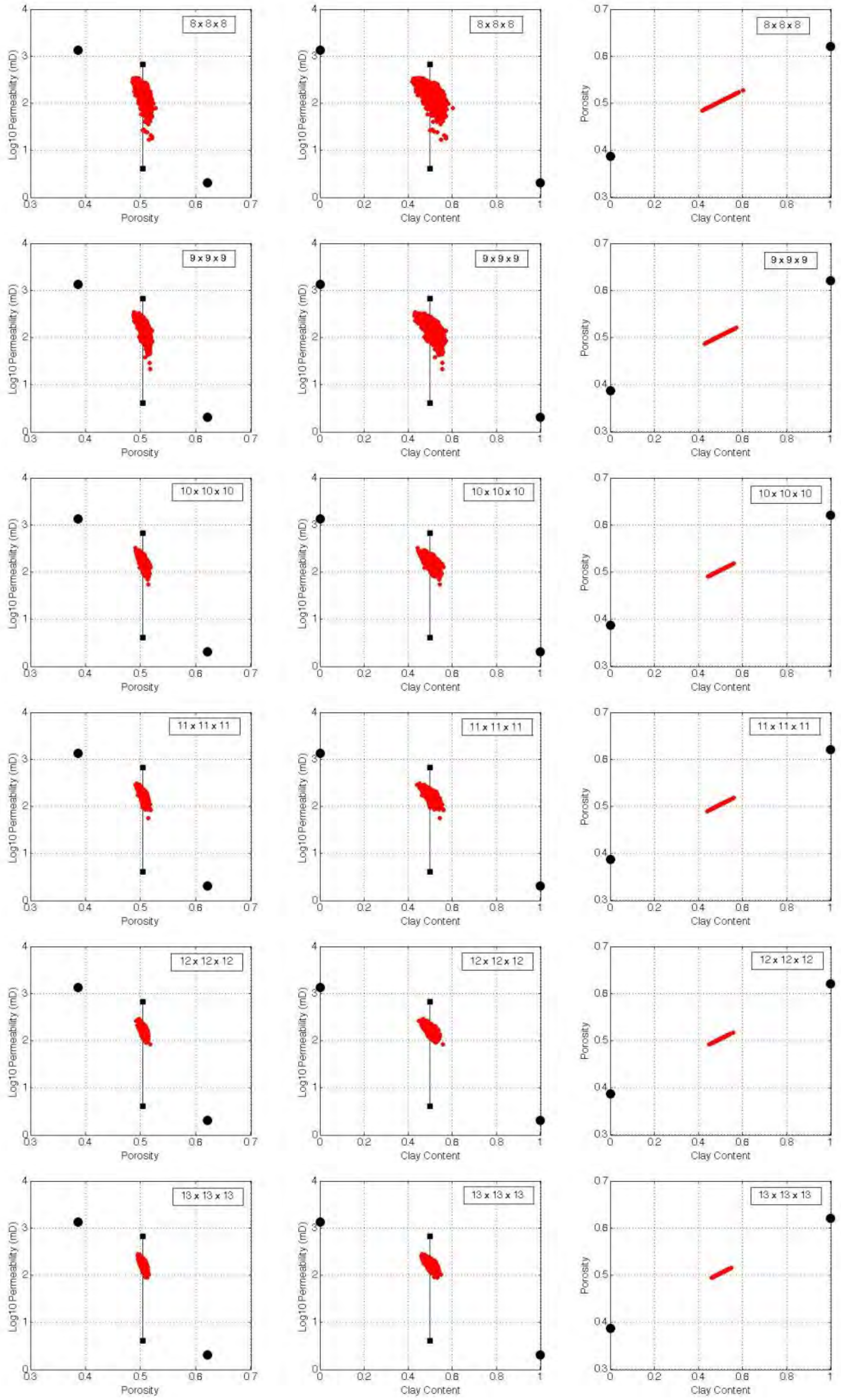

Figure 7.4 continued. Composite cube (Binary A) sizes from 8 x 8 x 8 to 13 x 13 x 13.

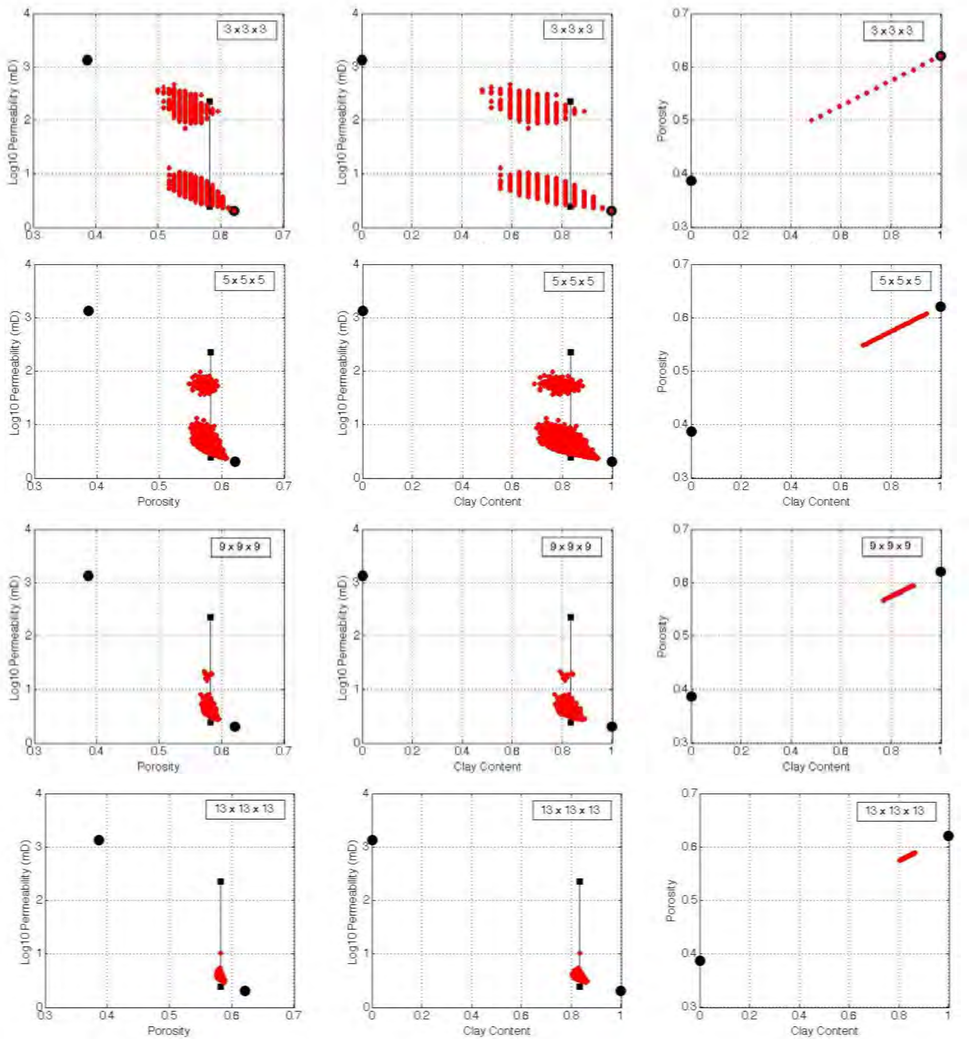

Figure 7.5. Same as Figure 7.4 but for a 6-element binary composite (Binary B, as explained in the text), sizes 3 x 3 x 3 up to 13 x 13 x 13.

The next binary composite (Binary C) is the opposite of Binary B. Here, we also have 6 elements but now 5 elements are pure Ottawa sand while the remaining one is pure kaolinite powder. The mean porosity for these 6 elements is 0.426 while the mean clay content is 0.167. The upper and lower permeability bounds are 1,111 and 12.2 mD, respectively. These bounds are plotted in Figure 7.6 together with the permeability simulation results.

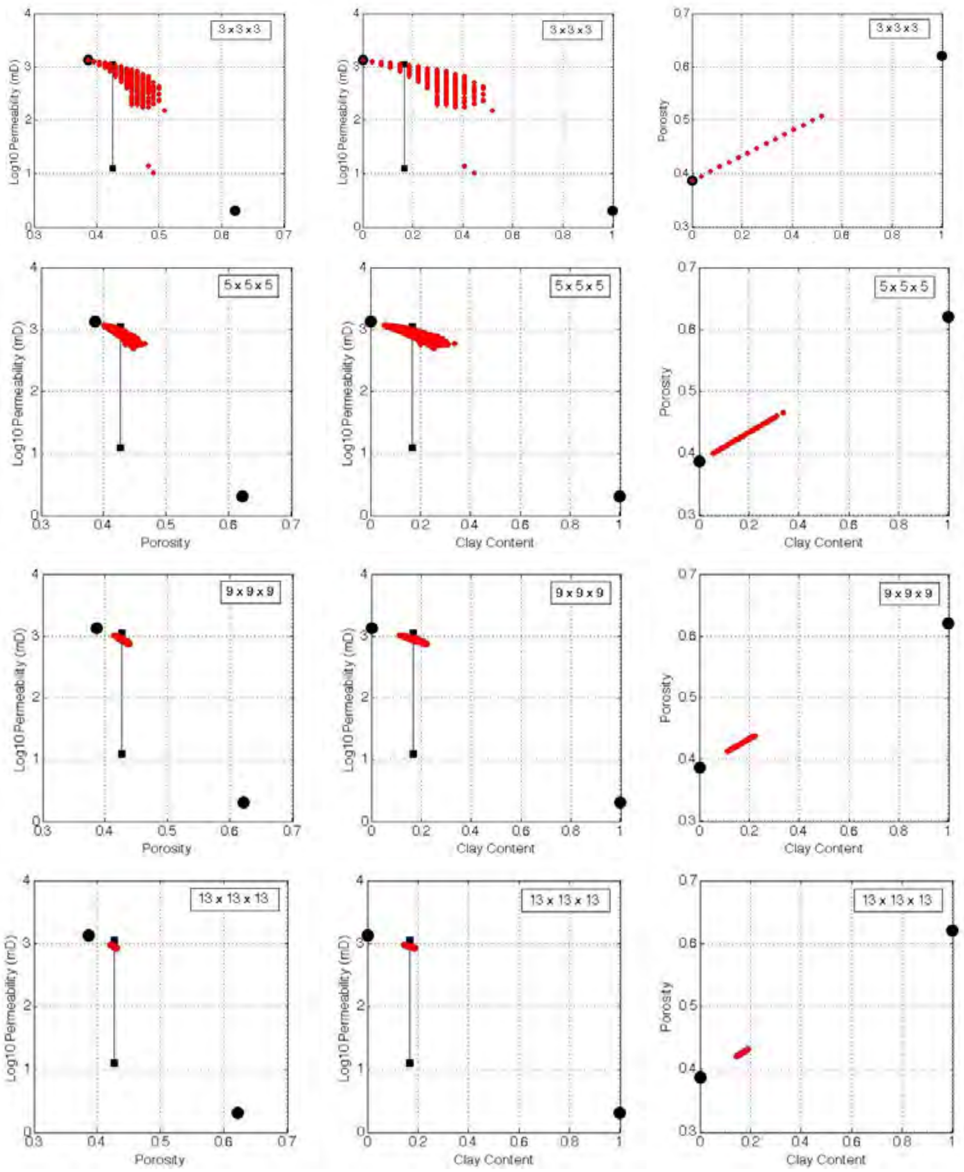

Figure 7.6. Same as Figure 7.4 but for a 6-element binary composite (Binary C, as explained in the text), sizes 3 x 3 x 3 up to 13 x 13 x 13.

7.9 Fontainebleau Data Set

The idea to explore with this other data set is the percolation threshold. The experiments will be focused on binary permeability composites, as those described for the Yin data set. The Fontainebleau data-set (Bourbie, et al., 1987) has a more typical porosity-permeability curve as shown in Figure 7.7. The extreme permeability values of

.21 and 4771 mD are colored in gray in Figure 7. These extreme values were used as the seeds for populating the permeability throughout the system.

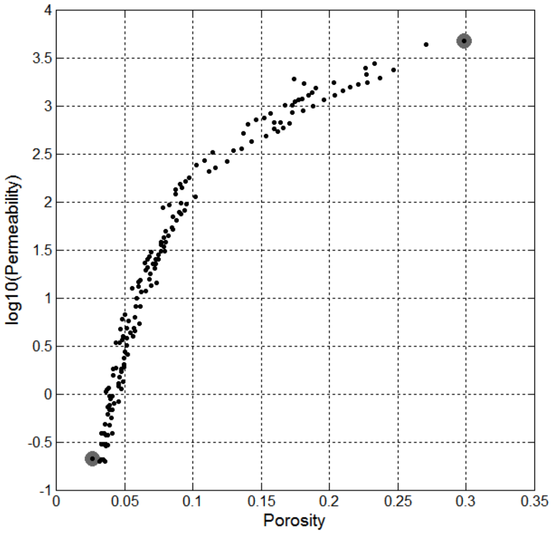

Figure 7.7. Porosity vs. $\log_{10}$(Permeability) for the Fontainebleau sandstone, where the binary permeability points are indicated in gray.

7.10 Percolation

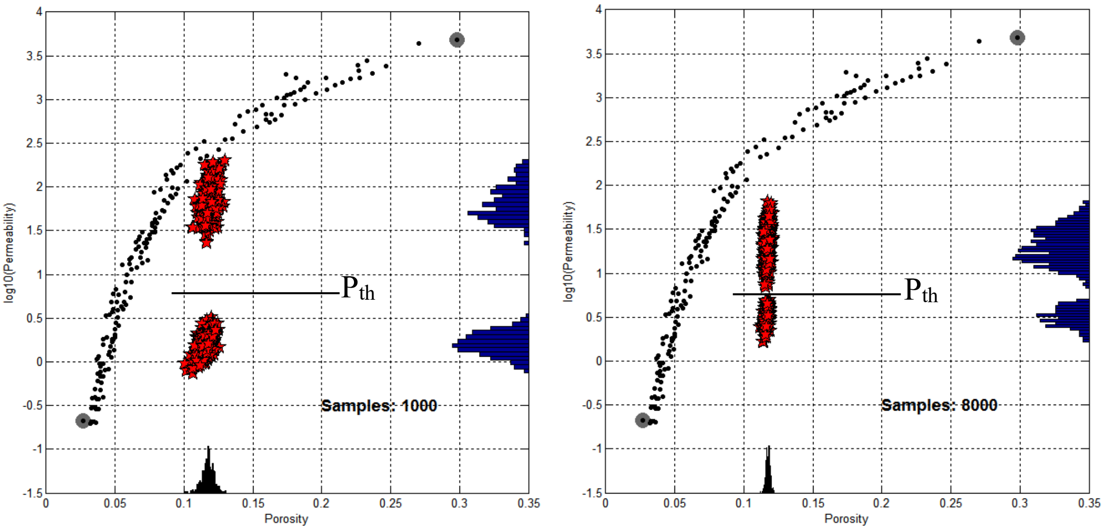

Figure 7.8: Porosity vs. $\log_{10}$(Permeability) for the Fontainebleau sandstone, where the two extreme permeabiilty points are indicated in gray; the red stars represent the effective permeability for 500 different realizations. The porosity histogram is shown along the horizontal axis, while the permeability histogram is shown on the vertical axis on the right. The horizontal line represents the percolation threshold drawn ad-hoc to approximately separate the high-permeability from low-permeability sets (about 6 mD). The left plot is for 10 x 10 x 10 composites while the right plot is for 20 x 20 x 20 composites.

The estimation of the effective permeability was performed as with the Yin data set, with a system containing 500 different composite models. The effective permeability results for the Fontainebleau dataset are shown as red stars in Figure 7.8. In this example, the composite was constructed using three subsamples, two of them with low permeability and one with high permeability. These three elements were drawn with equal probability (uniform probability distribution).

We call a permeable composite percolating if its effective permeability is larger than the ad-hoc introduced percolation threshold shown in Figure 8 (about 6 mD).

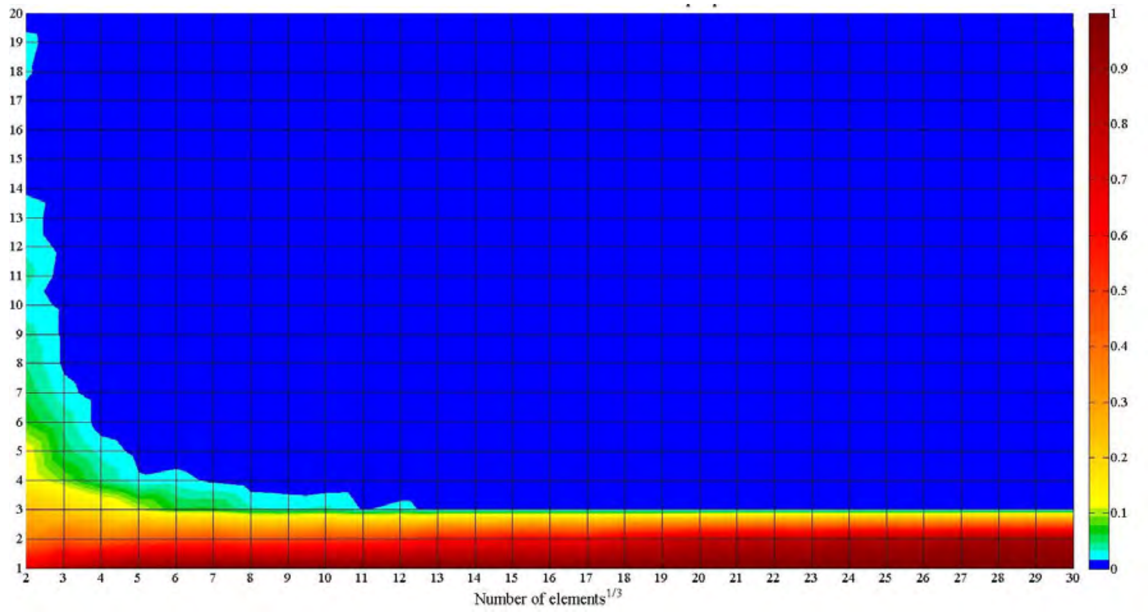

Figure 9: Percolation index (colorbar) versus the number of the subsamples in the composite (horizontal axis) and the ratio of low- to high-permeability elements in the elemental permeability set from which the subsample permeability is randomly drawn (vertical axis).

In the following example, we explore the effect of two variables on the effective permeability of the composite: (1) the ratio of low- to high-permeability elements in the elemental permeability set from which the subsample permeability is randomly drawn; and (2) the number of the subsamples in the composite. The first variable spans the range between 1 and 20, while the second variable is between 2 x 2 x 2 = 8 and 30 x 30 x 30 = 27000.

The percolation threshold was set at about 6 mD, same as in the preceding example. Then the *percolation index* (or threshold) was defined as the ratio of the composite realization whose permeability fell above this threshold to the total number of realizations. The results of this experiment are shown in Figure 7.9.

7.11 Conclusion

The results of the simulations shown in Figure 7.9 indicate that two effective permeability regimes exist. The first regime (the percolation regime) starts for composite cubes with the size greater than 13 x 13 x 13 elements. In this regime, further increase in the number of the composite size has no effect on the percolation index which is only controlled by the proportion of low-permeability to high-permeability elements. The result is consistent with the percolation threshold for connectivity in a 3D cubic system (Sahimi, M, 1990). The other regime, called the double percolation (Sumita et al., 1992), is below the composite size 13 x 13 x 13. In this regime, both the number of the elements and the proportion of low- to high-permeability subsamples control percolation.

The second regime is also illustrated in our examples using the Yin data set:

- The higher the number of elements in the composite, the tighter is the cluster of effective permeability values (as shown by the merging of the high- and low-permeability clusters in Figures 7.3 to 7.6).
- The initial permeabilities control the final effective permeability.

- The porosity and the effective permeability converge to a point as the size of the composite cube increases.

Chapter 8

Azimuthal filter to attenuate ground roll and scatter noise in the f-k_x-k_y domain for land 3D-3C seismic data with uneven acquisition geometry

8.1 Summary

The vertical component of seismic wave reflections is contaminated by the ground roll. A common method of removing this ground roll elements from the vertical component is via velocity filtering and/or multichannel stacking. 3C acquisition technology allows for directly estimating the ground roll components and then removing their effects from the vertical component. Our goal is to first test this operation in the Fourier domain by (a) estimating the azimuth of the ground roll propagation from the 3C horizontal components; (b) phase rotating the horizontal field by 90°; and (c) subtracting the result from the vertical component. A major obstacle is uneven acquisition geometry where typically the cross-line sampling is sparser than the in-line sampling. Directly using the differently spaced data distorts the kx-ky representation of the ground roll. To address this issue, we modified the filter used with even sampling to tackle the actual

geometry. The method was successfully tested on a synthetic dataset based on a 5-layer (4 interface) earth model which also included shallow scatterers to simulate near-surface inhomogeneities. Our method also helps remove the effect of these scatterers on the vertical component.

8.2 Introduction

Multi-component seismic acquisition developed over the last 40 years improves the quantification of the S-wave velocity and, by doing so, may improve lithology identification as well as fracture direction and density estimates (e.g., Barkved et al., 2004). Most land seismic reflection data have surface waves and scatterers that pose obstacles to proper migration. These waves often have low frequency and high amplitude that interfere with subsurface reflections. A typical approach to suppress them in single-component acquisition is by multichannel stacking. However, in multi-component acquisition there is additional information that could be used to attenuate the effect of these interferences.

The amplitude of surface waves, specifically that of ground-roll pseudo-Rayleigh waves, depends on the direction of propagation. Having the two directional horizontal amplitudes from 3C, we can reconstruct the amplitudes at any azimuth in the Fourier domain. Next, by using velocity filtering, we attenuate in this reconstructed field everything that is not the ground roll. Finally, via phase rotation, and scaling we subtract the ground-roll effect from the vertical component. As a result, we have created a filter for 3C seismic data that uses the azimuthal contribution of the surface noise (ground roll and scattering) in the horizontal components to remove it from the vertical component.

The traditional method of suppressing the surface noise in single component (1C) seismic is by multichannel stacking. However, such method is rarely applicable to 3C seismic data due to sparse deployment of the receivers. Yet, utilizing multi-component seismic data is essential to get access to other variables such as P-to-S information. Hence, removing surface noise present in 3C data is important. Here I discuss the application of a new filtering method in the f-k_x-k_y domain to attenuate this noise and provide synthetic examples with both even and uneven acquisition geometry.

It has been shown that if the 3-dimensional Fourier transform is applied to a shot point the energy of the surface noise is located in a cone in the f-k_x-k_y domain (Vassallo, et. al., 2011). In addition, the wave propagation is completely defined azimuthally in the k_x-k_y coordinates. These two facts allowed us to reconstruct the amplitudes at any azimuth in the Fourier domain from the two horizontal components of the 3C. Next, by using velocity filtering, we remove from this reconstructed field everything that is not the ground roll or scattering. Finally, after phase rotation, we subtract the surface noise from the vertical component in the Fourier domain.

8.3 Surface Noise

The term ground roll is applied to the seismic waves that travel close to the surface of the Earth (Rayleigh waves). They are characterized by low velocity, high amplitude, and a retrograde elliptic particle movement in the vertical plane containing the propagation vector. The velocity of the Rayleigh waves can be expressed as a function of the P- and S-wave velocities (V_p and V_s respectively) as (Liner, 1999):

$$V_R \approx V_s \left[\frac{20-\sqrt{256\gamma^4-336\gamma^2+130}}{16\gamma^2+9} \right];\ \gamma = \frac{V_s}{V_p}. \qquad (1)$$

Because the Rayleigh waves are surface waves, their amplitude for a given frequency, decreases exponentially with depth. However, as their velocity is low, they arrive at the receivers at the same times as the subsurface reflections that travel at higher velocities.

The high variability in the properties of the near-surface earth layers makes the kinematic modeling of the surface wave a difficult task. Still, we know that the ground roll triggered at a source follows a conical shape that is centered in the physical shot point in the temporal/spatial domain (t, x, y).

At the same time, noise from scatterers is due to the diffracted energy generated by near surface inhomogeneities. The velocities, frequencies, and amplitudes of these scatter-produced surface waves are the same as of those from the ground roll, yet, their temporal/spatial domains are represented by the cones tangent to the ground roll cone. These cones are centered under each scatterer (Meunier et al., 2001).

8.4 Azimuthal Filter in f-k_x-k_y Domain

The ground roll and scattering, although they have the same velocities along the surface of the earth, appear in different cones in the time/space domain. In the Fourier domain, they appear over the same cone centered at $k_x=k_y=0$ (Figure 8.1). However, they are now defined by their azimuth with respect to the center of the k_x-k_y plane for each frequency. This azimuthal distribution of the energy needs to be taken into account to reconstruct the surface noise from the horizontal components in the Fourier domain.

To implement the filter we first compute the 3D Fourier transform for the 3C seismic amplitude cubes in the shot point domain $z(t,x,y)$, defined as:

$$Z(f,k_x,k_y) = \iiint_{-\infty}^{\infty} z(t,x,y) e^{-i2\pi(tf+xk_x+yk_y)} dydxdt, \qquad (2)$$

where f is frequency, k_x and k_y are the wave numbers in the x and y directions, respectively.

In the amplitude data thus transformed, the surface noise energy is concentrated in a cone defined as:

$$\frac{f}{v} = \frac{\sqrt{k_x^2 + k_y^2}}{2}, \tag{3}$$

where, once again, kx and ky are the wave number coordinates, f is the fixed frequency, and v is the velocity of the surface wave. Equation 3 defines a circle in the kx-ky plane whose radius 2f/v increases with increasing frequency.

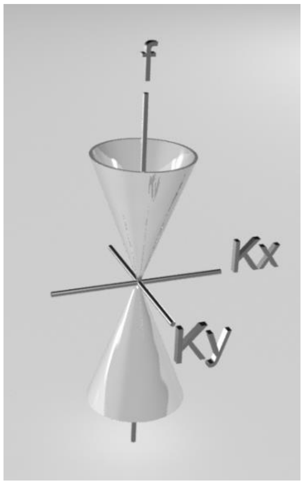

Figure 8.1. Surface noise representation in the Fourier domain.

Because we are sampling the spatial domain xy where the separation between the in-lines (along the x direction) is e_x and the separation between the cross-lines (along the y direction) e_y, this cone is sampled at the nodes of the inline/crossline mesh. This means that in the k_x-k_y plane, the cone (Equation 3) is sampled on a mesh whose lines are separated by $1/e_x$ along k_x and by $1/e_y$ along k_y. Mathematically, this means that the cone is convolved with a filter (comb) with steps $[1/e_x, 1/e_y]$. As a result, the unaliased wave number domain for frequency f and velocity v is defined as:

$$\frac{-1}{2e_x} < \frac{2f}{v} < \frac{1}{2e_x} \cup \frac{-1}{2e_y} < \frac{2f}{v} < \frac{1}{2e_y}\,. \tag{4}$$

Inside these bounds, we select a tapering function for each frequency slice defined as:

$$D(k_x, k_y) = e^{\left(\frac{(-abs\left((k_x - k_{x0})^2 + (k_y - k_{y0})^2 - r^2\right))^{\alpha}}{\varepsilon\beta}\right)}, \tag{5}$$

where k_{xo} and k_{yo} are the coordinates of the origin, $r = f/v$, and ε is ¼(min(e_x,e_y)). Also, the parameters α and β control the thickness of the velocity filter.

We ad-hoc selected α and β by first plotting D from Equation 5 and for $k_{xo} = k_{yo} = 0$ in the k_x-k_y plane, f = 15 Hz, and v = 1000 m/s. This 2D function was plotted for visual convenience as a surface whose elevation varied between 0 and 1 and the width at each elevation was simply D and also colored-coded by the D value. Figure 8.2 shows these surfaces as a function of α and for fixed β = 7.7. Similarly, Figure 8.3 shows these surfaces as a function of β and for fixed α = 4.0. By inspecting these figures, we decided to select α = 4.2 and β = 7.7.

In each frequency plane, the angle φ of the direction of energy propagation was calculated as:

$$\varphi(k_x, k_y) = sign(k_y)\cos^{-1}\left(\frac{k_x}{\sqrt{k_x^2 + k_y^2}}\right), \text{ or } atan2(ky,kx) \tag{6}$$

and is shown in Figure 8.4.

The horizontal projection GR of the surface noise (the ground roll and scatterers combined) was calculated combining the Fourier transforms (X and Y) of the two horizontal signal components at 3C receivers as follows:

$$GR_{horizontal} = D(X\cos\varphi + Y\sin\varphi). \tag{7}$$

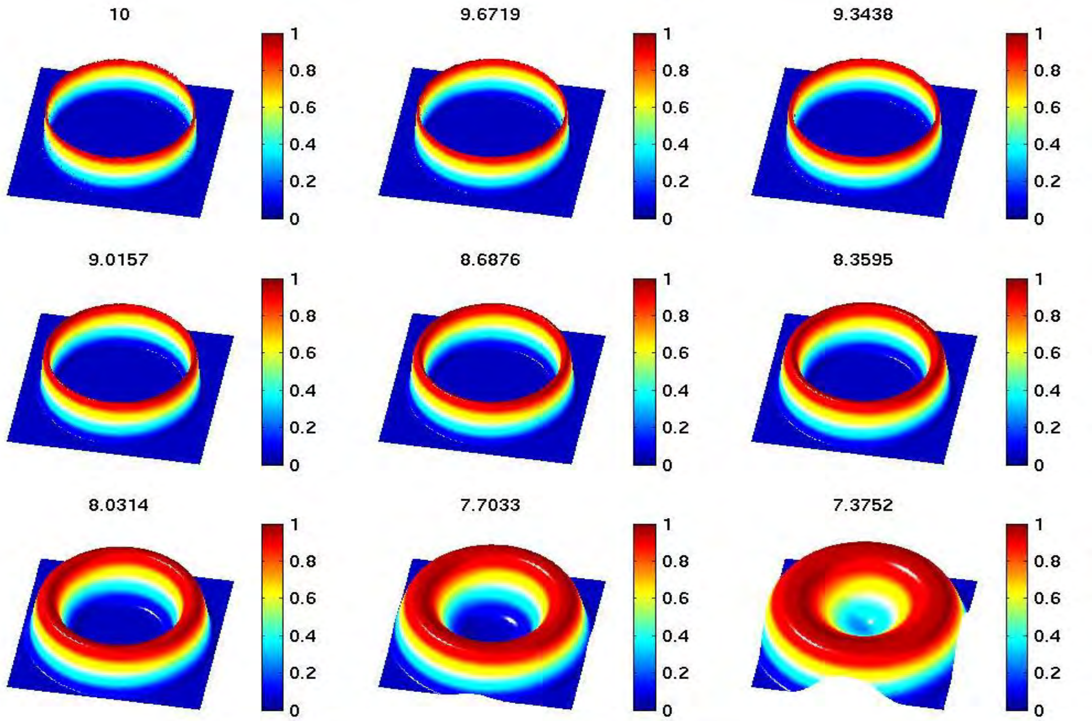

Figure 8.2. D as a function of α (Equation 5) for 15 Hz frequency, 1000 m/s velocity, and $\beta = 7.7$. The α values are listed above each panel.

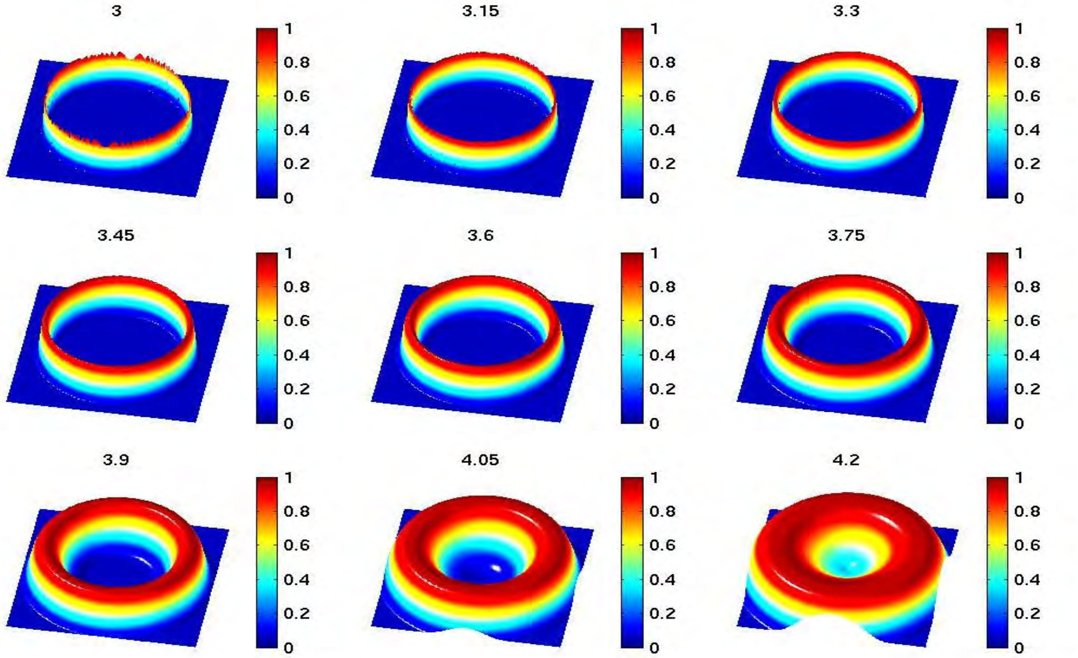

Figure 8.3. D as a function of β (Equation 5) for 15 Hz frequency, 1000 m/s velocity, and $\alpha = 4.0$. The β values are listed above each panel.

The contribution of the surface noise $GR_{vertical}$ to the vertical component of the geophone in the Fourier domain is estimated by using the so-called ellipticity E as:

$$GR_{vertical} = -i * E * GR_{horizontal}. \tag{8}$$

In our synthetic dataset we assumed the $E = 2$. In practical applications, where E is a-priori unknown it can be estimated by minimizing the difference between the measured vertical component GR_Z and the product of E and the horizontal component, which can be done by, e.g., the least squares optimization of the signals from several receivers:

$$\|GR_z - i * E * GR_{horizontal}\|^2 \approx 0. \tag{9}$$

The surface noise $GR_{vertical}$ thus reconstructed is subtracted from the vertical component. In real datasets where the velocity v may vary in space thus making the radius defined by Equation 3 smeared, in order to suppress potential tails in velocity distribution, this difference between the registered vertical component at the receiver and the vertical component of the ground noise is multiplied by

$$H = 1 - \frac{\sqrt[3]{k_x^2+k_y^2}}{\max(\sqrt[3]{k_x^2+k_y^2})}. \tag{10}$$

(Levin, 2016, personal communication).

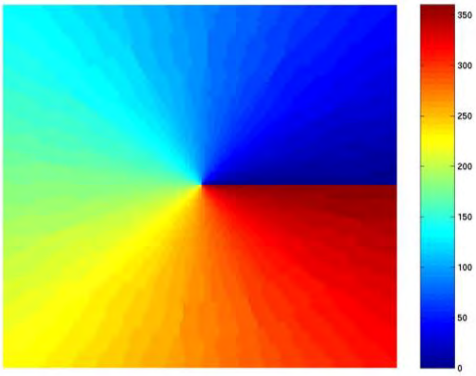

Figure 8.4. The angle of energy propagation (color) according to Equation 6 for a fixed unaliased frequency in the k_x-k_y plane (k_x is the horizontal axis while k_y is the vertical axis).

8.5 Azimuthal Filter for Aliased Frequencies

Recall Equation 4 where the unaliased wave number domain for frequency *f* and velocity *v* is defined. The higher frequencies will be aliased and, hence, cannot be reconstructed at given sampling rate, this zone is defined by:

$$\frac{-1}{2e_x} > \frac{2f}{v} > \frac{1}{2e_x} \cup \frac{-1}{2e_y} > \frac{2f}{v} > \frac{1}{2e_y}. \tag{11}$$

To address this problem and apply the azimuthal filtering over the aliased frequencies, aliasing is conceptualized by additional f-k_x-k_y cones positioned next to the original cone on all sides (Figure 8.5). These additional cones are constructed with their centers having coordinates (c_x/n_xe_x, c_y/n_ye_y), where n_x and n_y are the number of samples in the x- and y-direction, respectively, c_x and c_y are integers, in our case c={±1, ±2, ±3, ±4, ±5}.

In order to incorporate the presence of the new cones in the tapering filter (Figure 8.6) we modified the Equation 5 as follows:

$$D(k_x, k_y) = e^{\left(\frac{(-abs\left(\left(\frac{k_x-c_x}{e_x}\right)^2+\left(\frac{k_y-c_y}{e_y}\right)^2-r^2\right))^{\alpha}}{\varepsilon^{\beta}}\right)}, \tag{10}$$

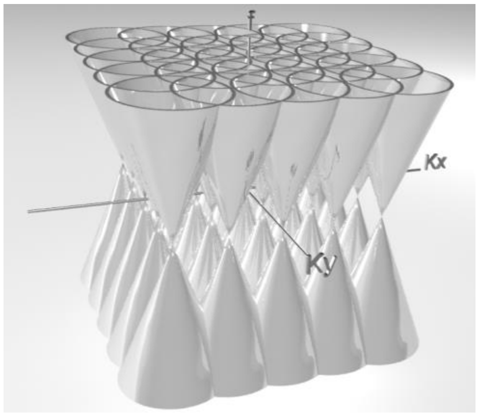

Figure 8.5. Surface noise for aliased frequencies, showing c={±1, ±2, ±3}.

The direction of propagation is calculated in the same fashion using Equation 6 for each decentralized cone (Figure 8.7), however at the intersection between cones coming from different neighbors there is an indetermination of the angle. Therefore, we selected the crossings and computed their inverse to produce zero where they exist, as shown in Figure 8.8, which is included in the horizontal surface noise reconstruction, given by the formula:

$$GR_{horizontal} = Crossings \cdot D \cdot (X \cos\varphi + Y \sin\varphi)\mathrm{c} \tag{11}$$

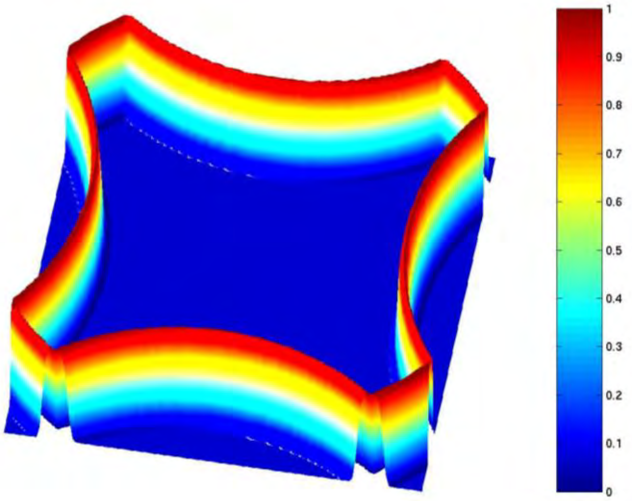

Figure 8.6. Velocity filter at an aliased frequency.

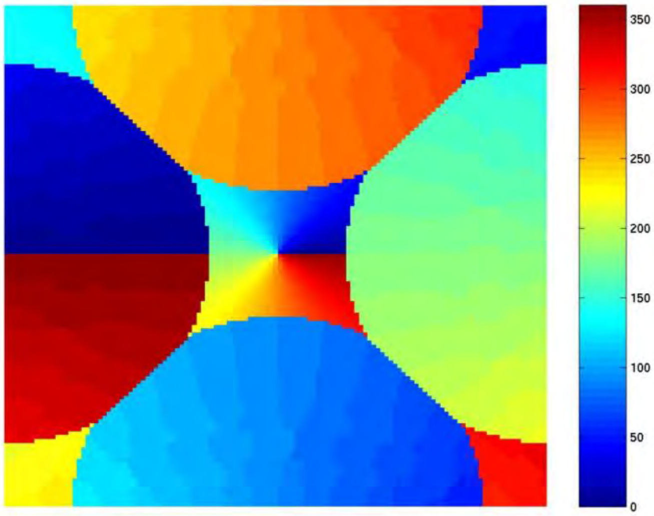

Figure 8.7. Angles of propagation for an aliased frequency of 25 Hz.

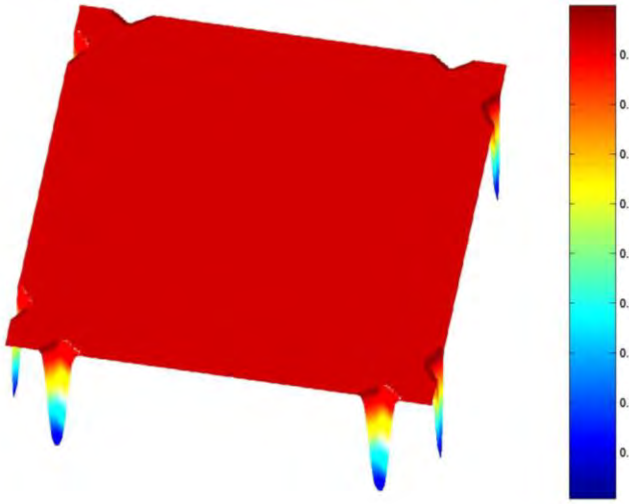

Figure 8.8. Crossings taper at the positions of the intersections for an aliased frequency of 25 Hz.

8.6 Tapering to suppress noise at the boundaries

The manipulation of the finite data in the Fourier domain leads to important boundary noise in the results. To alleviate this we implemented three tapers during the suppression of the surface noise.

1) Tapering in the *(t,x,y)* domain:

   This taper will attenuate the artifacts produced by the truncation at the borders of the seismic cubes. It is applied by multiplying a Hanning bell (Figure 8.9) to the data in the time domain previous to the Fourier transform. In order to remove this bell a small value of 0.1 needs to be added to recover the data after the surface noise suppression.

2) Tapering in the (k_x,k_y) domain:

   To attenuate the effects of the transformation in the wave number we applied a Hamming taper (Figure 8.10) to each frequency.

Figure 8.9. Hanning bell applied to the time slices previous to the Fourier transformation.

Figure 8.10. Hamming taper applied at each frequency in the reconstructed surface noise.

3) Taper in the frequency domain

   The surface noise has lower frequency extension than the reflections; therefore the reconstruction needs to be constrained to the presence of the surface noise and have a smooth transition towards the higher frequencies. A Hanning bell was applied to the frequency axis of the reconstructed surface noise.

8.7 Synthetic model construction

The synthetic model was created with the software Geovecteur® (Appendix B). We calculated three seismic cubes, corresponding to one vertical cube and two horizontals over one Earth model. The idea of the synthetic is as follows: we calculated the travel times of a wave of known velocity and we place one spike at each trace, then we convolved a Ricker wavelet for each wave type and finally we add each different wave to the final cube. The equations to compute the travel times for each wave are:

a) Reflections:

$$t_{reflection} = \sqrt{t_{zero}^2 + \frac{(x_s - x_r)^2}{v^2}}, \tag{12}$$

where t_{zero} is the time at zero offset, x_s the position of the seismic source, x_r the position of the receiver and v the velocity for the reflections (2500 m/s).

b) Refraction:

$$t_{refraction} = t_{intercept} + \frac{x_s - x_r}{v_{refraction}}, \tag{13}$$

where $t_{intercept}$ is the time at where the refraction first appears, and $v_{refraction}$ is the velocity of the refraction (2500 m/s).

c) Ground roll:

$$t_{ground\,roll} = \frac{x_s - x_r}{v_{ground\,roll}}, \tag{14}$$

where $v_{ground\,roll}$ is the velocity of the radial noise (1000 m/s).

d) Scatters:

$$t_{scatter} = \sqrt{\frac{(x_s - x_d)^2}{v_{ground\,roll}^2} + \frac{(x_s - x_r)^2}{v_{ground\,roll}^2}}, \tag{15}$$

where x_d is the position of the scatter, in this synthetic we placed 3 scatterers.

Figure 8.11 shows the final synthetic where all the independent waves have been added. To construct the horizontal cubes, we assumed that the contribution of the reflected and refracted waves were not present in any horizontal receiver, then we dephased by 90° the surface noise from the vertical cube and multiplied it by the ellipticity. Then projected towards the radial and transversal direction, taking into account the source-receiver azimuth.

8.8 Simulation of uneven acquisition geometry

The uneven acquisition geometry is typical in most seismic acquisition patterns due to physical and budget constraints. In order to simulate it, we decided to select one every three traces in one direction of the three seismic cubes. This subsampling is shown in the right on Figure 8.11 for the inline direction, this pattern is common in seismic land surveys.

8.9 Filtering methodology

The surface noise suppression involves the following steps:

1) Hanning tapering of the three components.
2) Fourier transformation applied to time data, to obtain the X, Y and Z cubes.
3) Calculation of the angles, velocity filter and crossings.
4) Estimation of the horizontal surface noise.
5) Hamming tapering of the estimation.
6) Dephasing, velocity filtering and Hanning tapering in the frequency axis.
7) Subtraction from the Z cube.

8) Multiplication by the filtered cubic root of the magnitudes of horizontal ground roll.

9) Inverse Fourier transform.

The result of the application of this methodology is shown in Figure 8.12.

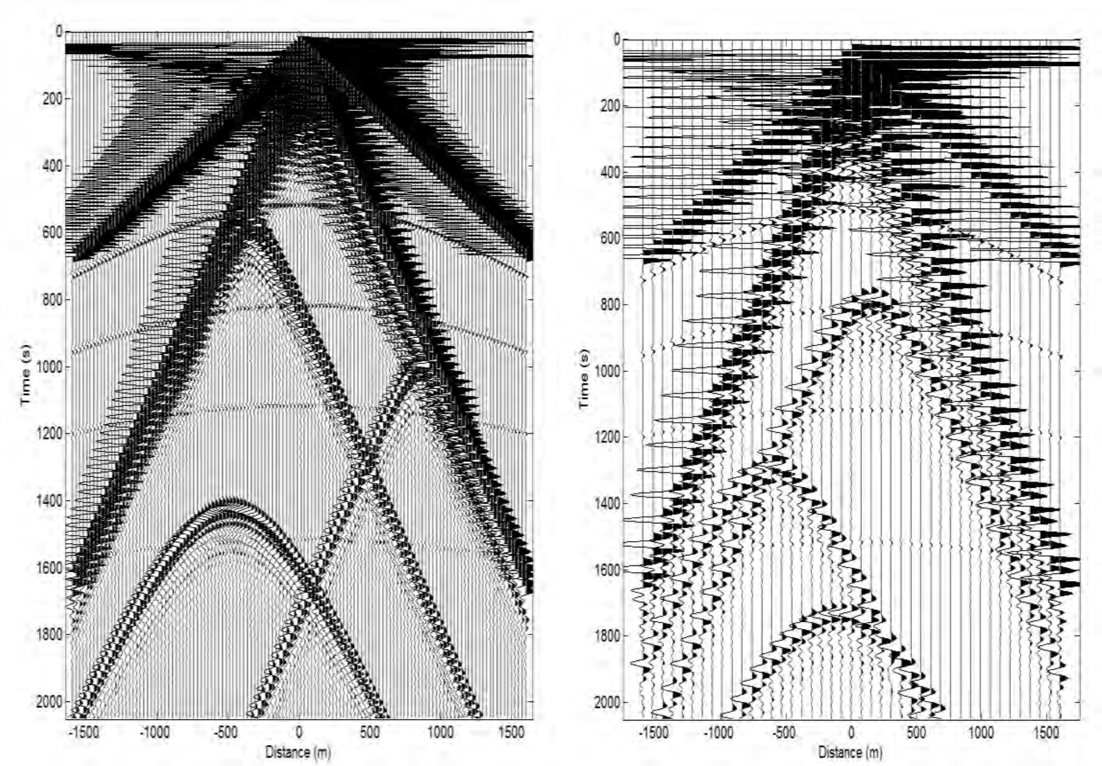

Figure 8.11. Crossline synthetic seismic section (left) and inline subsampled section simulating an irregular acquisition pattern(right). Both in the time-distance domain showing the ground roll (sharp high-amplitude triangle); refraction (blunt triangle); three scatterers (high-amplitude hyperbolas); and four actual P-to-P reflections (blunt low-amplitude hyperbolas).

8.10 Conclusion

The azimuthal filtering is working, the remnant boundary problems can be resolved with better tapering, but the results indicate a satisfactory noise reduction of +40 dB (100 times less noise).

The scattered noise and the ground roll have very high amplitude and therefore adverse impact on land seismic data, the Fourier domain is the only method known able to group them.

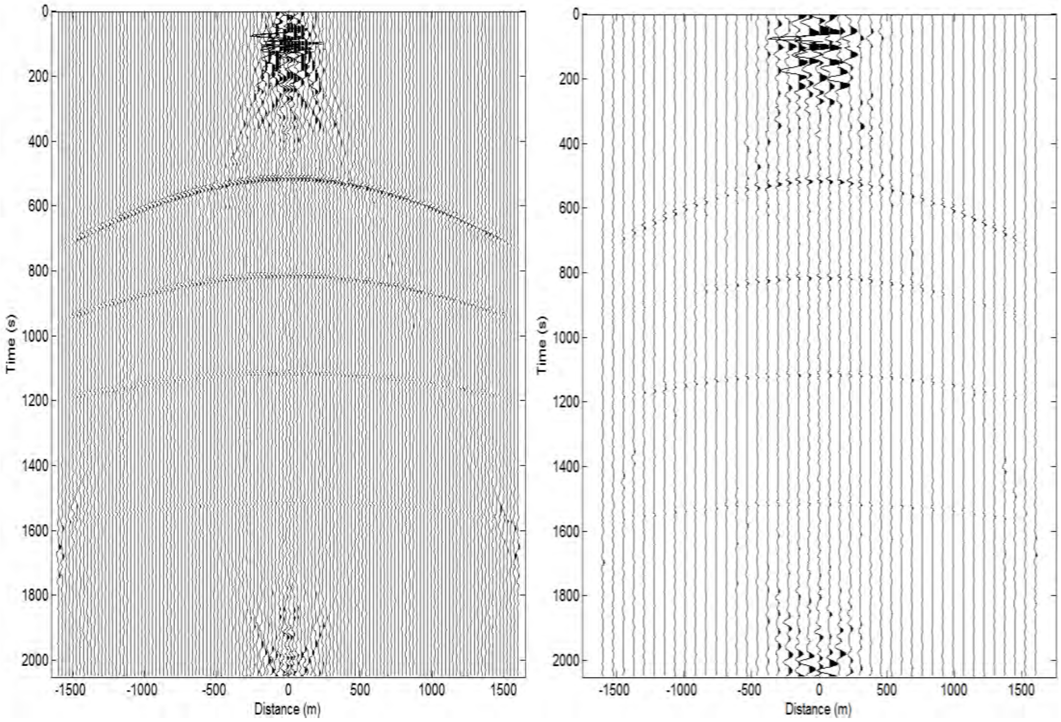

Figure 8.12. Result from the application of azimuthally filtering as explained in the text. The filtering artifacts are in the borders of the seismic section, leaving the reflections clean from ground roll and scatterers.

This method of noise suppression, although applied in synthetic data, gives good expectation that can be successfully applied in real multicomponent seismic data with uneven acquisition.

Final acknowledgements

This material is based upon work supported by Pemex Exploración y Producción, Consejo Nacional de Ciencia y Tecnología (CONACYT), and the Stanford Rock Physics and Borehole Geophysics project. I also thank BHP Billiton, specifically, Sharma Tadepalli ands Juan-Mauricio Florez-Nino for providing the data and advice. Thank you to CGG for providing the inversion software. Thank you to Gary Mavko for sharing the ray tracer used in the applets. Finally, I am deeply grateful to the editors for their helpful comments and suggestions.

Appendices

Appendix A

```
clear
%   Fait par Julien Meunier, Tomas Bianchi et Humberto Arévalo
%%%%%%%%%%%%%%    ENTREE DES VARIABLES      %%%%%%%%%%%%%%%%%%%%%
ssi=0.004;                          % Intervalle d'échantillonnage
lineasy=128;                          % Nombre de géophones en X et Y
lineasx=43;                         % Nombre de géophones en X et Y
% mitad=lineas/2;                     % Moitie de nombre de géophones
muestras=512;                       % Nombre d'échantillons
espaciosy=25;                       % Intervalle entre traces
espaciosx=75;                       % Intervalle entre traces
vitesse=1000;                       % Vitesse du ground roll
lty=6;%32;%24; %32;                                 % Longueur du taper en x y
ltx=ceil(lty/2); %32;                               % Longueur du taper en x y
pwh=.3;%%.19;%0.1;                               % Proportion du taper rajoute
lt=50;
taperty=hann0Orig(lty,lineasy-2*lty,lty)+pwh;  % Taper en x y avec la fonction décrit dans l’appendice A.3
tapertx=hann0Orig(ltx,lineasx-2*ltx,ltx)+pwh;  % Taper en x y avec la fonction décrit dans l’appendice A.3
tapertt=permute(repmat(hann0Orig(lt,muestras-2*lt,lt)+pwh,[1,lineasy,lineasx]),[1,2,3]);
tapert=
permute(repmat((taperty*tapertx')./max(max(taperty*tapertx')),[1,1,muestras]),[3,1,2]).*tapertt./max(max(
max(tapertt)));
lk=6;%6;%5;                                   % Longueur du taper en nombre d'ondes
% taperky=hann0Orig(lk,lineasy-2*lk+1,lk);    % Taper en nombre d'ondes symétrique
taperky=hann0Orig(lk,lineasy-2*lk,lk);    % Taper en nombre d'ondes symétrique
taperky=taperky(1:lineasy);               % Réduction du taper en nombre d’ondes
% taperkx=hann0Orig(lk,lineasx-2*lk+1,lk);    % Taper en nombre d'ondes symétrique
taperkx=hann0Orig(lk,lineasx-2*lk,lk);    % Taper en nombre d'ondes symétrique
taperkx=taperkx(1:lineasx);               % Réduction du taper en nombre d’ondes
fmin=3;%3;%2;                             % Fréquence minimale
fmax=40;%70;%80;%80;                          % Fréquence maximale
tapcroix=18;%11;%15;                        % Taper de croix
fcroix=90;%90;%100;                           % Fréquence maximal de application de croix
tapf=2;%20;%30;%20;                              % Taper en fréquence
ep1=3.75;%4.2;%4.2;%4.3;%4;%4.5;%4.8;%4.2;%3.8;%4;                              % Exposant1 de ampl
ep2=7.7;%7.7;%6.8;%6.9;%7;%7.8%7.7;%7.6;%7.7;%7.3;%7.7;                              % Exposant2 de ampl
```

```
%%%%%%%%%          CALCULS   PRELIMINAIRES   ET   CONSTRUCTION   DES   TAPERS
%%%%%%%%
% correspondance fréquences <-> échantillons
%    fréquence           échantillon
%    -1/2ssi                    1
%      0                   muestras/2+1
% 1/2ssi-1/(muestras*ssi)     muestras
% f = (n-1)/(ssi*muestras) - 1/2ssi   n = 1 + ssi*muestras*(f + 1/2ssi)
n1 = round(1 + ssi*muestras*(-fmax-tapf + 1/(2*ssi)));
n2 = round(1 + ssi*muestras*(-fmin+tapf + 1/(2*ssi)));
n3 = round(1 + ssi*muestras*( fmin-tapf + 1/(2*ssi)));
n4 = round(1 + ssi*muestras*( fmax+tapf + 1/(2*ssi)));
n5 = round(1 + ssi*muestras*(-fcroix + 1/(2*ssi)))-n1;
n6 = round(1 + ssi*muestras*( fcroix + 1/(2*ssi)))-n1;
tf = round(tapf*ssi*muestras) ;
tc = round(tapcroix*ssi*muestras);
taperf =hann0Orig(tf,n4-n1+1-2*tf,tf);
taperf0 =ones(muestras,1)-[zeros(muestras/2-tf-(n3-n2)/2,1) ;...
       hann0Orig(tf,n3-n2,tf);zeros(muestras/2-tf-(n3-n2)/2,1)];
tapc=[zeros(n5,1);hann0Orig(tc,n6-n5+1-2*tc,tc); zeros(n5,1)];
tapf=hann0Orig(tf,muestras-2*tf,tf);
tapf0=ones(muestras,1)-[zeros(muestras/2-2*tf,1) ;...
       hann0Orig(tf,2*tf,tf);zeros(muestras/2-2*tf,1)];
tapfreq=tapf.*tapf0;
taperkk=taperky*taperkx';
taperff=permute(repmat(tapfreq,[1,lineasy,lineasx]),[1,2,3]);
taperfkxky= permute(repmat(taperkk,[1,1,muestras]),[3,1,2]).*taperff;
%% %%%%%%%%%%%%%%%%%     COMPOSANTE X       %%%%%%%%%%%%%%%%%%%
fnx='kadajoX25.cst';
[fidx,nech,ntr,si,ntr_gather,n_gather,bloc,nbytes] =...
   loadcst_gather_preOrig(fnx,22);            % Lecture des données horizontaux, appendice A.4
S=1i.*ones(muestras,lineasy,lineasy);           % Preallocation de mémoire
for Q=1:lineasy                          % Boucle pour réaliser la fft en temps
   [S(:,:,Q),E] = loadcst_gatherOrig(fidx,bloc,nbytes,9,4000,lineasy,nech);
end                                      % Lecture d'un gather, appendice A.5
S=fftshift(fftn(S(:,:,1:3:end).*tapert)).*taperfkxky;%.*permute(repmat(taperty*tapertx',[1,1,muestras]),[3,1
,2])));
Zx(1:n4-n1+1,:,:) = S(n1:n4,:,:);           % Transforme de Fourier 3D et taper
%% %%%%%%%%%%%%%%     COMPOSANTE Y       %%%%%%%%%%%%%%%%%%%%%%
fny='kadajoY25.cst';
[fidy,nech,ntr,si,ntr_gather,n_gather,bloc,nbytes] =...
   loadcst_gather_preOrig(fny,22);
for Q=1:lineasy                          % Boucle pour réaliser la fft en temps
   [S(:,:,Q),E] = loadcst_gatherOrig(fidy,bloc,nbytes,9,4000,lineasy,nech);
end                                      % Lecture d'un gather
S=fftshift(fftn(S(:,:,1:3:end).*tapert)).*taperfkxky;%.*permute(repmat(taperty*tapertx',[1,1,muestras]),[3,1
,2])));
Zy(1:n4-n1+1,:,:) = S(n1:n4,:,:);
%% %%%%%%%%%%%%%%     COMPOSANTE Z       %%%%%%%%%%%%%%%%%%
fnz='kadajoZ25.cst';
[fidz,nech,ntr,si,ntr_gather,n_gather,bloc,nbytes] =...
  loadcst_gather_preOrig(fnz,22);
for Q=1:lineasy                            % Boucle pour réaliser la fft en temps
  [S(:,:,Q),E] = loadcst_gatherOrig(fidz,bloc,nbytes,9,4000,lineasy,nech);
```

```
end
Z=S;
il=linspace(-64,64,128);
[inl,xln]=meshgrid(il);
radi=2.52.*sqrt(inl.^2+xln.^2)+19;
for ii=1:128
  for iii=1:128
    S(1:radi(ii,iii),ii,iii)=0;
  end
end
S=fftshift(fftn(S(:,:,1:3:end).*tapert)).*taperfkxky;%.*permute(repmat(taperty*tapertx',[1,1,muestras]),[3,1
,2])));
Zz(1:n4-n1+1,:,:) = S(n1:n4,:,:);

%%    %%%%%%%%%         EVALUATION    DU    GROUND    ROLL    HORIZONTAL
%%%%%%%%%%%%
%%% Pour économiser la mémoire on peut placer cette évaluation dans Zy
load('norainbow3.mat')
figure('Color','w')
for  c=[1:n4-n1+1]
  f = (c+n1-1)/(ssi*muestras) - 1/(2*ssi);      % Fréquence associée à c
  [phi,ampl,croix]=filpolviejoOrigUneven(lineasx,lineasy,espaciosx,espaciosy,f,vitesse,ep1,ep2);
  % Filtre pour le fréquence tm voir appendice A.2
  % ampl=ones(size(ampl));
  croix=ones(size(croix));
  %    Zxy(c,:,:)=-2i*ampl.*(squeeze(Zx(c,:,:)).*cos(phi)...
  %           +squeeze(Zy(c,:,:)).*sin(phi));   % Reconstruction du ground roll
  Zxy(c,:,:)=(sqrt(Zx(c,:,:).^2+Zy(c,:,:).^2)./max(max(sqrt(Zx(c,:,:).^2+Zy(c,:,:).^2)))).^(1/3);
      cruz(c,:,:)=croix.*tapc(c)+(1-tapc(c)).*ones(lineasy,lineasx);
  med=.4;%median(median(abs(Zxy(c,:,:))));
  for ii=1:lineasy
    for iii=1:lineasx
      if abs(Zxy(c,ii,iii))>= med
        Zxy(c,ii,iii)=1;
      else
      end
    end
  end
 h=1/25*ones(5);
 zZxy(c,:,:)=filter2(h,squeeze(Zxy(c,:,:))');
 Zxy(c,:,:)=filter2(h,squeeze(zZxy(c,:,:))');
 Zxy(c,:,:)=Zxy(c,:,:)./max(max(Zxy(c,:,:)));
  med=.4;%1.*median(median(abs(Zxy(c,:,:))));
  for ii=1:lineasy
    for iii=1:lineasx
      if abs(Zxy(c,ii,iii))>= med
        Zxy(c,ii,iii)=1;
      else
      end
      if isnan(Zxy(c,ii,iii))
        Zxy(c,ii,iii)=0;
      end
    end
  end
```

```
    D(c,:,:)= (Zz(c,:,:) .*(1- Zxy(c,:,:))) .*cruz(c,:,:);
    subplot(231)
    surf(phi); shading flat;axis tight;axis square;view(2);title('\Phi');colorbar; caxis([0 2*pi])
    xlabel('Inline'); ylabel('Xline')
    subplot(232)
    surf(squeeze(ampl)); shading flat;axis tight;axis square;view(2);title('Ampl');colorbar;caxis([0 1])
    subplot(233)
    surf(squeeze(cruz(c,:,:))); shading flat;axis tight;axis square;view(2);title('Cruz');colorbar;caxis([0 1])
    subplot(234)
    surf(squeeze(abs(Zxy(c,:,:)))); shading flat;axis tight;axis square;
    view(2);
    view(-10, 86);
    title('Zxy');colorbar;
    caxis([0 6e6])
    caxis([0 3e6])
    caxis([ 0 1])
    subplot(235)
    surf(squeeze(abs(D(c,:,:)))); shading flat;axis tight;axis square;
    view(2);
    view(-10, 86);
    title('After substraction');colorbar;caxis([0 6e6])
    caxis([0 3e6])
    subplot(236)
    surf(squeeze(abs(Zz(c,:,:)))); shading flat;axis tight;axis square;
    view(2);%
    view(-10, 86);
    title('Vertical');
    title(['frequency =' num2str(f)])
    colorbar;caxis([0 6e6])
    caxis([0 3e6])
    pause(.05); colormap(norain)
end                                       % Taper des croisements
%%              %%%%%%%%%%%%%%%%              Rapport              SIGNAL/BRUIT
%%%%%%%%%%%%%%%%%%%%
for  c=[n1:n4-1]
   rau(c-n1+1) = 10*log(mean(mean(squeeze(S(c,:,:)+ 1.*Zxy(c-n1+1,:,:)).*...
     conj(squeeze(S(c,:,:)+1.*Zxy(c-n1+1,:,:))))))./...
     mean(mean(squeeze(S(c,:,:)).*conj(squeeze(S(c,:,:))))));
end
% figure;plot(rau(isnan(rau)~=1))
%% %%%%%%%%%%%%%%%%   RECONSTRUCTION  %%%%%%%%%%%%%%%%%%%%
taperf=ones(size(taperf));
taperkx=ones(size(taperkx));
taperky=ones(size(taperky));
S(n1:n4,:,:)= D;%(S(n1:n4,:,:) + 1.* Zxy);
S(n1:n4,1,:)=0;                   % Annulation de la fréquence de Nyquist
S(n1:n4,:,1)=0;
S(257,:,:)=0;
taperf0=ones(size(taperf0));
S2 =S;%.*repmat(taperf0,[1,lineasy,lineasx]);   %Taper en fréquence
S3=ifftn(ifftshift(S2));%./((permute(repmat(taperty*tapertx',[1,1,muestras]),[3,1,2])));
%%%%%%%%%%%%%%%%%   figures de contrôle en fréquence (ft)        %%%%%%%%%%%%%
load('sism.mat')
figure('Color','w','Position',[80,40,1780,940]);
```

```
wigc(squeeze(Z(:,64,1:3:end))./max(max(squeeze(Z(:,:,64)))).*50....
      ,1,ceil(linspace(-1600,1600,43)),ceil(linspace(4,2048,512)))
    set(gca, 'Fontsize', 14), xlabel ('Distance (m)');ylabel('Time (s)') , axis square
figure('Color','w','Position',[80,40,1780,940]);
wigc(squeeze(real(S3(:,64,:)))./max(max(squeeze(Z(:,:,64))))*50....%300
    ,1,ceil(linspace(-1600,1600,43)),ceil(linspace(4,2048,512)))
    set(gca, 'Fontsize', 14), xlabel ('Distance (m)');ylabel('Time (s)') , axis square
figure('Color','w','Position',[80,40,1780,940]);
wigc(squeeze(Z(:,:,64))./max(max(squeeze(Z(:,:,64)))).*100....
    ,1,ceil(linspace(-1600,1600,128)),ceil(linspace(4,2048,512)))
    set(gca, 'Fontsize', 14), xlabel ('Distance (m)');ylabel('Time (s)'), axis square
figure('Color','w','Position',[80,40,1780,940]);
wigc(squeeze(real(S3(:,:,22)))./max(max(squeeze(Z(:,:,64))))*100....
    ,1,ceil(linspace(-1600,1600,128)),ceil(linspace(4,2048,512)))
    set(gca, 'Fontsize', 14), xlabel ('Distance (m)');ylabel('Time (s)') , axis square

%[phi,amplitude]=FILTREPOLFK(NL,E,F,VIT,NC)
%   L'idée de cette programme c'est de trouver l'aliasing et les angles de propagation
%   qu'existent dans le problème de ground roll dans un acquisition sismique
%   NL = nombre de traces
%   E = intervalle entre traces
%   F = fréquence
%   VIT = vitesse
%   La fréquence maximale traitée est nc*vit/(2*e);
%   Fonction fait par Julien Meunier, Tomas Bianchi et Humberto Arévalo
function [phi,ampl,croix]=filpolviejo(nl,e,f,vit,ep1,ep2)
nc=9;
if abs(f) < abs(7*vit/(2*e)); nc=7;end
if abs(f) < abs(5*(vit/(2*e))); nc=5;end
if abs(f) < abs(3*(vit/(2*e))); nc=3;end
%if abs(f) < abs((vit/(2*e))); nc=1;end
%nc=5;
n0=4;
d1=1/(4*e);
warning off;
d0=1/(n0*e);                                          % Distance de reference
x=(-1/(2*e):1/(nl*e):1/(2*e)-1/(nl*e))+(1/(2*nl*e));  % KX cellule central
y=(-1/(2*e):1/(nl*e):1/(2*e)-1/(nl*e))+(1/(2*nl*e));  % KY cellule central
xx=repmat(x,length(y),1);                             % Duplicación en Y
yy=repmat(y',1,length(x));                            % Duplication en X
u=nc^2;                                               % Nombre de cercles
ampl=ones(nl,nl);                                     % Déclaration de matrice des amplitudes
phi=zeros(nl,nl);                                     % Déclaration de matrice des angles
maxi=zeros(nl,nl);                                    % Maximum des angles
A=zeros(nl,nl,u);                                     % Matrice des amplitudes
B=zeros(nl,nl,u);                                     % Matrice des angles
D=zeros(nl,nl,u);                                     % Matrice des taper pour les cercles
r=(f/(vit));                                          % Radius
for kx=1:nc                                           % Nombre d'onde X
    x0=(kx-(nc+1)/2)/e;                               % Coordonnée X du centre
  for ky=1:nc                                         % Nombre d'onde Y
      y0=(ky-(nc+1)/2)/e;                             % Coordoné Y du centre
      k=nc*(kx-1)+ky;                                 % Nombre de tranches
      A(:,:,k)=exp((-abs((xx-x0).^2+(yy-y0).^2-r^2))/d1^2);     % Amplitudes
```

```
      D(:,:,k)=exp((-abs((xx-x0).^2+(yy-y0).^2-r^2).^ep1)/d0^ep2);  % Taper
      B(:,:,k)= mod(sign(yy-y0+eps).*acos((xx-x0)./...
            sqrt((xx-x0).^2+(yy-y0).^2)),2*pi);              %  Angles
   end
end
C=floor(1000000000000.*A)+B./1000;                            % Mélange entre l'angle et les cercles
[maxi(:,:),fff]=max(C,[],3);                                  % Maximisation pour la composition
CC=floor(1000000000000.*D)+B./1000;                  % Mélange entre l'angle et les cercles
phi(:,:)= (maxi(:,:)-floor(maxi(:,:))).*1000;        % Composition des angles avec les cercles
ampl=max(D,[],3);                                             % Sélection de valeurs pour composition
ampl=ampl./max(max(ampl));
F=sort(CC,3);
G=(F(:,:,nc^2-1)./max(max(max(F)))).^.5;
croix=(1.-G);
```

Appendix B

```
******************************************************************************
* LIBRI BD              (M777001-M777011)(RW),STG
******************************************************************************
** REFLEXIONS
* LIBRI CN  1           L40,RI20,SI4,MINFAZE
******************************************************************************
** GROUND ROLL
* LIBRI CN  5           L500,B(4,12,35,40),SI4,MINFAZE
**
* LIBRI CN  6           L1084,ANGLE90,SI4
**
******************************************************************************
** Coordonnees
** MOT60     X recepteur
** MOT61     Y recepteur
** MOT62     X source
** MOT63     Y source
** MOT50     X difr1
** MOT51     Y difr1
** MOT52     X difr2
** MOT53     Y difr2
** MOT54     X difr3
** MOT55     Y difr3
** distances
** MOT20     Distance source récepteur (cm)
** MOT30     Distance source difr1 récepteur (cm)
** MOT31     Distance source difr2 récepteur (cm)
** MOT32     Distance source difr3 récepteur (cm)
** MOT56     Distance difr1 récepteur (cm)
** MOT57     Distance difr2 récepteur (cm)
** MOT58     Distance difr3 récepteur (cm)
** angles
** MOT34     azimut Source récepteur
** MOT35     azimut difr1 récepteur
```

```
** MOT36     azimut difr2 récepteur
** MOT37     azimut difr3 récepteur
********************************************************************************
* BOUCL           1
* DAGEN PL            EA     RL2048,SI4,T4,A1
* MODET       EA      EA      *MOT2=64,
                         *MOT29=64,
                         *MOT18=1,
                         *MOT28=1,
                         *MOT23=1,
                         *MOT24=1,
                         *MOT25=1,
                         *MOT26=1,
                         *MOT50=60,2500,MULT,
                         *MOT51=98,2500,MULT,
                         *MOT52=40,2500,MULT,
                         *MOT53=45,2500,MULT,
                         *MOT54=70,2500,MULT,
                         *MOT55=50,2500,MULT,
* MODET       EA      EA      *MOT60=MOT18,.5,PLUS,2500,MULT,
                         *MOT61=MOT28,2500,MULT,
                         *MOT62=MOT29,2500,MULT,
                         *MOT63=MOT02,.5,PLUS,2500,MULT,
* SELEC       EA             BRANCH=B2,N128
* FINBO
*******************************************************************************
* BOUCL           2
* TRANS       EA      EH
* SELEC       EH             BRANCH=B7,N128
* MODET       EA      EA      *MOT60=MOT60,2500,PLUS,
                         *MOT18=MOT18,1,PLUS,
* FINBO
*******************************************************************************
* BOUCL           7
* MODET       EH      AA      *MOT4=MOT18,MOT29,PLUS,
                         *MOT19=MOT28,MOT2,PLUS,
                         *MOT20=MOT62,MOT60,MIN,2,PUIS,
                              MOT63,MOT61,MIN,2,PUIS,PLUS,SQRT,
                         *MOT65=1000000
                         *MOT30=MOT50,MOT62,MIN,2,PUIS,MOT51,MOT63,MIN,
                              2,PUIS,PLUS,SQRT,MOT50,MOT60,MIN,2,PUIS,
                              MOT51,MOT61,MIN,2,PUIS,PLUS,SQRT,PLUS,
                         *MOT31=MOT52,MOT62,MIN,2,PUIS,MOT53,MOT63,MIN,
                              2,PUIS,PLUS,SQRT,MOT52,MOT60,MIN,2,PUIS,
                              MOT53,MOT61,MIN,2,PUIS,PLUS,SQRT,PLUS,
                         *MOT32=MOT54,MOT62,MIN,2,PUIS,MOT55,MOT63,MIN,
                              2,PUIS,PLUS,SQRT,MOT54,MOT60,MIN,2,PUIS,
                              MOT55,MOT61,MIN,2,PUIS,PLUS,SQRT,PLUS,
                         *MOT56=MOT50,MOT60,MIN,2,PUIS,MOT51,MOT61,MIN,
                              2,PUIS,PLUS,SQRT,
                         *MOT57=MOT52,MOT60,MIN,2,PUIS,MOT53,MOT61,MIN,
                              2,PUIS,PLUS,SQRT,
                         *MOT58=MOT54,MOT60,MIN,2,PUIS,MOT55,MOT61,MIN,
                              2,PUIS,PLUS,SQRT,
```

```
* MODET      EH     EH     *MOT61=MOT61,2500,PLUS,
                           *MOT28=MOT28,1,PLUS
* MODET      AA     AA     *MEM=MOT61,MOT63,MIN,
                           *IFZ5
                           *MEM=MOT61,MOT63,MIN,MOT61,MOT63,MIN,ABS,DIV
                           *GOTO6
                           *MEM=1
                           *MOT34=MOT60,MOT62,MIN,MOT20,DIV,
                            ACOS,MEM,MULT,3.1415926535,DIV,180000,MULT
                           *IFGTZ9
                           *MOT34=MOT34,360000,PLUS
* MODET      AA     AA     *MEM=MOT61,MOT51,MIN
                           *IFZ5
                           *MEM=MOT61,MOT51,MIN,MOT61,MOT51,MIN,ABS,DIV
                           *GOTO6
                           *MEM=1
                           *MOT35=MOT60,MOT50,MIN,MOT56,DIV,ACOS,MEM,MULT
                           ,3.1415926535,DIV,180000,MULT
                           *IFGTZ9
                           *MOT35=MOT35,360000,PLUS
* MODET      AA     AA     *MEM=MOT61,MOT53,MIN
                           *IFZ5
                           *MEM=MOT61,MOT53,MIN,MOT61,MOT53,MIN,ABS,DIV
                           *GOTO6
                           *MEM=1
                           *MOT36=MOT60,MOT52,MIN,MOT57,DIV,ACOS,MEM,MULT
                           ,3.1415926535,DIV,180000,MULT
                           *IFGTZ9
                           *MOT36=MOT36,360000,PLUS
* MODET      AA     AA     *MEM=MOT61,MOT55,MIN
                           *IFZ5
                           *MEM=MOT61,MOT55,MIN,MOT61,MOT55,MIN,ABS,DIV
                           *GOTO6
                           *MEM=1
                           *MOT37=MOT60,MOT54,MIN,MOT58,DIV,ACOS,MEM,MULT
                           ,3.1415926535,DIV,180000,MULT
                           *IFGTZ9
                           *MOT37=MOT37,360000,PLUS
* MODET      AA     AA     *MOT40=2
*****************************************************************************
* FILTR      AA     A0     LCN1
*****************************************************************************
* MODET      A0     BB     *MOT22=1500,2,PUIS,MOT20,3700,10,DIV,DIV,2,PUIS,
                            PLUS,SQRT,-1000,MULT
                           *MOT33=MOT22,1000,DIV
* EVERY DI   BB     BC     MOT33
* HISTA LA   BC     R1
*****************************************************************************
* MODET      A0     BB     *MOT22=1100,2,PUIS,MOT20,3600,10,DIV,DIV,2,PUIS,
                            PLUS,SQRT,-1000,MULT
                           *MOT33=MOT22,1000,DIV
* EVERY DI   BB     BC     MOT33
* HISTA LA   BC     R2
*****************************************************************************
```

```
* MODET       A0      BB      *MOT22=800,2,PUIS,MOT20,3200,10,DIV,DIV,2,PUIS,
                        PLUS,SQRT,-1000,MULT
                       *MOT33=MOT22,1000,DIV
* EVERY DI    BB      BC       MOT33
* HISTA LA    BC      R3
****************************************************************************************
* MODET       A0      BB      *MOT22=500,2,PUIS,MOT20,3100,10,DIV,DIV,2,PUIS,
                        PLUS,SQRT,-1000,MULT
                       *MOT33=MOT22,1000,DIV
* EVERY DI    BB      BC       MOT33
* HISTA LA    BC      R4
****************************************************************************************
* EVERY AD    R1      R0      IS1=R2
* EVERY AD    R0      RA      IS1=R3
* EVERY AD    RA      RR      IS1=R4
****************************************************************************************
** GENERATION D'UNE REFRACTION A 2500 m/s INTERCEPT 12 MS AMPLITUDE 1000
* MODET       A0      BB      *MOT22=MOT20,2500,10,DIV,DIV,-1000,MULT,
                        12,1000,MULT,MIN
                       *MOT33=MOT22,-1000,DIV,SQRT,
* EVERY DI    BB      BC       MOT33
* HISTA LA    BC      AE
****************************************************************************************
** GENERATION DE GROUND ROLL RADIAL AMPLITUDE 1000000 ET VITESSE 1000 M/S
* FILTR      AA      A1      LCN5
* MODET       A1      BB      *MOT6=0,
                       *MOT22=MOT20,1000,10,DIV,DIV,-1000,MULT
                       *MOT33=MOT22,-10000,DIV,SQRT
* EVERY DI    BB      BC       MOT33
* HISTA LA    BC      GR
****************************************************************************************
** DIFRACTIONS
* MODET       A1      BB      *MOT22=MOT30,1000,10,DIV,DIV,-1000,MULT,
                       *MOT33=MOT22,-1000,DIV,SQRT,
                       *MOT11=7
* EVERY DI    BB      DD      MOT33
* HISTA LA    DD      D1
* MODET       A1      BB      *MOT22=MOT31,1000,10,DIV,DIV,-1000,MULT,
                       *MOT33=MOT22,-1000,DIV,SQRT,
                       *MOT11=7
* EVERY DI    BB      DD      MOT33
* HISTA LA    DD      D2
* MODET       A1      BB      *MOT22=MOT32,1000,10,DIV,DIV,-1000,MULT,
                       *MOT33=MOT22,-1000,DIV,SQRT,
                       *MOT11=7
* EVERY DI    BB      DD      MOT33
* HISTA LA    DD      D3
* EVERY AD    D1      DD      IS1=D2
* EVERY AD    DD      DE      IS1=D3
* MODET       DE      DE      *MOT11=7
****************************************************************************************
* EVERY AD    RR      A1      IS1=AE
* EVERY AD    A1      A0      IS1=GR
* EVERY AD    A0      A1      IS1=DE
```

```
*****************************************************************************
********GENERATION DE DONNES DEFASSES POUR LE SYNTETIQUE DE TROI
COMPOSANTES**
* FILTR      D1     Q1     LCN6
* EVERY DI   Q1     P1     MOT40
* MODET      P1     Q1     *MOT46=10000
                    *MOT41=MOT35,180000,DIV,3.1415926535,MULT,COS
                    ,MOT46,MULT
                    *MOT42=MOT35,180000,DIV,3.1415926535,MULT,SIN
                    ,MOT46,MULT
                    *MOT11=7
* EVERY DI   Q1     P1     MOT46
* EVERY MU   P1     X1     MOT41
* EVERY MU   P1     Y1     MOT42
***********
* FILTR      D2     Q2     LCN6
* EVERY DI   Q2     P2     MOT40
* MODET      P2     Q2     *MOT46=10000
                    *MOT41=MOT36,180000,DIV,3.1415926535,MULT,COS
                    ,MOT46,MULT
                    *MOT42=MOT36,180000,DIV,3.1415926535,MULT,SIN
                    ,MOT46,MULT
                    *MOT11=7
* EVERY DI   Q2     P2     MOT46
* EVERY MU   P2     X2     MOT41
* EVERY MU   P2     Y2     MOT42
***********
* FILTR      D3     Q3     LCN6
* EVERY DI   Q3     P3     MOT40
* MODET      P3     Q3     *MOT46=10000
                    *MOT41=MOT37,180000,DIV,3.1415926535,MULT,COS
                    ,MOT46,MULT
                    *MOT42=MOT37,180000,DIV,3.1415926535,MULT,SIN
                    ,MOT46,MULT
                    *MOT11=7
                    *MOT11=7
* EVERY DI   Q3     P3     MOT46
* EVERY MU   P3     X3     MOT41
* EVERY MU   P3     Y3     MOT42
***********
* FILTR      GR     G1     LCN6
* EVERY DI   G1     T1     MOT40
* MODET      T1     G1     *MOT46=10000
                    *MOT41=MOT34,180000,DIV,3.1415926535,MULT,COS
                    ,MOT46,MULT
                    *MOT42=MOT34,180000,DIV,3.1415926535,MULT,SIN
                    ,MOT46,MULT
* EVERY DI   G1     T1     MOT46
* EVERY MU   T1     X4     MOT41
* EVERY MU   T1     Y4     MOT42
*******************ADITION
* EVERY AD   X1     X7     IS1=X2
* EVERY AD   X7     X8     IS1=X3
* EVERY AD   X8     X9     IS1=X4
```

```
* EVERY AD    Y1      Y7      IS1=Y2
* EVERY AD    Y7      Y8      IS1=Y3
* EVERY AD    Y8      Y9      IS1=Y4
* MODET       X9      X5      *MOT20=MOT20,100,DIV,
                      *MOT6=0,
                      *MOT1=2000,4,MIN
                      *MOT2=MOT29
                      *MOT17=MOT28
* MODET       Y9      Y5      *MOT20=MOT20,100,DIV,
                      *MOT6=0,
                      *MOT1=2000,4,MIN
                      *MOT2=MOT29
                      *MOT17=MOT28
**********************************************************************************
* MODET       A1      A3      *MOT20=MOT20,100,DIV,
                      *MOT6=0,
                      *MOT1=2000,4,MIN
* MODET       A3      A6      *MOT2=MOT29
                      *MOT17=MOT28
**********************************************************************************
** WUNET      RR              FILE=/proj/POLAR/DATA/aversynthreflex25.cst,
** WUNET      D1              FILE=/proj/POLAR/DATA/aversynthdifrac125.cst,
** WUNET      D2              FILE=/proj/POLAR/DATA/aversynthdifrac225.cst,
** WUNET      D3              FILE=/proj/POLAR/DATA/aversynthdifrac325.cst,
** WUNET      AE              FILE=/proj/POLAR/DATA/aversynthrefrac25.cst,
** WUNET      GR              FILE=/proj/POLAR/DATA/aversynthground25.cst,
* WUNET       X5            FILE=/proj/POLAR/DATA/kadajoX25.cst,
* WUNET       Y5            FILE=/proj/POLAR/DATA/kadajoY25.cst,
* WUNET       A6            FILE=/proj/POLAR/DATA/kadajoZ25.cst,
** ECRITURE SUR UNE FICHIER
* FINBO
* PROCS                1B1 **INDIQUE COMBIEN DE FOIS LES LOOPS DOIT ETRE FAITS
```

List of References

Aki, K., and Richards, P.G., 2002, Quantitative seismology: Theory and methods, University Science Books.

Alves Vanzeler, F. J., Hounie, J. N., Fernandes Coelho, F. S., 2014, A strategy for simultaneous joint inversion applied to 3D depth migrated PP and PS seismic data, SEG Technical Program Expanded Abstracts, 3102-3105.

Angeleri, G.P., and Carpi, R., 1982, Porosity prediction from seismic data, Geophys. Prosp., **30**, 580-607.

Arévalo-López, H.S., and Dvorkin, J., 2016, Porosity, mineralogy, and pore fluid from simultaneous impedance inversion, The Leading Edge, **35**, 423-429.

Arévalo-López, H.S., and Dvorkin, J.P., 2017, Rock physics diagnostics of a turbidite oil reservoir offshore Northwest Australia, Geophysics, **82**(1), MR1-MR13.

Avseth, P., Dvorkin, J., Mavko, G., 2000, Rock physics diagnostics of North Sea sands: Link between microstructure and seismic properties. Geophys. Res. Lett. **27**, 2761-2764.

Avseth, P., Mukerji, T., and Mavko, G., 2005, Quantitative seismic interpretation: Applying rock physics tools to reduce interpretation risk, Cambridge University Press.

Avseth, P., Mukerji, T., Mavko, G., and Dvorkin, J., 2010, Rock-physics diagnostics of depositional texture, diagenetic alterations, and reservoir heterogeneity in high-porosity siliciclastic sediments and rocks — A review of selected models and suggested work flows, Geophysics, **75**(5), 75A31-75A47.

Barenblatt, G. I., 2003, Scaling, Cambridge University Press.

Barkved, O., Bartman, B., Gaiser, J., Johns, T., Kristiansen, P., Robert, T. and Thompson, M., 2004, The many facets of multicomponent seismic data, Oilfield Review, **16**, 42-56.

Batzle, M., and Wang, Z., 1992, Seismic properties of pore fluids, Geophysics, **57**(11), 1396-1408.

Berner, Robert A., 1980, Early diagenesis, a theoretical approach, Princeton University Press.

Bourbie, T., Coussy, O.,and Zinszner, B., 1987, Acoustics of porous media, IFP publications, Editions Technip.

Cheng, A., 2015, Can we ever trust the shear-wave log? The Leading Edge, **34**, 278-284.

Daniel, R. and Kaldi, J., 2012, Atlas of Australian and New Zealand Hydrocarbon Seals: Worldwide analogs for cap rocks and intraformational barriers in clastic depositional settings, Am. Assoc. Pet. Geol. Studies in Geology, **60**.

Dolberg, D. M., Helgesen, J., Hanssen, T. H., Magnus, I., Saigal, G., and Pedersen, B.K., 2000, Porosity prediction from seismic inversion, Lavrans Field, Halten Terrace, Norway, The Leading Edge, **19**, 392-399.

Draege, A., 2011, A diagenetic rock physics approach for siliciclastics, The Leading Edge, **30**, 1368–1375.

Dvorkin, J., 2007, Self-similarity in rock physics, The Leading Edge, **26**, 946-950.

Dvorkin, J. P., 2007b, Yet another Vs equation, Geophysics, **73**(2), E35-E39.

Dvorkin, J., Gutierrez, M., and Grana, D., 2014, Seismic reflections of rock properties, Cambridge University Press.

Dvorkin, J., Mavko, G. and Nur, A., 1991, The effect of cementation on the elastic properties of granular material, J. Mech. Mat., **12**, 207-217.

Ementon, N., Hill, R., Flynn, M., Motta, B., Sinclair, S., 2004, Stybarrow oil field – from seismic to production, the integrated story so far, Society of Petroleum Engineers Asia Pacific Oil and Gas Conference and Exhibition, Perth, Australia.

Gal, D., Dvorkin, J., and Nur, A., 1999, Elastic-wave velocities in sandstones with non-load-bearing clay, Geophys. Res. Lett., **26**, 939-942.

Gassmann, F., 1951, Über die Elastizität poröser Medien, Veirtel. Naturforsch. Ges., **96**, 1–23.

Gavin, L., Lumley, D., Shragge, J., 2012, Seismic azimuthal anisotropy analysis for estimating reservoir properties at Stybarrow Field, NW Shelf, Australia, ASEG Extended Abstracts, 22th International Geophysical Conference and Exhibition.

Geoscience Australia, 2014, Release Areas W14-17 and W14-18, Exmouth Sub-basin and southern Exmouth Plateau, Northern Carnarvon Basin, Western Australia, Australian Government. Department of Industry.

Geoscience Australia, 2015, Regional Geology of the Northern Carnarvon Basin. Australian Government, Department of Industry and Science, Australia 2015.

Geoscience Australia, 2016, Release Areas W16-24 and W16-25, Exmouth Sub-basin Northern Carnarvon Basin, Western Australia, Australian Government, Department of Industry, Innovation and Science, Australia 2016.

Greenberg, M. L. and Castagna, J. P., 1992, Shear-wave velocity estimation in porous rocks: Theoretical formulation, preliminary verification and applications, Geophys. Prospect, **40**, 195–209.

Gutierrez, M.A., and Dvorkin, J., 2010, Rock physics workflows for exploration in frontier basins, 80th Annual International Meeting, SEG, Expanded Abstracts, 2441-2446.

Hampson, D. P., Russell, B. H., and Bankhead, B., 2005, Simultaneous inversion of prestack seismic data, SEG Technical Program Expanded Abstracts, 1633-1637.

Han, D., Nur A., and Morgan D., 1986, Effects of porosity and clay content on wave velocities in sandstones, Geophysics, **51**(11), 2093-2107.

Hill, R., 1952, The elastic behavior of a crystalline aggregate, Proc. Phys. Soc. Sec. A, **65**, 349-354.

Hilterman, F., 1989, Is AVO the seismic signature of rock properties?, 59th Ann. Mtg: Soc. of Expl. Geophys., 559.

Hossain, Z., and Newton, P., 2013, Advanced rock physics diagnostic: A new method for cement quantification, SEG Technical Program Expanded Abstracts, 2681-2685.

Jeong, W., and Min, D. J., 2012, Application of acoustic full waveform inversion for density estimation, SEG Technical Program Expanded Abstract, 1-5.

Kittridge, M. G., 2006, Modulus-domain rock physics diagnostics: New insights in realistic granular media: SEG Technical Program Expanded Abstracts, 1871-1875.

Krief, M. J., Garat, J., Stellingwerff, J. and Ventre, J., 1990, A petrophysical interpretation using the velocities of P and S waves (full-waveform sonic), The Log Analyst, **31** , 355 –369.

Landes, K. K., 1946, Porosity through dolomitization, Am. Assoc. Pet. Geol. Bull., **30**, 305-318.

Latimer, R. B., Davidson, R., and van Riel, P., 2000, An interpreter's guide to understanding and working with seismic-derived acoustic impedance data, The Leading Edge, **19**, 242-256.

Leiceaga, G. G., Silva, J., Artola, F., Marquez, E., and Vanzeler, J., 2010, Enhanced density estimation from prestack inversion of multicomponent seismic data, The Leading Edge, **29**, 1220-1226.

Liner, Christopher L. 1999, Elements of 3-D Seismology, PennWell Publishing, 50-51.

Mavko, G., Chan, C., Mukerji, T., 1995, Fluid substitution: Estimating changes in VP without knowing VS, Geophysics, **60**(6), 1750-1755.

Mavko, G., Mukerji, T., and Dvorkin, J., 2009, The rock physics handbook: Tools for seismic analysis of porous media, Cambridge University Press.

Meunier, J., Beckey, M., 2001, Application of two ground roll reduction techniques to scattered ground roll, 63th European Association of Geoscientists and Engineers Conference & Exhibition.

Mindlin, R.D., 1949. Compliance of elastic bodies in contact, J. of Appl. Mech., **16**, 259-268.

Murray, R. C., 1960, Origin of porosity in carbonate rocks, J. of Sediment. Petrol., **30**, 59-84.

Napalowski, R., Hill, R. A., Stomp, R. J., Fagervik, E. N., Derkach, E., and Manning, D. K., 2010, Successful implementation of horizontal openhole gravel packing in the Stybarrow field, offshore western Australia, Soc. Petrol. Eng., **116434**, 123-136.

Ostrander, W.J., 1982, Plane-wave reflection coefficients for gas sands at nonnormal angles of incidence, 52nd Annual International Meeting, SEG, Expanded Abstracts, 216-218.

Ostrander, W. J., 1984, Plane-wave reflection coefficients for gas sands at nonnormal angles of incidence, Geophysics, **49**(10), 1637-1648.

Pendrel, J., 2006, Seismic inversion — Still the best tool for reservoir characterization, CSEG Rec., **31**, 1, 5–12.

Pevzner R., Gurevich B. and Urosevic M., 2011, Estimation of azimuthal anisotropy from VSP data using multicomponent S-wave velocity analysis, Geophysics, **76**(5), D1–D9.

Qin, B., and Lambare, G., 2016, Joint inversion of velocity and density in preserved-amplitude full-waveform inversion, SEG Technical Program Expanded Abstracts, 1325-1330.

Reuss, A., 1929, Berechnung der Fließgrenzen von Mischkristallen auf Grund der Plastizitätsbedingung für Einkristalle, Z. Angew. Math. Mech., **9**, 49-58.

Ricker, N., 1943, Further developments in the wavelet theory of seismogram structure, Bull. Seism. Soc. America, **33**, 197-228.

Ross, M.I., and Vail, P.R., 1994, Sequence stratigraphy of the lower Neocomian Barrow delta, Exmouth Plateau, northwestern Australia, Purcell, P. G. & Purcell, R. R., eds., The sedimentary basins of western Australia, Proceedings of Petroleum Exploration Society of Australia Symposium, Perth, 435-447.

Sahimi, M.,1994, Applications of percolation theory, Taylor & Francis.

Schlumberger Limited, 1987, Log interpretation principles/applications, Schlumberger Educational Services.

Shuey, R. T., 1985, A simplification of the Zoeppritz equations, Geophysics, **50**(4), 609-614.

Soldo, J., 2006, Petro-acoustic properties estimation using seismic simultaneous inversion: Are we there yet? SEG Technical Program Expanded Abstracts, 2077-2081.

Spikes, K.T., 2008, Probabilistic seismic inversion based on rock physics models for reservoir characterization, Ph.D. Thesis, Stanford University.

Stagg, H.M.J., Alcock, M.B., Bernardel, G., Moore, A.M.G., Symonds, P.A. and Exon, N.F., 2004, Geological framework of the outer Exmouth Plateau and adjacent ocean basins. Canberra, Geoscience Australia Publication.

Sumita M., Sakata K., Hayakawa Y., Asai S., Miyasaka K., and Tanemura M., 1992, Double percolation effect on the electrical conductivity of conductive particles filled polymer blends, J. Colloid Polym. Sci., **270**, 134-139.

Thomas, E. C., and Stieber, S. J., 1975, The distribution of shale in sandstones and its effect upon porosity, 16th Annual Logging Symposium, Society of Petrophysicists and Well Log Analysts, Paper T.

Tosaya, C., and Nur, A., 1982, Effects of diagenesis and clays on compressional velocities in rocks, Geophys. Res. Lett., **9**, 5-8.

Uden, R., Dvorkin, J., Walls, J., and Carr, M., 2003, Rock physics diagnostic in a sand/shale sequence: SEG Technical Program Expanded Abstracts, 1676-1679.

Valenti, J., 2009, Porosity prediction from seismic data using multiattribute transformations, N Sand, Auger Field, Gulf of Mexico, M.S. Thesis, Pennsylvania State University.

Vassallo, M., Ozebek, A., Eggenberger, K., Ozdemir, K, van Manen, D.J., and Robertsson, J.O.A., 2011, Matching pursuit methods applied to multicomponent marine seismic acquisition: the issue of crossline aliasing, 73th European Association of Geoscientist and Engineers Conference and Exhibition, A043, 1-5.

Vernik, L., Fisher, D., and S. Bahret, 2002, Estimation of net-to-gross from P and S impedance in deepwater turbidites: The Leading Edge, **21**, 380–387.

Williams, D. M., 1990, The acoustic log hydrocarbon indicator, Society of Petrophysicists and Well Log Analysts, 31st Annual Logging Symposium, W1-W22.

Yin, H., 1992, Acoustic velocity and attenuation of rocks: Isotropy, intrinsic anisotropy, and stress induced anisotropy, Ph. D. thesis, Stanford University.

Yu, G., Zhang, Y., Newton, P., and Azizov, I., 2014, Rock physics diagnostics and modeling for shale gas formation characterization in China, 85th Annual International Meeting, SEG, Expanded Abstracts, 3031-3035.

Zoeppritz, K. B., 1919, Erdbebenwellen VIIIB, Über Reflexion und Durchgang seismischer Wellen durch Unstetigkeitsflächen, Gottinger Nachrichten, **I**, 66-84.